Title

Integrated electrophoretic cytometry separations and immunoassays for proteins and their complexes

Author

Vlassakis, Julea

Publication Date

2018

Peer reviewed|Thesis/dissertation

Integrated electrophoretic cytometry separations and immunoassays for proteins and their complexes

By

Julea Michelle Vlassakis

A dissertation submitted in partial satisfaction of the

requirements for the degree of

Joint Doctor of Philosophy

with the University of California, San Francisco

in

Bioengineering

in the

Graduate Division

of the

University of California, Berkeley

Committee in charge:

Professor Amy E. Herr, Chair
Professor Bo Huang
Professor Jennifer Doudna

Summer 2018

Integrated electrophoretic cytometry separations and immunoassays
for proteins and their complexes

By

Julea Michelle Vlassakis

Abstract

Integrated electrophoretic cytometry separations and immunoassays
for proteins and their complexes

By

Julea Michelle Vlassakis

Joint Doctor of Philosophy in Bioengineering

With University of California, San Francisco

University of California, Berkeley

Professor Amy E. Herr, Chair

Protein complexes, such as filamentous actin (F-actin) complexes, regulate key cell processes such as cell motility and division. Disruption of F-actin result in highly motile and invasive cancer cells. Cancer therapeutics have thus aimed to maintain F-actin, but cell-to-cell variation in F-actin levels in response to such therapeutics necessitate single-cell measurements of dynamic actin protein complexes, including the binding actin binding proteins that determine actin polymerization state. Protein complex levels cannot be inferred from an immunoassay, as most lack selective antibodies. Size-based separations of such protein species provide selectivity when coupled with an immunoassay for protein detection and quantitation. While this selectivity has been demonstrated at the single-cell level by the introduction of electrophoretic (EP) cytometry in our lab, we sought to establish a single-cell electrophoretic assay for protein complex identification and quantitation.

In order to understand the regulation of actin polymerization and depolymerization in heterogeneous cells requires four key separation assay features: i) quantifiable technical variation to discern biological variation in the cell population ii) sufficient analytical sensitivity to detect F-actin bound actin binding proteins, iii) high-selectivity separations to detect actin and its binding proteins, and iv) sample preparation with assay stage-optimized buffers to isolate dynamic complexes without disrupting the complexes. We will share our studies to elucidate chemical and physical underpinnings of each of these needed features. First, we will describe algorithm development and applications to establish a technical variation threshold and protein sizing standards for electrophoretic (EP) cytometry to distinguish biological variation of protein expression and size in single cells. Next, we will discuss the impact of in-gel immunoassay performance and open microfluidic device design on analytical sensitivity. Given fundamental tradeoffs between in-gel immunoassay sensitivity and separation performance, we consider alternative sieving matrices tuned to separate proteins in specific molecular weight ranges. We then describe unique impacts of Joule heating on separation performance in open microfluidic electrophoresis. Joule heating is mitigated with a buffer exchange approach that reduces variation in separation performance and introduces assay stage-optimized buffers without further protein loss.

Finally, we will discuss the design of EP cytometry to fractionate actin protein complexes from single cells with assay stage-optimized buffers. The microscale device achieves rapid, arrayed on-chip sample preparation and EP fractionation without perturbing complexes. We demonstrated F-actin separations from monomeric actin, and the measurement of F-actin binding proteins that regulate actin polymerization. We anticipate the single-cell protein complex measurements described here will be broadly applicable to protein complexes that drive human health.

TABLE OF CONTENTS

LIST OF FIGURES

CHAPTER 1 INTRODUCTION

CHAPTER 2 ALGORITHM DESIGN FOR ELECTROPHORETIC CYTOMETRY

CHAPTER 3 DISSECTING BIOLOGICAL FROM TECHNICAL VARIATION IN ELECTROPHORETIC CYTOMETRY

CHAPTER 4 EFFECT OF POLYMER HYDRATION STATE ON IN-GEL IMMUNOASSAYS

CHAPTER 5 ALTERNATIVE HYDROGELS FOR ELECTROPHORETIC CYTOMETRY TUNED FOR PROTEINS OF SPECIFIC MOLECULAR WEIGHTS

CHAPTER 6 JOULE HEATING-INDUCED DISPERSION IN OPEN MICROFLUIDIC ELECTROPHORETIC CYTOMETRY

CHAPTER 7 ELECTROPHORETIC CYTOMETRY COMPLEX FRACTIONATION ISOLATES ACTIN CYTOSKELETAL COMPLEXES FROM SINGLE CELLS

APPENDICES

To my family.

"*I am not throwing away my shot.*"
-Alexander Hamilton in *Hamilton* by Lin Manuel Miranda

Acknowledgements

I am thankful to so many people and organizations for the role that they have played in my journey as a PhD student. Among those I am most (literally) indebted to are the funding agencies that have supported my research. Thank you to UCSF for the Matilda Edlund Fellowship, the National Science Foundation for the Graduate Research Fellowship, and the Society for Lab Automation and Screening for the Graduate Education Fellowship Grant. Additionally, Amy's funding from the National Institutes of Health, Department of Defense and Chan Zuckerberg Initiative have all been pivotal in enabling me to pursue cutting edge research.

I have been afforded outstanding opportunities to tackle major research challenges alongside fantastic collaborators. I enjoyed joining for meetings with Dr. Stefanie Jeffrey as the circulating tumor cell project was being defined. The last two years it has been amazing working with Dr. Ryo Higuchi-Sanabria and Dr. Andrew Dillin as we establish new methods for measuring protein complexes at the single-cell level. Ryo's patience, positive energy and unstoppable nature has been exactly what we needed to invent and apply these novel assays.

I am grateful to have had fantastic interactions with Berkeley and UCSF faculty members who have advanced my research and career with their feedback. My qualifying exam committee was balanced and thoughtful, so thank you to Dave Schaffer, Laura Waller, Danielle Tullman-Ercek, and Adam Abate. It has been a thrill meeting with my dissertation committee members, Bo Huang and Jennifer Doudna and your incisive comments and enthusiasm were extremely motivating. Finally, I must thank my informal mentors, including Aaron Streets and Markita Landry, both of whom provided invaluable feedback on my future research directions as I prepared to give my first department seminar this spring.

All of this research would also not be possible without a slough of un-sung heroes who did not contribute directly to the science and engineering but supported me in other ways. Thank you to Paul Lum and Mary West for always helping to make sure that the BNC and Stem Cell Facility resources were serving me well as a researcher. I am very appreciative for administrative figures such as Kristin Olson, Catherine Dea, April Alexander, SarahJane Taylor, Kathleen Tronnes and Jeanne Powers who handled items such as ensuring I had health insurance and approving BearBuy purchases that got stuck in the ordering system (among other things). Dawn and Danny, thank you for your hard work to keep Stanley Hall sparkling clean. Every time I had to buy Danny a soda for losing bets that the Red Sox would beat the Yankees was worth it. Thank you to Mike Bentley for running a tight ship and getting deliveries to us in lab, and for fun chats about our fantasy football teams. Finally, thank you to Thom Opal, Dave Rogers and Jerry for playing important roles in keeping researchers and students at Berkeley safe.

My time at Berkeley has also been enriched by fantastic peers and friends. Thank you to Cohort 2012 for being great ski cabin trip friends, and for your continued creativity for five straight years of retreat skit hijinks. I am especially grateful to have gone on numerous adventures with Britta in which we wrote unique song parodies (largely while in kayaks) and road tripped to Disney land. Also, I am thankful to (roommate) Amy for being the easiest person to live with ever. I am further proud to have established the Fenton's Sundae of the Month Club and am thankful to core members Sophie, Donald, Kevin and George for eating so many sundaes with

me and helping me de-stress. To all of the friends I made and reconnected with in graduate school: the laughs, smiles, failures and triumphs we have shared made these years so special and formative for me.

It has also brought me tremendous joy to mentor and teach as a graduate student. From serving as a GSI in Amy's microfluidics course to the two fantastic summers at Cold Spring Harbor Lab's Single Cell Analysis Course, I have been so fortunate to work with outstanding and curious students. The seven rotation students and undergraduate that I had the thrill of mentoring during their time in the lab taught me at least as much as I taught them. I am grateful to Sabrina Soracco and Linda Von Hoene for furthering my training in the Mentoring in Higher Education course, SMART research and mentoring program, and the Summer Institute for Preparing Future Faculty.

I am proud to be a member of the Herr lab—both for the science and the people. My time in the Herr lab was shaped by crucial peer and senior colleague mentors. These mentors included Rob, Augusto, Todd (both for research and pun-related feedback), Monica, Rachel, Ginny and Kevin. Thank you to Kevin for numerous coffee or lunch trips in which we shared our latest research findings, discussed troubleshooting or an exciting new paper we had read and entertained ourselves (e.g., by intentionally mispronouncing names of restaurants on Euclid street until they were practically unrecognizable). I learned so much about engineering from you during those discussions. I am forever grateful to have had such a great lab buddy and to have made a friend for life. Ginny, working alongside "the machine" was invigorating to me. Your energy and drive are awesome. There is a spot waiting for Chloe in my future lab. Ginny's and Eli's international weddings were among one of the greatest experiences of my time as a graduate student. Exploring (really just eating our way through) Taipei and Barcelona with Kevin, Eli, Rob, Hector, Ginny, Elaine, Andoni, John and Amy was a blast. Herr lab members are not just fun people to be around. I have been pushed by these world-class scholars day in and day out. Lab members ask deep and thoughtful questions non-stop during group meeting. We rally around each other when preparing for stressful times like qualifying exams. Herr lab members help one another every day, both with technical research items and facing the challenges and failures of research. The supportive through and through environment of the Herr lab is no accident, and it stems from the example set by Amy as our adviser.

It has been the utmost privilege working with Amy Herr throughout my PhD. Amy will literally traverse the globe in order to help her students. Despite having just traveled 12 hours from Switzerland, she came to campus just to provide feedback on a practice presentation for my first conference talk. In support of her mentees, no task is too small or too great for Amy. She darts between her student's posters at conferences, delivering water so that we stay hydrated while presenting. She has spent countless hours carefully scrutinizing manuscript drafts or figure outlines and discussing finer points of proposal-writing with me. She became co-director of a hands-on laboratory course at Cold Spring Harbor Labs (CSHL) in New York, just to give myself and other students the teaching and networking opportunity. At CSHL we shared many special experiences, (including saving a baby bird). One instance that stands out was the time that she assembled a sandwich for me (with bacon despite her vegetarianism) when I was too busy working with the students in the lab to get lunch. She is quite simply the most devoted research mentor that I know and wants the best for her students. She once told me to "sit at the

table” during group meeting, a symbolic reminder to make my presence known as a female engineer. Amy opened up doors to once-in-a-lifetime opportunities, such as nominating me so I could attend to the Lindau Meeting of Nobel Laureates. Her confidence that I would make the most of such opportunities prompts me to dream bigger for the future. Every day I am thankful to have found not just an outstanding graduate adviser, but a mentor for life. Thank you, Amy.

I have obviously had an incredible time as a graduate student but being away from my family was equally difficult. Observing my sister, Janine, overcome substantial adversity around this same time in her life was a source of strength for me. Graduate students tend to complain a fair amount (some of which is completely warranted), but Janine’s continued positivity motivates me to see silver linings even when I may be struggling. I am also so thankful for my parents’ support and patience these last 6 years (and all the previous years too!). My parents invested in my education from the very beginning when I was a Montessori student. They have always helped me find educational environments where I could thrive and supported my decisions to attend the Commonwealth School and Smith College. Something I so appreciate is that throughout this investment in my intellectual growth, they have never put pressure on me. Instead, they stand by with the compassion to remind me when I am being too hard on myself, and the confidence that I can do anything to which I set my mind. Their love has fueled me all the way to this point. I am thankful for our countless Skype calls, which have brightened my spirits daily (and resulted in them learning quite a bit about single-cell protein electrophoresis). Thank you to my family for everything, and I love you all so much.

Chapter 1

Introduction

Single-cell protein analysis benchmarking table and summaries of techniques was originally produced in collaboration with Kevin Yamauchi. Portions of the content are reproduced with permission from C. Kang, K. A. Yamauchi, J. Vlassakis, E. Sinkala, T.A. Duncombe and A. E. Herr. Single-cell resolution western blotting (2016) *Nat. Prot.* **11**, 1508-1530.

1. The need for single-cell protein analysis

Individual cells are molecularly unique. Cell-to-cell heterogeneity necessitates single-cell analysis, as bulk measurements have been shown to be unrepresentative of the expression level of any individual cell[1]. Heterogeneity does not inherently have functional importance. However, specific instances of cellular heterogeneity have been shown to drive processes including acquisition of cancer drug resistance[2] or metastasis[3]. Therefore, single-cell analysis has been a growing field in the last several decades, with major technical emphasis on achieving sensitivity needed to measure low copy numbers at the single-cell level.

Microfluidics is uniquely suited to the challenges of single cell biochemical analysis, as small device length scales and automated fluidic handling maintain high local concentration of sparingly small numbers of molecules from the cell. For example, microwell arrays and microfluidic PDMS devices with pneumatic valves enabled RT-PCR, RNA sequencing and genotyping on 10-1000s of single cells despite low copy numbers of nucleic acid targets being assayed[4–9]. As a result, we are gaining insight into the cell to cell heterogeneity in processes such as genome changes and mutations during gametogenesis[9]. Furthermore, large strides have been taken towards personalized medicine in cancer treatment as we better understand the role of WNT signaling in cancer metastasis by the capture and RNA analysis of rare circulating tumor cells in micropillar devices[10]. Thus, microfluidic measurements of nucleic acids have already begun to be transformative translationally.

Yet, many studies have demonstrated the limitations of the central dogma of molecular biology[1-2] and thus, protein levels may not be inferred from nucleic acid levels. Recent studies support that nucleic acid levels may not be well correlated with protein at the single cell level[11,12]. Though DNA is transcribed to RNA, which is translated to protein, many other regulatory events, such as transcription factor binding and non-coding RNA binding contribute to DNA, RNA and protein expression levels[1]. Also, after translation, additional regulatory events include post-translational modification and enzymatic cleavage result in alternate forms of a given protein, called proteoforms (Figure 1.1). Furthermore, proteins participate in interactions that are still being discovered[13]. Understanding dysregulation of expression of proteoforms and complexes is critical for cancer[6], and processes such as aging[3] and neurodegeneration[14].

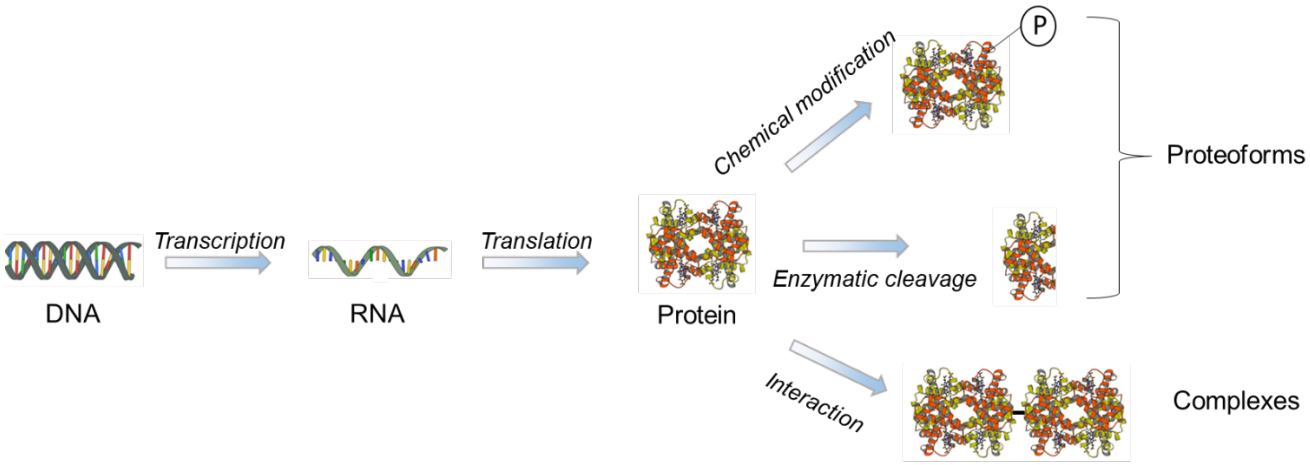

Figure 1.1: Numerous regulatory events determine the expression levels of protein, proteoforms and complexes in cells. After translation, proteins may be chemically modified (e.g., phosphorylated) or enzymatically cleaved, becoming proteoforms. Proteins may also interact to form complexes with proteins or other macromolecules.

A variety of single cell proteomic assays (summarized in detail in the next section) have been developed including immunocytochemistry, flow cytometry, mass cytometry, proximity ligation assay, and antibody barcode chips[15–22]. Such techniques are providing information on cell-to-cell heterogeneity of protein expression at the single cell level, enhancing the knowledge provided by single-cell nucleic acid assays in areas such as cancer signaling pathways[21,22].

2. Benchmarking the state-of-the-art in single-cell protein analysis

No measurement is a panacea, and single-protein assays are no exception. Single-cell protein analysis key metrics include: multiplexing, throughput and lower limit of detection (LLOD). The necessary multiplexing, or number of protein targets detected per cell, depends of course on the intended application. Measurement of only a few specific targets, such as identification of isoforms of Her2 along with key regulators, can be sufficient to inform a therapeutic decision in the treatment of cancer[2]. On the other hand, for assessing protein signaling networks in immunology, measurement of 10s-100s or proteins within the same cell may be necessary[23]. Similarly, throughput (or number of cells assayed) is application dependent. Detailed measurement of just a few cells in the case of rare cell analysis (e.g., of circulating tumor cells) may be sufficient[24]. In contrast, combined multiplexing with large numbers of cells (>1000s) can be used to stratify cellular subpopulations[25]. Finally, the LLOD is a critical metric for single-cell protein analysis owing to the low copy numbers of proteins within each cell (Figure 1.2)[26]. Microfluidic technologies minimize protein dilution by matching device length scales to those of individual cells to maintain the nM-μM concentrations of many proteins in the cell. Here we summarize the current measurement landscape for single cell protein analysis.

Table 1-1: Summary of key performance metrics for the single-cell proteomic technologies outlined here. The last column describes any competitive advantages to EP cytometry (described in the next section) over the specified technology.

Assay	**Multiplexing (targets per cell)**	**Throughput (number of cells)**	**LLOD**	**EP cytometry**
EP cytometry	~10 targets	1000s	27,000 copies of protein in the gel	-
Immunofluores-cence (IF)	5 (conventional filter sets[27]; 61 with quenching[28])	100-1000s	Not reported	Antibody selectivity
Mass Cytometry	~37[29] (protein targets as well as nucleic acid targets)	1000 cells/s[19]	500 copies per pixel, or 1 μm^2 (imaging cytometry)[30]	-Antibody selectivity -handling losses (only 30% of cells measured)
Immobilized Antibody Barcode	11 cytoplasmic or membrane proteins[21]; 42 secreted proteins[31]	120 cells/device[21]	~2000 copies (100 pg/mL 45 kDa protein in 2 nL chamber)[21]	-Antibody selectivity -Nuclear proteins
Proximity Ligation Assay	~3-4	100s	Single molecule[3233]	-higher abundance targets (typical PLA dynamic range ~3 orders of magnitude[32])
Flow Cytometry	~17 targets[17]	10,000 minimum; ~20,000/s for FACS (BD Bioscience Technical Bulletin)	Not reported	-Antibody selectivity -Handling losses (minimum number of cells required 100-1000[34])
Capillary Electrophoresis	~5 (spectral channels); up to 100	-typically ~10s of cells[36]	~1000 copies of protein[37]	-Antibody selectivity

	with capillary zone electrophoresis[35]			-throughput
Mass spectrometry	At single cell level only very high abundance targets measured, limiting proteomic multiplexing to ~1 demonstrated[38]	Rate of ~0.2 cells/s for up to 24 cells[38]	~270,000,000 copies[38]	-sensitivity -multiplexing -integration with upstream assays -throughput

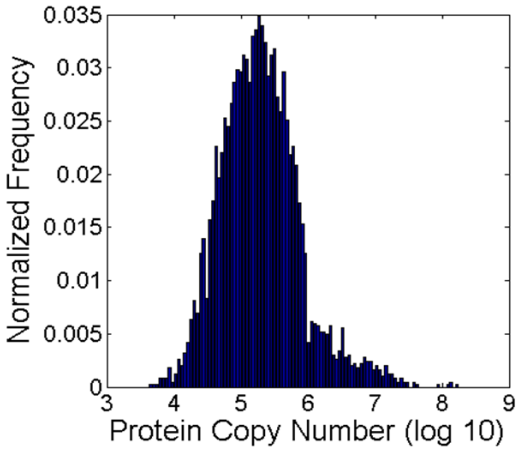

Figure 1.2: Histogram of estimated protein copy number within a mammalian cell from data presented in Li et al.[26]

Immunofluorescence

Immunofluorescence (IF) is a method for mapping the epitopes of fixed and permeabilized cells with fluorescently-labeled antibodies. IF can be performed in either fixed tissue sections (immunohistochemistry) or fixed cells (immunocytochemistry). In IF, the proteins are chemically cross-linked during fixation and permeabilized. Fluorescently-labeled antibodies are introduced via diffusion, which bind to the protein of interest and the cells are imaged with fluorescence microscopy.

Advantages:

IF can be used to visualize subcellular structures and determine protein localization[18]. Traditionally, the spatial resolution of IF is diffraction limited. However, recent advances in super resolution microscopy have improve spatial resolution to 20-50 nm[19,20]. Multiplexing capabilities are limited is by the spectral separation of the fluorescent labels. Up to 5 targets

(including DNA) can be spectrally resolved using standard filter sets[3,21]. However, a chemical quenching technique has been developed to push the number of targets up to 61[4].

Disadvantages:

The primary limitation of IF is the selectivity of the method, which is limited by the availability of antibodies that bind only to the target of interest as detection is purely by immunoaffinity. Antibodies can cross-react with off-target species resulting in false signal and localization[18]. Furthermore, choice of fixation and permeabilization protocol can alter the observed subcellular localization of proteins[18,22,23].

Mass Cytometry

Mass cytometry increases the multiplexing capabilities of immunofluorescence of fixed and permeabilized cells by labeling the antibodies with metal isotopes. Similar to immunofluorescence, metal-labeled antibodies are introduced into the cells. Upon ionization of the heavy metal tags in an inductively coupled plasma mass spectrometer, the abundance of each protein is quantified. Multiplexing is conferred by the unique m/z of each metal label species[6].

Advantages:

The primary advantage of mass cytometry is multiplexing as the method does not rely on spectral multiplexing like fluorescence-based readouts. Thus far, mass cytometry has been demonstrated on 37 simultaneous targets[5]. Mass cytometry can measure up to 1000 cells per second[5,6]. Quantitative limits of detection are difficult to find in the literature, but mass cytometry has been shown to have similar sensitivity to flow cytometry[5,25]. Recently, mass cytometry has been extended to image histological sections at subcellular resolution[7,26]. Imaging mass cytometry has been performed with a spatial resolution of 1μm on 32 simultaneous protein targets with a lower limit of detection of 500 molecules per pixel[7].

Disadvantages:

Like immunofluorescence, the selectivity of mass cytometry is limited by the available antibodies. Furthermore, less than 30% of the cells input into the mass cytometer are analyzed[6]. Consequently, rare cell analysis (e.g., for rare patient samples such as circulating tumor cells) is not yet possible with mass cytometry.

Immobilized Antibody Barcode

Immobilized antibody barcode assays feature microprinted arrays of antibodies on a surface in the presence of living cells in suspension. The devices comprise a series of microchambers with antibody barcodes printed on the bottom surface. The antibody barcodes are created by first printing ssDNA and then introducing complimentary ssDNA-labeled antibodies[27]. To carry out the immobilized antibody barcode assay, cells are loaded into the chambers such that there is approximately one cell per chambers. Cells are chemically lysed within the microchambers, and the solubilized proteins bind to the immobilized antibody barcode. Finally, fluorescently-labeled secondary antibodies are introduced to the chamber and imaged.

Advantages:

The primary advantage of the immobilized antibody barcode assay is multiplexing of protein measurements. This device has been demonstrated with 120 chambers, each assayed for 11 cytoplasmic and membrane protein targets[8]. Immobilized antibody barcodes have also been used to detect protein-protein interactions[8] and have been expanded to secretomic analysis[9,28]. In the secretomic assay, up to 42 targets have been simultaneously measured[9].

Disadvantages:

In addition to the selectivity limitations due to non-specific antibody-antigen interactions, the immobilized antibody barcode assay has not been demonstrated for nuclear proteins [8,28]. This may be due to chemical incompatibility between the denaturing buffers needed to solubilize the nuclear membrane and the need to preserve the native, antigen-recognizing conformation of the antibody.

Proximity Ligation Assay

The proximity ligation assay (PLA) is a sensitive in situ targeted proteomics tool that facilitates measurement of individual proteins[20], protein-protein complexes[48] and protein-nucleic acid complexes[49]. PLA has been employed to measure cell surface and intracellular proteins from fixed cells and tissue, including human cancer samples[48,50]. PLA is a multi-step assay using antibodies (or aptamers) that bind to the target molecule(s) and are conjugated with complementary nucleic acid linkers. Upon enzymatic ligation of nucleic acids on proximate antibodies (~a few nm apart)[51], the proximity probe can be used as primer for quantitative PCR[20] or for rolling circle amplification (RCA) [48]. In the case of RCA, the final readout is fluorescence of labeled oligos that bind to the RCA product bound to the antibody.[48]

Advantages

One of the greatest strengths of PLA is its sensitivity, as even single protein complexes are detectable with the RCA readout.[48] Additionally, it has been argued that PLA can be made more specific than other immunofluorescence readouts if two different antibodies against a given protein target are used[48,52].

Disadvantages

Unfortunately, multiplexing of more than a few targets has not been demonstrated with in situ PLA. Additionally, the typical dynamic range is only ~3 orders of magnitude.[51] This is because the signals from the rolling circle amplification products coalesce within the cell at around 100 amplified products, meaning individual products can no longer be discerned (and without an in-situ calibration curve, absolute quantitation of spots is not possible)[53]. Additionally, it is not currently possible to distinguish homo-oligomeric species from monomers of the same protein because the primary detection antibody could bind to both. Finally, throughput is imaging window-dependent only (e.g. typically ~100s of cells assayed). This is a current practical limitation that may be overcome with advanced high-content imaging systems.

Flow Cytometry

Introduction:

Flow cytometry is a high-throughput analogue to IF, in which fluorescently labeled antibody-stained cells flow through a channel and signal is detected when the cells pass an excitation laser. The cell sample may be fixed and permeabilized as in IF, or proteins expressed on the surface of living cells may be detected.

Advantages

Flow cytometry is an exceptional single-cell proteomics tool with regards to multiplexing and throughput. Up to 17 different protein targets have been measured per cell with fluorescence barcoding-based strategies.[17,54] Furthermore, high throughput is achieved with a minimum of 10,000 cells per population analyzed and up to 20,000 cells per second for fluorescence activated cell sorting (BD Biosciences Technical Bulletin, 2008). Finally, flow cytometry provides additional information beyond protein expression level as forward and reverse scattering of laser light may be used to estimate cell size.[18]

Disadvantages

Measurement of rare cell populations by flow cytometry is challenging due to handling losses[55] (though integrated microfluidic flow cytometry platforms have permitted measurement of ~100-

1000 cells[56,57]). Additionally, appropriate controls to ensure selectivity (e.g. isotype controls to assess true background level) can be difficult to acquire and standards for gating controls are not universally used. Both of these factors can make flow cytometry results difficult to interpret or compare from study-to study.[58]

Capillary Electrophoresis

Capillary electrophoresis based single-cell immunoassays are comprised of on-chip/in-capillary chemical lysis, antibody probing of protein target and capillary electrophoresis-based separation of protein-antibody complexed species[36]. In single-cell capillary electrophoresis live cells are lysed on-chip prior to electrophoresis.

Advantages

The main strength of capillary electrophoresis-based single-cell protein detection is sensitivity, as down to ~1000 copies of protein have been detected with laser-induced fluorescence and cylindrical optics.[37] While in general, multiplexing is spectrally limited with this method, capillary zone electrophoresis has been performed to isolate ~100 different protein targets from a single cell.[35]

Disadvantages

Typically only very low throughput is achieved (~10 cells) due to device fabrication and cell handling challenges[36]. It is worth noting, however, that one group measured sphingosine kinase enzymatic activity in up to ~200 single cells using capture arrays and laser-based lysis of cells.[59]. Finally, while capillary electrophoresis does involve a separation, the limitations of antibody selectivity are not fully addressed with this method (there has been no clear demonstrations of protein-sizing based confirmation of antibody selectivity)

Single Cell Mass Spectrometry

Mass spectrometry is a bottom-up proteomics technique in which living cells are destroyed and their protein contents ionized into peptide fragments, which may be uniquely identified by the mass to charge ratio (m/z)[60]. Electrospray ionization (ESI) is one method for producing the ion species, whereby the sample is aerosolized and under a high electric field, droplets containing analyte dissociate. In matrix-assisted laser desorption/ionization (MALDI), the ionic species is ionized directly out of a dried sample with a laser. Recently, this approach has been applied to measurement of proteins from single cells[61], and can be applied for tissue-scale analysis..

Advantages

The primary advantage of mass spectrometry is the ability to attain label-free detection of proteins[38]. This enables high multiplexing and obviates the need for selective antibodies. Furthermore, mass spectrometry can detect other types of molecules, such as metabolites and lipids[61].

Disadvantages

Sensitivity is the primary limitation of single-cell MS. Thus far, only highly abundant proteins (> $2.7x10^8$ copies) have been detected[38]. Additionally, some techniques, such as MALDI are sensitive to the chemicals present in the sample matrix (e.g. salts). Single-cell mass spectrometry can analyze cells at a rate of 0.2 cells/s and has been demonstrated for up to ~24 cells[38].

3. Electrophoretic cytometry: addressing the need for selective single-cell proteomics

Our lab has introduced an electrophoretic cytometry assay with enhanced selectivity compared to the state-of-the-art methods that rely only on immunoassays[39,62–64]. Single cell protein electrophoresis is performed prior to an in-gel immunoassay to identify proteoforms and off-target antibody binding that could not be distinguished using methods such as IF. A standard electrophoretic cytometry assay simultaneously utilizes thousands of arrayed millimeter-long separation lanes (and microwells that house single cells at the beginning of the measurement), and the assay completes in 4 to 6 hours. Electrophoretic cytometry has been employed to study stem cell differentiation[65] and cell-to-cell heterogeneity in cancer[2,24].

The electrophoretic cytometry device consists of a microwell array patterned in a polyacrylamide gel that is polymerized onto a methacrylated glass slide. The microwell array is cast by polymerizing gel on an SU-8 micropillar mold that is generated via standard SU-8 photolithography protocols.

The 5 steps of a standard electrophoretic cytometry assay are outlined below (and summarized in Figure 1.3):

1. *Cell settling.* Cell suspension solution is introduced to the EP cytometry microwell array and cells settle by passive gravity. Microwell dimensions crucially determine the number of cells measured per separation lane. The microwell diameter should be close to the average cell diameter. Meanwhile, microwell array spacing designates the length of the separation lane, and lateral spacing is set to prevent crossover of protein from adjacent lanes (due to protein

diffusion during the assay, Figure 1.4). A microwell aspect ratio of ~4:3 (height to diameter) prevents multiple cells from landing in a given microwell by passive gravity cell settling. Shorter microwells would result in higher diffusive losses during in-well chemical cell lysis. In an assay of neural stem cells, we measured ~46% single-cell wells in an EP cytometry device with several thousand wells[65].

2. *Chemical cell lysis and protein solubilization.* We rapidly introduce a bifunctional lysis and electrophoresis buffer to the entire array in an attempt to minimize diffusive loss of proteins out of the open microfluidic device. Additionally, it was determined that pouring the buffer yields convection that sweeps protein out of the microwell as recirculating vortices in the top 2/3 of the microwell are present[65]. This top region of the microwell consequently has a Peclet number greater than 1 ($Pe = Lu/D$, where L is the characteristic diffusive length, u is the fluid velocity and D is the diffusion coefficient, Figure 1.3). We experimentally determined loss of GFP out of the microwell was ~40.2% ± 3.6% (with 4 ^{o}C lysis)[65,66].

   The use of the bifunctional buffer allows us to rapidly proceed between assay steps in an effort to reduce protein loss throughout the assay. Thus, this bifunctional lysis and electrophoresis buffer balances assay requirements for cell lysis (i.e., it contains ionic detergents, and is maintained typically near 55 °C) and electrophoresis (i.e., the buffer is also low conductivity, and an alkaline pH so proteins electromigrated towards the positive terminal). One tradeoff between using elevated temperature buffer is enhanced diffusion of protein out of the microwell. However, most proteins are denatured above 55 °C, so the elevated temperature assists with rapid protein denaturation that limits the typical lysis times to less than 30s. The cell membrane is solubilized with a combination of detergents including sodium dodecyl sulfate (SDS), sodium deoxycholate, and Triton X-100[65].

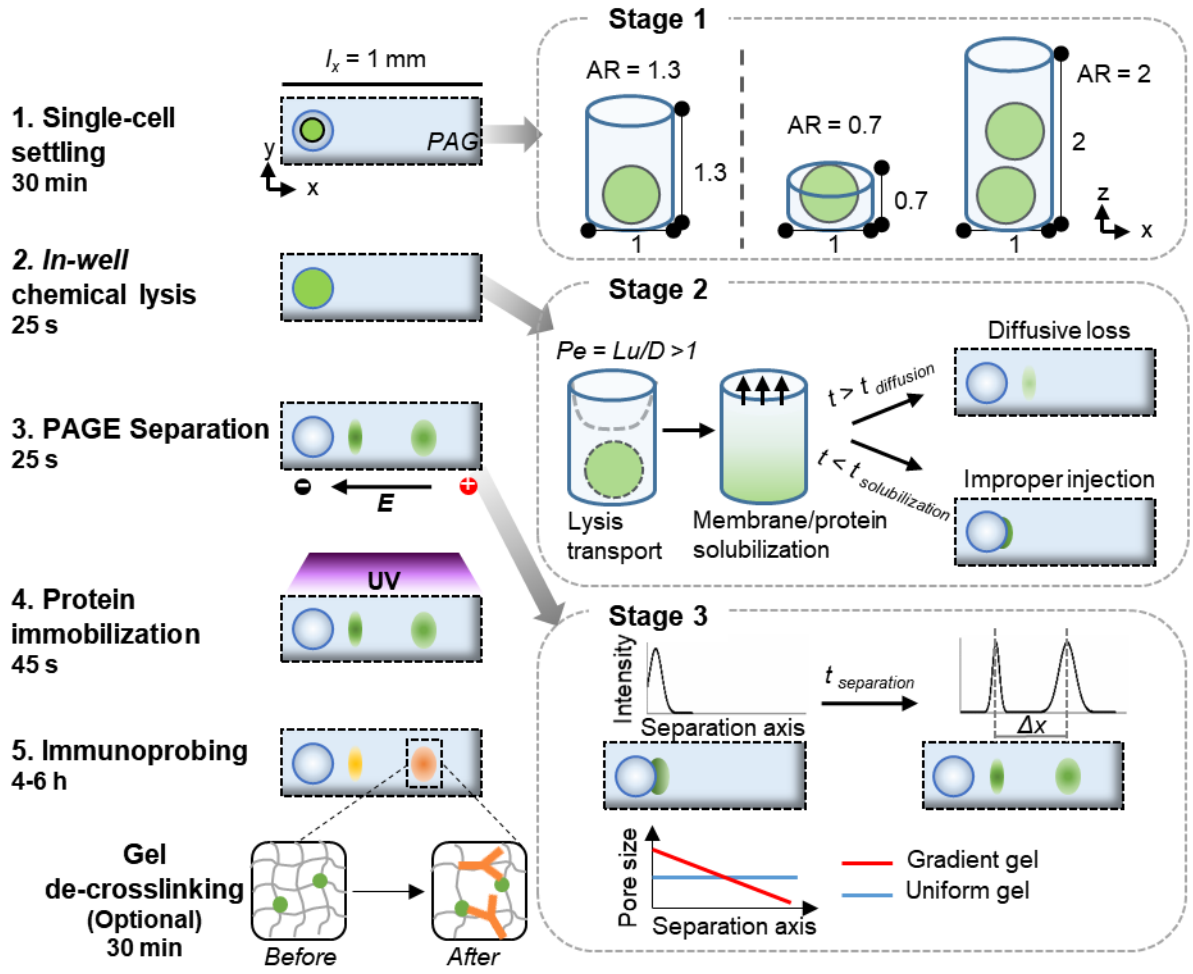

Figure 1.3: EP cytometry assay workflow and design principles. The five stages of the assay are schematically shown with a top-down view of a single separation lane. The corresponding design principles include: i) optimizing the well aspect ratio (AR) to attain single cell settling; ii) balancing efficient protein solubilization while minimizing diffusive losses during cell lysis; and iii) optimizing the electrophoretic separation to attain maximal separation resolution while balancing diffusive loss of protein out of the open microfluidic device (reproduced from Kang et al.)[67].

3. *Polyacrylamide gel electrophoresis.* The electrophoretic separation confers the unique advantage of electrophoretic cytometry compared to other single-cell protein measurements: high-selectivity. Consequently, we have demonstrated the capability to electrophoretically separate proteoforms responsible for drug resistance in Her2 positive breast cancer[2]. The electrophoretic separation is carried out in a custom electrophoresis chamber with platinum electrodes that directly interface with the bifunctional lysis/EP buffer (Figure 1.4). The

physical underpinning of polyacrylamide gel electrophoresis are described in a later section of this Chapter.

4. *Photoimmobilization of protein into the polyacrylamide gel.* Immobilization of protein within the gel achieves two goals: i) protein diffusion is halted, keeping the local concentration of protein sufficiently high for detection; and ii) the gel becomes an immobilization scaffold in which an in-gel immunoassay with standard fluorescence readout can be performed. Rapid and efficient protein immobilization is required for suitable scWB performance. For protein immobilization, we used a UV-mediated covalent capture chemistry that binds proteins to N-[3-[(4-benzoylphenyl) formamido]propyl] methacrylamide[68] (BPMAC) incorporated in the gel. The degree of photoimmobilization (percentage of protein that becomes covalently bonded to the gel) is impacted by protein molecular weight, solution pH, and protein conformation[69,70]. More basic pH levels and SDS denaturation result in higher photoimmobilization[69]. The measured photoimmobilization efficiency was found to be 97.5% ± 0.7% for a 116 kDa protein and only 75.2% ± 0.8% for a 21 kDa protein[70]. For a detailed summary of benzophenone photophysics, the reader is referred to a recent comprehensive review article[71].

5. *In-gel immunoassay.* Protein detection is ultimately carried out via an in-gel immunoassay with primary and then fluorescently labeled secondary antibodies. Antibodies enter the gel by diffusion, and upon immunocomplex formation, unbound antibodies are washed diffusively as well. The chemical and physical properties of in-gel immunoassays are described in detail later in this chapter.

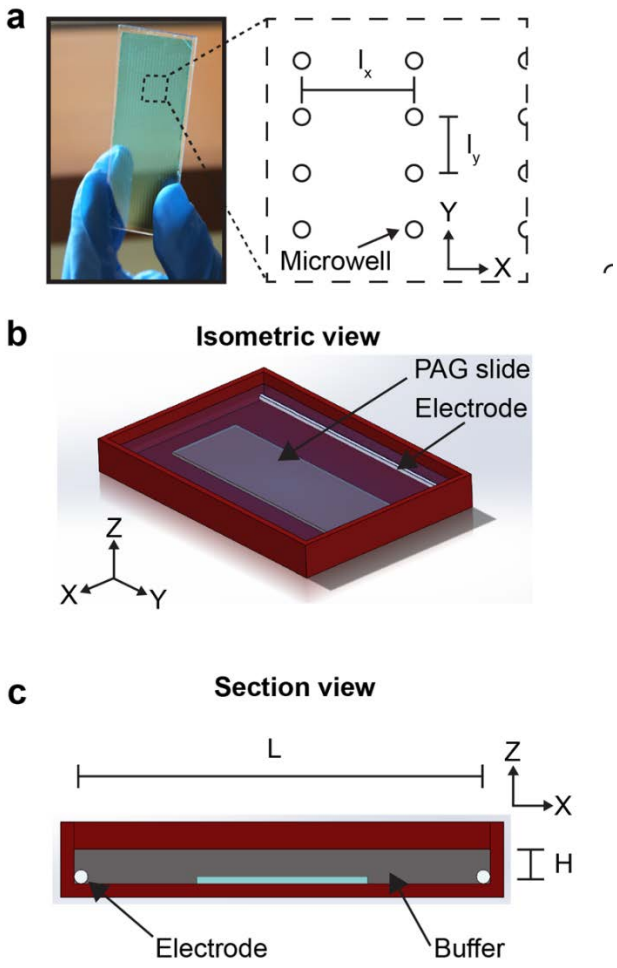

Figure 1.4: EP cytometry device and custom electrophoresis chamber design. (A) Image of a standard EP cytometry device patterned on a glass microscope slide and schematic representation of the microwell array with a separation length l_x (typically ~1 mm) and well-to-well spacing l_y set to prevent crossover of protein from adjacent separation lanes. (B) Isometric view 3D-rendering of a custom EP chamber in which the polyacrylamide gel (PAG) device is placed. Platinum electrodes flank the edges of the chamber. (C) Section view of a 2D rendering of the chamber shows the platinum electrode spacing L, and height of the chamber, H in which bifunctional lysis/EP buffer is introduced. (reproduced from Kang et al.)[67].

4. Thesis Overview

This dissertation presents advances in EP cytometry analysis with focuses on: i) EP cytometry image analysis algorithm development; ii) quantitative assessment of assay technical variation; iii) alternate hydrogels for EP cytometry; iv) EP cytometry immunoassays in dehydrated gels; v) Joule heating impacts on EP cytometry separations and vi) design of EP cytometry assays capable of measuring protein complexes. The overarching fundamental goals of the work

presented were to elucidate physical and chemical principles that govern EP cytometry separation performance and immunoassay sensitivity. Engineering goals included establishing quantitative algorithms and first-in-kind platform design to fractionate protein complexes from single cells. Much of the work that is presented was the result of collaborative efforts, and thus each chapter begins with acknowledgement of the specific collaborators and co-authors who contributed to the research.

The remainder of the introduction provides a theoretical overview of critical electrokinetic and in-gel immunoassay phenomena. The electrokinetics section first introduces the physicochemical properties of the electric double layer as a basis for understanding the mechanism of electrophoresis. In the electrophoresis section, the Navier-Stokes equation is solved in the thin-EDL limit to derive the electrophoretic velocity and mobility. Next, native and SDS-polyacrylamide gel electrophoresis are described and key metrics of separation performance such as separation resolution are introduced. Key EP cytometry parameters that can be tuned to attain higher separation resolution are discussed. In the hydrogel immunoassay section, bimolecular kinetics, thermodynamic partitioning and hindered diffusion in hydrogels are all described in order to understand how EP cytometry immunoassays may be optimized. The dependence of immunoassay sensitivity on the in-gel antibody concentration (dictated by thermodynamic partitioning between the free solution and hydrogel phase) is established. Finally, models of hindered diffusion in hydrogels are introduced such that the effect of transport on system equilibrium may be understood. In that vein, the Damköhler number is presented as a dimensionless parameter that may be used to understand when maximum immunocomplex formation will occur.

Chapter 1 focuses on EP cytometry image analysis and describes a suite of algorithms that can be used to quantify critical metrics such as protein expression levels, separation resolution and peak location (towards application of EP cytometry for proteoform sizing). The entire analysis pipeline is described from EP cytometry array alignment and region of interest selection, to user-based quality control. Design decisions regarding background subtraction methods and quality control metrics are presented.

In Chapter 2, EP cytometry algorithms are applied to the challenge of assessing EP cytometry technical variation in order to distinguish true biological heterogeneity from assay-induced variation. In the first set of analyses, we sought to understand both inter and intra-assay variation in protein expression as part of a study of protein expression heterogeneity in single circulating tumor cells from cancer patients[24]. We describe a method to establish a threshold for technical variation in protein expression with a GFP-expressing cancer cell line. In the second set of analyses, we focus on measuring technical variation in protein separations and assessment of protein size. For the latter, we introduce a microparticle-delivered protein ladder containing

fluorescent proteins of known molecular weight. Thus, we determine the molecular weight and error in molecular weight measurement for individual cells.

The emphasis of Chapter 3 is on tuning EP cytometry hydrogel materials for separation of proteins in specific molecular weight ranges. For small molecular weight proteins, acid-decrosslinkable gels are assessed for balancing immunoassay and separation needs. Swelling-induced patterns in the decrosslinked gels are observed in line with previous literature descriptions of surface-constrained hydrogels. Methods for mitigating such patterns based on the osmolarity of the solution, crosslinking density and polymerization approach are described. Towards tuning separations for large molecular weight proteins, alternative methods for generating agarose hydrogels for EP cytometry are explored. A protocol for patterning a microwell array in agarose grafted to a glass slide is described. Steps towards further optimization and design of alternative hydrogels for EP cytometry are presented in the concluding section.

Chapter 4 investigates an alternative approach for balancing in-gel immunoassay and separation needs by introducing rehydration of gels in limiting volumes of antibody solution as a method to overcome thermodynamic partitioning limits on the in-gel concentration of detection antibody. Kinetic models indicating the dependence of immunoassay sensitivity on system parameters such as the partition coefficient and antibody dissociation constant are presented. Gel rehydration kinetics and volumes are determined, and increases in the in-gel antibody concentration by loading a dehydrated gel with antibody are reported (along with evidence of spatial variation). The dependence of immunoassay signal SNR, and signal variation on the loaded antibody concentration is determined.

In Chapter 5, we provide insight on the impacts of resistive (Joule) heating on separation performance and analytical sensitivity in open microfluidic EP cytometry. Temperature increases in the bifunctional lysis/EP buffer throughout electrophoresis, operating in the “autothermal runaway” regime, which is rarely observed in micro-scale electrophoresis. We use scaling analysis to anticipate how separation resolution scales based on the increased temperature. A method for exchanging buffer in the open microfluidic device is quantitatively characterized. Buffer exchange results in increased separation resolution and reduced variation in separation resolution. The work presented in this chapter highlights how assay stage-optimized buffers can impact the separation and analytical sensitivity in EP cytometry.

The focus of Chapter 6 is on the design of EP cytometry for the fractionation of actin cytoskeletal protein complexes. Actin is a main structural protein of the cell that polymerizes to filamentous F-actin (100s of monomers) and depolymerizes to regulate processes from cell

migration to division. F-actin has been shown to be disrupted in cancer progression, likely altering the migratory behavior of subpopulations of cells. Consequently, it is an intriguing model protein with which to establish EP cytometry for protein complexes to understand how chemical stimuli or physical cues regulate actin polymerization. We employ non-ionic detergent assay chemistries that lyse the cell without disrupting F-actin protein complexes. Joule heating induced disruption of complexes is mitigated by using a thin polyacrylamide gel to deliver the buffers and interface with electrodes. The F-actin is electrophoretically fractionated from monomeric actin via size-exclusion before depolymerization and EP in the opposite direction. We validate the method by measuring the F-actin and monomeric actin levels upon drug treatment with an F-actin destabilizing drug. The method is extended to measure actin binding proteins responsible for regulating F-actin polymerization. Finally, we introduce a method for detecting F-actin complexes from adherent cells towards being able to assess stimuli that alter cell morphology (e.g., heat shock, or substrate stiffness) and the associated changes in F-actin levels at the single cell level.

In Chapter 7 several intriguing future directions are described. Additionally, protocols and algorithm code are shared in several appendices at the end of the dissertation.

5. Electrokinetic theory

Polyacrylamide gel electrophoresis is the separation method employed in the electrophoretic cytometry methods described throughout this work. As such, in the following sub-sections, an overview of electrokinetic theory is presented with a focus on: i) the electric double layer; ii) electrophoresis; and iii) SDS/native polyacrylamide gel electrophoresis

A. The electric double layer (EDL)

Electrophoresis leverages either negatively charged detergent (e.g., sodium dodecyl sulfate), or the charge of a protein owing to its amino acid side chains to separate protein species. The underlying mechanism of electrophoresis stems in part from the ionic species surrounding the protein, which we will explore in this section. When a charged surface is submerged in an electrolyte solution, the diffuse electric double layer (EDL) forms as counterions (of the opposite charge of the surface) assemble at the surface[72]. Co-ions and counterions form a diffuse layer due to the thermal energy of the system until electroneutrality is met in the bulk solution (Figure 1.5). An electric potential is established within the EDL owing to the concentration of charged species.

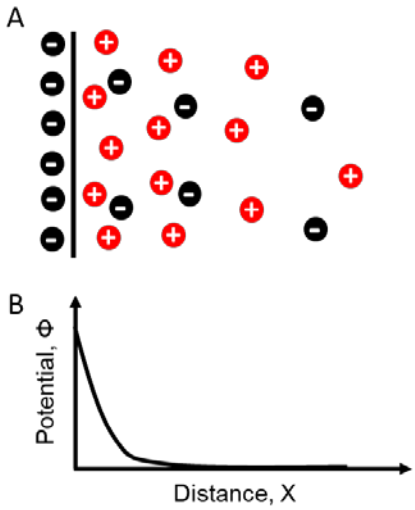

Figure 1.5: The electric double layer (EDL) is established at a charged surface in an electrolyte solution. (A) Schematic representation of the EDL with a negatively charged surface and positive counter ions. (B) The electric potential decreases exponentially away from the charged surface.

The concentration of ions, EDL thickness and the resulting spatially varying electric potential may be derived from first principles. Here, these equations are presented assuming a 1-D diffuse double layer. The electrolyte solution is "infinitely dilute" such that ions do not interact with each other. In the case of the charged proteins described here, the surface in the double layer beyond which ion species are mobile is referred to as the slipping plane. Mobile ionic species can be said to "slip" past the charged surface. The potential at the slipping plane is defined as the zeta potential (ζ).

First, we assume that the electrolyte is fully dissociated such that charge (z) is distributed as:

$$z_+ = z_- = z \qquad \text{Eq. 1.1}$$

Based on the Poisson equation, the electric potential may be written as:

$$\frac{\partial^2 \Phi}{\partial x^2} = \frac{Fcz}{\varepsilon} \qquad \text{Eq. 1.2}$$

Where F is Faraday's constant, ε is the electrical permittivity of the medium, and c is the average counterion concentration in the EDL.

We can calculate the electric potential energy (W) normalized per mole of counterion:

$$W = -Fz\Phi \qquad \text{Eq. 1.3}$$

and we integrate Eq. 1.2 to find the change in potential energy in a finite distance along x:

$$\Delta W = \frac{F^2 z^2 c x^2}{2\varepsilon} \qquad \text{Eq. 1.4}$$

The x position, called the Debye length (λ_d), where the change in potential energy is equal to RT is thus:

$$x \equiv \lambda_d = (\frac{\varepsilon RT}{2F^2 z^2 c})^{1/2} \qquad \text{Eq. 1.5}$$

The Debye length is also referred to as a shielding distance because it represents the location in the diffuse double layer where the thermal energy and potential energy is balanced. Importantly, the expression for the Debye length reveals an inverse square root dependence on concentration and a proportional square root dependence on thermal energy.

We can now consider that the concentration distribution of ions will follow a Boltzmann distribution:

$$c_{\mp} = c_0 e^{(\frac{\mp zF\Phi}{RT})} \qquad \text{Eq. 1.6}$$

where c_0 is the bulk ion concentration sufficiently far from the charged surface such that the potential goes to zero. As the charge density (ρ_E) can be expressed in terms of the ion concentration:

$$\rho_E = F \sum z_i c_i \qquad \text{Eq. 1.7}$$

we can recast the charge density in terms of the ion concentration:

$$\rho_E = Fzc_0 (e^{\frac{-zF\Phi}{RT}} - e^{\frac{zF\Phi}{RT}}) \qquad \text{Eq. 1.8}$$

Which can be re-written as:

$$\rho_E = -2Fzc_0 \sinh(\frac{zF\Phi}{RT}) \qquad \text{Eq. 1.9}$$

We are now in a position to determine the charge distribution in the double layer. Recasting the Poisson equation, we find:

$$\frac{\partial^2 \Phi}{\partial x^2} = \frac{2Fzc_0}{\varepsilon} \sinh(\frac{zF\Phi}{RT}) \qquad \text{Eq. 1.10}$$

While this differential equation can be solved, we make one more simplifying assumption by utilizing the Debye-Hückel approximation. Namely, for small potentials in the limit of $zF\Phi \ll RT$ (i.e., within the Debye length away from the surface), the above expression simplifies to:

$$\frac{\partial^2 \Phi}{\partial x^2} = \frac{\Phi}{\lambda_d^2} \qquad \text{Eq. 1.11}$$

We readily solve for the potential by integrating and using boundary conditions including $\Phi(0)=\zeta$, and as x approaches infinity, $c=c_0$ and $\Phi=0$:

$$\Phi = \zeta e^{(-\frac{x}{\lambda_d})} \qquad \text{Eq. 1.12}$$

Having established the dependence of the potential on critical EDL parameters such as the zeta potential and Debye length, we can now understand the phenomenon of electrophoresis as the motion of a charged particle in a stationary fluid in the presence of an external electric field.

B. Electrophoresis

Considering the Coulomb force of an electric field acting on a charged particle (in this case a protein which we will approximate as a sphere of radius a) and the opposing viscous drag force is a tempting strategy to derive the velocity of the particle. However, from the previous section we can already anticipate that such a force balance would be inaccurate in the thin EDL limit (i.e., $\lambda_d \ll a$). Instead we must understand the interplay between the external field and ions within the EDL (Figure 1.6).

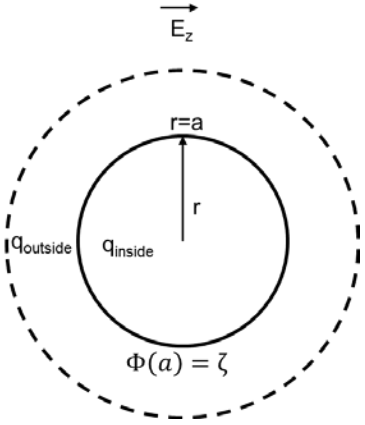

Figure 1.6: Schematic representation of a charged particle of radius a in an electrolyte solution and under an external electric field E_z.

The charge in the EDL can be surmised by integrating the charge density within the EDL (in spherical coordinates and accounting for electroneutrality in the bulk, which requires that:

$$q = q_{particle} = q_{inside} = -q_{outside} = -\int_a^{\infty}\int_0^{\pi}\int_0^{2\pi} \rho_E \sin\vartheta r^2 \, d\theta d\vartheta dr \qquad \text{Eq. 1.13}$$

We can rewrite this expression using the Poisson equation (relating the potential to the charge density) to find:

$$q = \int_a^{\infty} 4\pi\varepsilon \frac{d}{dr}\frac{d\Phi}{dr} r^2 dr \qquad \text{Eq. 1.14}$$

and thus:

$$q = 4\pi\varepsilon a^2 \left(\frac{d\Phi}{dr}\right)_{r=a} \qquad \text{Eq. 1.15}$$

As in the previous section, we can utilize the Poisson-Boltzmann equation as well as the Debye-Hückel approximation to determine an expression that relates $(\frac{d\Phi}{dr})_{r=a}$ and the potential within the Debye layer:

$$\frac{1}{r^2}\frac{d}{dr}\left(r^2\frac{d\Phi}{dr}\right)=\frac{\Phi}{\lambda_d} \qquad \text{Eq. 1.16}$$

We can integrate this expression again employing the boundary conditions $\Phi(0)=\zeta$, and as x approaches infinity, $c=c_0$ and $\Phi=0$:

$$(\frac{d\Phi}{dr})_{r=a}=-\zeta(\frac{1}{a}+\frac{1}{\lambda_d}) \qquad \text{Eq. 1.17}$$

The relation between zeta potential and charge of the charged particle can be determine by plugging Eq. 1.17 back into Eq. 1.15 to find:

$$\zeta=(\frac{1}{4\pi\varepsilon a}-\frac{q}{4\pi\varepsilon a(a+\lambda_d)}) \qquad \text{Eq. 1.18}$$

In order to understand how the electrophoretic velocity depends on the zeta potential of the charged protein, we assess a thin EDL-limit and accordingly write the 1D Navier-Stokes equation (in the low Reynolds number regime) for the system:

$$\mu\nabla^2\vec{u}+\rho_E\vec{E}=0 \qquad \text{Eq. 1.19}$$

The Poisson equation may be substituted into the Navier-Stokes equation and re-arranged:

$$\mu\nabla^2\vec{u}=\varepsilon\nabla^2\Phi\vec{E} \qquad \text{Eq. 1.20}$$

Finally, we may integrate the above expression and apply the boundary conditions that at infinity the bulk solution has zero velocity and the potential at the particle radius is the zeta potential to find the electrophoretic velocity (u_{EP}):

$$u_{EP}=\frac{\varepsilon\zeta}{\mu}\vec{E}=\mu_{EP}\vec{E} \qquad \text{Eq. 1.21}$$

Consequently, for any particle with a thin EDL, the electrophoretic mobility depends on the zeta potential (and thus, in turn the ion concentration in the buffer). The above expressions represent a simplified depiction of the underlying physics governing electrophoresis of proteins. Non-idealities may result based on the specific buffer composition or electrophoresis set up. While in this work we consider electrophoresis in polyacrylamide gel matrices that largely suppress the counterpart to electrophoresis, electroosmotic flow (motion of a fluid relative to a stationary charged surface in an electric field), in certain systems electroosmotic flows may counter-balance electrophoresis. This would result in a modified expression for the electrophoretic velocity.

C. Native and SDS Polyacrylamide Gel Electrophoresis

Electrophoresis became a practical method for the separation of protein species when Dr. Oliver Smithies recognized that starch gels could serve as a sieving material[73] and improve otherwise poor separation of serum proteins. Dr. Smithies recounted at the 2014 Lindau Meeting of Nobel Laureates that laundry was the inspiration for his innovation. He recalled his mother used starch to stiffen his father's shirt collars and hypothesized that stiffening the separation material (chromatography paper) could aid in the separation. Over the years other sieving materials have been adopted, and now agarose and polyacrylamide are the most common. Consequently, substantial insight into the sieving properties of polyacrylamide has been achieved in order to design and tune separations. Both theoretically and empirically, the Ferguson relation[74] has been supported and it relates the electrophoretic mobility in free solution and in the sieving matrix by:

$$\log\left(\mu_{EP,gel}\right) = \log(\mu_0) - K_R T \qquad \text{Eq. 1.22}$$

where K_R is a retardation coefficient, T is the total acrylamide concentration, and $\mu_{EP,gel}$ and μ_0 are the in-gel and free solution electrophoretic mobilities, respectively. The retardation coefficient depends on the size of the protein and the particular sieving matrix employed.

Electrophoretic separations may be performed in native or denaturing conditions depending on the intended sample and application. Native electrophoretic separations are particularly useful when the native protein conformation must be preserved, such as zymography measurements of enzymatic activity[75]. In the present work, we will address the other major sample for which native separations are required: protein complexes[76,77]. One drawback of native protein electrophoresis is that it cannot provide accurate molecular sizing information because the electrophoretic mobility depends on the zeta potential, and not explicitly the protein size. In contrast, denaturing polyacrylamide gel (PAGE) electrophoresis does separate proteins based on their size. In sodium dodecyl sulfate (SDS)-PAGE, negatively charged detergents uniformly coat the proteins. SDS is thought to first associate with proteins via long-range hydrophobic-hydrophobic interactions between the carbon chain of the detergent and hydrophobic domains of the protein. As multiple SDS molecules bind to the amino acid chains, charge-charge repulsion drives protein unfolding, resulting in a linearized protein molecule[78–80]. The linear denatured protein molecule has a uniform mass-to-charge ratio, which results in proteins of different sizes having the same free solution electrophoretic mobility. Therefore, by the Ferguson relation, proteins are separated based on their retardation in the sieving matrix (essentially dependent on their size).

The efficacy of an electrophoretic separation may be assessed various ways, but one key metric is the separation resolution (R_s):

$$R_s = \frac{\Delta x}{\frac{1}{2}(4\sigma_1 + 4\sigma_2)} \qquad \text{Eq. 1.23}$$

where Δx is the distance between two protein peak centers and σ_1 and σ_2 are the peak widths (Figure 1.7). Owing to molecular diffusion, protein peaks assume a Gaussian concentration profile. Consequently, for two protein peaks with the same width, a fully resolved separation (R_s=1) corresponds with a separation with only 0.3% overlap.

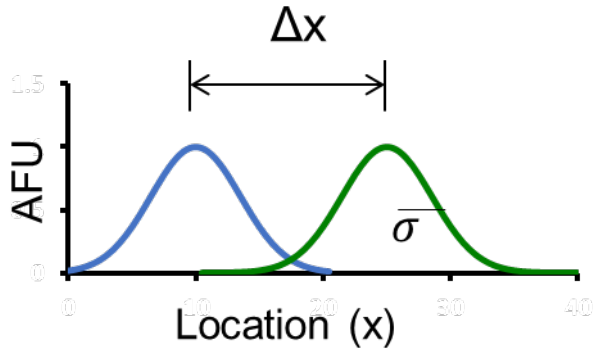

Figure 1.7: Schematic representation of the concentration profile (in arbitrary fluorescence units, AFU) of a separation of two Gaussian protein peaks. The distance between peak centers is Δx and the peak width is given by σ.

Separation resolution can be re-written in term of tunable parameters of the electrophoretic setup. Namely, the numerator can be expressed as the product of the differential electrophoretic velocity and time, and the denominator can be written as a function of the initial injected peak width (σ_0) and the effective diffusion coefficient (D_{eff}):

$$\sigma(t) = \sqrt{\sigma_0^2 + 2D_{eff}t} \qquad \text{Eq. 1.24}$$

resulting in a separation resolution expression:

$$R_s = \frac{\Delta\mu_{EP}Et}{\frac{1}{2}(4\sqrt{\sigma_{0,1}^2+2D_{eff,1}t} + 4\sqrt{\sigma_{0,2}^2+2D_{eff,2}t})} \qquad \text{Eq. 1.25}$$

The equation above highlights how a separation may be designed to achieve maximal separation resolution given other system constraints. Within certain limits, high electric fields should be applied and dense sieving materials should be employed both to increase $\Delta\mu_{EP}$ and to decrease D_{eff}. The practical limitations of altering these particular parameters in open microfluidic, in-gel EP cytometry are explored at length when thermodynamic partitioning and immunoassay efficiency dependence on gel density are characterized, and when Joule heating impacts are discussed.

6. Hydrogel Immunoassays

Electrophoretic cytometry utilizes an in-gel immunoassay for detection of proteins of interest. Primary antibodies diffuse into the 30-40 micron-tall polyacrylamide gel and bind to their target proteins. Upon diffusive washes, incubation of fluorescent secondary antibody and further washes, the immunoassay signal is readout with a laser fluorescence microarray scanner. Here

we describe the key aspects of binding kinetics, thermodynamic partitioning and diffusive mass transport in hydrogels that determine the amount of detected immunoassay signal.

A. Bimolecular binding kinetics

Bimolecular binding kinetics govern the antibody-antigen immunocomplex formation both in general and for in-gel immunoassays:

$$[Ab^*]_{gel} + [Ag] \rightleftharpoons [C] \qquad \text{Eq. 1.26}$$

where $[Ab^*]_{gel}$ is the in-gel concentration, $[Ag]$ is the concentration of antigen or protein, and $[C]$ is the immunocomplex concentration. The concentration of complex can be determined by writing the rate law for the reaction:

$$\frac{d[C]}{dt} = k_{on}[Ab^*]_{gel}[Ag] - k_{off}[C] \qquad \text{Eq. 1.27}$$

where k_{on} is the forward reaction rate (in units of $M^{-1}s^{-1}$) and k_{off} is the backward reaction rate.

The total immobilized concentration of antigen in the gel is equal to the sum of the concentration of non antibody-bound and antibody-bound antigen in the complex ($[Ag]_0 = [Ag]$+[C]), allowing us to re-write the differential equation:

$$\frac{d[C]}{dt} = k_{on}([Ag]_0 - [C])[Ab^*]_{gel} - k_{off}[C] \qquad \text{Eq. 1.28}$$

Rearranging the expression above gives:

$$\frac{d[C]}{dt} + \left(k_{on}[Ab^*]_{gel} + k_{off}\right)[C] - k_{on}\,[Ag]_0[Ab^*]_{gel} = 0 \qquad \text{Eq. 1.29}$$

In order to solve this differential equation, we assume that $[Ab^*]_{gel} \gg [Ag]_0$ and thus the in-gel antibody concentration is treated as a constant. Additionally, we use the boundary conditions that at t=0, [C]=0 and as t approaches infinity, [C]=$[C]_{max}$ to find:

$$[C] = [C]_{max}\left(1 - e^{-(k_{on}[Ab^*]_{gel} + k_{off})t}\right) \qquad \text{Eq. 1.30}$$

and

$$[C]_{max} = \frac{k_{on}\,[Ab^*]_{gel}[Ag]_0}{k_{on}[Ab^*]_{gel} + k_{off}} \qquad \text{Eq. 1.31}$$

From the exponential expression for complex formation as a function of time, we can extract a time constant for equilibration of binding (τ_{rxn}):

$$\tau_{rxn} = \frac{1}{k_{on}[Ab^*]_{gel} + k_{off}} \qquad \text{Eq. 1.32}$$

The above expressions highlight the effect of the in-gel antibody concentration and k_{off} both on the maximum complex that forms and the time it takes for the complex to form. While we cannot control k_{off}, which is intrinsic to each individual antibody-antigen pair, the in-gel antibody concentration is dictated by design choices that we will describe next.

B. Thermodynamic partitioning

Macromolecules in hydrogels partition between the gel and free-solution phases in order to minimize the free energy of the system:

$$\Delta G^0 = -RT \ln(K_{eq}) \qquad \text{Eq. 1.33}$$

This free energy minimization lowers the equilibrium concentration of Ab in gel by a factor of the partition coefficient, $K_{partition}$:

$$[Ab]^*_{gel} = K_{partition} \times [Ab]^*_0 \qquad \text{Eq. 1.34}$$

where $[Ab]^*_0$ is the solution concentration of antibody (Figure 1.8). The partition coefficient depends on all physical and chemical interactions that influence the free energy of the system:

$$ln\, K_{partition} = ln\, K_{el} + ln\, K_{hphob} + ln\, K_{biosp} + ln\, K_{size} + ln\, K_{conf} + ln\, K_{other} \qquad \text{Eq. 1.35}$$

where K_{el} is the partitioning owing to electrostatics interactions (which are solvation, ion and distance dependent), K_{hphob} is the partitioning due to hydrophobic interactions (e.g., pi-pi stacking between benzophenone aromatic rings and aromatic amino acid sign chains of the antibody in an EP cytometry gel), K_{biosp} is partitioning owing to biospecific affinity (e.g., affinity of antibody for protein-containing media), K_{size} is entropic size exclusion partitioning, and K_{conf} and K_{other} are partitioning owing to conformation constraints and other factors (e.g., hydrogen bonding, etc.) respectively[81].

For macromolecules in polyacrylamide the free energy terms expected to dominate are macromolecule interactions with the hydrogel matrix, and entropic-based size-exclusion.[82] Consequently, the Ogston model was developed to describe partitioning owing to excluded volume effects[83]. The Ogston model approximates the hydrogel as a matrix of randomly distributed fibers with known radius (a_f), and the macromolecule as a hard sphere (of radius a, for which hydrodynamic radius is an appropriate real-world proxy). Based on the excluded volume, the partition coefficient for the sphere in the fiber matrix can be shown to be:

$$K_{partition} = e^{-(\varphi(1+\frac{a}{a_f})^2)} \qquad \text{Eq. 1.36}$$

where φ is the polymer volume fraction. The hydrodynamic radius of an IgG antibody is ~5 nm[84], while estimates of average polyacrylamide gel pore size for 3-4% C (% bisacrylamide crosslinker) and 7-8% T PA indicate average pore size is ~50-90 nm.[85] Of note, the distribution of pores sizes may make certain pores inaccessible, while other pores are entropically less

favorable for Ab to enter due to reduced conformational states available compared to bulk solution. The experimentally measured partition coefficient of 0.17 for Ab in 8%T gel indicates only ~17% of bulk concentration of Ab will be in gel phase at equilibrium.[65] Studies of partitioning of globular proteins in polyacrylamide gel indicate increasing the volume fraction of the polymer even by a factor of two can reduce the partition coefficient by over an order of magnitude.[82]

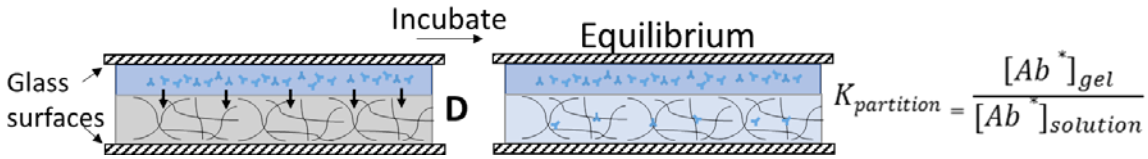

Figure 1.8: Side-view schematic of antibody partitioning in a hydrogel for EP cytometry immunoprobing. The antibody (shown in blue) diffuses from the solution layer (top) in to the hydrogel (bottom). The equilibrium concentration of antibody in gel depends on the partition coefficient.

The implications of antibody partitioning on in-gel immunoassay complex formation is described utilizing kinetic models in the chapter focused on the effect of hydrogel hydration state on immunoassay performance. Furthermore, alternative hydrogel matrices are described later in the dissertation as well.

C. Diffusive mass transport in hydrogels

The last major design consideration for in-gel immunoassays is hindered diffusive transport in the gel and how the transport time scale influences the overall equilibration time of immunocomplex formation. The free solution diffusivity of antibodies and other molecules is given by the Stokes-Einstein equation:

$$D = \frac{kT}{6\pi\mu a} \qquad \text{Eq. 1.37}$$

where a is the radius (for the antibody here), k is Boltzmann's constant, and μ is the solution viscosity. The concentration of diffusing antibody along a dimension x, is given by solving the 1-D diffusion equation:

$$\frac{\partial Ab}{\partial t} = D\frac{\partial^2 Ab}{\partial x^2} \qquad \text{Eq. 1.38}$$

Solving the above differential equation assuming limited-source diffusion gives:

$$Ab(x,t) = \frac{1}{\sqrt{4\pi Dt}} e^{\left(-\frac{x^2}{4Dt}\right)} \qquad \text{Eq. 1.39}$$

with the expression in the exponential term providing an estimate for the time constant for diffusive transport:

$$\tau \sim \frac{x^2}{D} \qquad \text{Eq. 1.40}$$

Of course, depending on the relative size of the diffusing macromolecule and pore size of the hydrogel, diffusion can be hindered in hydrogels. Several models have been proposed to describe such hindered transport. The Brinkman model, originally derived to describe the viscous drag force exerted by flowing fluid on a dense collection of particles[86], can be employed to estimate the hindered diffusion in gel (D_{gel}) versus solution ($D_{solution}$) as:

$$\frac{D_{gel}}{D_{solution}} = \frac{1}{1+\kappa a+1/3(\kappa a)^2} \qquad \text{Eq. 1.41}$$

and κ is a constant that can be calculated by measuring the Darcy's permeability of the hydrogel. However, this idealized model does not account for hydrogel matrix Brownian diffusion, which has been shown to be appreciable for polyacrylamide[87]. The following empirically derived expression for diffusion in polyacrylamide gels was presented[87]:

$$\frac{D_{gel}}{D_{solution}} = e^{-3.03R_H^{0.59}\%T^{0.94}}$$

where R_H is the macromolecule hydrodynamic radius, and %T is the total acrylamide concentration (in g/mL). If using other hydrogels or crosslinking densities that dramatically alter pore structure (e.g., ultra-high crosslinked polyacrylamide[88,89]), methods such as fluorescence recovery after photobleaching (FRAP) can be employed to directly measure the hindered diffusion in gel[82].

The impact of hindered in-gel diffusion on the equilibration of in-gel immunoassay depends on whether the transport rate or reaction rate is limiting. Non-dimensionalizing the reaction-diffusion equation yields the dimensionless Damköhler number (Da), which is the ratio of the reaction and transport rates.

$$Da = \frac{reaction\ rate}{diffusion\ rate} = \frac{\tau_{transport}}{\tau_{rxn}} = \frac{(k_{on}[Ab^*]_{gel}+k_{off})x^2}{D} \qquad \text{Eq. 1.42}$$

A system is reaction-limited if Da<<1, meaning transport is much faster compared to the reaction. On the other hand, the system is diffusion limited if Da>>1 and depletion zones may form. In diffusion-limited systems, the complex formation equilibration time scales as the product of Da and the reaction equilibration time[90].

Thus, optimization of in-gel immunoassays for EP cytometry requires knowledge of each of the key effectors of the in-gel concentration of antibody and equilibration of immunocomplex formation. Consequently, design of EP cytometry assays balances the often orthogonal requirements of the separation and immunoassay stages.

Chapter 2

Algorithm design for electrophoretic cytometry quantitation

This work was performed in collaboration with Dr. Kevin Yamauchi.

2.1 Introduction

Electrophoretic separations provide critical information regarding the physicochemical properties and abundance of a given protein or proteoform. Examples of physicochemical properties that separations can quantify include the protein molecular mass (as in SDS-polyacrylamide gel electrophoresis[91]), isoelectric point (determined by isoelectric focusing[89]), or both (via 2-D electrophoresis[92]). Such separations are performed in a variety of formats including slab gels, microchannels[93,94], and capillaries[38,95,96], each with specially designed analyses to quantify properties of the electropherogram.

However, some analyses of electrophoretic separations still require substantial manual processing, such as the non-standardized and poorly documented practices employed for densitometry of western blotting[97]. Western blotting utilizes a size-based electrophoretic separation followed by transfer (blot) to a membrane on which proteins are detected with fluorescent or chemiluminescent antibodies. Currently, it is still typical for the user to manually outline regions of the image to quantify (e.g., selecting the protein bands) using commercially available software sold with western blot imagers. In a random survey of 100 publications from PubMed that utilized densitometry for western blotting quantitation, only one paper provided sufficient details for the analysis to be reproduced[97] (e.g., how bands were selected, whether peak integrals or heights were used for quantification, type of intensity profile background subtraction, etc.).

Manual processing becomes impractical for high-throughput electrophoretic separations. Our group and others have introduced high-throughput electrophoretic separations with up to 100-1000s of separations performed in parallel across an array[65,98–102], or with 1300 separations in series in a capillary[103]. Impactful applications of arrayed separations include assessing cell-to-cell heterogeneity in DNA damage via single-cell comet assays[104], and quantifying proteoforms responsible for cancer drug resistance in breast cancer with EP cytometry[2].

EP cytometry performs 1000s of single-cell protein separations in a device patterned on a standard microscope slide, and protein peaks are detected with fluorescent antibodies. We previously developed quantitative algorithms for EP cytometry to determine protein expression levels by area-under-the-curve analysis[65]. However, the previous algorithm was cumbersome (with over 20 functions), and not designed for reproducible analysis.

In this section we describe algorithm development to quantify EP cytometry images in a streamlined workflow that preserves key analysis variables to facilitate rapid, reproducible quantitation. Functional decomposition was employed to establish an algorithm with four functions. The algorithm requires minimal user interaction through the use of GUIs, making it accessible to researches of all computational backgrounds. Design choices, including data storage in a MATLAB structure, background subtraction and quality control thresholding are described. Finally, examples of quantitative information extracted from EP cytometry separations are presented.

2.2 Materials and Methods

The EP cytometry image analysis algorithm was written for MATLAB 2016b. The algorithm employs built-in MATLAB functions including statistical tests such as the Pearson correlation. The complete algorithm code is provided in the Appendix.

2.3 Results and Discussion

Design goals for the EP cytometry algorithm

Extracting quantitative information from EP cytometry images allows both the protein expression and molecular weight to be estimated (when using appropriate sizing standards described in Chapter 2). We had three specific design goals for the quantitative algorithm: i) streamlined scripts with minimal user input required; ii) scripts that could be implemented by novice users with no computational background; iii) scripts designed for reproducible analysis.

We sought to streamline EP cytometry arrayed separation image analysis. Towards improving quantitative efficiency and minimizing user intervention, the initial EP cytometry analysis pipeline was reduced from 20 separate analysis scripts[65] to 4. Functional decomposition guided the design process and four key steps were determined to be necessary (and each step is performed as a discrete function). The four steps of the EP cytometry algorithm are shown in Figure 2.1, below. The raw image in Figure 2.1 contains 895 individual separation lanes that are processed as follows: 1) Regions of interest (ROIs) are segmented); 2) A 1-D intensity profile is generated and background subtracted; 3) The intensity profile is fit to a Gaussian curve and 4) The user inspects the fitted peaks as a final quality control step. User interaction is limited to selection of array boundaries in the ROI segmentation function, selection of peak boundaries in the curve-fitting function, and the quality control function. There are options to input thresholding parameters to assist with quality control, or the user may choose to manually inspect each separation lane, as described in more detail in the quality control section.

In order to be easily adopted, we wrote the algorithm to be simple to use. We aimed for algorithm implementation to be readily performed by users with minimal to no experience with MATLAB software or computer science in general. The algorithm was tested with 36 users at the Cold Spring Harbor Lab Single-Cell Analysis Course in the summers of 2016 and 2017. Computational backgrounds varied from no experience to expert biostatisticians. Each user was

able to follow a tutorial and quantify EP cytometry images. Feedback received indicated that the GUI and clear tutorial steps made the process easy to follow.

We further designed the algorithm to bolster quantitative reproducibility. Emerging guidelines for computational research in the age of the scientific reproducibility crisis[62] suggest that individual steps of code that affect the final analysis should be logged[105]. Thus, the choice of how to store output of both the analysis of interest, and variables used to execute the functions is crucial for making a given analysis reproducible. By selecting a data structure for algorithm output variable storage, variables of different data types can be saved within a single file (Figure 2.2) and accessed by field in the command line. Some output variables such as the angle of image rotation, or the user selected peak boundaries allow the analysis to be reproduced by another user if they have access to the data structure.

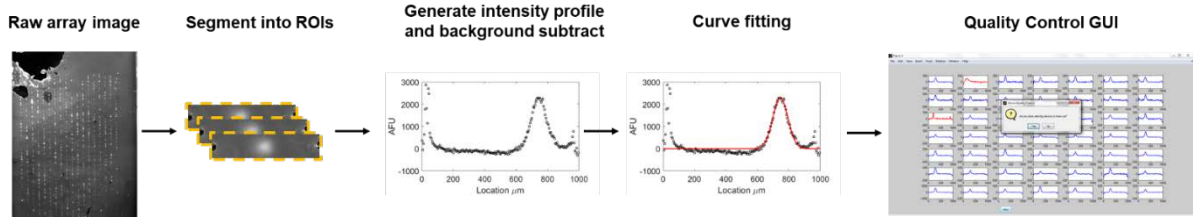

Figure 2.1: Algorithm pipeline for extracting quantitative parameters such as protein peak area-under-the-curve and peak location from EP cytometry images. The raw image of the array is segmented into regions of interest (ROIs). Intensity profiles are generated by averaging the pixel intensities vertically, and background subtraction is performed. The resulting curve is fit to a Gaussian function. A quality control GUI allows the user to eliminate data that was erroneously fit (e.g., auto-fluorescent dust, etc.).

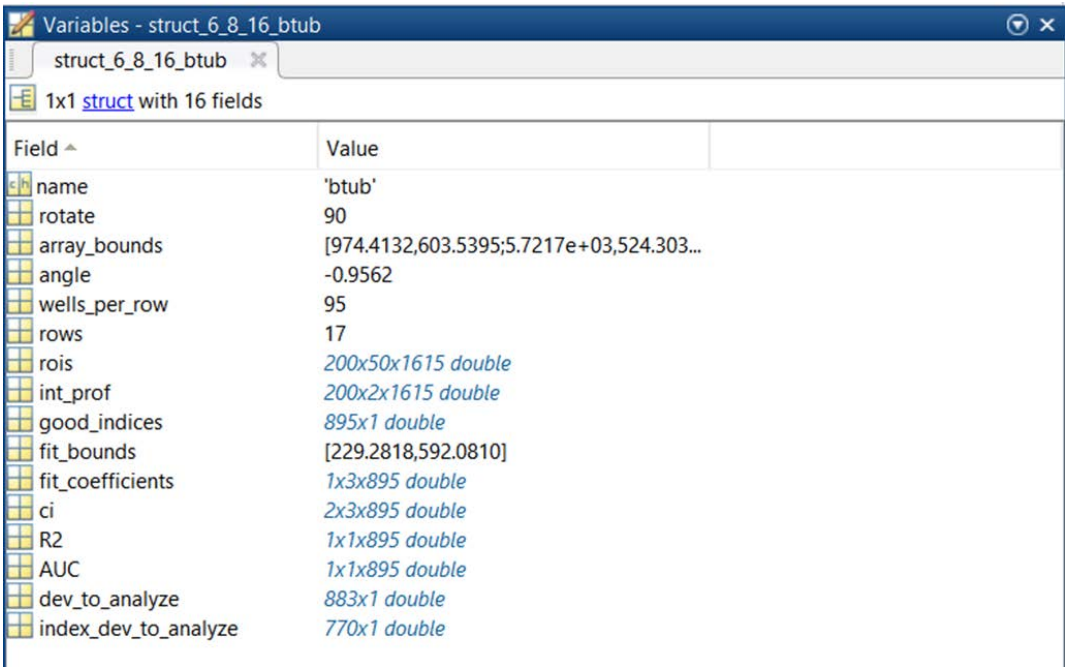

Figure 2.2: Example data structure output from EP cytometry algorithm.

ROI generation

The arrayed format of most EP cytometry separation devices is leveraged in the image segmentation process to generate the ROIs for each separation lane (Figure 2.3). In order to establish array boundaries and determine the necessary rotation to align the array, a GUI prompts the user to select the upper left microwell, the upper right microwell and the lower right microwell of the horizontal image. The necessary angle of rotation to straighten the image is calculated from those three points, and after alignment each ROI is segmented based on the user-input well-to-well spacing.

Image alignment is carried out with an image rotation (Figure 2.3C). The rotation is performed with a built-in MATLAB function, imrotate(), which takes inputs of an image and an angle. The function first translates the image centroid to the origin (the upper left corner of the image), and then the image matrix is rotated around the origin by the angle calculated from the dot product of two direction vectors between the upper left and upper right microwell coordinates. Following rotation, the matrix is translated back to the original centroid location.

The aligned image is next segmented into ROIs based on the user-input well-to-well spacing (Figure 2.3D). The length (L) and width (W) of each lane sets the ROI dimensions. The ROIs are then stored in the data structure as an W x L x N array, where N is the number of separation lanes (Figure 2.3E).

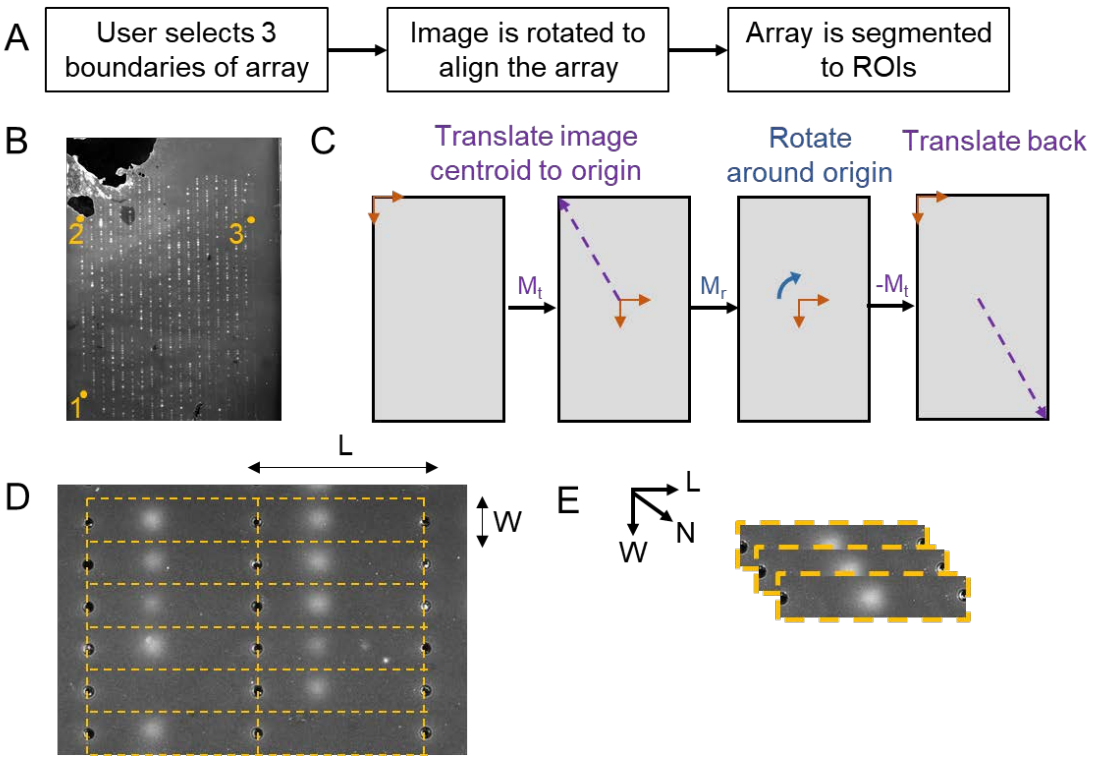

Figure 2.3: The EP cytometry image is rotated to align the array before segmentation into 1000s of individual ROIs. (A) Process work flow. (B) Example of user selected array boundaries (in yellow). (C) Array alignment proceeds with translation of the image centroid to the origin followed by rotation and translation back. (D) The ROIs have a length (L) and width (W) that are input by the user based on the array geometry. (E) The resulting matrix of ROIs is an W x L x N array, where N is the number of separation lanes.

Intensity profile generation and background subtraction

Once each ROI is segmented, we generate 1-D intensity profiles from each 2-D image. This is achieved by averaging each pixel along the width of the ROI, which collapses the 2-D image to a 1-D profile.

Background subtraction of electropherograms remains a challenge to robust quantitation of western blotting. The choice of the background subtraction method strongly influences the measured quantity of protein[97]. Common background subtraction approaches include the rolling ball method and baseline subtraction[97]. However, the rolling ball method has been shown to yield densitometry protein measurements that are less correlated with a radioimmunoassay than if no background subtraction was performed[97]

In EP cytometry, the background subtraction challenge is compounded because 100s to 1000s of individual separation intensity profiles must be background subtracted across the device. Furthermore, non-uniform background, for example in gradient gel EP cytometry[106], requires a subtraction other than the straight-forward and computationally inexpensive baseline subtraction. Thus, we aimed to select a background subtraction that could address non-uniform background (across the device, or within an ROI), and balance computation time.

We investigated two approaches for background subtraction for each individual ROI: i) mean background subtraction and ii) axial background subtraction. Both subtraction methods take “gutter” regions adjacent to the separation lane as the background region (Figure 2.4A). For mean background subtraction, all pixels within the two gutters are averaged and the average value is subtracted from the 1-D profile. Axial background subtraction calculates an average gutter background at every position along the length of the separation lane. For example, for a 5-pixel gutter width, 10 total pixels are averaged and that average value is subtracted from the corresponding intensity value at that location along the separation axis. As shown in Figure 2.4B, the background intensities in the gutter regions are sometimes non-uniform (even when not using a gradient gel). As a result, mean background subtraction can poorly offset the intensity profile to zero, as is the case for the β-Tubulin peak shown in Figure 2.4C. The underlying physical mechanism for non-uniform background in EP cytometry is still not understood. Thus, we currently recommend axial background subtraction (and this is the current default in the algorithm).

Gaussian curve fitting

We utilize Gaussian curve fitting to determine peak width and location parameters that are used in the quantification of protein expression and metrics of separation performance such as separation resolution. The Gaussian fit function, f(x), employed is:

$$f(x) = ae^{-(\frac{x-\mu}{\sigma})^2} \qquad \text{Eq. 2.1}$$

where a is the amplitude, μ is the peak center, and σ is the peak width. The protein peaks should assume a Gaussian distribution owing to protein diffusion during the electrophoretic separation[107]. For quantifying protein expression, integral, or area-under-the-curve analysis is the recommended best practice[97]. By performing Gaussian curve fitting of each intensity profile, we establish the boundaries of the peak as $\mu \pm 2\sigma$. These bounds can be used to calculate the area-under-the-curve by summing the background subtracted intensity profiles (thus summing over the 99.7% confidence interval for a standard Gaussian[108]).

In order to improve the quality of the Gaussian fit, the region of the intensity profile to be fit must be selected, and seed parameters for each of the fit parameters must be provided. For both of these to be accomplished for 1000s of separations, merely requires the user to select peak boundaries, as shown in Figure 2.5. The initial guesses for the parameters are: $0 < a < a_{max}$ (where a_{max} is the maximum intensity across all of the intensity profiles), left bound $< \mu <$ right bound, and $0 < \sigma <$ right bound - left bound. MATLAB uses a least-squares curve fitting algorithm for Gaussian fitting of each curve. Only peaks with an estimated signal-to-noise ratio > 3 are fit to the Gaussian function. If multiple peaks are present in the separation the user has the option to input the number of peaks in the curve-fitting function, and fitting is performed within a for loop. Goodness-of-fit metrics such as the R-squared value, and confidence intervals for each fit parameter are stored in the data structure. While the current algorithm uses Gaussian curve fitting, in the case of protein peaks with substantial skew, other curve-fitting options could be included in the future (e.g., Lorentizan-modified Gaussian[109])

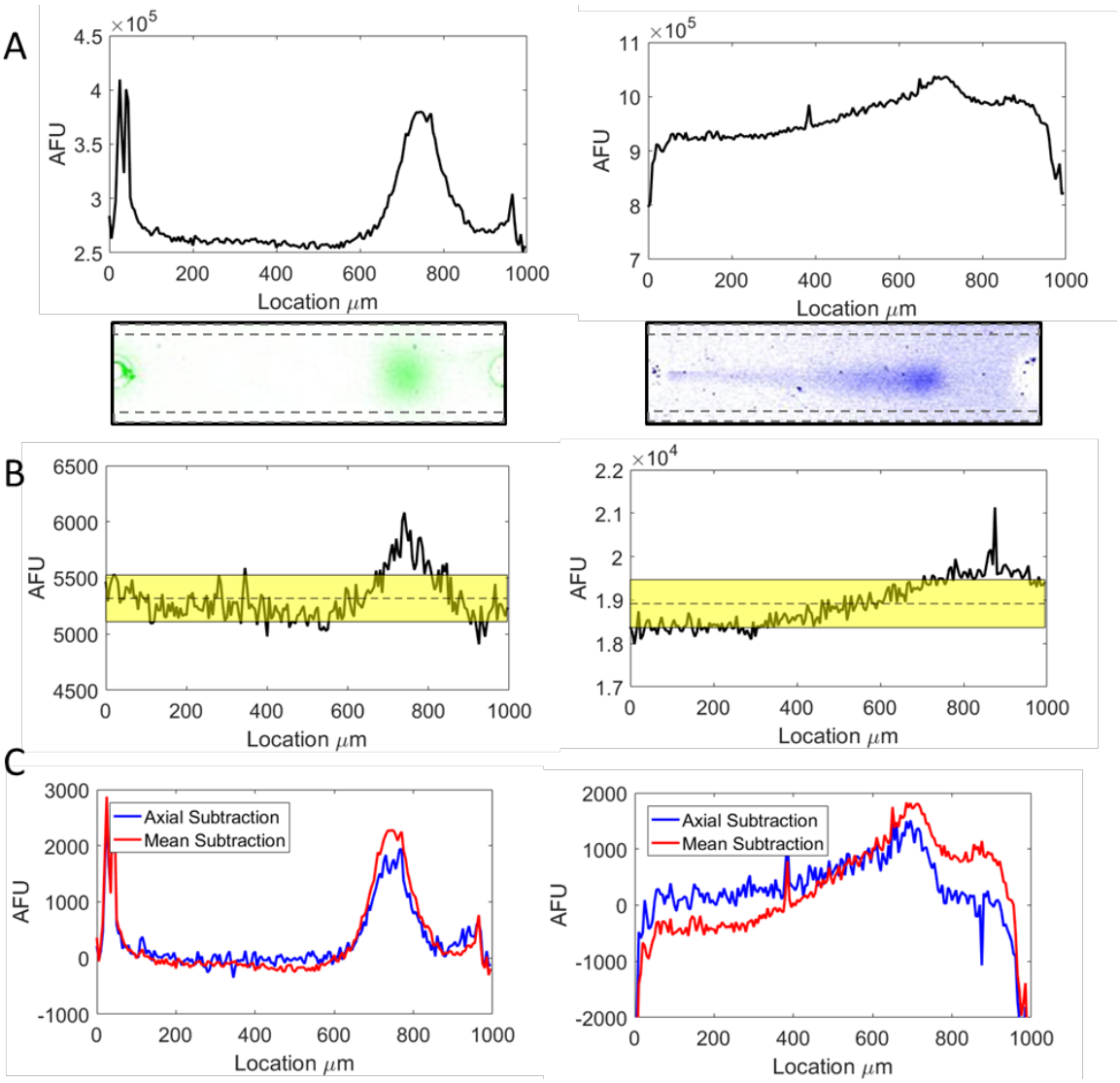

Figure 2.4: Comparison of mean and axial background subtraction for EP cytometry intensity profile background subtraction. (A) Raw intensity profiles and false-colored fluorescence micrographs for GFP (green, left) and GAPDH (blue, right). A 5-pixel background gutter region of the separation lane is shown with a grey outline in the micrographs. (B) Background in the 5-pixel gutter region at each location of the lane (averaged, black line), and mean of the entire gutter region (black dashed line) along with the standard deviation of the background gutter region (yellow shading). (C) Intensity profile of the raw profile in A with axial background subtraction or mean background subtraction.

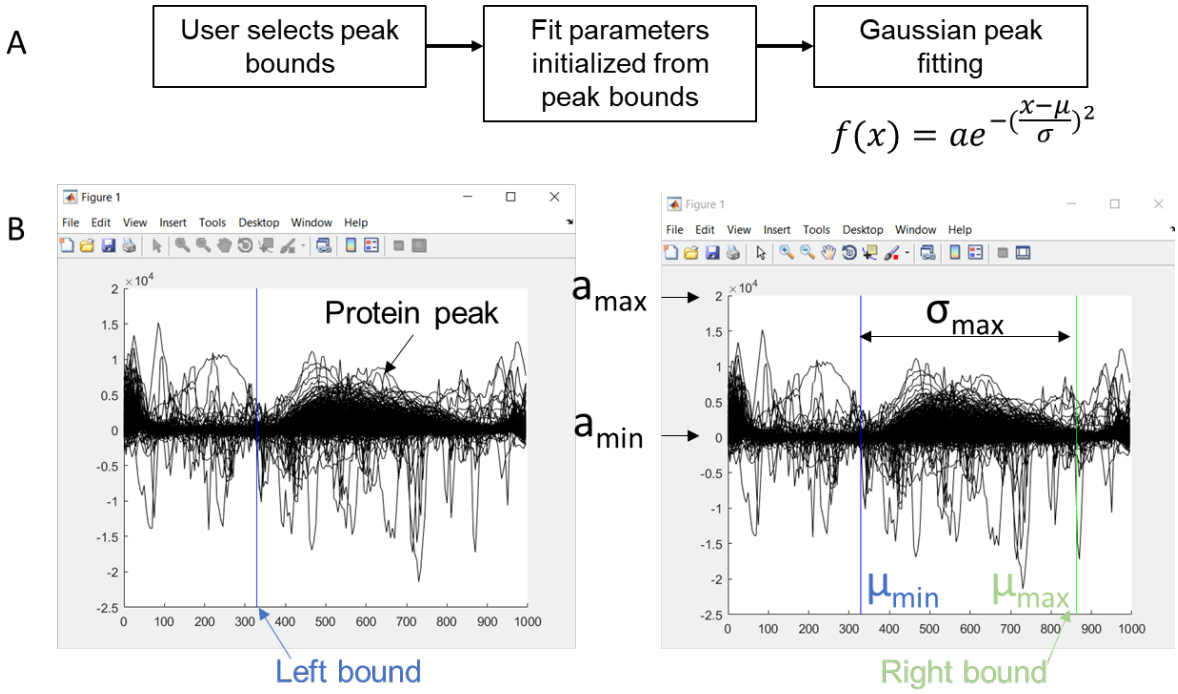

Figure 2.5: Gaussian peak fitting proceeds upon user selection of peak bounds. (A) Workflow for Gaussian peak fitting function. (B) GUI for user selection of peak left bound and right bound. Seed parameters for Gaussian fitting including amplitude maximum (a_{max}), amplitude minimum (a_{min}), peak center minimum x-value (μ_{min}), peak center maximum x-value (μ_{max}), and peak width maximum ($\sigma_{max} \times \sqrt{2}$) for Gaussian fitting are determined from the peak and axis bounds. Minimum peak width is set to zero.

Quality control

Before extracting quantitation information from the separations, we require a quality control step to assess that each ROI actually contained cellular protein and the background subtracted intensity profile is not impacted by punctate noise[110]. To assist with quality control, we generated a GUI that allows the user to inspect 25 separation lanes at a time and select any curves to be discarded (Figure 2.6). Examples of data to be discarded include: i) peaks with salt and pepper or other types of noise in the peak region; ii) erroneous Gaussian fits to punctate noise in the separation lane (with no discernible peak); and iii) completely empty lanes (no peak and no strong noise). Furthermore, peaks that appear with substantial dispersion or skew may result from non-specific background (arising from lysis of stray cells on the EP cytometry gel surface instead of only from the cell in the microwell).

Depending on the number of potentially quantifiable separation lanes, manual inspection may be unwieldy. Thus, the user has the option to set an R-squared value quality control threshold. We have previously used an R-squared value of 0.7[24,110]. With this threshold, we found a strong linear correlation between fluorescence microscopy integrated fluorescence quantitation of GFP-expressing cells and the EP cytometry quantitation of the cells (R^2=0.83 for a linear fit of the data)[24]. Furthermore, we assessed confidence interval variation in the peak center and peak width parameters as a function of R-squared value (Figure 2.7). The confidence interval

variation was calculated as the normalized absolute difference between the fit parameter and the lower bound confidence interval. We found that the peak center confidence interval variation was minimal (< 2.5% for each peak, n=538 and 770 for GFP and β-Tubulin, respectively). In contrast the peak width confidence interval variation was largely less than 20% for R-squared values greater than 0.7. In this instance, thresholding at R-squared > 0.7 would reduce the number of quantified lanes by less than 10 (2% of all data points). At the same time, thresholding would reduce the number of lanes for the user to inspect from 834 to 625, cutting down on inspection time by ~25%. Thus, there is a tradeoff between analysis time and the number of quantified lanes. For rare cell analysis, removing the R-squared thresholding may be prudent to ensure quantitative information is extracted from each cell.

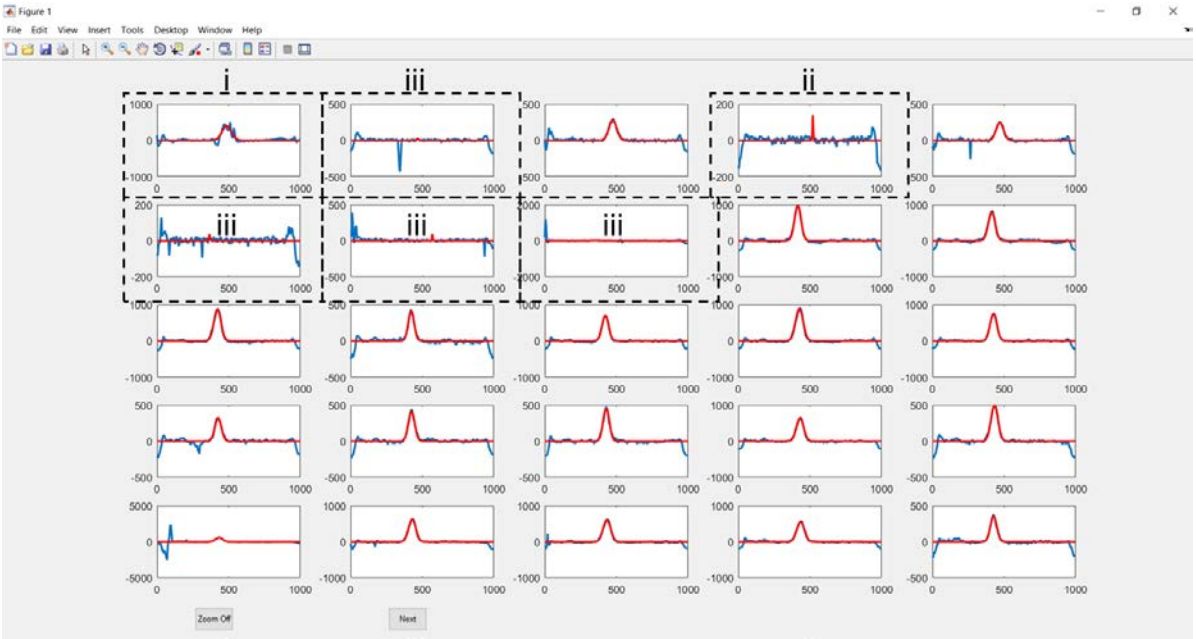

Figure 2.6: Quality control GUI after fitting the background subtracted β-Tubulin peak (blue) to a Gaussian function (red). Peaks are reviewed 25 separation lane ROIs at a time. The user manually selects peaks not to be quantified by clicking on the background subtracted peak. A dashed black box highlights examples of peaks that should not be quantified owing to: (i) noise in the vicinity of the peak; (ii) fits to auto-fluorescent puncta; and (iii) no peak (when no R-squared threshold is set).

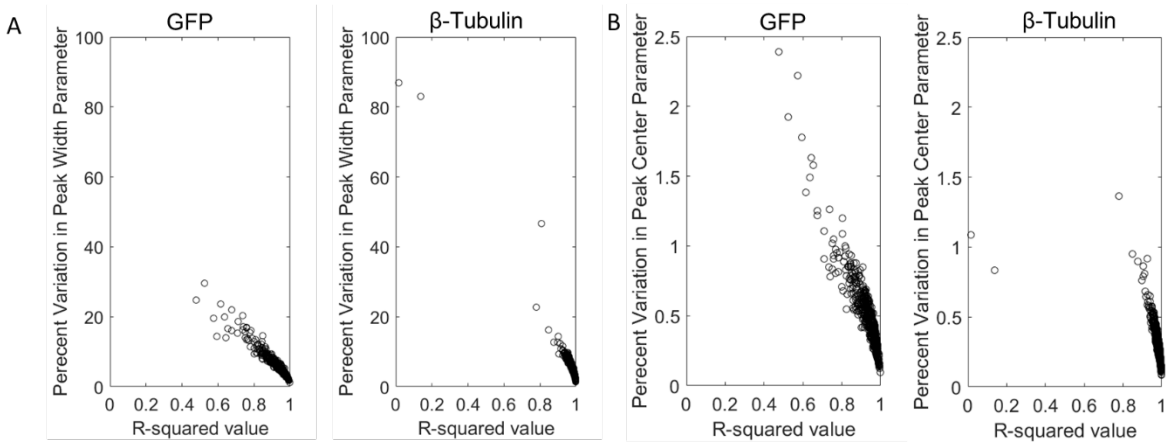

Figure 2.7: Assessing variation in Gaussian fit parameters as a function of fit R-squared value for EP cytometry of GFP and β-Tubulin from MCF7-GFP cells highlights that few lanes containing high variation in the fit parameter pass user inspection and those lanes tend to have lower R-squared values. (A) Percent variation in the peak width Gaussian fit parameter as a function of the R-squared value. Percent variation is reported as the absolute difference between the peak width fit parameter and the 95% confidence interval bound normalized to the peak width fit parameter (n=538 and n=770 fit peaks for GFP and β-Tubulin, respectively). (B) Percent variation in the peak center location Gaussian fit parameter as a function of the R-squared value. Percent variation is reported as the absolute difference between the peak center fit parameter and the 95% confidence interval normalized to the peak center fit parameter (n=538 and n=770 fit peaks for GFP and β-Tubulin, respectively).

Example of quantitation from EP cytometry algorithm

Once curve-fitting and quality control are complete, protein separation metrics and expression levels may be quantified. Two examples of the quantitation are provided below (Figure 2.8 and Figure 2.9). In the first example, separation resolution is calculated across the array and a representative separation with separation resolution closest to the mean separation resolution is displayed. Mean separation resolution was 1.41 ± 0.24 (n=512 separation lanes). In the second example a matrix of protein expression distributions and scatter plots are shown and the Pearson correlation coefficient between each protein target is quantified. The Pearson correlation coefficient for GFP and β-Tubulin is found to be 0.41 (p-value = 0.000; n=512 separation lanes), meaning that the two proteins are significantly positively correlated.

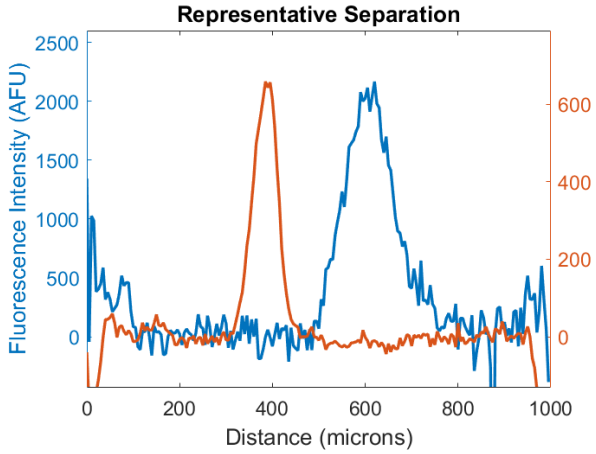

Figure 2.8: Output of separationPlot. This function determines the lane with the separation resolution closest to the mean separation resolution across the array and plots the two proteins in a figure window. The two protein peaks of interest are located around 400 microns (beta tubulin, orange trace) and 600 microns (GFP, blue trace). Mean separation resolution across the array was 1.41 ± 0.24 (n=512 separation lanes).

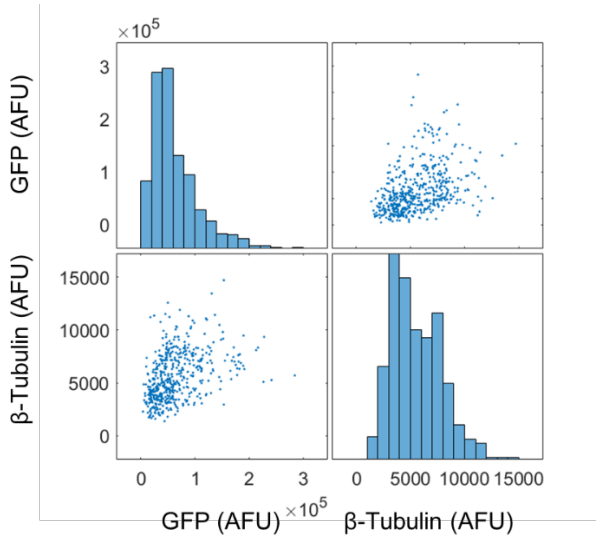

Figure 2.9: Matrix plot shows the relationships between expression levels of pairs of targets. The Pearson correlation coefficient for GFP and β-Tubulin is 0.41 (p-value = 0.000; n=512 separation lanes).

2.4 Conclusions

Robust quantitative analysis of electrophoretic separation data can unveil invaluable information regarding the presence and abundance of proteoforms responsible for processes such as cancer progression[111–114]. For quantitation to be truly robust requires algorithm design for reproducibility and minimal contributions to assay technical variation. The EP cytometry algorithm presented here are built for reproducible quantitation based on the storage of all critical output variables in a data storage. To assess assay technical variation, the algorithm is applied to

discerning biological from technical variation in protein expression and to size proteins with a microparticle-delivered protein ladder in Chapter 2.

Adaptability is also a desirable feature of quantitative algorithms if a core set of analysis scripts can be applied to similar types of data with only small optimizations. The EP cytometry algorithms described here have been applied to both size-based separations (in the standard arrayed format shown here, and custom lab-on-a-disk devices[115]) and single-cell isoelectric focusing assays[102]. For the latter, geometric differences between the 1-mm sizing EP cytometry separation lanes and 9-mm focusing zones were readily modified as input variables in the algorithm. We anticipate aspects of the algorithm (such as the ROI generation and intensity profile background subtraction) could be applied to arrayed separations of biomolecules for which the separated peak is non-Gaussian (e.g., the arrayed comet assay for DNA damage[101]). Furthermore, this algorithm could be adapted to standard western blotting densitometry as an alternative to some subjective practices currently employed.

In the future the EP cytometry algorithm could be further optimized for non-Gaussian profile protein species and to increase assay throughput. Alternative curve-fitting functions have been investigated in chromatography (such as the Lorentizan-modified Gaussian[109,116]), and such approaches may shed insight on proteins that are poorly solubilized in EP cytometry (e.g., proteins originating from circulating tumor cells[24]). In terms of throughput, in the present work we described tradeoffs between throughput and analysis time. However, our analysis is currently limited by the 1-D profile generation to protein peaks with no noise adjacent to the peak in the ROI. We are currently investigating machine learning-based algorithms for image segmentation (and benchmarking against gold-standard image segmentation practices) and automated quality control. Furthermore, in user testing at Cold Spring Harbor Labs, researchers suggested that the quality control step could be made less subjective (and machine learning based quality control could address this concern). Thus, we anticipate the algorithms may be fine-tuned to increase the number of quantifiable separations per device, allowing for rare cell subpopulations to be assayed in EP cytometry.

Chapter 3.

Dissecting Biological from Technical Variation in Electrophoretic Cytometry

This work was performed in collaboration with John Kim, Dr. Peggy Chan and Elisabet Rosas-Canyelles. Portions of the content are reproduced with permission from E. Sinkala, E. Sollier-Christen, C. Renier, E. Rosas-Canyelles, J. Che, K. Heirich, T.A. Duncombe, J. Vlassakis, K.A. Yamauchi, H. Huang, S. S. Jeffrey, and A.E. Herr, "Profiling protein expression in circulating tumour cells using microfluidic western blotting", *Nature Communications*, 2017; and Kim, J.J.*, Chan, P*., Vlassakis, J., Geldert, A. and Herr, A.E. Microparticle delivery of protein sizing standards for electrophoretic cytometry *(in preparation).*

3.1 Introduction

While single-cell analysis is advancing knowledge of biomolecule heterogeneity that drives processes from immune cell response to cancer progression[21,117,118], molecular standards are crucial to determine if assay technical variation masks biological variation of interest[8,24]. For sequencing technology, synthetic spike-ins and unique molecular identifiers (short-random DNA sequence) are used as standards to directly measure sequencing error rates, sensitivity, and sample preparation biases[119–121]. Meanwhile, flow cytometry assays utilize fluorescence-labelled microparticles for laser calibration before cell sorting[122,123]. In microfluidic protein assays (e.g., single-cell barcode chip assay), multiple measurements from the same lysate allow for estimates of technical variation[21]. Beyond measuring variation in abundance of biomolecules, standards have also been introduced for protein sizing in single-cell capillary electrophoresis[124]. Thus, each cellular measurement requires distinct methods to distinguish biological heterogeneity from technical variation.

In EP cytometry, technical variation in the electrophoretic separation can prevent accurate identification of a proteoform of interest based on its migration distance (used for sizing). The metrics used to assess the separation technical variation include variation in: migration distance (peak location), dispersion due to injection or diffusive broadening (peak width)[96], and separation resolution (a metric combining migration distance and dispersion). Variation in separation resolution, as quantified with the coefficient of quartile variation, decreased upon performing a buffer exchange to a lower conductivity and lower temperature electrophoresis buffer[125]. Of course, attaining fully resolved separations (with R_s>1) improves confidence in peak identification, but owing to the tradeoff between separation performance and analytical sensitivity in EP cytometry[125], this is not always possible. An appropriate sizing standard included in each separation lane could facilitate identification of proteoforms.

Identifying useful reference standards to assess technical variation in measured protein expression in EP cytometry is another major challenge. First, the measured protein expression level is impacted by protein loss out of the open microfluidic device during cell lysis, electrophoresis and UV immobilization[110], and the efficiency of the in-gel immunoassay[126]. Each of these factors may be biased by protein molecular mass (e.g., due to the diffusion coefficient dependence on hydrodynamic radius), or photo-immobilization efficiencies of protein to the benzophenone methacrylamide depending on the amino acid side chain groups of the protein[71]. Thus, no single protein can serve as an "ideal" reference standard. Furthermore, cell-to-cell variation in protein expression prevents the use of "housekeeping" proteins for normalization in single-cell analysis[127]. In order to discern biological from technical variation requires alternative reference standard methodologies be developed specifically for EP cytometry.

In this section, methods and analyses to quantify technical variation in separation and protein abundance metrics in EP cytometry are described. First, we assess intra-assay variation in protein expression by measuring GAPDH protein expression in replicate EP cytometry runs with three different cancer cell lines. Second, a method to establish a technical variation threshold for protein expression heterogeneity is introduced. The technical variation threshold estimate employs GFP-expressing cells with which variation induced by the different assay stages can be inferred. This threshold is then applied to assess cell-to-cell variation in expression of a panel of protein markers in circulating tumor cells of cancer patients. Third, a protein sizing approach is introduced utilizing microparticles to release fluorescently labeled proteins of known size (a ladder) to each separation lane in the EP cytometry device. Quantification of variation is a critical first step towards tuning and optimizing assay performance to measure biological variation with confidence. The section concludes with proposed next-generation technical variation measurement approaches for EP cytometry.

3.2 Materials and Methods

Cell culture

To assess inter-assay variation of protein expression, three cancer cell lines were employed: BT-20, MCF7, and SK-BR-3. BT-20, MCF7 and SK-BR-3 cells were obtained from the American Type Culture Collection and authenticated using short tandem repeat analysis (Promega). All cell lines tested negative for mycoplasma. BT-20 was maintained in Eagle's minimal essential medium supplemented with 1% penicillin/streptomycin and 10% FBS. MCF7 was maintained in RPMI 1640 supplemented with 1% penicillin/streptomycin, 0.01 mg ml^{-1} insulin (Invitrogen) and 10% FBS; this cell line was also utilized in the electrophoretic separation and peak migration technical variation study with microparticle-delivered protein standards. SK-BR-3 was maintained in McCoy's 5A supplemented with 1% penicillin/streptomycin and 10% FBS.

A GFP-expressing MCF7 cell line, used to determine the technical variation threshold for protein expression, was obtained from the American Type Culture Collection and authenticated using short tandem repeat analysis (Promega), and tested negative for

mycoplasma. The cell line was maintained in RPMI 1640 supplemented with 1% penicillin/streptomycin, 0.01 mg ml^{-1} insulin (Invitrogen) and 10% FBS. Cells were cultured in an incubator held at 37 °C under 5% CO_2 and tested for mycoplasma contamination.

Protein Loading on Nickel Microparticles

Magnetic microparticles (5 μl) were suspended in a buffer solution containing 50 mM sodium phosphate, 10 mM imidazole, and 300 mM sodium chloride at pH 8. Protein solution (500 μl) including His Tagged proteins in 30% v/v ethanol in PBS was introduced to the particles and mixed on a rotator at 4 ˚C for two hours. Microparticles were washed three times on a magnetic rack in a buffer containing 50 mM sodium phosphate, 20 mM imidazole and 300 mM sodium chloride at pH 8 before ultimately being resuspended in 1X PBS solution.

EP cytometry protocol

The EP cytometry assay comprises six steps within a single device on which microwells are cast into a thin layer of a photoactive PA gel seated on microscope glass slide. For the circulating tumor study, once aliquoted into the mesofluidic insert, cell nuclei were stained (Hoechst 33342) to identify target cells, and a micromanipulator (Eppendorf Transferman) and aspiration (Eppendorf Cell Vario) manually positioned individual cells into each microwell. For the separation technical variation study using magnetic microparticles, cells were passively settled in the microwells by gravity before excess cells were washed off and microparticles were loaded into the microwells by passing a permanent magnet under the microwell array. A combined lysis and electrophoresis buffer was poured directly onto the PA gel where the cells were lysed in-well and then subjected to PAGE (E=40 V cm^{-1}). Lysis buffer was heated in a water bath and the temperature was recorded with a thermometer immediately before use. The combined lysis and electrophoresis buffer for microparticle release of proteins contained: 1M of imidazole, 2.5 g of SDS, 1.25 g of sodium deoxycholate, 500 μl of TritonTM X-100, 25 ml of 10x Tris/glycine buffer and 474.5 ml of ddH2O. This buffer was exchanged after brief electrophoretic injection of protein for a typical 1X RIPA buffer used in EP cytometry[67], following a similar buffer exchange protocol as previously described[125]. After the PAGE separation, proteins were immobilized in the gel via brief ultraviolet activation (Lightningcure, LC5 Hamamatsu) of benzophenone methacrylamide cross-linked into the PA gel. Immobilized proteins were probed in-gel by diffusing primary and then fluorescently labelled secondary antibody probes into the PA gel layer. A fluorescence microarray scanner (Genepix 4300A, Molecular Devices) equipped with four-laser lines (488, 532, 594 and 635) acquired fluorescence readout. Subsequent rounds of antibody stripping were performed for multiplexed protein analysis as detailed previously[65,67]. The EP cytometry assay can be completed within ~20 h. For analysis of the MCF7-GFP cell line, an anti-GFP antibody (ab6673, Abcam) followed by anti-goat AlexaFluor 555-conjugated secondary antibody (A21432, Invitrogen) were applied at a 1:20 dilution. Antibodies used to detect endogenous proteins from MCF7 cells to assess sizing of the microparticle-delivered ladder included: rabbit anti-β-tubulin (ab6046, Abcam), goat anti-GAPDH (SAB2500450, Sigma), mouse anti-cytokeratin 8 (C5301, Sigma), rabbit anti-estrogen receptor α (ab16660, Abcam), rabbit anti-STAT3 (79D7, Cell Signaling), Alexa Fluor 555-labeled anti-mouse secondary (A31570), Alexa Fluor 488-labeled anti-rabbit secondary (A21206), and Alexa Fluor 555-labeled anti-goat secondary (A21432).

Assay Reproducibility

To measure the run-to-run variation in rare-cell EP cytometry performance (including cell lysis), we performed technical replicates on two separate EP cytometry devices from the same suspension of each cell line (BT-20, SK-BR-3 and MCF7). Each cell suspension was pipetted on top of the EP cytometry device and gravity-settled into microwells with excess cells washed off using a solution of 1 × PBS. After completing the assay, GAPDH expression levels were measured; statistical equivalence of the GAPDH expression distributions between the technical replicates was tested using the Mann–Whitney *U*-test ('ranksum' function in MATLAB R2013A). Mann–Whitney *U*-test *P*-values were 0.1257, 0.7578 and 0.7815 for BT-20 (n=59 and 65), SK-BR-3 (n=34 and n=30) and MCF7 (n=42 and 40), respectively. The null hypothesis that the GAPDH protein expression distributions are equivalent across the technical replicates was supported.

Threshold for technical variation

Using a model GFP-expressing MCF7 cell line, we compared variation in GFP expression levels obtained by (i) fluorescence imaging of whole cells with (ii) EP cytometry analysis of probed GFP from those same cells. After establishing correlation between the two modalities, we established a technical variation threshold as described in the Results section. To perform the analyses, a suspension of GFP-expressing MCF7 cells (~1 million cells per ml in 1 × PBS) was pipetted onto the EP cytometry device and cells settled by passive gravity into microwells. Excess cells were washed off with 1 × PBS as described elsewhere[67].

For whole-cell imaging, epifluorescence microscopy recorded GFP fluorescence from MCF7-GFP cells seated in microwells (Olympus IX71 inverted fluorescence microscope, Andor iXon+ EMCCD camera, X-cite Lumen Dynamics mercury excitation lamp, ASI motorized stage controlled in Metamorph software, Molecular Devices). Fluorescence images were taken of cells within microwells (10× Olympus UPlanFLN, numerical aperture 0.45 objective, GFP filter set Chroma 49011 ET, a binning of 1 and an exposure time of 200 ms). For EP cytometry analysis, the protocol described was used after imaging with MCF7-GFP cells lysed (15 s in 55 °C RIPA-like lysis buffer (0.5% SDS, 0.25% Na-DOC, 0.1% Triton X-100 in 0.5 × Tris-glycine), followed by PAGE (20 s at 40 V cm^{-1}), photo-blotting (45 s), antibody probing for GFP (1:10 dilutions of anti-GFP antibody in 1 × TBST with 5% BSA, 2 h), wash (30 min in 1 × TBST), secondary immunoprobing (1:10 anti-goat AlexaFluor 555-conjugated secondary antibody in 1 × TBST, 1 h), wash (30 min in 1 × TBST), rinsed in water and dried in a nitrogen stream. For whole-cell images, a fluorescence intensity profile was generated in the microwell region of interest in ImageJ and the AUC was determined.

For EP cytometry peaks, the AUC for the immunoprobed GFP peak was calculated using the EP cytometry analysis protocol. Cells with similar (<5% variation) GFP AUC were binned and considered a homogeneous GFP-expressing sample, with a 1.27–3.37% difference in AUC from the lowest and highest GFP AUC of each bin observed. The technical variation cutoff was defined as 3 s.d. above the average CV of protein expression (for a 99.7% confidence interval)

Data analysis and processing

Quantification of protein PAGE and probing used in-house MATLAB scripts as described previously[67]. Band widths were characterized by Gaussian curve fitting in MATLAB (R2014b, Curve Fitting Toolbox) if the Gaussian had a R^2-value>0.7. If R^2-value was <0.7 for a marker, the integrated intensity for the region of interest was calculated.

3.3 Results and Discussion

Inter-assay variation in GAPDH EP cytometry protein expression in BT20, SK-BR-3 and MCF7 cell lines.

Run-to-run variation in EP cytometry protein expression measurements of GAPDH was evaluated by comparing GAPDH expression in technical replicates using the cell lines employed in the main text (BT20, SK-BR-3 and MCF7). Technical replicate experiments were performed with two aliquots of cells from the same cell suspension (post-trypsinization) processed on two separate devices. The measured GAPDH expression levels are shown for the two replicates for each cell line in the box plots in F Figure 3.1. In order to evaluate whether the distributions of protein expression were statistically equivalent between the technical replicates, the Mann-Whitney U-test was performed. Mann-Whitney U-test p-values were 0.1257, 0.7578 and 0.7815 for BT20 (n=59 and 65), SKBR3 (n=34 and n=30) and MCF7 (n=42 and 40) respectively. Thus, we affirm the null hypothesis that the measured GAPDH protein expression levels of the single-cells are drawn from the same distribution across the technical replicates.

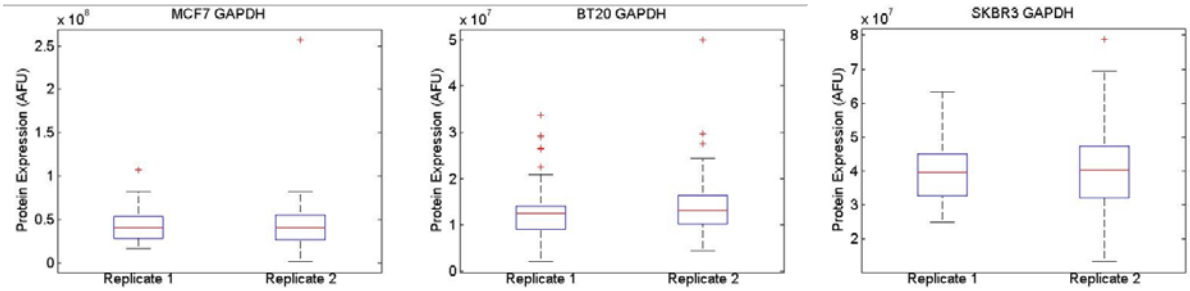

Figure 3.1: Assessing inter-assay technical variation of protein expression in EP cytometry. Comparison of GAPDH protein expression in EP cytometry technical replicates using the indicated cell lines. Mann-Whitney U-test p-values were 0.1257, 0.7578 and 0.7815 for BT20 (n=59 and 65), SKBR3 (n=34 and n=30) and MCF7 (n=42 and 40) respectively[24].

Assessment of intra-assay variation of EP cytometry protein expression measurements using MCF7-GFP cells with uniformly expressed GFP. In order to establish whether variation in protein expression observed in cancer cell lines and patient-derived circulating tumor cells (CTCs) could be attributed to biological and not technical variation, we sought to determine a technical variation threshold for EP cytometry. Sources of variation in protein expression in EP cytometry can include biological variation and four main sources of technical variation: i) membrane lysis and protein solubilization; ii) diffusive losses during lysis and electrophoresis; iii) photoblotting efficiency and iv) antibody probing efficiency. Performing analysis of technical variation in protein expression with GFP expressing cells instead of purified protein enables the estimation of a technical variation cutoff value that encompasses all sources of technical

variation in the EP cytometry. The calculation of a technical variation threshold to distinguish biological and technical variation has been demonstrated previously in proteomics and single-cell RNA sequencing analyses[8,128]. We adapt the analysis of technical variation to the EP cytometry here.

We considered variability in protein expression measurements by benchmarking (i) epifluorescence imaging of intact, green fluorescent protein (GFP)-expressing MCF7 cells (MCF7-GFP cells) seated in microwells against (ii) EP cytometry analysis of immunoprobed GFP from those same cells (Figure 3.2). We observed an appreciable linear correlation between the GFP signal measured in intact MCF7-GFP cells and the corresponding immunoprobed GFP signal (R^2=0.83). If no sources of technical error contributed to the measurement, we would anticipate the GFP and immunoprobed GFP signal relation to be linear with R^2=1. Thus, we sought to establish a technical variation threshold to assess whether protein expression variation is attributable to biological variation or the induced technical variation introduced by the measurement.

The technical variation threshold is estimated as follows. Very few cells possessed identical intact GFP fluorescence intensities imaged in the microwell. Instead, we calculated the % difference in GFP AUC given in Table 3-1 and grouped cells that differed in GFP AUC by less than 5% (ranging from 1.27-3.37% difference in AUC from the lowest and highest GFP AUC of each bin). The antibody probed AUC is listed in the column next to GFP AUC. For each group of three cells, the coefficient of variation of probed AUC, which is the standard deviation of probed AUC divided by the mean probed AUC (CV probed), was calculated and reported as a percent in Table 3-1. The CV probed values varied from 3.3 to 20.4% across the five groups of cells with similar GFP AUC analyzed (total n=15 cells). We averaged the five CV probed values in the table and found CV average=11.0% and the standard deviation was 7.1%. The technical variation cutoff is set as the CV average plus three standard deviations=32.4% (for a 99.7% confidence interval), as has been utilized elsewhere[8]. Thus, if the CV of protein expression for any protein analyzed by EP cytometry exceeds 32.4%, we can conservatively conclude with 99.7% confidence that the variation represents biological cell-to-cell variation distinct from assay-induced technical variation. Notably, all protein expression CVs from patient CTCs in Figure 3.3 (12 proteins, all three cell lines) are above the technical variation threshold, and thus we measure biological variation in the cell lines.

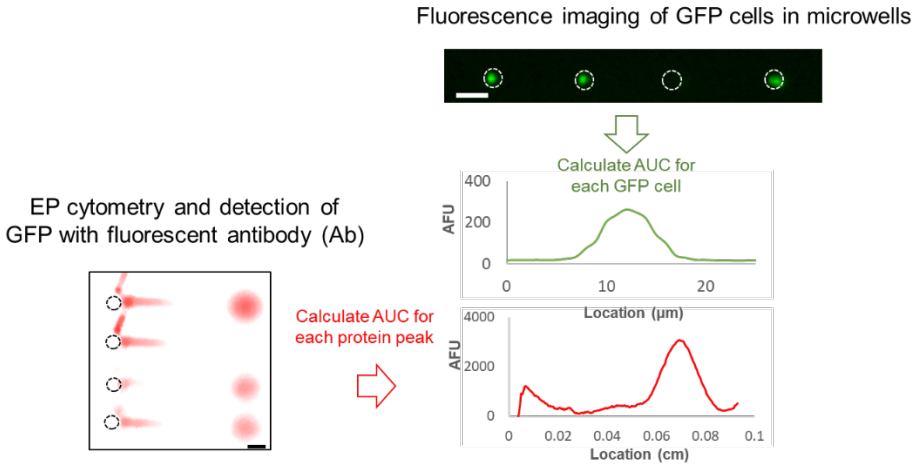

Figure 3.2: False-colored fluorescence images of MCF7-GFP cells in microwells, and representative fluorescence micrograph and intensity profiles of GFP in the well and anti-GFP antibody probe signal. GFP-expressing cells are imaged by fluorescence microscopy in EP cytometry wells prior to cell lysis and fluorescence of the cell is quantified. The EP cytometry is performed and GFP is detected with anti-GFP antibodies. Both the fluorescence images of GFP cells in wells and the antibody probe gel image are used to establish the technical variation threshold[24].

Table 3-1: Groupings of MCF-7 GFP cells with less than 5% CV in GFP fluorescence as imaged in the microwells. The corresponding antibody probe signal (area-under-the curve, AUC) and coefficient of variation (CV) is quantified. The technical variation threshold is calculated as the mean CV (11.0) plus three standard deviations (7.1, for a 99.7% confidence interval) yielding a CV threshold of 32.4%[24].

Cell	GFP AUC	Probed AUC	% Difference GFP	CV Probed (%)
1	166	95046	2.99	10.0
2	170	77774		
3	171	88965		
4	275	120137	1.27	5.5
5	275	132753		
6	278	132067		
7	367	145921	3.37	20.4
8	372	164309		
9	380	214914		
10	408	168585	3.14	15.9
11	414	153812		
12	421	208114		
13	1139	241967	1.63	3.3
14	1152	246009		
15	1157	230755		

CV Average	CV StDev	CV Threshold=avrg+3*stdev
11.0	7.1	**32.4**

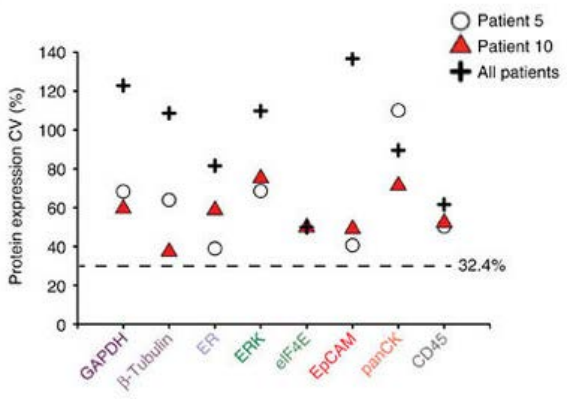

Figure 3.3: CVs for protein expression (AUC) from patient-derived CTCs. Dashed line indicates the threshold in protein expression variation established using GFP-expressing MCF7 cells[24].

Assessment of intra-assay variation of EP cytometry protein sizing as determined with a microparticle-delivered protein ladder.

In order to establish a sizing standard for EP cytometry, we investigated rapid-in microwell microparticle delivery of a fluorescent protein ladder. While purified protein electrophoresis has been demonstrated in a standard EP cytometry device[66,67] with low separation resolution variation as needed for a standard, the time scale of protein convective and diffusive loss out of the microwell is incompatible with the typical lysis times for EP cytometry. Specifically, in the first few seconds of lysis, the majority of the purified protein solution is swept out of the microwell due to the recirculating flow vortices[65]. Thus, purified protein electrophoresis in EP cytometry is typically performed immediately after applying the lysis/run buffer to the array. The microparticle-based protein delivery chemistry employed here uses imidazole competitive binding to displace histidine-tagged fluorescent proteins coordinated with a nickel magnetic microparticle in 10s of seconds.

We directly visualized electrophoresis of fluorescent proteins delivered by microparticles in an EP cytometry device to establish if discrete protein bands would be detected (Figure 3.4). The false-colored fluorescence micrograph time-lapse montage depicts protein A and protein A/G injecting from a microwell into the 1-mm EP cytometry separation lane. Within 20s, two protein peaks are observed, while the signal-to-noise ratios of each peak remain above the detection threshold of 3. Thus, we established that proteins released from a microparticle can be electrophoretically separated in the EP cytometry device.

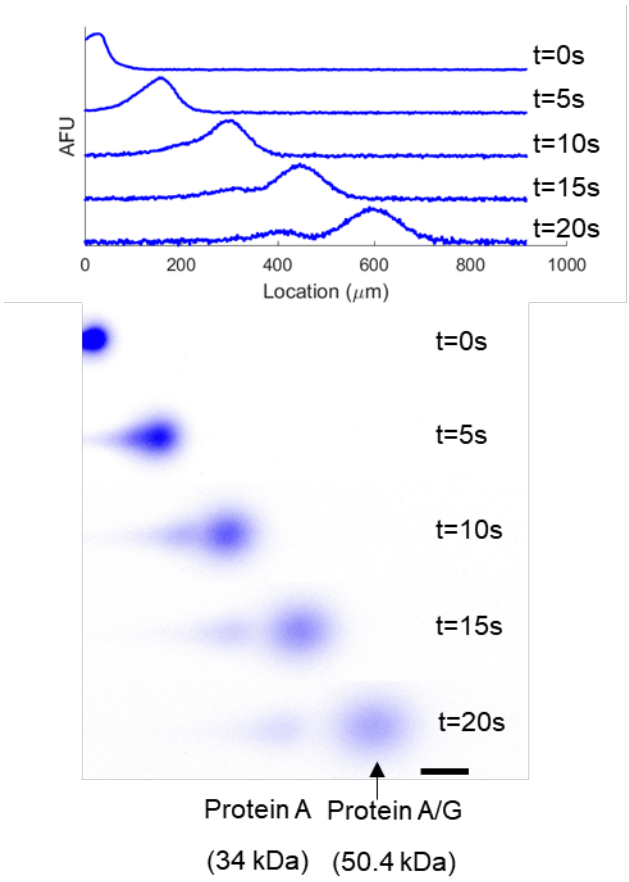

Figure 3.4: Proteins released from microbeads are electrophoretically separated in an electrophoretic cytometry device. Representative false-color micrograph montage and y-offset intensity profiles (maximum normalized) of a time-lapse image of electrophoretic separations of Protein A (34 kDa) and Protein A/G (50.4 kDa) released from the microbeads.

Towards establishing multi-protein standard ladders for each individual separation lane, we sought to optimize the separation and analysis of four proteins varying from ~42-100 kDa in molecular weight. Gaussian curve fitting of such data can be performed one of two ways: i) sum of Gaussian fits; or ii) individual Gaussian fits to each protein peak. Both Gaussian fitting methods are compared for representative separations of the four-protein ladder in Figure 3.5, below. While sum of Gaussian fitting resulted in some fits that poorly approximated the peak center or width, the individual fits to each peak yield high-fidelity fits to each peak of the intensity profile. As a result, individual fitting of each peak was performed instead of sum of Gaussian fitting.

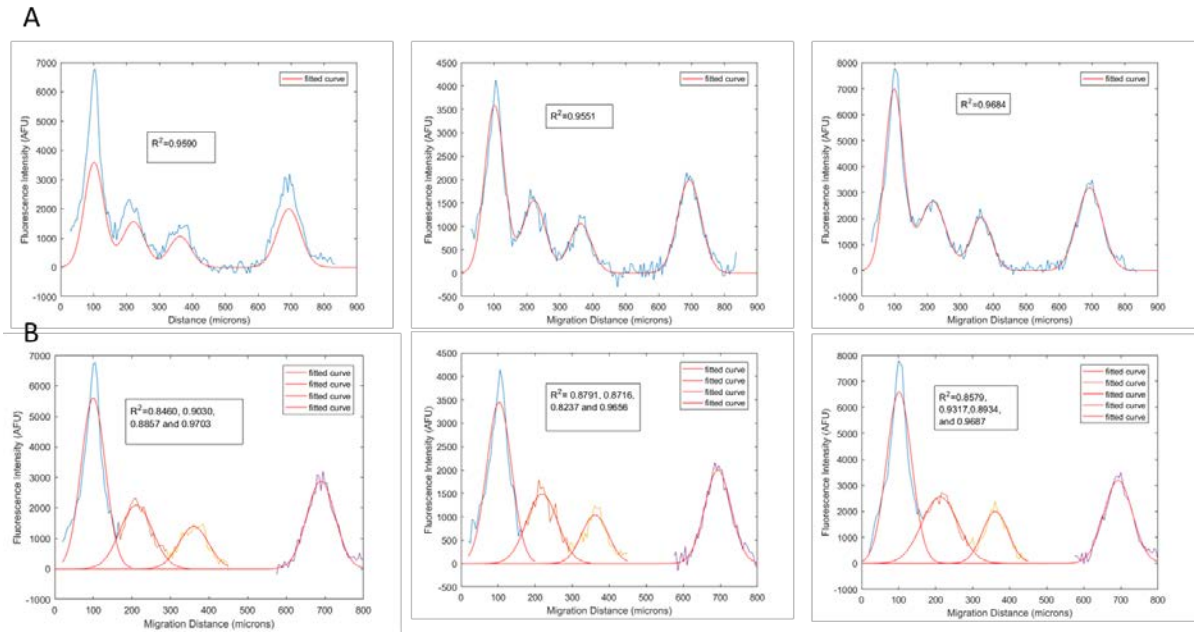

Figure 3.5: Optimization of multi-peak Gaussian fitting of bead ladder protein separations (ladder contained ICAM1, 100 kDa, KDR, 84.6 kDa, PDGFRA, 57.7 kDa and CHI3L1, 42.3 kDa). (A) Example fits and R^2 values for a sum of four Gaussians fit (in red) to the intensity profile (in blue). Inaccurate peak width estimates would arise from some fits (e.g., upper left fit). (B) Example fits and R^2 values for four individual Gaussian fits (in red) to portions of the intensity profiles (based on user peak boundary selection). Peak location and width estimates from the fits improve compared with the sum of four Gaussians model.

In order to assess separation performance with a microparticle-delivered protein ladder, we quantified the separation resolution between adjacent protein peaks of the ladder. The separation resolution (R_s) is defined as:

$$R_s = \frac{\Delta x}{\frac{1}{2}(4\sigma_1 + 4\sigma_2)} \qquad \text{Eq. 3.1}$$

where Δx is the center-to-center distance between the protein peaks and σ is the peak width. A separation resolution greater than one is achieved for each adjacent protein pair in a four-protein ladder spanning ~40-100 kDa (Figure 3.6). Such separation resolution is crucial for accurate peak location estimation to use the ladder as a sizing standard. Comparable separation resolution is achieved in a 1-mm separation lane in an 8%T gel for ladder proteins in the ~40-60 kDa range as was previously demonstrated with endogenous proteins from cells (~30% molecular mass difference[66]). The separation resolution is notably improved over the previously reported method for electrophoresing fluorescently labeled purified proteins incubated in the EP cytometry array[66,67]. The incubation-based method yielded R_s less than 0.75 for BSA (66 kDa) and TI (21 kDa) in a 1-mm separation lane in 8%T gel (E=40 V/cm), while here we fully resolve Eph B4 (58 kDa) from CHI3L1 (42.3 kDa). We hypothesize the separation resolution was lower in the incubation method because larger microwells were used to attain sufficient protein loading.

Since the injected peak widths are larger when using larger microwells, by $R_s = \frac{\Delta x}{\frac{1}{2}(4\sigma_1 + 4\sigma_2)}$ Eq. 3.1, the separation resolution is reduced. In the present work, sufficient microparticle protein loading allows us to settle microparticles in microwells just larger than a cell diameter to maintain low peak widths.

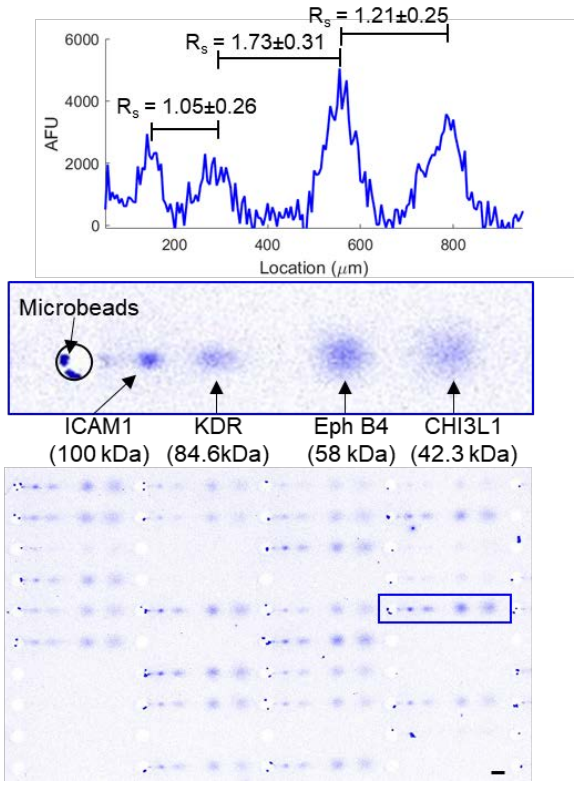

Figure 3.6: Broad molecular weight-range protein ladders serve as sizing standards for thousands of simultaneous single-cell electrophoretic separations. Representative false-color micrographs and intensity profiles of a four-protein ladder that was separated and immobilized. Inset shows the microwell outlined with black and microbeads remaining in the well. Mean separation resolution (R_s) for each protein pair is shown on the intensity profile (error bars are standard deviation for n=322 separations). Scale bars are 100 microns.

Given our design goal to achieve accurate protein sizing using the microparticle-delivered protein ladder, we also assessed technical variation in separation performance. The coefficient of variation (CV) in separation resolution is ≤25% for 322 ladder protein separations across the EP cytometry device (Figure 3.6). While the CV of peak location was less than 10% for each ladder protein, the peak width CV varied substantially between ~19-40% (Table 3-2). Thus, the separation resolution variation arises largely from peak width variation. The ~6-10% CV in peak location of the ladder proteins highlights the need for a ladder for each separation lane to achieve accurate sizing of endogenous cellular proteins. Previous single-cell capillary electrophoresis systems performed separation of fluorescent ladder proteins prior to single-cell electrophoresis[124]. In capillary electrophoresis, low CVs for protein retention time (~1.3-1.4%) for all proteins in a broad molecular-mass ladder allowed sizing without running the single-cell

lysate and ladder simultaneously. We aimed for the microparticle ladder delivery approach to allow 100s-1000s of simultaneous endogenous single-cell and ladder protein separations, which marks a considerable advance in throughput for the use of sizing standards in microscale electrophoresis.

Table 3-2: Quantitation of peak location and width for microparticle-delivered ladder proteins from main text Figure 3 (n=322 separations). Peak location was determined from the peak center parameter, and peak width from the sigma parameter of a Gaussian fit in MATLAB.

Protein	Mean Peak Width (μm)	Standard Deviation of Peak Width (μm)	CV of Peak Width (%)	Mean Peak Location (μm)	Standard Deviation of Peak Location (μm)	CV of Peak Location (%)
ICAM1	28.96	11.63	40.1%	134.04	12.99	9.7%
KDR	41.37	12.27	29.7%	274.303	19.58	7.1%
Eph B4	37.79	7.10	18.7%	539.87	30.94	5.7%
CHI3L1	52.25	14.71	28.2%	750.05	42.95	5.7%

We further assessed the linearity of the relationship of log molecular weight versus migration distance for the ladder proteins, as expected in SDS-PAGE[129]. As shown in Figure 3.7, below, hundreds of separations yielded highly linear log molecular weight versus migration distance fits (R^2 fit value 0.99 ± 0.004). Thus, despite the previously noted CV in peak location, migration distances within a given lane are self-consistent. Consequently, for each lane we can use the log molecular weight versus migration distance standard curve to assess the molecular weight of endogenous proteins based on their migration distance.

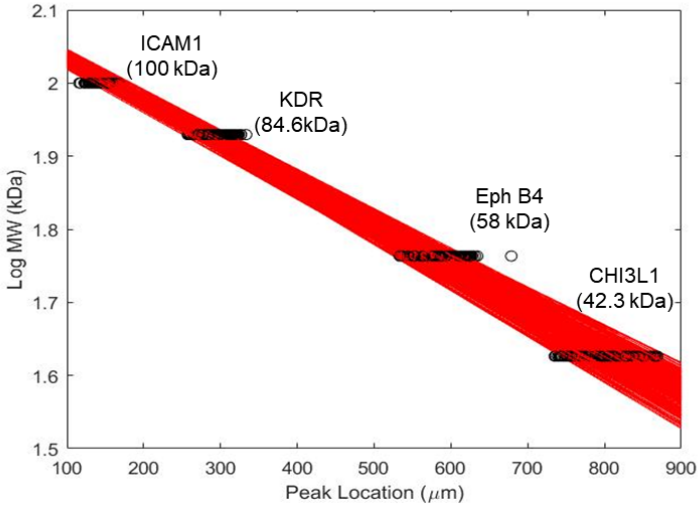

Figure 3.7: Plot of log molecular weight (MW) versus peak location the four-protein ladder delivered by microparticles to the EP cytometry array. Peak location was determined from the Gaussian fit to each peak. The R-squared value for the linear fit was 0.99 ± 0.004 (n=323 separation lanes).

Having established that the protein ladder migration for a given separation lane is highly self-consistent, we applied the ladder of protein standards to approximate the molecular weights of several endogenous proteins from single cancer cells (Figure 3.8). The five endogenous proteins measured vary in molecular weight between 37 kDa (GAPDH) to 80 kDa (STAT3), and thus we hypothesized they should be accurately sized with the ladder proteins that range from 42.3 (CHI3L1) to 100 kDa (ICAM1). As shown in panel B of Figure 3.8, the estimated molecular weights are in close agreement to the expected molecular weights. For the proteins with no known isoforms or antibody cross-reactivity (i.e., GAPDH, β-TUB, and CK8), the median percent mass error across the EP cytometry array was 10% or less. On the other hand, higher percent mass errors were measured for ER-α, which is known to express a 44 kDa isoform, and STAT3, which was determined by slab gel western blotting to possess multiple protein bands in the 70-100 kDa range. Consequently, if sufficient separation resolution can be attained to electomigrate proteoforms of interest outside of this 10% mass error range, the protein ladder employed here may be used to accurately identify specific protein peaks by their migration distance/molecular weight. Given the abundance of alternative splicing isoforms thought to drive tumor metastasis and cancer drug resistance[114,130], microparticle-delivered protein standards hold tremendous promise for single-cell alternative splice isoform identification at the protein level.

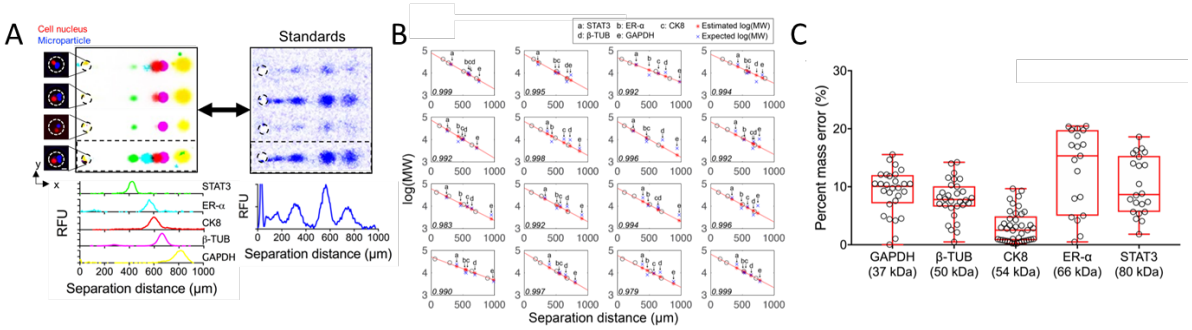

Figure 3.8: Microparticle-delivered protein ladder employed in EP cytometry sizes endogenous proteins from single cancer cells. (A) False-color micrographs and intensity profiles of the cells and microparticles co-localized in a microwell in the polyacrylamide gel, the immunoprobed endogenous proteins (STAT3, ER-α, CK8, β-Tubulin and GAPDH) and the fluorescent protein standards (ICAM1, 100 kDa, KDR, 84.6 kDa, Eph B4, 58 kDa and CHI3L1, 42.3 kDa. (B) Fits (red lines) of log(MW) versus separation distance for the standard proteins (open circles) with the expected and estimated molecular weights from the standard curve. The R-squared values of the fits are shown in the lower left corner (C) Quantification of the percent mass error between the expected and measured molecular weights for the endogenous proteins STAT3 (n = 22), ER-α (n = 19), CK8 (n = 41), β-TUB (n = 30), and GAPDH (n = 28).

3.4 Conclusions

Increasingly in single cell analysis, we aim to dig deeper beyond the observation that there is cell-to-cell heterogeneity to actually assess functional implications of that heterogeneity. However, with this goal comes the challenge of defining what is true biological heterogeneity, as distinct from the variation induced by the measurement itself. There is no silver bullet for such analyses. In this section we described three different analyses all aimed at understanding the magnitude of technical variation in EP cytometry in terms of protein abundance and electrophoretic migration.

With the conservative estimates provided, we found substantial technical variation in protein expression or abundance measurements by EP cytometry (~30% technical variation among cells with highly similar, less than 5% variation in, GFP expression). Now, the challenge is to assess the origins of this technical variation in EP cytometry as a means to control and reduce variation. Microparticle-delivered fluorescent proteins may be useful for this endeavor, but are fundamentally limited by the fact that they do not currently face similar sample preparation challenges to solubilization as some endogenous proteins[24]. Instead, epitope-tagged fluorescent proteins[131] expressed within engineered cell lines may hold promise for unlocking specifically how sample preparation and any associated electrophoretic injection dispersion affects the amount of quantified protein. Extending the technical variation threshold analysis described here to epitope-tagged proteins of different molecular weights and subcellular localizations will help uncover systematic biases in EP cytometry measurements. Ultimately, advances in understanding and reducing sources of technical variation for single-cell protein measurements will aid in the identification of rare cell subpopulations for a wide range of diagnostic, prognostic and therapeutic applications.

The unique advantage of EP cytometry over other single-cell protein measurements is the selectivity conferred by the electrophoretic separation, but clearly technical variation in the separation may also be further improved. Peak migration coefficients of variation are higher than in similar (albeit lower throughput) single-cell capillary electrophoresis[124]. We are only now beginning to identify sources of separation resolution variation in EP cytometry, including the role of Joule heating across the open microfluidic array[125]. Thus far it is unclear why lower separation resolution variation is observed when Joule heating is lower. Further dissection of the role of temperature versus buffer composition is needed.

The use of microparticle-delivered protein ladders is an exciting advance to EP cytometry for on-chip protein sizing. Future applications will include identification of proteoforms implicated in cancer progression. An interesting challenge will be adopting the release buffer chemistry for less stringent lysis conditions (e.g. subcellular western blotting[132], or to maintain and size protein complex species[77]). Finally, reducing the percent mass error in the estimated molecular weight will be necessary to discern proteoforms that differ by small molecular masses (e.g., single exon skipping events in alternative splicing)[133].

Chapter 4

Effect of Polymer Hydration State on In-Gel Immunoassays

Reproduced with permission from J. Vlassakis and A.E. Herr, "Effect of Polymer Hydration State on In-Gel Immunoassays", *Analytical Chemistry*, 2015.

4.1 Introduction

For applications spanning from macromolecule release (e.g., drug delivery[134–137]) to detection (e.g., immunoassays[138–140]), thermodynamic partitioning hinders diffusive entry of macromolecules into a wetted hydrogel. For 'in-gel' immunoassays where target is immobilized in a hydrogel, detection antibodies applied to the gel partition between the gel and free-solution phase. We can describe the partitioning of detection antibodies (*Ab**, where '*' indicates detection probe is labeled with a fluorophore) with an in-gel Ab* concentration $[Ab^*]_{gel}$ given by:

$$[Ab^*]_{gel} = K_{partition} \times [Ab^*]_0 \qquad \text{Eq. 4.1}$$

where $K_{\text{partition}}$ is the equilibrium partition coefficient and $[Ab^*]_0$ is the solution concentration of antibody. A $K_{\text{partition}} < 1.0$ indicates an in-gel macromolecule concentration lower than the solution phase concentration. Partitioning arises from both size-exclusion and macromolecule interactions with the hydrogel and solvent, including hydrophobic-hydrophobic and electrostatic interactions.[81,82] The equilibrium in-gel concentration of macromolecule may be lowered by up to 1000-fold from the starting solution concentration.[81,82] As a result, numerous approaches aim to alter the partition coefficient with addition of salts or molecules such as PEG[141–143] to the solution or hydrogel. Another class of approaches actively loads the hydrogel with macromolecule using mechanical or electrical forces.[144,145] Such methods increase in-gel macromolecule concentrations by over 10-fold, with utility dependent on scalability and compatibility with the specific drug delivery or immunoassay system. As a result, more generalizable approaches to overcome partitioning for hydrogel loading would prove useful.

Low in-gel concentrations of detection antibody can reduce the analytical sensitivity of an immunoassay even with a high density of immobilized target (e.g., in a 3D hydrogel matrix).[90,146,147] Based on bimolecular binding kinetics, the maximum immunocomplex formed by the reaction of detection antibody with target antigen (*Ag*) is given by

$$[C]_{max} = \frac{k_{on}\,[Ab^*]_{gel}[Ag]_0}{k_{on}[Ab^*]_{gel} + k_{off}} \qquad \text{Eq. 4.2}$$

where $[Ag]_0$ is the target protein concentration, k_{on} ($M^{-1}s^{-1}$) is the association rate constant and k_{off} (s^{-1}) is the dissociation rate constant. Thus, for in-gel immunoassays, the maximum immunocomplex formation and analytical sensitivity depends on the local concentration of detection antibody in the gel.

Enhancing the analytical sensitivity of an in-gel immunoassay is an outstanding analytical challenge in the single-cell western blot (scWB) format we recently introduced.[65] Existing single cell proteomic measurements such as immunocytochemistry, flow cytometry and other immunoassay based methods[15–22] have provided fundamental insight into the heterogeneity of protein expression driving cancer[21] and stem cell differentiation[148]. However, non-specific antibody binding has been implicated in false signal and incorrect localization, necessitating the development of the scWB.[63,149] The scWB utilizes a microfabricated polyacrylamide (PA) hydrogel for single-cell protein electrophoresis, covalent photo-immobilization of protein bands to the gel, and subsequent immunoprobing (Figure 4.1A).[65,66] Single-cell electrophoresis identifies off-target antibody binding and protein isoforms.[65] We perform immunoprobing in the separation gel by diffusively introducing primary and then fluorescently labeled secondary antibodies (Figure 4.1B). During immunoprobing in the PA gel thermodynamic partitioning lowers $[Ab^*]_{gel}$ and, thus, the analytical sensitivity of the assay.[65,66] In the scWB, we observed $K_{partition}$ ~ 0.17 (8%T gel) meaning that just ~17% of the applied concentration of detection antibody will be in-gel at equilibrium.[65] Antibody size-exclusion from the dense molecular sieving gel occurs even though the hydrodynamic radius of an IgG antibody is ~5 nm[84] and estimates of average PA gel pore size are ~50-90 nm for a 7-8%T (total monomer concentration) gel (with 3-4%C, percent bis-acrylamide crosslinker).[85] While reducing the gel density (and increasing the gel pore-size) would increase the partition coefficient, the resolving performance of protein electrophoresis would be reduced. Low in-gel immunocomplex formed at equilibrium, thus impacting analytical sensitivity for certain targets. Consequently, immunoprobing of the scWB requires higher antibody consumption than competing single-cell technologies including flow cytometry.[58]

To overcome partitioning limitations for in-gel immunoassays, we introduce a detection antibody loading method based on rehydration of hydrogels (in which protein is immobilized) with a volume of detection antibody solution closely matched to the water volume fraction of the hydrogel. This yields near-bulk concentrations of antibody in the gel. To our knowledge, this is the first report of matched volume gel rehydration as a mechanism to reduce the solution phase volume and macromolecular partitioning into the solution phase and to enhance the in-gel concentration of detection antibody. Here for the scWB, we demonstrate reduced detection antibody consumption and increased detection signal from in-gel immunoassays for protein targets with a trade-off in spatial signal variation.

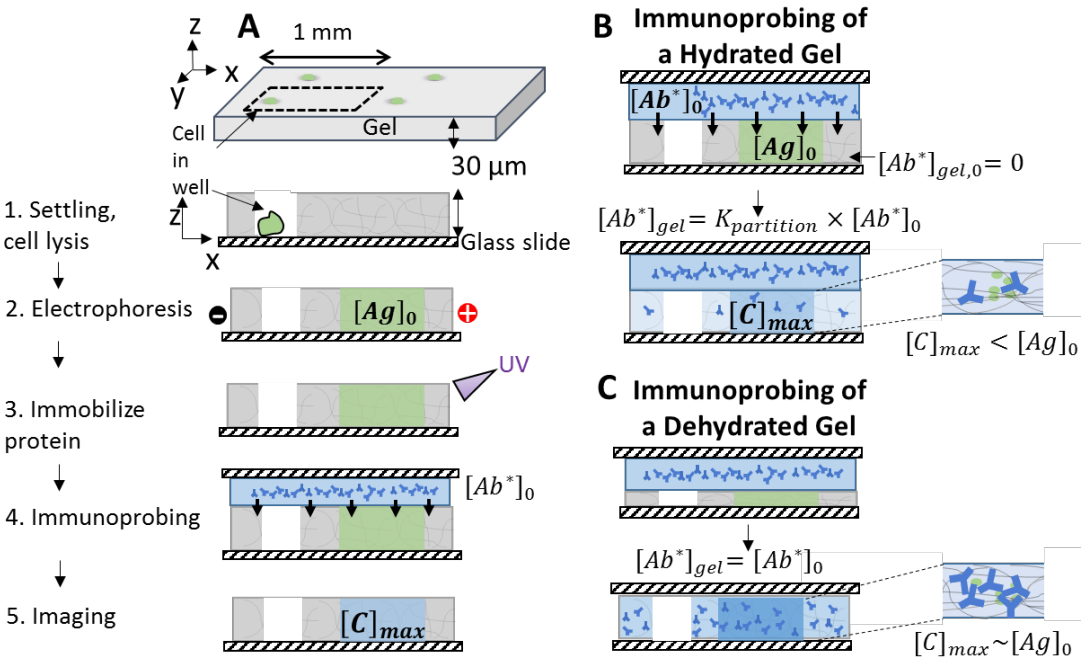

Figure 4.1: In-gel immunoassays are affected by preferential partitioning of detection antibody out of the hydrogel and into a solution phase as is relevant to the immunoprobing step in single-cell western blotting. (A) The scWB utilizes a thin layer of micropatterned PA gel attached to a microscope slide with an assay workflow that consists of: 1) settling and lysis of single cells in microwells cast into the PA gel layer, 2) PA gel electrophoresis (PAGE) of each single-cell lysate in the supporting PA gel layer, 3) UV immobilization of protein in the gel, 4) in-gel immunoprobing using fluorescently-labeled detection antibodies ($[Ab^*]_{gel}$), and 5) fluorescence imaging. (B) Schematic of immunoprobing in a hydrated gel, including diffusion and partitioning of detection antibody and immobilized protein target, $[Ag]_0$. Partitioning lowers the in-gel concentration of detection antibody, $[Ab^*]_{gel}$, at equilibrium thus yielding $[C]_{max} < [Ag]_0$. (C) Schematic of immunoprobing by rehydrating a dehydrated gel with a matched volume of detection antibody solution. A dried gel is re-hydrated with a volume of detection antibody on the order of the hydrogel water volume fraction, such that at equilibrium, the majority of the detection antibody is located in the gel, which drives immunocomplexation to saturation thus yielding $[C]_{max} \sim [Ag]_0$.

4.2 Materials and Methods

Chemicals/reagents. Acetic acid (A6283), 3-(Trimethoxysilyl)propyl methacrylate (662275), 30%T, 3.4%C acrylamide/bis-acrylamide (29:1) (A3574), N,N,N',N' Tetramethylethylenediamine (TEMED, T9281), bovine serum albumin (BSA, A7030), ammonium persulfate (APS, A3678), sodium deoxycholate (D6750) and sodium dodecyl sulfate (SDS, L4509) were purchased from Sigma-Aldrich. Triton X-100 (BP-151) was attained from ThermoFisher Scientific. Tris buffered saline with tween (20X TBST, 281695) was acquired from Santa Cruz Biotechnology. Premixed 10× Tris/glycine electrophoresis buffer (25 mM Tris, pH 8.3; 192 mM glycine) was procured from BioRad. Phosphate buffered saline (10X PBS,

45001-130) was purchased from VWR International. Deionized water (18.2 MΩ) was obtained using an Ultrapure water system from Millipore. N-[3-[(3-Benzoylphenyl)formamido]propyl] methacrylamide (BPMAC) was custom synthesized by PharmAgra Laboratories. Lentiviral infection (multiplicity of 10) was performed to produce U373 MG cells expressing Turbo GFP, which were generously provided by Dr. Ching-Wei Chang in Prof. S. Kumar's Laboratory. Rabbit anti-Turbo GFP antibodies (PA5-22688) were acquired from Pierce Antibody Products. Donkey anti-rabbit Alexa-Fluor 647-labeled secondary antibodies (A31573) were procured from Invitrogen. Recombinant Turbo GFP (FP552) was obtained from Evrogen.

Cell culture. The U373-GFP cells were cultured in a humidified 37 °C incubator kept at 5% CO2 with high glucose DMEM media (11965, Life Technologies) containing 1× MEM nonessential amino acids (11140050, Life Technologies), 1% penicillin/streptomycin (15140122, Invitrogen), 1 mM sodium pyruvate (11360-070, Life Technologies), and 10% calf serum (JR Scientific).

Hydration kinetics experiments. PA gels were dried in a nitrogen stream for ~1 minute. Dry gel mass was measured on an analytical balance (Ohaus, DV215CD), and gels were rehydrated in 1X TBST buffer. Upon removal of the gel from the TBST, gels were blotted dry using Kimwipes and weighed.

In-gel antibody concentration quantitation experiments. PA gels with benzophenone methacrylamide incorporated (7%T, 3 mM BPMAC) without microwells or protein immobilized were fabricated as described elsewhere[65] for the in-gel antibody concentration quantitation experiments**.** The experiments were performed with antibody solution in excess volume (15 mL of 0.02 mg/mL fluorescent secondary Ab) or approximately the gel hydration volume (50 µl for dehydrated gels, 25 µl for hydrated gels; 0.02 mg/mL concentration, 0.5 µg of antibody per half slide). Following 1 hr antibody incubation, antibody was immobilized in the gel using the benzophenone capture reaction upon UV exposure (OAI Model 30 Collimated UV Light Source, 25.5 mW/cm^2 for 2 min), and gels were washed in 1X TBST and imaged.

Single cell western blots. The scWBs were performed as previously described[65] up until the immunoprobing stage. To study the impact of gel hydration state on in-gel detection antibody concentration, we: (i) used diffusive probing of a hydrated gel or (ii) introduced detection antibody solution to a PA gel previously dried with a nitrogen stream (probing of a dehydrated gel), as indicated in the discussion of results. Briefly, the scWB was performed utilizing a PA gel that was grafted to a methacrylate treated glass microscope slide. The microwell array was created by chemically polymerizing a 7%T PA gel precursor solution on an SU-8 mold sandwiched to the glass microscope slide. A cell suspension (~10^6 cells/mL in 1X PBS) was introduced to the PA gel surface, cells were settled by gravity into the microwells, and excess cells were washed off the gel. Cells were lysed (~12s) within the wells in a 1X modified RIPA buffer[65], and the proteins were electrophoresed into the gel at ~40V/cm (~25s) in a custom electrophoresis chamber**.** The proteins were immediately photo-immobilized in the gel by a UV-mediated covalent reaction between abstractable hydrogens[68] on the proteins and the BPMAC groups incorporated in the gel matrix (Lightningcure LC5, Hamamatsu, 100% Power 45s exposure)**.** At the immunoassay step, antibody in 1X TBST with 5% BSA (25 µl per half slide for immunoprobing of hydrated gels, 50 µl per half slide for immunoprobing of dehydrated gels was loaded at the edge of the gel and sandwiched between the gel and another glass slide.

Immunoprobing of hydrated and dehydrated gels proceeded for 2 hours (primary antibody), and for 1 hour with secondary antibody. Gels were washed two times in 1X TBST for 30 minutes each on an orbital shaker between probing steps. Imaging was performed on a fluorescence microarray scanner (Genepix 4300A, Molecular Devices) with filter sets for the GFP and AlexaFluor 647-labeled antibodies chosen to minimize spectral cross-talk between the fluorescent protein and antibody used to detect the GFP.

Image analysis and quantitation. Analysis of scWB images was performed using custom scripts in ImageJ, and Matlab (2013a)**.** Area under the curve (A.U.C.) fluorescence was calculated by curve-fitting the scWB bands (both the detection antibody and expressed Turbo GFP fluorescence bands) to a Gaussian function, and summing the intensity values between ~three standard deviations of the peak center**.** A.U.C. was only reported for scWB bands with a Gaussian fit R-squared value >0.7, for accurate selection of peak boundaries**.** Statistical analysis was carried out with custom and existing Matlab functions.

4.3 Results and Discussion

In-gel immunoassays in dehydrated PA gels. We sought to satisfy two general in-gel immunoprobing design criteria and one additional specific scWB immunoprobing criterion: (*i*) transport times for detection antibody into the gel that are comparable to or faster than diffusive transport of detection antibody into the gel, (*ii*) in-gel concentrations of detection antibody that approximate concentrations in the solution phase (Figure 4.1C) and (*iii*) reduced scWB consumption of detection antibody mass, as compared to diffusive antibody introduction in hydrated gels. Immunoprobing in the scWB is an immunoassay in a PA gel; the gel also performs molecular sieving during electrophoretic protein sizing (Figure 4.1A). A PA gel with 7-10% T can resolve the majority of cytosolic proteins (~15-90 kDa[129] range). However, attaining baseline separation for ~21 kDa and ~65 kDa protein targets requires denser gels.[66] Increasing the volume fraction of the polymer even by a factor of two can reduce the partition coefficient by over an order of magnitude.[82] As a result, increasing the density of the gel for improved separation performance would dramatically lower the in-gel concentration of antibody. An analytical model of bimolecular binding kinetics showed only 50% of the total possible immunocomplex will form at equilibrium (with typical antigen concentrations from single cells and a low-to-moderate affinity antibody), thus limiting the analytical sensitivity of the assay (Figure 4.1B). Antibody-antigen binding to form immunocomplex, C, is governed by the following equilibrium reaction with forward rate constant k_{on} and backward rate constant k_{off}.

$$[Ab^*]_{gel} + [Ag]_0 \rightleftharpoons [C] \qquad \text{Eq. 4.3}$$

From bimolecular or Langmuir binding kinetics the concentration [C] as a function of time is given as:

$$[C] = [C]_{max}\left(1 - e^{-(k_{on}[Ab^*]_{gel} + k_{off})t}\right) \qquad \text{Eq. 4.4}$$

For the anticipated partition coefficient K=0.17 for detection antibody in an 8%T gel, we show the complex concentration normalized to the starting antigen concentration as a function of time in Figure 4.2, below. The equilibrium antibody-antigen complex concentration is expected to be

90% of saturation with a K_D of 10 nM at 1:10 dilution of 1 mg/mL antibody, and 1 nM antigen in gel (given the losses during scWB this would be a median expressed mammalian protein). Only 50% of saturated binding is achieved with a K_D of 100 nM (see Figure 4.2-Figure 4.3). With just a 5 times higher local antibody concentration in gel can drive reaction to 98% and 85% saturation respectively (Figure 4.3), so clearly increasing local Ab concentration is important goal for analytical sensitivity.

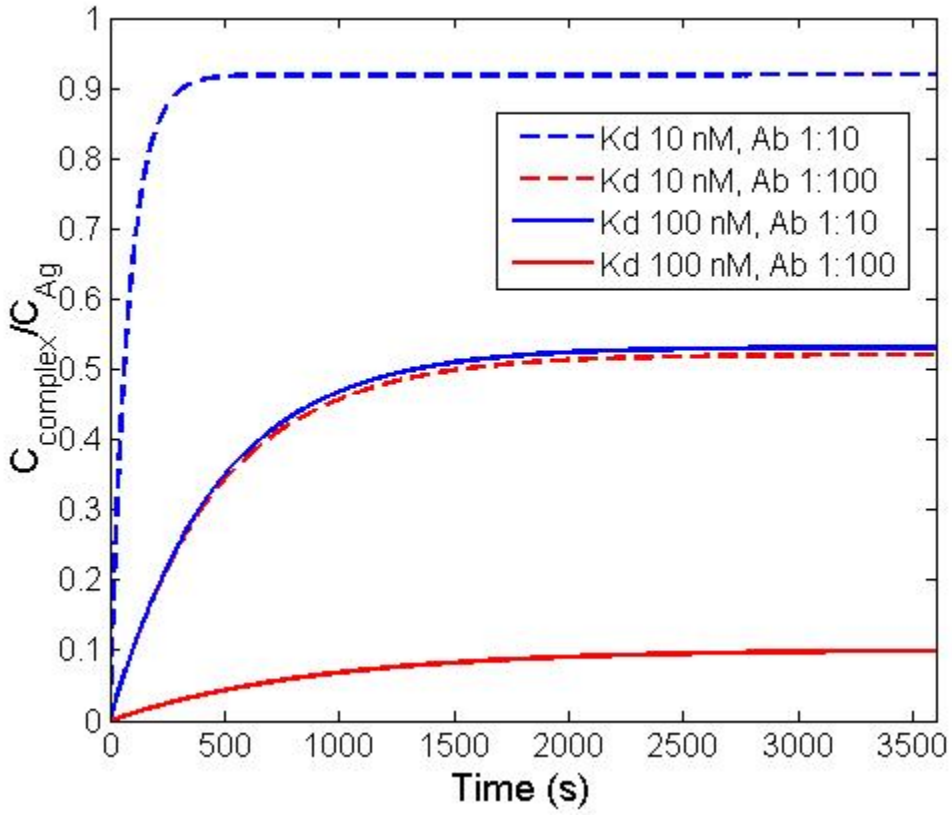

Figure 4.2: Analytical kinetics model of antibody-antigen binding assuming ideal transport with a partition coefficient of 0.17 for the Ab in the PA gel. Antigen concentration $[Ag]_0$=1 nM, $k_{off}=10^{-3}s^{-1}$and $k_{on}=10^{5}M^{-1}s^{-1}$ or $10^{4}M^{-1}s^{-1}$. Antibody concentrations are $[Ab^{*}]_{gel}=6.7x10^{-7}$ M for 1:10 and $6.7x10^{-8}$ M for 1:100.

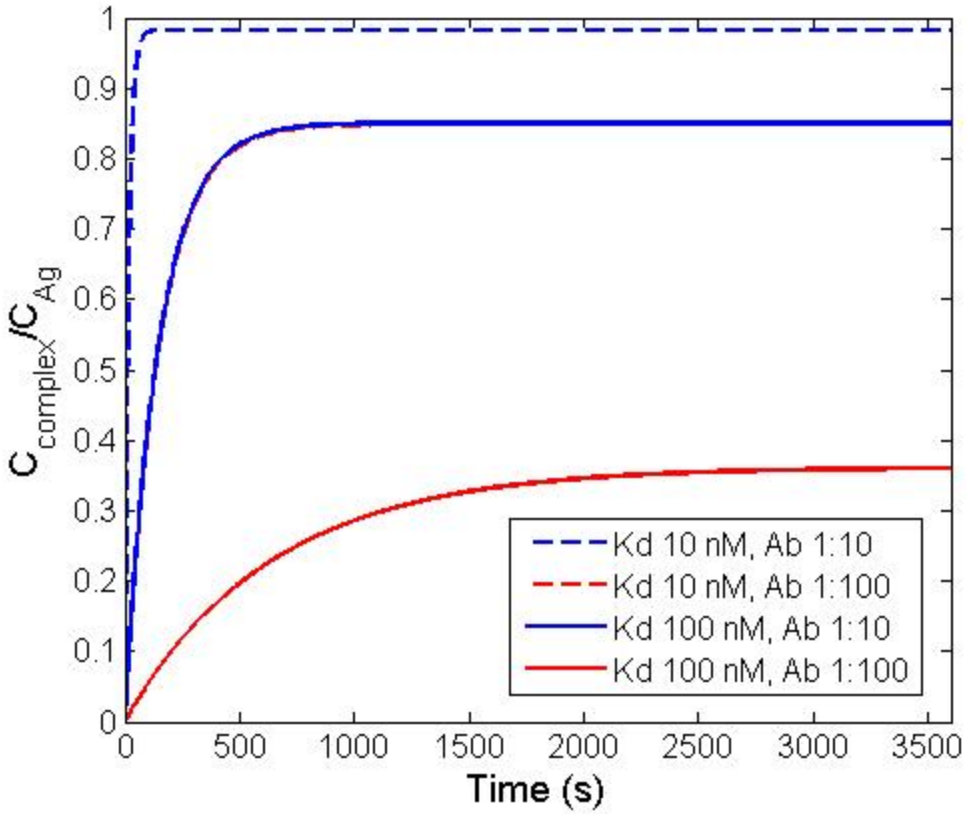

Figure 4.3: Analytical kinetics model of antibody-antigen binding assuming ideal transport with a partition coefficient of 0.85 for the antibody in the PA gel. Antigen concentration $[Ag]_0$=1 nM, $k_{off}=10^{-3}s^{-1}$and $k_{on}=10^5M^{-1}s^{-1}$ or $10^4M^{-1}s^{-1}$. Ab concentrations are $[Ab^*]_{gel}=6.7x10^{-7}$ M for 1:10 and $6.7x10^{-8}$.

To overcome the observed mass transport and thermodynamic limitations, we studied swelling of a dehydrated gel during rehydration as a promising mechanism to drive detection antibody into the dense sieving gel (Figure 4.1C). Maximizing the local concentration of detection antibody ($[Ab^*]_{gel}$ from Eq. 4.2) drives immunocomplex formation to saturation with $[C]_{max}$~$[Ag]_0$. We hypothesized that with antibody solution volume closely matched to the volume required to rehydrate the gel, at equilibrium, all antibody mass would be contained in the gel. We determined a procedure for drying and subsequently rehydrating the gel with antibody solution, and we used the rehydration procedure to increase the local concentration of detection antibody in the dehydrated gel compared with a hydrated gel. Furthermore, we evaluated the impact of increased concentration of detection antibody on the scWB immunoassay theoretically (with a binding kinetics model) and in a proof-of-concept demonstration on single GFP-expressing cells with immunoprobing for detection of GFP in dehydrated gels.

Procedure for drying and rehydrating the gel in antibody solution. The goal of increasing the local concentration of detection antibody in the gel required a protocol for (i) drying the hydrogel and (ii) rehydrating the gel in antibody solution. We investigated two main approaches

for dehydrating the thin 30 μm PA gels grafted to the glass slide: drying in a nitrogen stream or overnight drying in a desiccator**.** When drying in the nitrogen stream, we observed the gel undergo a transition from initially clear, to briefly opaque and clear again (where opacity is indicative of light scattering off saturated pores[150]). After drying, in order to confirm the clear gel was in fact dehydrated, we compared the dry mass of the gel after one minute in the nitrogen stream to that of a gel dried in the nitrogen stream and stored overnight in a desiccator. We observed no difference in the dry gel mass with overnight drying versus drying in the desiccator, suggesting that one minute in the nitrogen stream was sufficient to dehydrate the gel.

To meet the design specification of near-bulk antibody concentration in-gel at equilibrium (Figure 4.1C), we determined the volume required to rehydrate a dehydrated gel. Additionally, determining the timescale of rehydration informs the choice of incubation period during immunoprobing of dehydrated gels. To determine the rehydration volume and timescale, we performed gel swelling kinetics experiments, weighing the gel as a function of rehydration time as performed elsewhere[151] and shown in Figure 4.4. In the "excess volume" method, the gel was submersed in a TBST buffer bath having a volume ~2 orders of magnitude larger than the anticipated water volume fraction of the hydrated polymer[152]. While in the "matched volume" method, 50 μl of TBST (matched to the order of the water volume fraction of the hydrated polymer) was added to the side of the dried gel and spread across the gel with a glass slide (as used in our scWB protocol). Notably, as demonstrated in Figure 4.4A, when TBST solution containing antibody was added to the dry gel surface, minimal lateral wicking or spreading of the solution across the gel was observed even up to 45 min after addition of the droplet. Thus, another glass slide was used to spread the drop across the top of the dried gel, so as to overcome interfacial surface tension. In both the "excess volume" and "matched volume" methods, ~34 μl of buffer rehydrated the PA gels, with most rehydration occurring within ~1 s and completing in ~10 s (Figure 4.4C). Swelling of gels anchored to a glass slide is less than swelling of non-surface constrained gels.[153] However, the rehydration volume of 34 μl is within 10% of the anticipated rehydration volume for a gel of this geometry and composition (water volume fraction of ~0.96[152]). Similarly, the rehydration timescale corroborates studies of surface-constrained N-isopropylacrylamide gels (height, h ~ 160-300 μm[154]). For comparison, the anticipated timescale for antibody diffusing in a hydrated gel is ten times longer than $\tau_{rehydration}$, as $\tau_{diffusion} \sim \frac{h^2}{D} \sim 100$ s , where h is the height of the gel (~30 μm) and D is the diffusion coefficient for antibody in an 8%T gel.[69]

As a corollary consideration, the in-gel immunoassay using the dehydrated gels imposes the requirement that protein target (bound to the gel matrix) also be dehydrated. Previous crystallography and Fourier-transform infrared spectroscopy findings show that some proteins undergo irreversible conformation changes upon dehydration[155,156], and the activity of dehydrated enzymes can decline significantly.[157] Our group has previously successfully demonstrated immunoprobing of scWB gels after gels were dried in a nitrogen stream and archived.[65,66] To multiplex protein target measurements, we rehydrated the gels, chemically stripped detection antibodies from the gels, and immunoprobed for new targets. We previously observed minimal change in immunoprobe signal (i.e., SNR of EGFP changed from 15 to 17 upon one stripping/re-probing cycle), suggesting protein dehydration did not hinder subsequent in-gel antibody binding.[65] Interestingly, the protein rehydration process is estimated to require ~4 min for water association with ionizable groups of an enzyme and > 30 min for the complete

water solvation shell to re-form.[158] Thus, while we observed rapid antibody transport into the rehydrating gel, antibody binding may not occur immediately. Proteins may need time to rehydrate, which will depend on the gel dehydration state. Consequently, in this work, we adopted antibody probing times in line with our previous scWB assays for comparison (two hours and one hour for primary and secondary antibody incubation, respectively).[65,66]

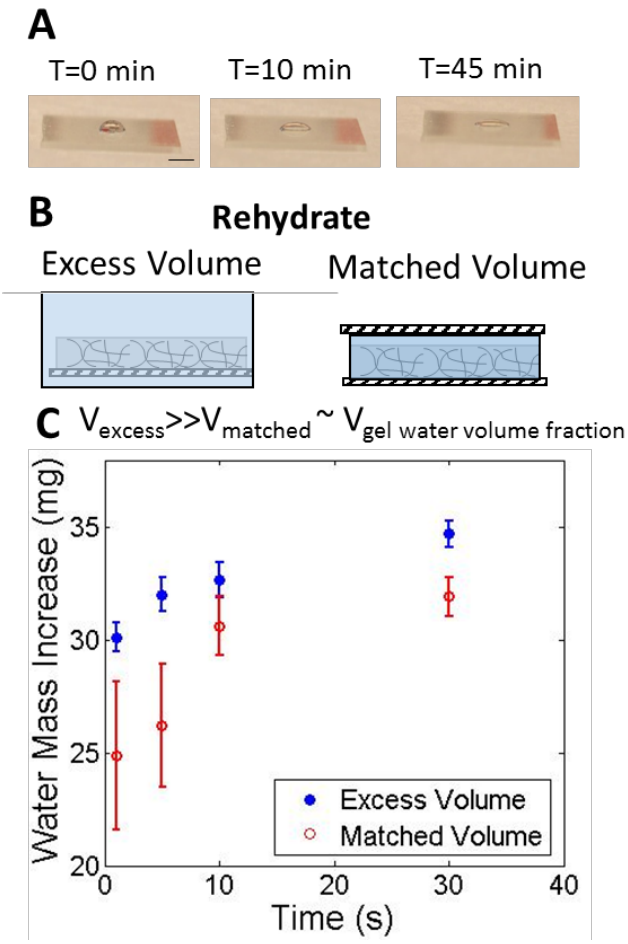

Figure 4.4: Hydration kinetics for determination of PA-liquid interfacing, and the volume of antibody solution required to match the hydrogel water volume fraction (A) Image of antibody droplet on the dry PA gel surface. Scale bar is 1 mm. (B) Schematic of PA gel slides were re-hydrated in an excess volume of several milliliters of TBST (left), or with 50 µl of TBST which matches the gel hydration volume (right). (C) Change in mass of water in the gel upon rehydration for both rehydration methods (n=3, error bar is standard deviation).

Characterization of antibody loading in hydrated versus dehydrated gels. We utilized our procedure for drying and rehydrating the gel and developed a protocol to determine whether introducing detection antibody in the dehydrated gels increased the in-gel detection antibody concentration. We used a gel that did not have microwells and had no immobilized target protein (a blank gel). We incubated the blank gel with fluorescently labeled detection antibody using

either the “excess volume” or “matched volume” approaches (depicted with fluorescently-labeled antibody solution in Figure 4.5A). The fluorescently-labeled antibody was immobilized in gel using UV-mediated benzophenone photocapture chemistry, as has been described and characterized previously.[68,69] Next, the gel was washed, dried and imaged. Imaging yielded a snapshot of the in-gel detection antibody concentration after incubation, with the important assumption that the UV immobilization was comparable in the hydrated and dehydrated gels. By drying the gel before imaging, we measured the in-gel antibody concentration eliminating out-of-plane fluorescence from a fluorescent liquid layer that would obscure the in-gel fluorescence. Probing using the “excess volume” method established the in-gel antibody concentration under well-characterized equilibrium partitioning behavior.[82]

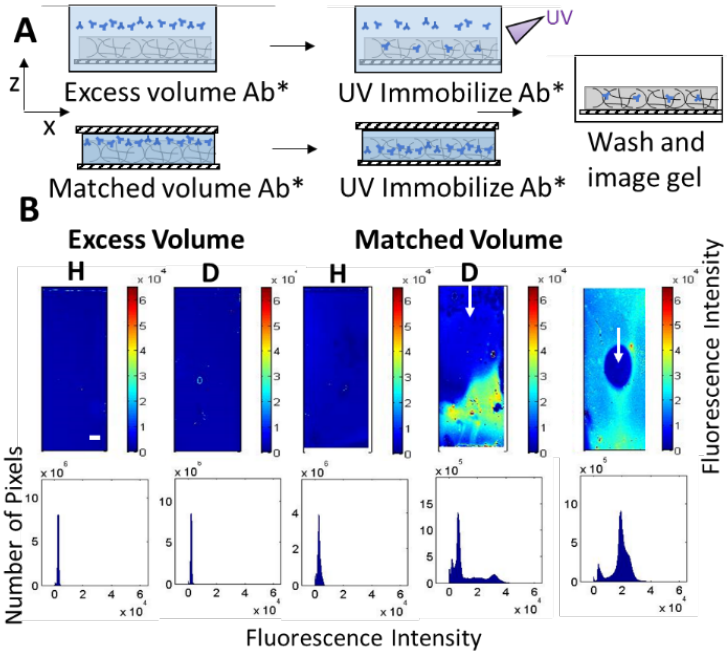

Figure 4.5: Detection of $[Ab^*]_{gel}$ in hydrated and dehydrated gels. (A) Schematic of “excess volume” (top row) and “matched volume” approaches to introduce antibody into gel. (B) Fluorescence intensity heat maps and fluorescence intensity histograms for hydrated (H) and dehydrated gels (D). White arrows indicate the location of antibody introduction in the matched volume approach. Scale bar is 5 mm. Mean peak intensity in “excess volume” approach for hydrated and dehydrated gels were both 1627 ± 973 A.F.U. (n=3 gels, error reported is standard deviation). In the ‘matched volume” method the mean intensity in the hydrated gel was 2056 ± 630 A.F.U. (n=4 gels) and the dehydrated gel was 8388 ± 2070 A.F.U. (n=4 gels), with a small second peak at 22738 ± 6802 A.F.U. (n=4 gels). When the droplet of antibody was added to the center of the gel the mean intensity was 25871 ± 11160 A.F.U. (n=6 gels), while the signal in the spot itself was 3104 ± 2107 A.F.U.

To assess the increase in local detection antibody concentration (in the dehydrated gels compared to hydrated gels), we incubated and immobilized antibody utilizing the “matched volume” (from Figure 4.4) approach. Figure 4.5B shows that the mean antibody fluorescence intensity for the

hydrated gel was within error of gels incubated in excess volume of antibody solution. In contrast, the mean antibody fluorescence intensity for the dehydrated gel was four times higher than the hydrated gel, with a second small peak in the intensity histogram that is 11 times higher than the hydrated gels. The 4-11 times higher antibody signal with the "matched volume" approach in dehydrated gels cannot be attributed to a change in the total liquid volume alone. Thus, we hypothesized the osmotic swelling pressure during rehydration[137] drives the solution of antibody into the gel. Finally, we observed the lowest signal at the gel location where the antibody solution first contacts the gel (see white arrows in Figure 4.5B). This suggests that spatial variation is associated with the dynamic process of rehydrating the dehydrated gel, a subject of continued investigation.

Since signal variation is large near the edge of the gel, as seen in Figure 4.5B, we sought to determine if gel edge defects impacted detection antibody transport through the gel. Thus, we investigated signal variation after depositing the droplet of antibody solution in the center of the gel and not near a gel edge. We observed the lowest antibody fluorescence signal (which was within error of the signal in the "excess volume" gels) at the location where the liquid first contacted the gel (Figure 4.5B). The mean antibody fluorescence intensity surrounding the center was ~16 times higher than in the "excess volume" approach. Therefore, the observed non-uniformity did not correspond with gel edge defects, but rather from interfacing of the antibody solution with the gel. Of note, the non-uniform antibody introduction shown in Figure 4.5 poses a challenge to establishing a limit of detection for immunoprobing of a dehydrated gel containing known quantities of GFP (as was previously performed in scWB gels immunoprobed in the hydrated state, and shown to have a limit of detection of ~27,000 copies of protein in the gel[65]). Future efforts to reduce spatial bias in the loading of antibody would allow for determination of this limit of detection in gels immunoprobed in the dehydrated state.

We attribute the observed non-uniformity to surface tension preventing spreading of the antibody droplet, thus leading to partitioning behavior where the antibody solution first contacts the gel. Gel hydration is a balance of the free energy of mixing from solvent-polymer interactions and the elastic free energy which opposes swelling.[159] However, this process did not occur initially because interfacial surface tension (Figure 4.4A) prevented spreading of the antibody droplet. The droplet volume exceeded the gel volume in contacted by 100x. Thus, before the antibody solution spread across the gel surface, the antibody droplet was effectively in the "excess volume" regime (at the location of the droplet), and "local partitioning" occurred. Diffusion of antibody to smooth the concentration gradient would require > 200 days (assuming the non-uniformity is ~10 mm characteristic diffusion length and the antibody diffusivity is as reported elsewhere[65]). Further experiments on the sensitivity of hydrogel loading to starting volume are warranted to determine if uniform macromolecule delivery to a dehydrated gel is feasible. Regardless, we have demonstrated a method of increasing the in-gel concentration of antibody (by ~4-11 times) in a hydrogel without changing the composition of the gel or solute as other groups have demonstrated.[141–143] Thus the "matched volume" approach for loading hydrogels with macromolecules may be generalizable to other in-gel immunoassays and drug delivery applications. For the latter, promising antibody therapies for cancer[160] may be realized with controlled release from hydrogels[161], which could be loaded with the necessary dose by the "matched volume" approach described here.

Implications of rehydration timescales and local antibody concentration in probing of dehydrated gels. To determine how the increased in-gel concentration of detection antibody attained with the "matched volume" approach of antibody loading will affect the analytical sensitivity of a typical in-gel immunoassay, we developed a bimolecular binding kinetics model for antigen and antibody binding to form immunocomplex. The binding efficiency is defined as $C^* = [C]_{max}/[Ag]_0$, where $[C]_{max}$ was given in Eq. 4.2. We use a concentration of $[Ag]_0 = 0.75$ nM, which is just below the single-cell concentration of a median expressed protein[26], as is relevant to our application of "matched volume" antibody loading for single-cell Western blot immunoprobing. However, the model is broadly applicable, and may be used to inform design of other in-gel immunoassays as long as the approximate values for the variables in Eq. 4.2 are known. The binding efficiency is evaluated as a function of K_D (the ratio of k_{off}/k_{on}) in the 0.1 μM to 1 μM range assuming no mass transport limitations (the in-gel concentration of antibody instantaneously reaches the equilibrium concentration anticipated from Figure 4.5, "matched volume" approach). While the K_D of commercially available antibodies will vary widely depending on target antigen, most antibody isolated from naïve libraries will have K_D's in the micromolar range[162]. Certain *in vivo* isolation techniques can yield picomolar affinity antibodies[163]. Thus the K_D range considered in Figure 4.6 is an estimate for low-to-moderate affinity antibodies.

As shown in Figure 4.6, the low concentration of antibody in the hydrated gel caused the binding efficiency to rapidly fall as a function of K_D. The concentration of antibody in the hydrated gel is estimated from Figure 4.5 using $K_{partition}=0.17$, and the concentration of antibody in the "matched volume" data. Notably, at $K_D \sim 0.4 \times 10^{-7}$ M, detection antibody binding efficiency is below the previously reported LOD of the scWB.[65] In contrast, when the concentration of antibody corresponded with the 4-11x higher concentrations measured in the dehydrated gels using the "matched volume" approach (gray solid and dashed lines respectively in Figure 4.6), we found increased antibody concentration will drive immunocomplex formation above the LOD. Clearly, this improved sensitivity comes at the cost of increased measurement variance and binding efficiency variation that is K_D dependent. (Figure 4.6).

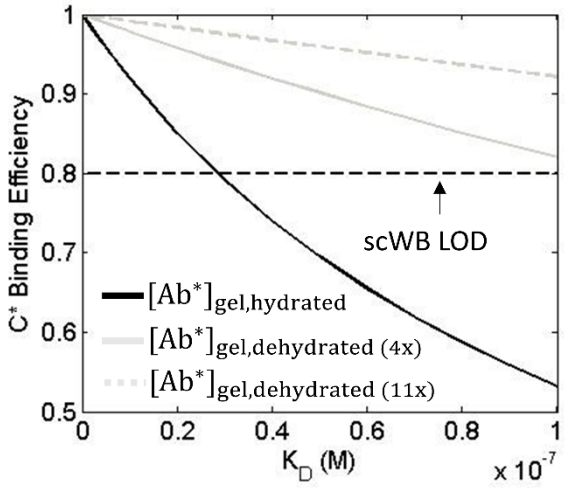

Figure 4.6: Binding kinetics model showing phase space where probing of dehydrated gels will improve scWB assay performance. The estimated in-gel antibody concentrations are based on the experiments in Figure 4.5 (with $[Ab^*]_0$=6.7x10^{-7} M, $K_{partition}$=0.17, and the in-gel concentration in the dehydrated gels 4-11 times higher than the hydrated gels). The black dashed line is the previously reported scWB limit of detection (LOD).

To increase model accuracy, we also consider any mass transport limitations on immunocomplex formation and, finally, in-gel immunoassay readout. We assessed such mass transport limitations on the assay by evaluating the Damköhler number of the system, which is defined as[72]:

$$Da = \frac{\tau_{transport}}{\tau_{rxn}} \qquad \text{Eq. 4.5}$$

where τ_{rxn} is the reaction equilibration time:

$$\tau_{rxn} = \frac{1}{k_{on}[Ab^*]_0 + k_{off}} \qquad \text{Eq. 4.6}$$

and $\tau_{transport}$ is the equilibration time for mass transport. For moderate-to-high affinity detection antibodies, any mass transport limitations will be exacerbated by the rapid reaction rates, so we consider k_{on}~10^4-10^6 M^{-1}s^{-1} and the concentration of antibody estimated from our antibody incubation experiments. For hydrated gels, the diffusive equilibration time was ~100 s. With an in-gel antibody concentration used in the kinetics model (Fig. 4) we found 0.10 < Da < 10.0, suggesting that the assay is largely mass transport limited. When dominated by mass transport limitations, assay time scales as the product of *Da* and the reaction equilibration time, and assay time increases.[90] In contrast in dehydrated gels, transport of antibodies (~10 s) completes before the anticipated protein rehydration time (~4 min[158]). The relevant antibody diffusion length scale once reactions can occur in this case is therefore the PA gel pore radius. This yields a reaction-limited assay (2.3x10^{-6} < *Da* < 2.4x10^{-4}). We anticipate probing of dehydrated gels could reduce assay duration, although further study is required to determine if protein-rehydration is a rate-limiting step.

Improved antibody probing performance in dehydrated gels compared with hydrated gels. To characterize the impact of increased local concentration of detection antibody in dehydrated gels in the scWB assay, we measured GFP in U373-Turbo GFP transfected cells. Robust characterization of assay variability utilizes direct correlation between the detection antibody signal and level of target protein immobilized on the PA gel. For direct measurement of target protein immobilization in this characterization study, we utilize signal from an expressed fluorescent protein (GFP). We compared probing efficiency in gels immunoprobed in the hydrated versus dehydrated state (Figure 4.7). When gels were immunoprobed in the dehydrated state, we observed both (1) a higher scWB immunoprobing signal (Figure 4.7A) and (2) a higher background signal (Figure 4.8), as compared to immunoprobing of gels in a hydrated state. We evaluated the A.U.C. for the bound detection antibody signal (immunocomplex, $[C]_{max}$) and normalized this A.U.C. to the expressed GFP A.U.C. ($[Ag]_0$) as a function of secondary antibody mass used ($[Ab]_0$, Figure 4.7B**).**

Strikingly, we found the median normalized A.U.C. for gels immunoprobed while dehydrated was ~2-14 times higher than in gels immunoprobed while hydrated at all of the antibody masses utilized (Mann-Whitney U-test p-value<0.00005 for each antibody mass used, Table 4-1; sample

sizes reported in Table 4-2). Additionally, we observed higher signal-to-noise ratio (SNR) when antibody was introduced in the dehydrated gel at all antibody masses utilized (Figure 4.9), except at 0.25 μg (where the Mann Whitney U-test p-value was higher than 0.05) and at 5 μg (where the median SNR was ~1.4x higher for the gels immunoprobed in the hydrated state). To determine if the overlap of the SNR distributions with the 0.25 μg antibody mass was reproducible we performed two replicates (Figure 4.9). Again, we found the SNR distributions overlapped (though the Mann Whitney U-test p-value for the second replicate was $p<0.05$). With application of 1 μg of detection antibody, we observed a maximum SNR in the gels immunoprobed in the dehydrated state (median SNR=228.7) which was five-times higher than the median SNR of the gels immunoprobed in the hydrated state (median SNR=43.6). The higher SNR in the gels that were dehydrated reflects an improved analytical sensitivity. Future work includes extending immunoprobing of dehydrated gel to measure low-abundance targets in single cells. Furthermore, we observed probing of dehydrated gels allows for up to 10-fold lower antibody consumption compared to hydrated gels. In Figure 4.7, we show nearly comparable median normalized A.U.C. for the gels immunoprobed in the dehydrated state utilizing 0.5 μg of antibody and the hydrated gel using 5 μg of Ab.

While the increased normalized A.U.C. and SNR show that probing dehydrated gels improved analytical sensitivity, we also observed high variation in the normalized A.U.C. when the gel was immunoprobed in the dehydrated state. For our gamma-distributed protein expression data[65,164] we required a metric of variance that accounts for skew of the distribution of protein expression. Thus we used the coefficient of quartile variation, CQV,[165], which was developed to accurately describe variation in skewed distributions, and is defined as

$$CQV = \frac{Q_3 - Q_1}{Q_3 + Q_1} \qquad \text{Eq. 4.7}$$

where Q3 is the 75th percentile, and Q1 is the 25th percentile of the statistical distribution. The CQV of the normalized A.U.C. was not dependent on the antibody mass used for immunoprobing hydrated or dehydrated gels (see Table 4.1 for all CQV values and comparison with the coefficient of variation). The mean CQV across all antibody masses used was 26.1% ± 10.2% and 25.0% ± 17.2% for gels probed in the dehydrated and hydrated states respectively, meaning variation was comparable in the two methods. Further study of the contributions of technical variation in immunoprobing is important to identify technical versus biological variation in our measurement of cell-to-cell heterogeneity in protein expression.[65,66]

We sought to better understand the observed variance in immunoprobing by evaluating the correlation between antibody fluorescence and expressed GFP fluorescence. In Figure 4.7C and Table 4-2, we show the correlation between detection antibody A.U.C. and expressed GFP A.U.C. and calculated Pearson correlation coefficients, r, for the data in each scatter plot (Table 4-1). Ideally, the antibody signal would be directly linearly correlated with the expressed GFP signal (r=1), though the highest observed r values were 0.97 and 0.8 for hydrated and dehydrated gels, respectively. To determine whether the measured correlation coefficients were statistically the same between gels immunoprobed in the dehydrated and hydrated states, we utilized a Fisher's r to Z transformation[166] and a two-tailed Z-test. Correlation coefficients must be transformed to attain a normally distributed Z test statistic for which we can determine the p-value. At the 0.08, 0.25, 0.5 and 5 μg antibody masses, we rejected the null hypothesis that the

Pearson r values in the hydrated and dehydrated gels were equivalent ($p<0.05$), and we found the measured correlation coefficients were higher for gels immunoprobed while hydrated versus dehydrated. The lower correlation between antibody A.U.C. and expressed GFP A.U.C. for gels immunoprobed in the dehydrated state indicates increased technical variance associated with the measurement. We hypothesize the spatial variation in detection antibody introduction in dehydrated gels (Figure 4.5: Detection of $[Ab^*]_{gel}$ in hydrated and dehydrated gels. (A) Schematic of "excess volume" (top row) and "matched volume" approaches to introduce antibody into gel. (B) Fluorescence intensity heat maps and fluorescence intensity histograms for hydrated (H) and dehydrated gels (D). White arrows indicate the location of antibody introduction in the matched volume approach. Scale bar is 5 mm. Mean peak intensity in "excess volume" approach for hydrated and dehydrated gels were both 1627 ± 973 A.F.U. (n=3 gels, error reported is standard deviation). In the 'matched volume" method the mean intensity in the hydrated gel was 2056 ± 630 A.F.U. (n=4 gels) and the dehydrated gel was 8388 ± 2070 A.F.U. (n=4 gels), with a small second peak at 22738 ± 6802 A.F.U. (n=4 gels). When the droplet of antibody was added to the center of the gel the mean intensity was 25871 ± 11160 A.F.U. (n=6 gels), while the signal in the spot itself was 3104 ± 2107 A.F.U.B) may contribute to the lower correlations between antibody A.U.C. and expressed GFP A.U.C. Further investigations will evaluate when increased technical variance might mask biological variance, as variance will be specific to the antibody, protein target and biological system.

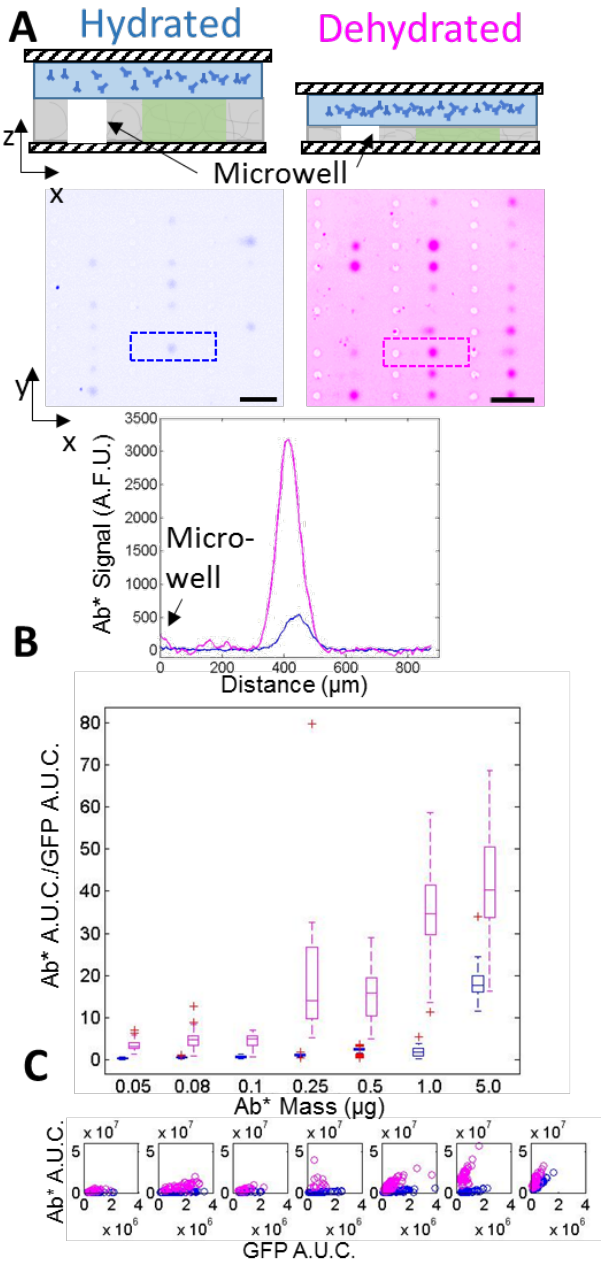

Figure 4.7: Increased scWB probing signal in dehydrated gels compared with hydrated gels. (A) Antibody fluorescence images and intensity plots of scWBs for GFP from U373-GFP cells in hydrated (left, blue) and dehydrated gels (right, magenta). Scale bar is 500 μm. (B) Antibody dilution dependence of area under the curve (A.U.C.) values for the fluorescently-labeled antibodies normalized to A.U.C. for the expressed GFP. Horizontal line in the box is the median (higher for gels immunoprobed while dehydrated, Mann-Whitney U-test p-value<0.0005) and box edges are at 25th and 75th percentile. (C) Scatter plots of antibody A.U.C. and GFP protein A.U.C. for each detection antibody mass tested in B (scatter plot is below its corresponding box plot).

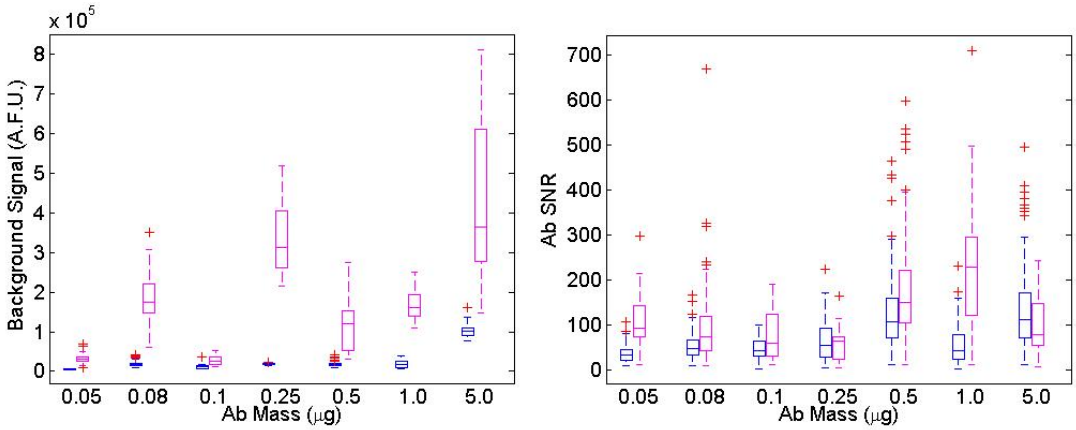

Figure 4.8: Background signal and signal-to-noise ratio (SNR) of the fluorescent detection antibody signal from the results depicted in Figure 4.7. For the SNR, Mann-Whitney U test p-value<0.05 for all Ab masses except 0.25 μg. The background region was chosen as 3-4 standard deviations away from the peak center. Results indicate that wash-out of the detection antibody was less effective in the dehydrated gels. Though the background signal was higher in gels immunoprobed in the dehydrated state (magenta) versus the hydrated state (blue), this did not impact the specificity or selectivity of the assay, as the peak signal was always distinguishable from the background.

Table 4-1: Summary of quantitation of median AUC and metrics of variability from Figure 4.7. D corresponds to immunoprobing of dehydrated gels and H is immunoprobing of hydrated gels. The CV is the coefficient of variation and the CQV is the coefficient of quartile variation.

Mass of Ab (μg)	**Median A.U.C. (D)**	**Median A.U.C. (H)**	**CQV (D)**	**CQV (H)**	**CV (D)**	**CV (H)**
0.05	3.0976	0.32503	20.35717	36.86089	35.478	45.595
0.083333	4.5943	0.48326	24.17221	14.59317	46.857	25.481
0.1	4.8139	0.64985	24.95586	33.28148	34.907	43.683
0.25	14.0011	1.0035	47.06971	15.38406	96.239	24.458
0.5	15.7653	2.3354	29.94712	9.076528	36.229	21.804
1	34.698	1.7587	16.66255	54.98288	28.421	64.111
5	40.3336	17.6025	19.98149	10.50667	29.04	18.138

Table 4-2: Pearson correlation coefficients for Figure 4.7C. Rejection of the null hypothesis that the correlation coefficient is zero indicated with * ($p<0.003$). The rejection of the null hypothesis that the Pearson r of the hydrated gel is equivalent to the Pearson r of the dehydrated gel at a given antibody mass is indicated with ** ($p<0.05$).

Antibody Mass (µg)	**0.05**	**0.08****	**0.1**	**0.25****	**0.5****	**1**	**5****
Hydrated Pearson r	r=0.33* n=50 cells	r=0.95* n=78 cells	r=0.62* n=78 cells	r=0.89* n=58 cells	r=0.88* n=165 cells	r=0.70* n=64 cells	r=0.97* n=74 cells
Dehydrated Pearson r	r=0.58* n=43 cells	r=0.43* n=48 cells	r=0.70* n=23 cells	r=-0.12 (p=0.70) n=12 cells	r=0.70* n=162 cells	r=0.75* n=23 cells	r=0.80* n=47 cells

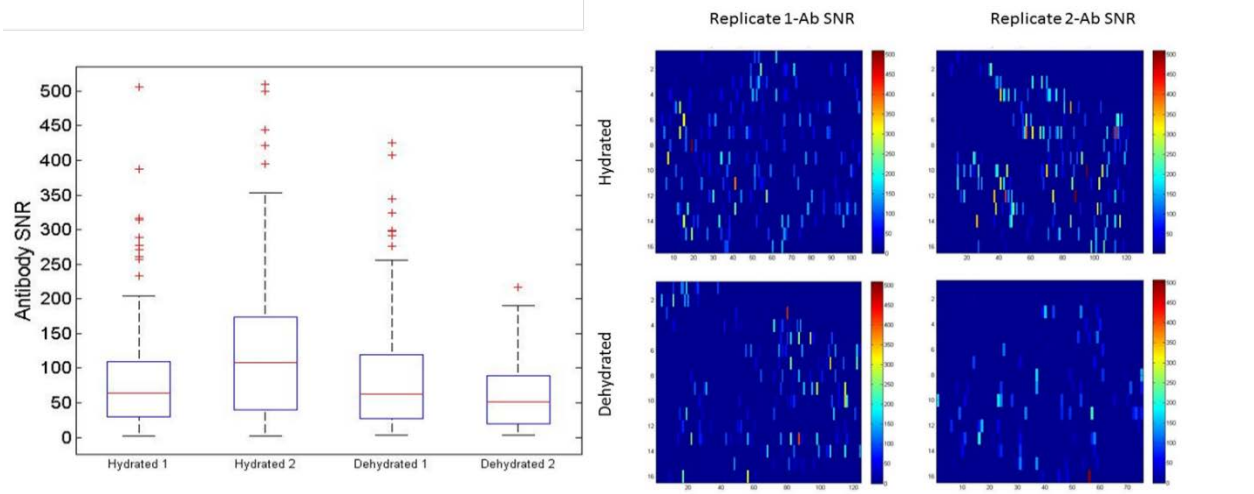

Figure 4.9: Box plots and heatmaps showing detection antibody fluorescence SNR run-to-run variability in probing of gels in the hydrated versus dehydrated state. The replicates were collected at the 0.25 µg of Ab condition (where no statistically significant difference between SNR distributions for probing in hydrated or dehydrated gels was observed). Left: box plots of SNR for two replicates each of gels probed hydrated and dehydrated. The replicates performed with probing of dehydrated gels and hydrated gels yielded Mann-Whitney U test p-values of $p<0.05$, and $p<0.000005$ respectively. Thus, we reject the null hypothesis that the distributions of the replicates are equivalent (inter-assay variability in SNR in gels immunoprobed with 0.25 µg of Ab is observed). The Mann-Whitney U test p-values comparing hydrated and dehydrated gels

(e.g. hydrated 1 SNR vs. dehydrated 1 SNR, etc.) yielded $p>0.9$ and $p<0.05$ for replicates 1 and 2 respectively. Right: heatmaps showing spatial distribution of SNR in the replicates.

4.4 Conclusions

We report on rehydration of dehydrated hydrogels in sparing volumes of macromolecule solution for enhanced loading of a PA hydrogel. Our hydrogel is utilized for a single-cell immunoassay, which allows for detection of protein isoforms[65] and identification of off-target antibody binding unmeasurable in other single cell proteomic approaches used with cancer and stem cells.[15,58] By rehydrating the dehydrated scWB gel in a volume of antibody solution closely matched with the hydrogel water volume fraction, we achieved higher scWB immunoprobing signals and achieved reduced consumption of costly antibody reagents. This approach to mitigate partitioning presents a trade-off with antibody probing signal that may be less well-correlated with target protein levels. We anticipate the impact of this increased technical variation will be antibody affinity specific, and thus future work includes a survey the impact of antibody affinity on technical variation in probing of hydrated versus dehydrated gels. Additionally, we observed an intriguing phenomena, whereby the region of the dehydrated gel that first made contact with the antibody solution yielded the lowest antibody fluorescence signal. Follow-up work could further characterize the hypothesized “local partitioning” effect, by measuring local antibody concentration as a function of the ratio of the antibody liquid volume and volume of the gel in contact with the antibody liquid. Given the straightforward nature of “matched volume” loading of macromolecule solutions in dehydrated gels, findings are relevant to numerous drug delivery and hydrogel assay applications.

Chapter 5

Alternative Hydrogels For Electrophoretic Cytometry Tuned For Proteins of Specific Molecular Weights

5.1 Introduction

In general, electrophoretic separations can be tuned to optimize the separation resolution by careful selection of the gel density[167]. From the Ferguson relationship[74], the differential electrophoretic mobility (μ_2- μ_1/μ_2) between two proteins can be expressed as:

$$\frac{\mu_2-\mu_1}{\mu_2} = 1 - 10^{-(K_{r,1}-K_{r,2})T} \qquad \text{Eq. 5.1}$$

where $K_{r,1}$ and $K_{r,2}$ are the retardation coefficients for each protein and T is the total acrylamide concentration. This relation highlights how the choice of gel density (%T) can push a separation to increase the differential mobility between proteins to improve the separation resolution. However, EP cytometry separations of small proteins balance tradeoffs between separation performance and in-gel immunoassay sensitivity. Namely as gel density increases (and pore size decreases), size exclusion-based partitioning lowers the partition coefficient for detection antibodies[82,168], and mass transport limitations are expected to arise. Consequently, low concentrations of detection antibody in the gel yield low immunocomplex signal[169].

The challenge of loading detection antibodies into EP cytometry gels has thus far been addressed by: i) rehydration of EP cytometry gels in limiting volumes of antibody solution[126] (described in Chapter 4); and ii) hydrogel pore-size modulation using acid hydrolysable crosslinkers[169]. The method of introducing an acid hydrolysable crosslinker was applied for the generation of photopolymerized gradient gels, allowing proteins from single cells ranging from 25-289 kDa to be separated in a 1-mm EP cytometry separation lane[169]. While the effective gel densities in the gradient gel ranged from 4.7-8.5%T, detectable antibody signal for GFP from single cells was reported even in a 16%T decrosslinked gel (when generally probe signal is undetectable at >10%T)[169]. Thus, acid decrosslinkable gels are an intriguing material to attempt to tune small molecular weight difference separations for low molecular weight species.

At the other end of the spectrum, large oligomeric proteins and complexes are separated in native conditions and in large pore-size gels[77]. For example, the filamentous (F)-actin polymer, which is on average ~2600 kDa[170], was electrophoresed in non-ionic detergent buffers in agarose-containing capillaries[171] (and could not be electrophoresed in denser sieving matrices such as polyacrylamide). Separation of F-actin from monomeric G-actin (a 42 kDa protein) can provide critical quantitative insight on the polymerization state of the actin cytoskeleton[172] (as described in a later chapter), which regulates vast cell migration and signaling processes[173]. Thus, adapting

EP cytometry hydrogels to accommodate large oligomeric species such as F-actin could open up new lines of inquiry to elucidate the link between cellular molecular and mechanical properties.

EP cytometry in alternative materials to polyacrylamide has not yet been demonstrated. The key limitation is the need to adapt the photoimmobilization chemistry to incorporate the UV-activatable benzophenone moiety within the hydrogel of interest. Previously described benzophenone modification of agarose yielded low photoimmobilization efficiencies (~10% for protein), and required arduous multi-stage synthesis schemes[174].

In this chapter, we evaluate and characterize hydrogels at the two size limits for protein separation (for small or large molecular weight species respectively). First, we assess antibody partitioning and separation performance in high-density decrosslinkable gels. Next, we describe swelling-induced buckling that is observed in the surface-constrained decrosslinked gels that obscures EP cytometry quantitation. For large-pore size gels we sought alternative methods to functionalize agarose with benzophenone groups. We describe a straight-forward method to fabricate agarose microwell arrays on a solid glass substrate. Finally, the section concludes with suggested paths forward to design alternative materials to balance separation and immunoassay performance in EP cytometry.

5.2 Materials and Methods

DK gel chemical and photopolymerization

Gels were chemically or photopolymerized with the compositions delineated in Table 1-2, below. All precursors were degassed for at least 2 minutes prior to polymerization. For chemical polymerization, reactions were allowed to proceed for 15-20 minutes. Photopolymerization times and UV doses varied between 20-26.5 mW/cm^2 and ~60-180s. Each gel polymerization condition must be optimized for the intended separation/application. After polymerization gels are stored in 1X Tris CAPS (pH=9.6) to prevent hydrolysis of the ketal functional group.

Table 5-1: Precursor solution for photopolymerization of DK gels.

%T	%C*	Crosslinker molar ratio	40%T 3.3% C acrylamide/bis	DK (400 mM)	25x Tris glycine	100 mM BPMAC	3% (w/v) VA-86 in 40% linear acrylamide	3% (w/v) VA-86 in water	40% linear acrylamide	Water
18	6	0.99	8.11	173.04	40	30	333.33	-	81.83	333.69
16	6	0.99	7.21	153.82	40	30	333.33	-	35.70	399.94
12	6	0.99	5.41	115.36	40	30	-	333.33	276.77	199.12
8	6	0.99	3.60	76.91	40	30	-	333.33	184.52	331.64

Table 5-2: Precursor solution for chemical polymerization of DK gels.

%T	%C*	Crosslinker molar ratio	40%T 3.3% C acrylamide/bis	DK (400 mM)	25x Tris glycine	100 mM BPMAC	10% APS	10% TEMED	40% linear acrylamide	Water
12	6	0.99	2.16	46.15	16	12	3.2	3.2	110.71	206.58
16	3.3	0.99	1.59	33.84	16	12	3.2	3.2	153.19	176.99
16	3.3	0.78	34.88	26.66	16	12	3.2	3.2	121	183.06

16	3.3	0.70	47.57	23.93	16	12	3.2	3.2	108.74	185.37

DK gel decrosslinking

Gels were decrosslinked in 1% HCl solution (pH 1.1-1.3) as previously described[169]. The gels were submerged in the 1% HCl solution in a petri dish for 30 minutes at room temperature. After decrosslinking, HCl solution was replaced with 1X Tris CAPS or TBST. An abundance of caution is required when handling the gels in the concentrated acid solution. Appropriate engineering controls (e.g., use of a fume hood), and personal protective equipment (including but not limited to: lab coat, lab goggles, close-toed shoes, nitrile gloves, and NitroSolve gloves) must be used to ensure safety.

Partition coefficient measurement

A photomask was laser cut from a folder leaving 3-mm x 3-mm cut-through squares. With each mask, two half slides can be fabricated at once, facilitating the fabrication of the gel squares to be kept crosslinked and those to be decrosslinked on the same mask at the same time. The procedure included preparing the precursor and pipetting it between the half glass slide and glass surface pre-treated to be hydrophobic (using GelSlick) separated by the 500-micron thick spacer. Following photopolymerization on OAI (as indicated below), excess precursor was wicked away and a new precursor with the next %T was introduced. For each polymerization step, the other squares of the mask were covered with tape to prevent UV transmittance. The mask was kept dry. If any precursor solution wicked under the gel-slicked glass slide that the mask is taped to, the mask went from transmitting ~0 mW/cm^2 to 1 mW/cm^2. This lead to over-polymerization and merged gel features. The polymerization conditions were as follows: 8%T (8%T, 6%C 99DK 26.5 mW/cm^2 175s), 12%T (12%T, 6%C 99DK 26.5 mW/cm^2 150s), 16%T (16%T, 6%C 99DK 26.5 mW/cm^2 140s) and 18%T (18%T, 6%C 99DK 26.5 mW/cm^2 130s). The mask required ~2 mm spacing or greater between features to prevent gel features from polymerizing into each other.

EP cytometry procedure

The full EP cytometry procedure is described in the Appendix. MCF7 cell culture and EP cytometry immunoprobing of GAPDH and PS6 were carried out as in Chapter 5.

Fabrication of agarose microwell arrays on glass

The complete protocols for allyl agarose functionalization on glass, and PDMS micropost fabrication are provided in the Appendix.

5.3 Results and Discussion

Dense decrosslinkable polyacrylamide gels for low molecular weight protein separations

We aimed to tune high-density decrosslinkable polyacrylamide gels to separate small molecular weight difference proteins in the low molecular weight range in an EP cytometry device. Utilizing the same principle assay steps, but employing the acid-hydrolyzable diacrylamide ketal (DK) crosslinker along with low percent bisacrylamide gel, we sought to overcome partitioning

limitations for antibody reagent delivery in the assay (Figure 5.1). Namely, immunoprobing efficiency depends on the gel %T, but with the inclusion of high ratios of DK:bisacryalmide, signal becomes detectable even in a 16%T gel[169]. Assessment of partition coefficients in crosslinked and decrosslinked gels can inform in-gel immunoassay design.

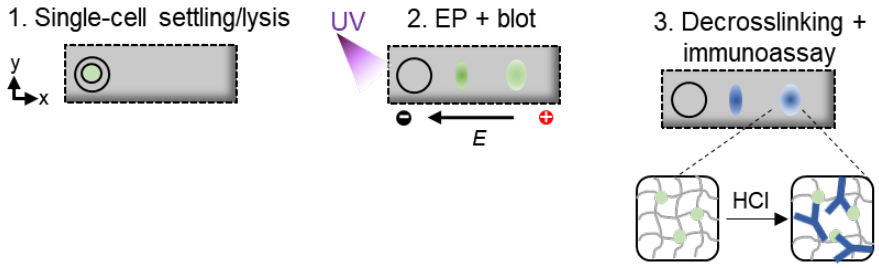

Figure 5.1: Stimuli-responsive microgel for EP cytometry separations of proteins with small molecular weight differences. (A) Electrophoretic cytometry schematic workflow. Cells are settled in microwells patterned in a stimuli-responsive polyacrylamide gel that serves as a separation matrix/immobilization scaffold (step 2), and a pore-modulatable volume for an immunoassay upon HCl-induced decrosslinking (step 3).

We designed a system for measuring the partition coefficients of crosslinked and decrosslinked gels in which gel squares of different density are serially photopolymerized on a glass slide (Figure 5.2). The system uses polyacrylamide gels that are 500 microns thick (as determined by using Teflon spacers) to attempt to minimize the effects of out of plane fluorescence on the measured partition coefficient[82].

The resulting slide with gels of different %T is shown in Figure 5.2. One half slide was decrosslinked for 30 min in 1% HCl and the slides were placed in 1x TBST prior to Ab incubation. Interestingly, through two attempts at the partitioning experiment, the 8%T decrosslinked gel popped off of the glass slide. This may be due to fewer crosslinks keeping the gel attached to the glass surface for the 8%T. Thus, in order to measure the partition coefficients for decrosslinked 8%T gels, we anticipate that larger gel squares would be needed.

By optimizing the imaging settings, partition coefficients down to ~3% could be measured (based on the dynamic range of the imaging and the intensity of the blank/background buffer). The gels were imaged prior to incubation in the 0.02 mg/mL AF647 Ab solution, and then again after 24 hours. Initially, the partition coefficient was identical across all gel densities (data not shown). In order to address this, a glass lid was used to cover the gels, antibody solution was pipetted between the slides, and the edges were sealed with Vaseline instead of imaging in a bath of fluorescent antibody solution.

As shown in Figure 5.2, we assessed the partition coefficients in the crosslinked and decrosslinked gels. The partition coefficient of the crosslinked 8%T gel of ~0.3 is higher than the previously reported 0.17 for 8%T polyacrylamide gels[65], however this is not surprising given the

gel is composed of the DK crosslinker, and the previous measurement was performed in SDS-containing RIPA buffer. Further, we have noticed that the DK gels are less wettable, which corresponds with the higher hydrophobicity of the DK crosslinker than bisacryalamide. Enhanced hydrophobic-hydrophobic interactions between the antibodies and the DK crosslinked gels compared with bisacrylamide crosslinked gels could contribute to the more favorable partition coefficient observed here. For the higher density gels, we observe that the partition coefficient in the decrosslinked gels is 4-10x higher than the crosslinked gels at the same %T. The 16%T and 18%T crosslinked gel partition coefficients are ~3%, which was the noise floor for the experiment; thus it is likely that the partitioning coefficients could be lower for the 16% and 18% T gels. The measured partition coefficient in the 12%T gel is in reasonable agreement with previously reported partition coefficients of coeruloplasmin (a 151 kDa protein) in 9%T 3%C polyacrylamide gels at ~0.01[168], as determined by molecular sieve chromatography.

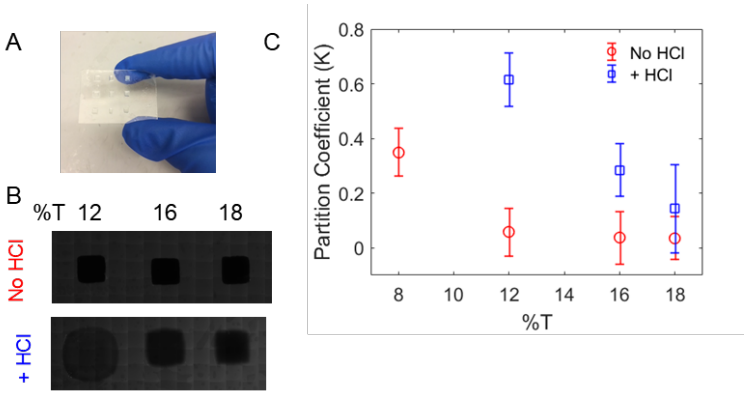

Figure 5.2: Quantifying the partition coefficient for antibodies in decrosslinkable hydrogels. (A) Image of polyacrylamide gel squares patterned on a glass slide used for quantitation of the partition coefficient for antibody in the gel. (B) Fluorescence micrographs of polyacrylamide gel at the specified gel density (%T) with or without HCl-induced gel decrosslinking. (C) Quantitation of partition coefficients from images in B.

Using the partition coefficients for the antibody in the 12%T and 16%T gels, we can estimate the impact of partitioning on the in-gel immunoassay complex formation (C_{max}). In Figure 5.3, C* versus K_D is plotted, where C* is $C_{max}/[Ag]_0$ and C_{max} is given by:

$$[C]_{max} = \frac{k_{on}[Ab]^*_{gel,0}[AG]_0}{k_{on}[Ab]^*_{gel,0}+k_{off}} \qquad \text{Eq. 5.2}$$

We observe that the higher local concentration of Ab in the decrosslinked gels yield a binding efficiency with a median expressed protein (0.75 nM) above the limit of detection for EP cytometry for moderate/low affinity Ab, while the binding efficiency falls below the limit-of-detection for crosslinked gels. This demonstrates the efficacy of decrosslinking for improving Ab delivery to the dense DK polyacrylamide gels.

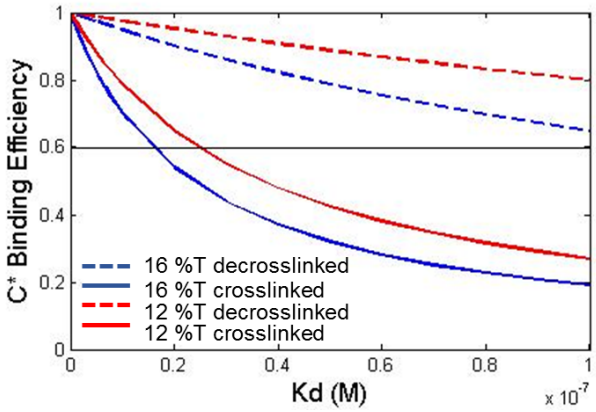

Figure 5.3: Kinetics model shows decrosslinking of dense gels and the resultant higher local concentration of antibody drives the binding interaction above the limit of detection (LOD) for EP cytometry. The solid line indicates the previously reported (LOD).

We aimed to highlight how dense polyacrylamide gels may be used to optimize separations of small molecular weight proteins (with small molecular weight differences), while decrosslinking enables the antibody probing of the dense gels. GAPDH (36 kDa) and phospho-S6 (PS6, 32 kDa) were selected for a model separation in the dense decrosslinkable gels at the low molecular weight range for mammalian proteins (bottom 25% of molecular weights)[26]. As shown in Figure 5.4, separation resolution was optimized first by increasing electrophoretic separation time as separation resolution is linearly proportional with time.

$$SR = \frac{\Delta\mu_{EP} E t}{\frac{1}{2}(4\sigma_1 + 4\sigma_2)} \qquad \text{Eq. 5.3}$$

Separation resolution increased with longer separation time (SR=0.81), but the PS6 reached the end of the separation lane. The combination of lower lysis temperature (for reduced diffusive band broadening) and higher E-field (50 V/cm versus 40 V/cm) yielded a separation of GAPDH and Phospho S6 with a SR of 1.04. Notably this 11% molecular weight difference is among the smallest molecular weight difference separations in micro-scale protein electrophoresis. Previously, immunocomplexes that differed by ~12-13% in molecular weight were separated in ~1 mm in microchannel electrophoresis[175]. Thus, dense decrosslinkable gels hold tremendous promise for open microfluidic EP cytometry of small molecular weight species.

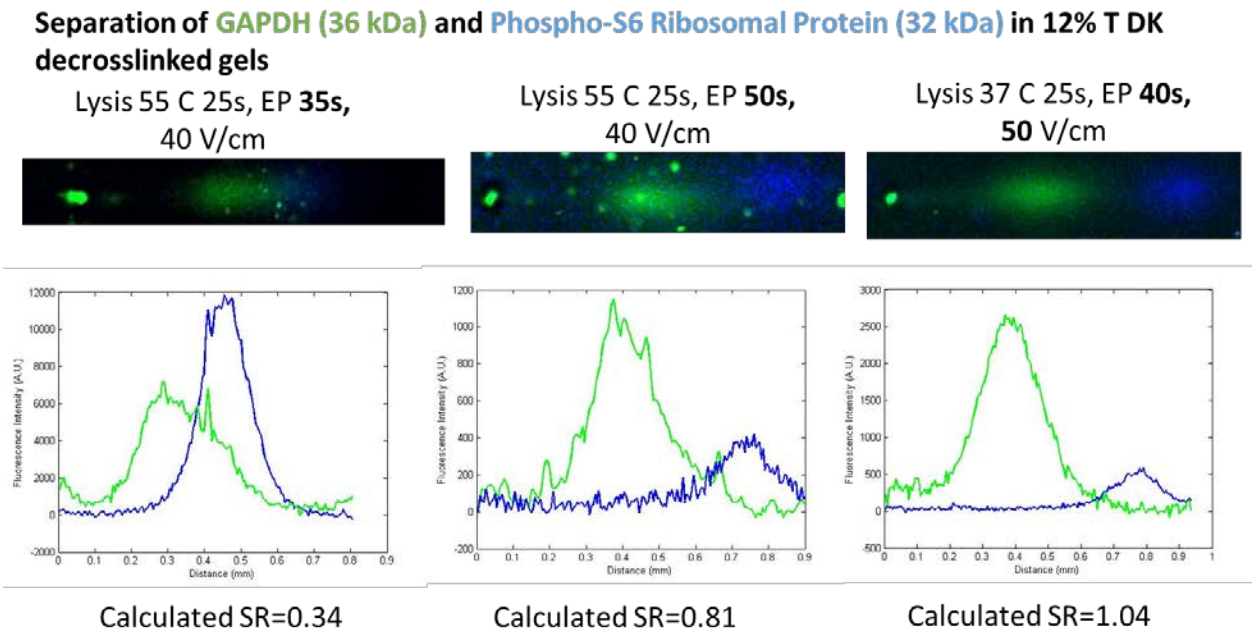

Figure 5.4: Optimization of the GAPDH and Phospho S6 separation in a 12%T DK gel. Micrographs (top) and intensity profiles (bottom) of representative separations in three different lysis and electrophoresis conditions. The optimal conditions yield a separation resolution of 1 within a 1 mm separation lane. Note: the middle separation was stripped and re-probed for the phosphoS6, and due to the low signal of the phosphoS6, the GAPDH signal was re-scaled (divided by 10 to show the separation on the same plot).

However, the results in Figure 5.4 were not reproducible, and instead we observed striking patterns on the hydrogel surface that obscured peak quantitation (Figure 5.5). The seminal publication by Tanaka describes that differential stress is present along the height of the gel owing to the swelling pressure and the surface attachment of the gel. At a critical pressure, called the critical osmotic swelling pressure, the gel surface buckles (Figure 5.6) to relieve the build-up of stress[176]. Other groups have demonstrated the ability to generate specific patterns by altering the crosslinking density of the gel along its height[177]. Numerous other groups have characterized the effect of hydrogel height, crosslinking density, and compressive strain on the observed swelling patterns[178–181]. Notably, one group reported that the surface creases can be removed by incubating surface-constrained gels in high molecular weight PEG[178]. The underlying mechanism is that PEG dramatically increases the osmolality (even deviating from anticipated osmolality based on the composition of a given solution[182]), and thus the osmotic swelling pressure is modified. In turn, the gel de-swells and the buckling pattern disappears. However, upon putting a gel back in another buffer solution, the creases re-form in nearly the same location in the gel[178]. Yet whether the patterns would return upon drying the gel while still in PEG solution was unknown.

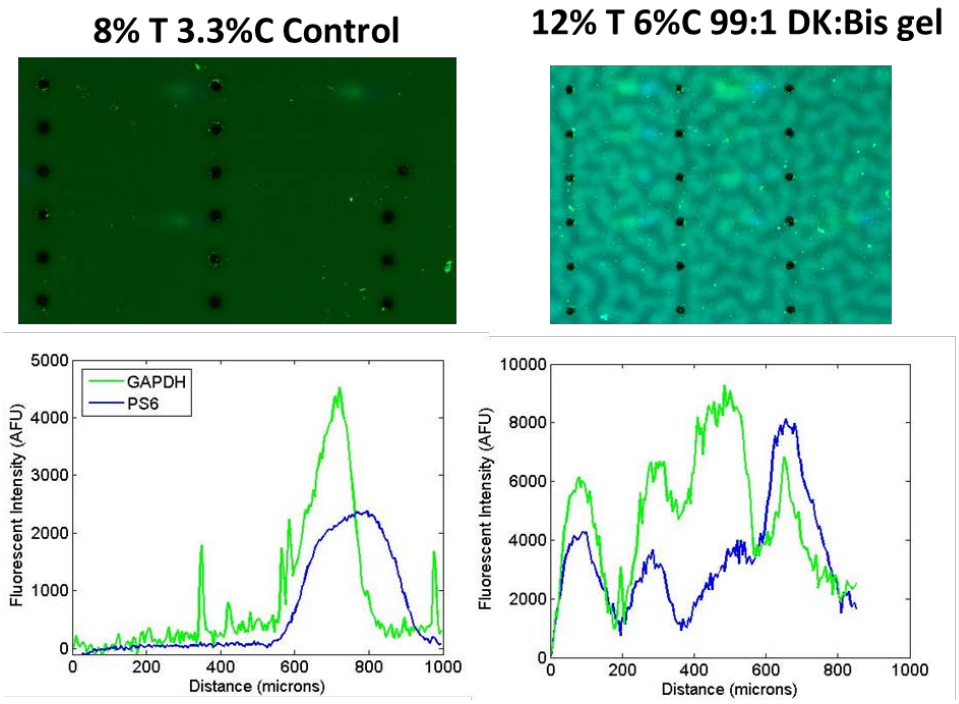

Figure 5.5: Replicate attempted separation of GAPDH and Phospho S6 separation in a 12%T DK gel displays a unique gel surface pattern that prevents accurate peak identification. False-colored fluorescence micrographs (top) and intensity profiles (bottom) of representative separations in 8%T (control) and 12%T decrosslinked gel separations.

We hypothesized that 200 kDa PEG (or polyethylene oxide, PEO) would have a sufficiently high osmolality to counteract the swelling observed in our system. Notably, the previous literature description of the use of PEO was with a surface-bound polyacrylamide/co-sodium acrylate hydrogel. A solution of 10% PEO in water was dissolved in a 55°C water bath. Upon overnight incubation of a decrosslinked 12%T 6%C* 99:1 DK:BIS ratio gel in 10% PEO, the surface patterns were eliminated (Figure 5.7).

In order to characterize whether the elimination of the surface pattern removes the non-uniform antibody probe signal in the gel, a spinner was used to spin the gel slide dry (after overnight PEO incubation). Spinning the gels for 2 min at 3000 rpm yielded gels with no visible PEG solution on the surface of the gel, but surface creasing re-emerged (Figure 5.7). Furthermore, upon fluorescence imaging of the gel, the fluorescence pattern in the antibody signal was still present. Also, notably, the PEG appears to have autofluorescence in the 488 nm wavelength range, introducing significant background. This may be due to light scattering by PEG aggregates that are visible under brightfield. Consequently, we determined that imaging the dried gels after PEO incubation would not be a suitable solution to mitigate the swelling-induced creasing patterns. In the future, if a fluorescence imaging setup is designed for hydrated EP cytometry gels, immunoprobing the decrosslinked gels and incubating the gels in PEO for imaging may be an option.

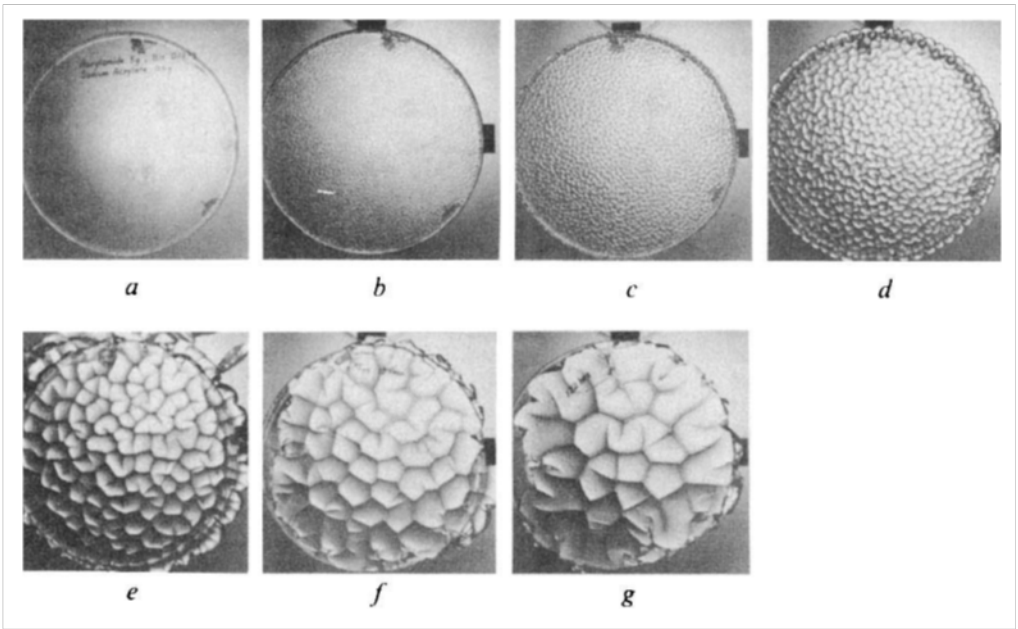

Figure 5.6: Examples of surface-constrained hydrogel swelling patterns previously described in the literature. Surface creasing instabilities observed in an ionic polyacrylamide gel in a petri dish. Reprinted by permission from the licensor: Springer Nature, Nature, “Mechanical instability of gels at the phase transition”, T. Tanaka, S.-T. Sun, Y. Hirokawa, S. Katayama, J. Kucera, Y. Hirose and T. Amiya, (1987)[176].

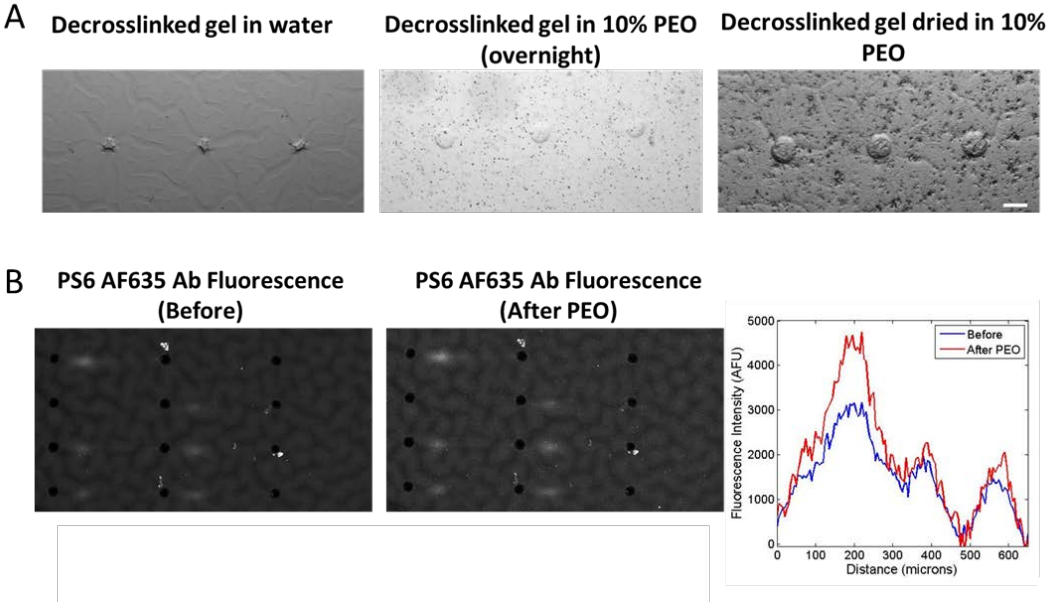

Figure 5.7: Effect of submerging a surface-constrained decrosslinked gel in high osmolarity polyethylene oxide (PEO). (A) Brightfield images of decrosslinked gels (12%T 6%C 99DK chemically polymerized and decrosslinked 30 min in pH 1.1 HCl; gels with high Ab background fluorescence in the creases) in water and PEO. Gel was spun dry at 3000 rpm for ~2 min (right) and microwell integrity was preserved, but some creasing is observed. Scale bar is 100 microns. (B) Fluorescence micrographs and intensity profiles before (left, blue trace) and after (right, red trace) a decrosslinked gel was incubated in 10% PEO solution for 6 hours and then spun dry (2 min, 3000 rpm). Scale bar is 500 microns.

As an alternative, we considered whether the gel crosslinking density could be altered to prevent surface creasing. The critical swelling pressure that yields gel buckling only depends on the elastic modulus of the gel[176]:

$$P_C = \frac{2}{3}(E_2 E_0)^{1/2} \qquad \text{Eq. 5.4}$$

where E_2 and E_0 represent the elastic modulus at the surface of the hydrogel and in the bulk, and thus the critical swelling pressure is approximately proportional to the elastic modulus of the gel[177]. When the osmotic pressure exceeds the critical swelling pressure, surface instabilities (including wrinkling and buckling) may form. However, if the elastic modulus of the surface-constrained gel is sufficiently high, and the critical swelling pressure is not reached, the hydrogel will not exhibit a pattern.

We hypothesized that we could determine a DK:bisacrylamide (bis) ratio in the decrosslinking gels that leaves a sufficient percent C after decrosslinking such that the elastic modulus remains high and the swelling-induced pattern is not observed. The key design parameters to test this hypothesis are the starting %C and the DK:bis ratio. From previously reported elastic modulus measurements[169], 16%T 6%C* 98:2 DK:bis gels (for which a surface pattern is observed after decrosslinking), the elastic modulus is ~5 kPa (about an order of magnitude lower than the ~50 kPa starting elastic modulus, Figure 5.8). To determine an acceptable ratio of DK:bis for which the elastic modulus would still be high enough upon decrosslinking to prevent the surface pattern formation, other published elastic modulus data for polyacrylamide gels was considered[183] (Figure 5.8). Estimated elastic moduli from a power law fits of the published data are provided in Figure 5.8. An elastic modulus of ~50 kPa for a 15%T 1%C gel was reported previously[183]. Thus, we hypothesized that with a 16%T 3.3%C 70:30 DK: bis ratio gel, that we would attain a gel with 1% effective percent C after decrosslinking, and the elastic modulus would still be high enough not to observe the surface pattern. In order to test the hypothesis 16%T 3.3%C gels with the indicated crosslinking ratios were fabricated and decrosslinked (Figure 5.9). No pattern is present prior to decrosslinking, however, after 30 min of decrosslinking in 1% HCl, we observe the surface pattern in the 99:1 DK to bis ratio gel, but not in the other two ratios tested. Notably, several small creases are observed directly surrounding the 70:30 and 78:22 ratio gels, indicating shear stresses in the gel, but these are not sufficient to yield the surface pattern as in the 99:1 DK:bis gel. Thus, lowered DK ratios of crosslinking do in fact influence the swelling patterns in the surface-constrained polyacrylamide gels.

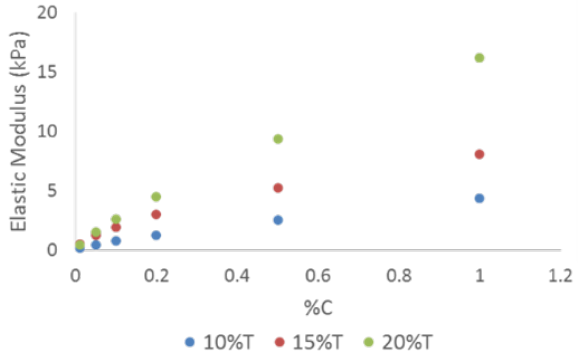

Figure 5.8: Estimated elastic modulus values for polyacrylamide as a function %C using fit values from Denisin et al. 2016 (private communication)[183]

The separation of PS6 and GAPDH in decrosslinkable gels was repeated in gels with the 16%T 3.3% 78:22 DK:bis gels in order to assess whether this gel composition would yield immunoprobe signal. As shown in Figure 5.10, below, distinct peaks were not observed. This prompted us to hypothesize that mass transport limitations may prevent appreciable immunocomplex formation.

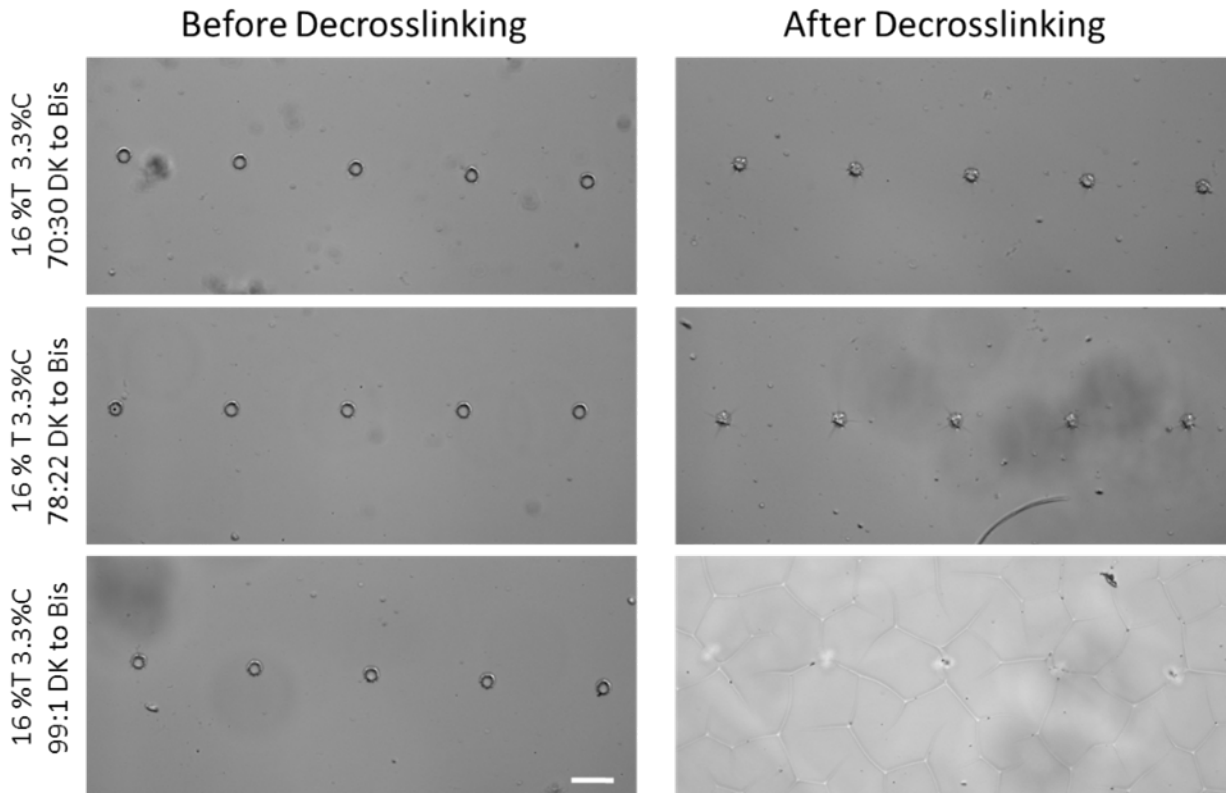

Figure 5.9: Appearance of the creasing pattern in decrosslinked DK gels depends on the DK:Bis ratio. Brightfield images of gels before and after decrosslinking with the indicated %T, %C and ratios of DK:Bis crosslinker.

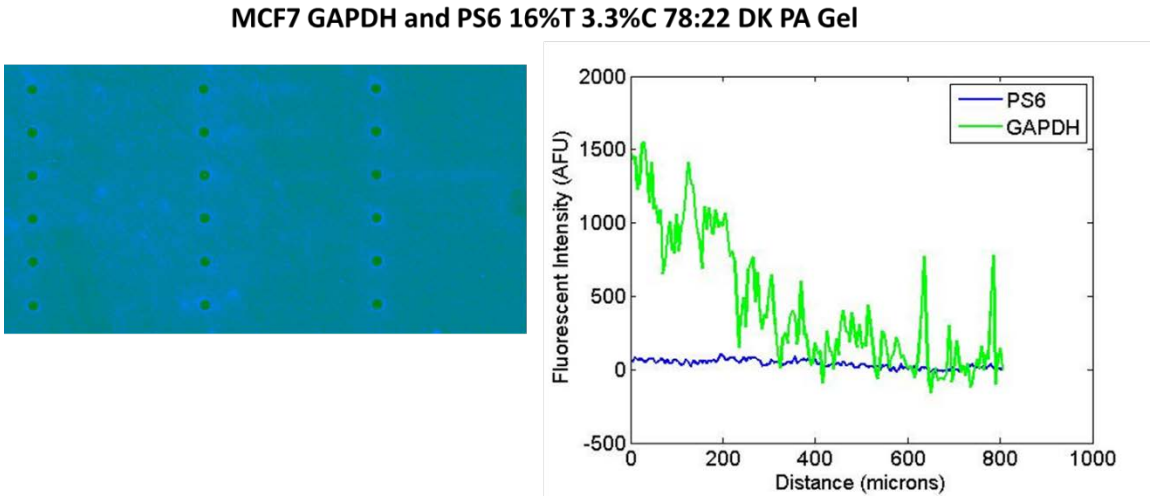

Figure 5.10: Representative false-color fluorescence micrograph and intensity profile of an MCF7 scWB for GAPDH and PS6 in a 16%T 3.3%C 78:22 DK gel. Cells were lysed for 25s in 55C 1X RIPA, electrophoresis was performed for 25s at 40 V/cm in 1X RIPA and the protein was photocaptured. Gels were decrosslinked in 1% HCl for 30 min, washed in TBST overnight and probed with 1:10 anti-GAPDH (goat, Sigma) and 1:10 anti-PS6 (Rb, CST) for 2 hr, washed 2x in 1X TBST for 30 min, incubated in 1:20 anti-goat AF488 and 1:20 anti-Rb AF647 and gel was washed 2x 30 min in 1X TBST prior to Genepix imaging (500 power 100% gain for GAPDH and 600 power, 100% gain for PS6). Separation resolution is ~0.2. Scale bar is 100 microns.

We aimed to estimate the in-gel diffusion coefficient in the 16%T 3.3%C 78:22 DK:Bis gels to evaluate whether mass transport limitations existed. Park et. al.[87] determined the following expression relating the ratio of in-gel diffusion to solution diffusion as a function of polymer volume fraction (ϕ):

$$\frac{D_{ge;}}{D_{solution}} = e^{-37.9\varphi^{0.92}} \qquad \text{Eq. 5.5}$$

Thus, to estimate the in-gel diffusivity at different %T, the in-solution diffusivity, and the volume fraction as a function of %T must be known. As shown in the plot of the experimental data of Baselga et. al.[152] (Figure 5.11), the polymer volume fraction depends heavily on %T and minimally on %T. Thus, for a decrosslinked gel that maintains some degree of crosslinking (e.g. our ~1%C gels) after acid hydrolysis, we can estimate that the polymer volume fraction is relatively constant. By performing a linear fit on the data in Figure 5.11, shown in Figure 5.12, we find the following expression for polymer fraction as a function of %T:

$$\varphi = 0.0096\%T - 0.0147 \qquad \text{Eq. 5.6}$$

We use the polymer volume fractions determined to find $D_{gel}/D_{solution}$. The in-gel diffusion coefficient is found by multiplying $D_{gel}/D_{solution}$ by the the solution diffusion coefficient. To estimate the in-solution diffusivity, we use the Stokes-Einstein equation for $D_{solution}$ as a function of Boltzmann's constant k, temperature t, the dynamic viscosity μ, and the hydrodynamic radius r_H:

$$D_{solution} = \frac{kT}{6\pi\mu r_H} \qquad \text{Eq. 5.7}$$

where we use the viscosity of water (0.00089 Pa s), and an antibody r_H of 5 nm determined experimentally[84] for a $D_{solution}$ of ~49 $\mu m^2/s$. Finally, we estimate the diffusion timescale τ as a function of in-gel diffusivity and gel height h and plot as a function of percent T in Figure 5.12, right.

$$\tau = \frac{h^2}{2D_{gel}} \qquad \text{Eq. 5.8}$$

Long diffusive equilibrium time scales (100s of minutes) are prohibitive to generation of detectable immunoprobe signal because of both the formation of depletion zones, and appreciable time for complex unbinding (with k_{off} values ~10^{-3} s^{-1}). Given previous estimates of the Damköhler number (Da) ~1 for immunoprobing with diffusive equilibrium ~100s in an ~8%T gel, we can anticipate a Da~3600 in the 16%T gels described here. Consequently, the equilibrium of complex formation, which scales as the reaction equilibration time multiplied by Da[90], can be expected to be on the order of 3600 minutes (or 60 hours). Alternative methods of antibody probing could address this mass transport limitation (e.g., dehydrated probing[126], or electrophoretic probing[70] adapted for EP cytometry).

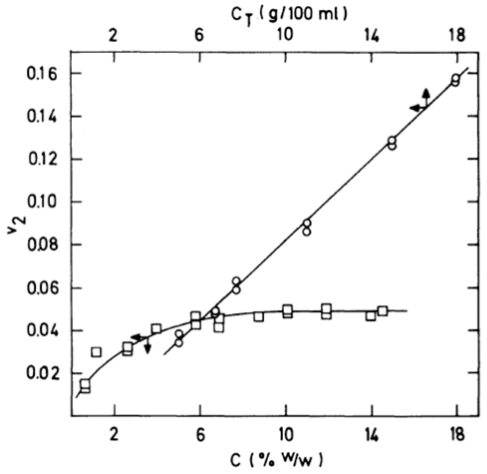

Figure 5.11: Plot of polymer volume fraction for PA gel as a function or either %T or %C[152]. %T was varied with a constant 10%C gel (circles) or %C was varied at constant 6%T (squares). The trends suggest that polymer volume fraction is significantly more dependent on %T than %C. Reprinted by permission from Springer Nature: Springer, Polymer Journal, "Effect of crosslinker on swelling and thermodynamic properties of polyacrylamide gels," J. Baselga, I.

Hernández-Fuentes, R. M. Masegosa and M. A. Llorente, (1989)[152].

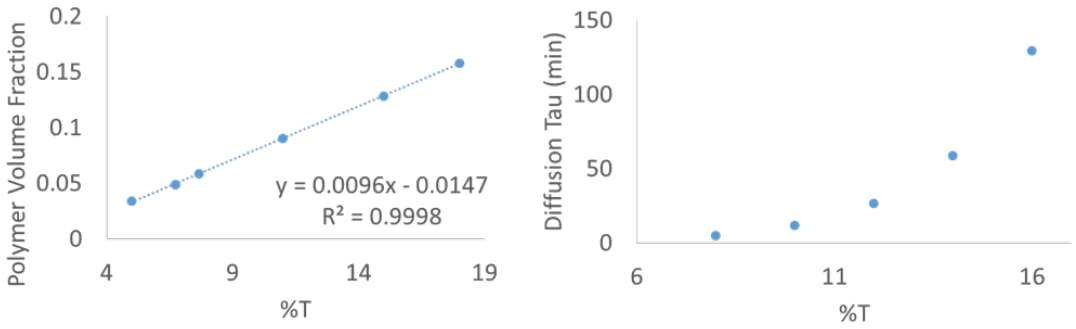

Figure 5.12: (Left) Linear fit of experimental data in Baselga et. al.[152] determining dependence of polymer volume fraction on %T. (Right) Estimates of diffusion timescales in 40 um tall PA gel using the model in Park et. al.[87] for $D_{gel}/D_{solution}$ as a function of polymer volume fraction for an IgG antibody in polyacrylamide gel at the indicated %T (polymer volume fractions from A, and Stokes-Einstein diffusivity for $D_{solution}$ with a hydrodynamic radius of ~5 nm).

Finally, we considered the implications of the fact that gel creasing was not observed the DK gels were first introduced for gradient gel fabrication[169]. One notable difference between the gels used in that study and described here is that polymerization method (photopolymerization through a gradient chrome mask for the gradient gels versus chemical polymerization here). Gel structure and mechanical properties are affected by the polymerization conditions, and thus we speculated that photopolymerization may not yield the buckling described previously. For proof-of-concept, we photopolymerized a 12%T 6%C* 99:1 DK:bis gel, and decrosslinked the gel as shown in Figure 5.13. The gel displays no creases, which is promising for future application of DK decrosslinkable gels for use in EP cytometry if photopolymerization conditions can be tuned to balance the needed density during the separation stage with the large-pore sizes needed for an efficient in-gel immunoassay.

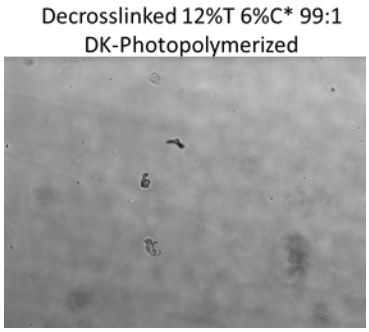

Figure 5.13: Brightfield image of a decrosslinked gel that was photopolymerized (no microwells present; gel is ~80 microns thick) and then decrosslinked. No gel creases are present.

Benzophenone modification of agarose gels for separations of large oligomeric proteins

We endeavored to attain agarose-benzophenone microwell arrays on glass to electrophoretically separate and photo-immobilize large oligomeric proteins, such as F-actin, in an EP cytometry gel. We first demonstrated the ability to modify a glass slide with allyl agarose, allowing the agarose microwell array to be patterned on the solid glass surface (Figure 5.14). Previously, patterning of microwells in agarose for a comet assay was described utilizing a plastic substrate[101].

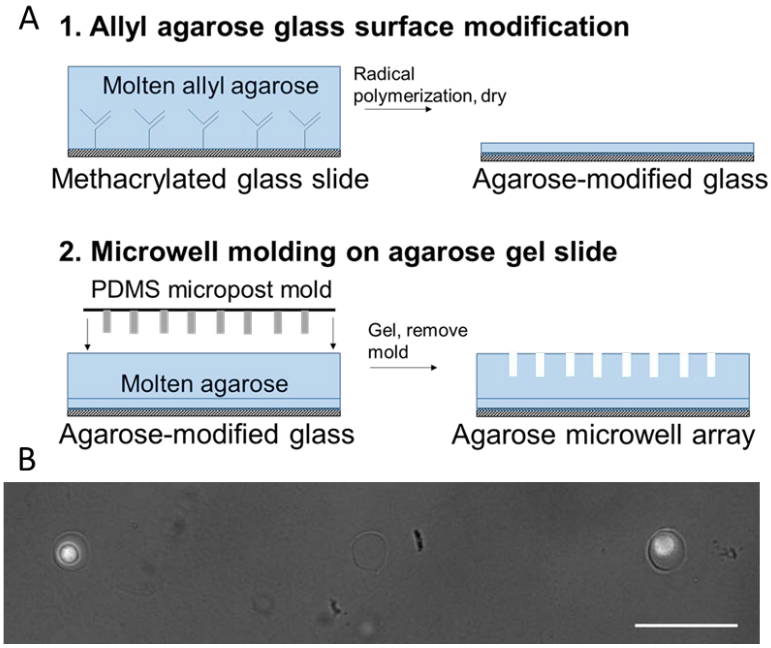

Figure 5.14: Fabrication of agarose microwell arrays on glass. (A) Schematic depiction of the workflow for polymerization of an allyl agarose base layer and molding of 1% agarose with a PDMS post array. (B) Fluorescence micrograph of GFP-actin expressing cells in agarose microwells fabricated on a glass slide. Scale bar is 100 microns.

Aiming to overcome limitations of existing methodologies for modifying agarose with benzophenone (namely, low ~10% photo-immobilization efficiencies for protein in gel, and arduous multi-step synthesis steps)[174], we proposed to perform a one-step polymerization of BPMAC and allyl agarose (Scheme 1). Allyl agarose was melted in 50% DMSO and 50% TAE in order to be able to add appreciable concentrations of BPMAC (e.g. at 3 mM, the BPMAC phase-separated in allyl agarose in 100% TAE buffer). After melting the allyl agarose and moving the tube to a lower temperature (60 °C) heat block to prevent gelation during the reaction (DMSO increased the gel temperature), BPMAC (3 mM final) and TEMED and APS were added. DMSO has been shown to reduce polymerization rates of polyacrylamide by an order of magnitude in 10% H_2O, 90% DMSO compared to 100% water (see Table 1)[184]. The main reasons for DMSO impacting the polymerization rates are i) higher self-association of acrylamide monomers in DMSO[185], which leads to higher activation energy for propagation reaction; ii) lower reactivity of the acrylamide radical because carbonyl oxygen not protonated in organic solvent, which leads to resonance stabilization of the radical; and iii) possible solvation

effects for chain propagation. Thus, we hypothesized that reducing the DMSO percentage would increase the polymerization rate and yield efficient allyl agarose and BPMAC reaction time.

Table 1: Influence of DMSO on polyacrylamide polymerization rate (Rp) from De Schryver[184].

% DMSO	10^2 Rp (mol/L s)
100	0.38
97	0.5
90	0.6
0	5

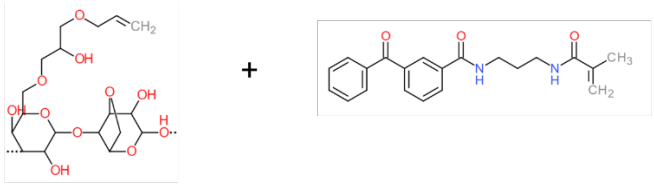

Scheme 1: Proposed molecules to conjugate through a polymerization reaction to incorporate benzophenone into an agarose hydrogel.

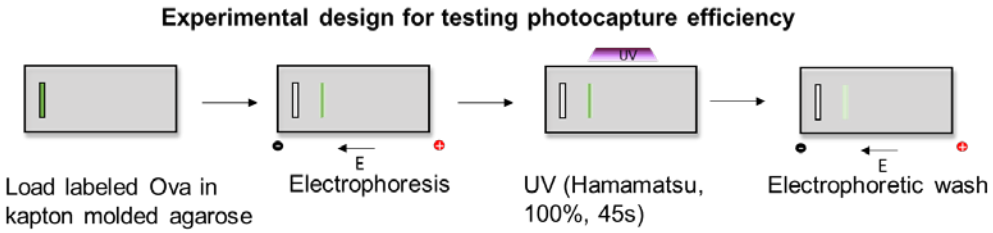

Figure 5.15: Schematic workflow for assessing protein photoimmobilization efficiency in agarose gels with BPMAC incorporation. Fluorescently labeled ovalbumin (Ova) is electrophoresed into the allyl agarose free standing gel and UV immobilized prior to electrophoretic wash that removes unbound Ova.

In order to assess photoimmobilization efficiency in the allyl agarose-BPMAC reacted gels, we characterized retained fluorescent protein in the hydrogel after UV exposure and electrophoretic wash as previously described[69] (Figure 5.15). However, for a range of reaction times and appropriate solvents for BPMAC, we did not observe appreciable photoimmobilization (Figure 5.16). We hypothesized that we could optimize the reaction of BPMAC with allyl agarose for longer times or in a lower DMSO percentage[186] but no photocapture was observed with 1-22 hour reaction times (at 60 °C in a tube on a heat block). Lowering the DMSO percentage did not yield photocapture potentially because the BPMAC was poorly solubilized (as the solution was slightly opaque). For the longer reaction time (22-hours) the heat block was moved to a stirring hot plate and small magnetic stir bar was included in the Eppendorf tube. We hypothesized that the lack of any substantial photoimmobilization may have been low numbers of immobilized

benzophenone groups within the agarose. Previously described benzophenone modification of agarose employed polyallylamine chains on which ~60 benzophenones could be attached prior to incorporation in an oxidized agarose gel[174]. Thus, any benzophenone modification chemistries for agarose should be optimized to incorporate large numbers of benzophenone groups in the gel.

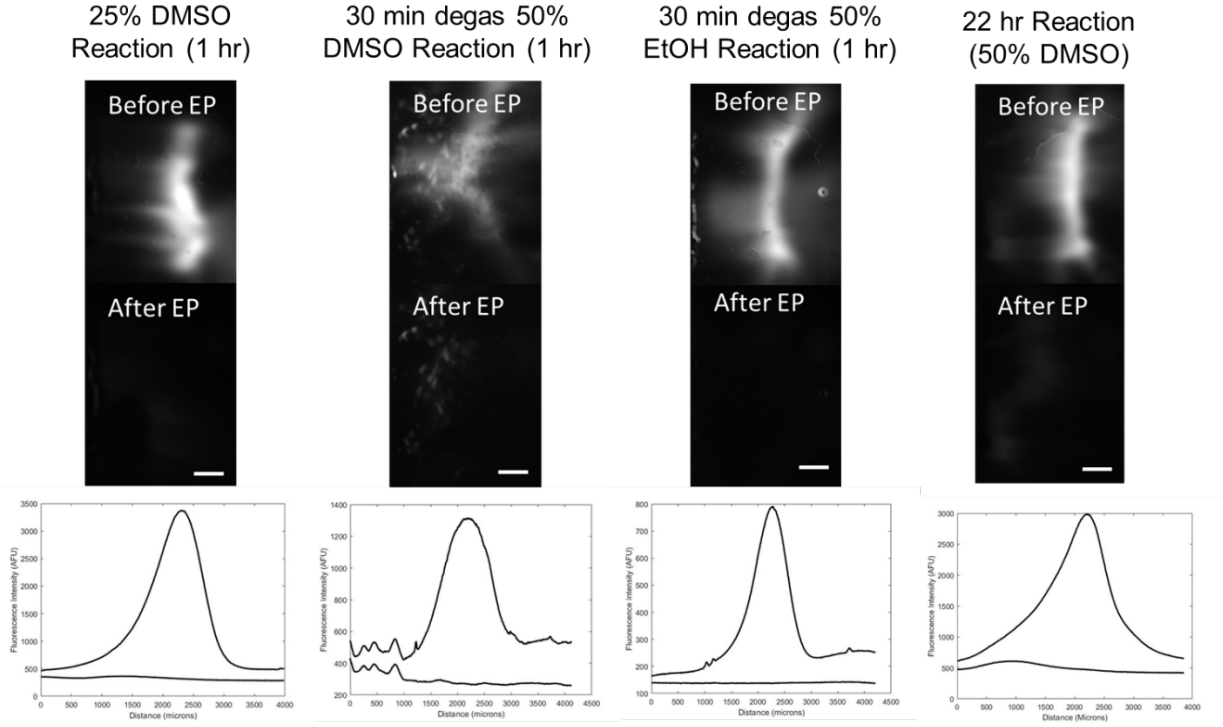

Figure 5.16: Fluorescence micrographs and intensity profiles before and after electrophoresis (EP, top row) of AlexaFluor-488 ovalbumin electrophoresed in 1% allyl agarose-3mM BPMAC free-standing gel on agarose-coated glass (chemically polymerized with APS/TEMED in the indicated solvent and the specified time at 60°C in an Eppendorf tube on a heat block). Following electrophoresis, the E-field was turned off, and photocapture was performed for 45s at 100% (Hamamatsu). Electrophoretic washout was performed. Scale bar is 1 mm.

5.4 Conclusions

Alternative hydrogels for EP cytometry of small or large molecular weight proteins were quantitatively assessed for properties such as antibody partitioning, separation performance and photoimmobilization efficiency. Swelling-induced buckling of surface-constrained decrosslinked polyacrylamide gels prevents accurate Gaussian peak fitting when observed. The surface buckling phenomenon does not consistently occur, prompting us to hypothesize we operate near the limit of the critical osmotic swelling pressure. For large molecular weight species, we attempted to simplify the synthesis of benzophenone-modified agarose with a one-pot reaction. However, negligible photoimmobilization efficiency was measured with numerous reaction conditions. Strategies that employ functionalization of many benzophenone groups per reactive

site remain the most promising for achieving high photoimmobilization efficiencies in large-pore hydrogels.

For small molecular weight protein separations in dense gels, controlling the surface buckling phenomenon is key. The observation that photopolymerized gels do not appear to buckle upon decrosslinking requires substantial further characterization. First steps could include systematic assessment of the effect of different gel compositions and photopolymerization conditions on the buckling phenomenon. Given the dependence of the critical osmotic swelling pressure on the elastic modulus, the elastic moduli of gels polymerized chemically or by photopolymerization should be investigated. Furthermore, removal of gels from the solid substrate may be a viable path forward. However, design of methods for handling the thin non-attached gels would be necessary to prevent gel damage during the immunoassay.

Chapter 6

Joule Heating-Induced Dispersion in Open Microfluidic Electrophoretic Cytometry

Reproduced with permission from J. Vlassakis and A.E. Herr, "Joule Heating-Induced Dispersion in Open Microfluidic Cytometry", *Analytical Chemistry*, 2017.

6.1 Introduction

While powerful in detecting proteins in single cells[117,187], immunoassays alone cannot detect important proteoforms (e.g., truncated isoforms), such as those implicated in the development of resistance to oncology drugs[111]. Electrophoretic separations complement immunoassays by providing orthogonal protein size or chemical composition information that aids in the selective identification of proteoforms. Microfluidic electrophoresis (e.g., in a microchannel or capillary) has been employed in single-cell separations of various analytes[188–190]. However, the biomedical applications of existing microchannel and capillary electrophoresis systems are limited due to reduced assay throughput (typically ~30 cells or fewer). Increasing assay throughput, an area of active research[94], is limited by difficulties in exchanging buffers in the enclosed geometries of capillaries or microchannels[59,191]. Ideally, the composition of each buffer is performance-optimized for each discrete assay stage.

Open microfluidics simplify fluidic interfacing, as compared to sealed microdevices, for high-throughput electrophoretic separations. Open microfluidic devices have been applied to parallelization of reactions (e.g., the generation and evaluation of cell culture microenvironments[192]) and separations by our group[98,193] and others[100]. We recently introduced an open microfluidic single-cell electrophoretic (EP) cytometry separation system capable of measuring up to ~11 endogenous proteins from 100s-1000s of single-cells (Figure 6.1)[65,67]. We perform simultaneous separations of single-cell protein lysates in microwells arrayed in a 40-micron thick polyacrylamide gel. A bifunctional lysis/EP buffer simultaneously addresses all wells of the open microfluidic device to allow for rapid integration of the lysis (i.e., sample preparation) and separation assay steps to minimize dilution of protein. To prevent protein loss out of the open microfluidic device into the bulk buffer reservoir through the immunoassay stage of the assay, proteins are covalently immobilized in the gel utilizing a rapid UV-initiated reaction with benzophenone incorporated in the gel matrix. Once the proteins are immobilized, fluorescently labeled antibody detects protein; chemical stripping and re-probing procedures enables multiplexing. We have detected proteoforms relevant in stem cell differentiation[65], and have applied the measurement platform to assess heterogeneity in expression of markers of drug resistance and Her2 signaling in cancer[66,106].

However, EP cytometry protein separations have only been demonstrated with protein molecular mass differences of 33% or higher (~15 kDa)[66]. Separations of intriguing proteoforms in cancer progression[113,130], such as single exon skipping events in alternative splicing (~35 amino acid[133], or 4 kDa molecular mass differences) remain inaccessible. While isoelectric focusing achieves separations of proteins differing by single charge units,[102] many proteins have similar isoelectric points but markedly different molecular mass[194]. Furthermore, as yet, the throughput of single-cell isoelectric focusing is on the order of 10 cells. Thus, to achieve measurements of cell-to-cell heterogeneity in proteoforms with small molecular mass differences, we require fundamental insight into critical parameters that affect EP separation performance in open microfluidics.

The impact of Joule heating on separation performance is well understood in capillaries and microchannel devices, but in open microfluidics unique heating consequences arise ranging from sample evaporation to analyte loss. The heat flux, $\dot{Q}$, generated from applying a current across a conductor (Joule heating) is given by

$$\dot{Q} = \frac{(IR)^2}{L^2}\sigma_c H \qquad \text{Eq. 6.1}$$

where I is the applied current, R is the resistance, L is the length of the conductor, σ_c is the conductivity of the buffer, and H is the buffer height in the capillary, channel or EP chamber (Figure 6.1)[195]. Joule heating reduces separation performance in capillary and microchannel EP and two key hypotheses have been set forth to explain this observation: (1) Joule heating decreases buffer viscosity, resulting in higher analyte diffusivity, and reducing separation performance[196]; and (2) heat transfer from the capillary/microchip to the surroundings yields radial temperature gradients inducing non-uniform velocity profiles and reduced separation performance[197–199]. Petersen and co-authors presented scaling relations that showed that increased diffusivity alone could not account for reductions in the number of theoretical plates, a metric of separation efficiency in capillary EP, and thus radial temperature gradients likely dominate in reducing separation performance[200]. In contrast, for EP cytometry devices, we observe no indication of thermal gradients yielding skewed (non-Gaussian) intensity profiles[67]. Rather we hypothesize that high starting temperatures and extensive Joule heating in the bifunctional lysis/EP buffer raises diffusivity (Figure 6.1A), lowering separation performance and yielding loss of protein out of the open microfluidic device. In open microfluidic electrophoresis performed in paper microfluidics[201,202], and in gels not in a fluid reservoir[100,193], Joule heating-induced liquid evaporation required device geometry optimization and active mitigation strategies.

We sought to understand the impact of Joule heating on separation performance and analytical sensitivity in open microfluidic devices. Direct measurement of Joule heating points to enhanced protein diffusivity and concomitant mass loss out of the open microfluidic device. To reduce Joule heating during electrophoresis, we exchange the high-conductivity bifunctional lysis buffer with a lower-conductivity EP buffer. We scrutinize the impact that the buffer exchange has on the lysed cell contents, with special attention to analytical sensitivity. Single-cell EP performed in the lower-conductivity buffer resolves 4 kDa (12%) mass differences in endogenous proteins with a 1.6-fold enhancement in separation resolution over the bifunctional buffer system. Critically, the buffer exchange also reduces lane-to-lane variation in separation resolution. Reductions in technical variation expand the utility of EP cytometry for the analysis of rare cells. The fundamental insights provided regarding Joule heating in EP cytometry will guide the design

of other open microfluidic electrophoretic separations seeking to achieve high throughput and selectivity in a single microdevice.

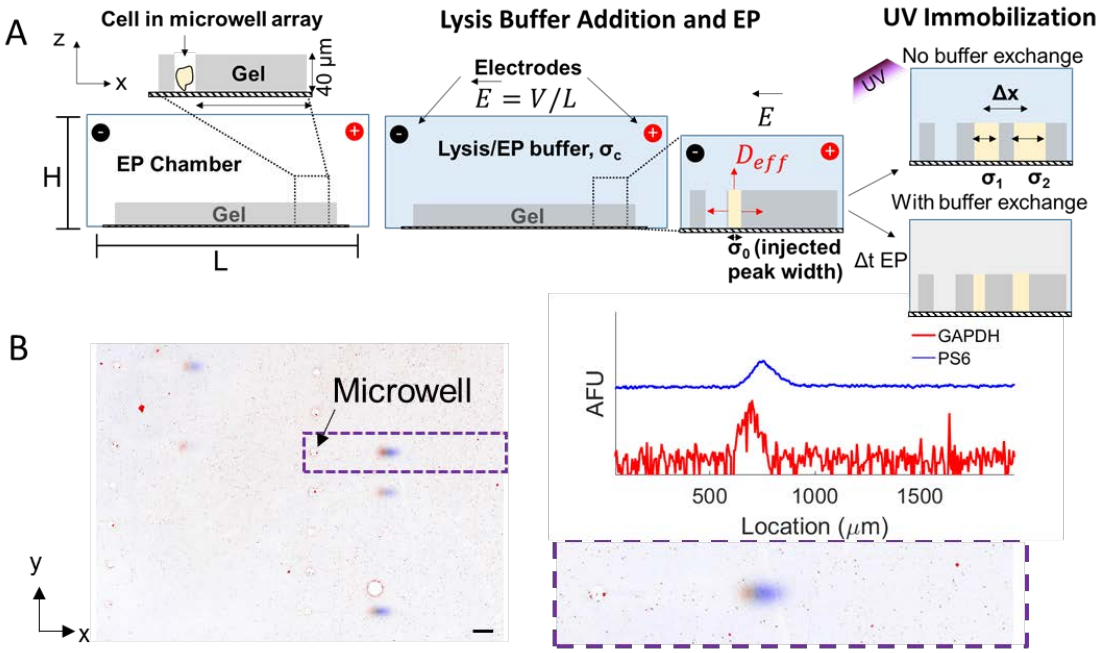

Figure 6.1: Joule heating impacts separation performance and diffusive protein losses in an open electrophoretic (EP) cytometry microdevice. (A) Cross-sectional schematic of the open microfluidic EP cytometry gel in an EP chamber (L is the distance between the electrode, and the height is H). Upon addition of bifunctional lysis/EP buffer and application of an electric field E (voltage V), protein injects into the gel and diffuses in all three dimensions at an increasing rate (D_{eff}) due to Joule heating of the surrounding buffer. A buffer exchange process enables evaluation of the effect of buffer composition on Joule heating and resulting separation performance. After EP, proteins are UV immobilized in the gel. Separations are visualized with fluorescent antibodies (protein peak widths σ_1 and σ_2 and peak center distance of Δx). (B) False-color fluorescence micrographs and representative offset intensity profiles (in arbitrary fluorescence units, AFU) of separations of GAPDH (red, 36 kDa) and phospho-S6 (blue, 32 kDa) from single MCF-7 cells in the bifunctional lysis/EP buffer. Scale bar is 200 µm. Separation resolution (R_s) is 0.36 ± 0.19 (n=37 cells), meaning the proteins are not well separated.

6.2 Materials and Methods

Chemicals/reagents. 40% T, 3.4% C acrylamide/bis-acrylamide (29:1) (A7802), N,N,N′,N′-tetramethylethylenediamine (TEMED, T9281), ammonium persulfate (APS, A3678), sodium dodecyl sulfate (SDS, L3771), sodium deoxycholate (NaDOC, D6750), triton X-100 (X100), bovine serum albumin (BSA, A7030), and goat anti-GAPDH primary antibody (SAB2500450) were purchased from Sigma Aldrich. Deionized water (18.2 MΩ) was attained from an Ultrapure Millipore filtration system. N-[3-[(3-Benzoylphenyl)- formamido]propyl] methacrylamide

(BPMAC) was synthesized by PharmAgra Laboratories. Phosphate buffered saline was acquired from VWR (10X PBS, 45001−130). Petroleum jelly was purchased (Cumberland Swan Petroleum Jelly, cat. no. 18-999-1829). Tris glycine (10X) EP buffer was procured from Bio-Rad (25 mM Tris, pH 8.3; 192 mM glycine, #1610734). Tris-buffered saline with tween was obtained from Santa Cruz Biotechnology (20× TBST, 281695). Antibodies used included: primary Phospho-S6 ribosomal protein Ser240/Ser244 (D68F8) attained from Cell Signaling Technology. Donkey Anti-Goat IgG (H+L) Cross-Adsorbed Secondary Antibody, Alexa Fluor 555-labeled (A21432), and Donkey Anti-Rabbit IgG (H+L) Cross-Adsorbed Secondary Antibody, Alexa Fluor 647-labeled (A31573) were purchased from Thermo Fisher Scientific.

Cell culture. MCF-7 breast cancer cells from American Type Culture Collection (ATCC) and U251 glioblastoma GFP cells (a misidentified U251 line determined to be genetically identical to U373 by the ATCC; GFP introduced by lentiviral transfection with multiplicity of 10, generously provided by S. Kumar's Lab), were authenticated by short tandem repeat analysis (Promega, see Appendix C), and tested negative for mycoplasma. The MCF-7 cells were maintained in RPMI 1640 media (ThermoFisher Scientific, 11875093) supplemented with 10% Fetal Bovine Serum (FBS, Gemini Bio-Products, 100-106), and 1% penicillin/streptomycin (ThermoFisher Scientific, 15140122). U251-GFP cells were cultured in high glucose DMEM (11965, Life Technologies) supplemented with 1% penicillin/streptomycin, 1× MEM nonessential amino acids (11140050), 1 mM sodium pyruvate (11360−070, Life Technologies), and 10% FBS. Both cell lines were grown in a humidified 5% CO_2, 37 °C incubator.

EP cytometry temperature measurements. Liquid crystal thermometers (Type B, 0-30 °C in 5 °C intervals; Type C, 30-60 °C in 5 °C intervals, ThermometerSite) were adhered to the bottom of a custom EP chamber filled with 12 mL (1.8 mm tall fluid layer) of either bifunctional lysis/EP buffer (0.5X Tris glycine, 0.5% SDS, 0.25% NaDOC, 0.1% Triton X-100, pH 8.3) or EP run buffer (0.5X Tris glycine, 0.1% SDS, pH 8.3). An electric field of 50 V/cm was applied (250 V across a chamber with electrode spacing of 5 cm; see SI for current). The bifunctional lysis/EP buffer was poured into the chamber at an initial temperature of 55 °C, and incubated for 25 s (to simulate cell lysis) before applying the electric field. The run buffer was poured into the chamber at 4 °C and the electric field was immediately applied. The time of the temperature change was recorded based on when the liquid crystal temperature sensor for each 5-degree interval changed in color from black to green. Rates of temperature rise were determined by performing linear fits of temperature versus time curve in MATLAB R2016B.

EP cytometry protein separations. Single-cell protein separations were performed as described elsewhere[65,67], with the exception of runs with EP buffer exchange. Briefly, MCF-7 cells in suspension were introduced to a microwell array (400 μm well-to-well spacing, and 2 mm-long separation lane) patterned in 8%T, 3.4%C polyacrylamide with 3 mM BPMAC chemically polymerized in 0.08% APS and 0.08% TEMED, attached to a methacrylate-silanized glass slide. Bifunctional lysis/EP buffer (12 mL at 55 °C) was poured into the EP chamber and cell lysis proceeded for 25 s. An electric field of 50 V/cm was applied. For buffer exchange experiments, the electric field was applied for 4s to inject proteins into the gel, the field was turned off, buffer was removed from the chamber and 12 mL of 4 °C EP run buffer was added to chamber (within ~10 s) before the electric field was turned on again for times specified in the Results and Discussion section. An abundance of caution is required when performing manual buffer exchange to ensure the electric field is turned off prior to removing the buffer to avoid electrocution hazards. After EP, protein was immobilized in gel by UV excitation (Lightningcure

LC5, Hamamatsu, 100% power, 45 s) of benzophenone incorporated in the gel. Following electrophoretic separation and UV-mediated covalent attachment of protein to benzophenone in the gel, the gels were washed for 30 min to overnight in 1X TBST on an orbital shaker. Gels were incubated in 25 µl of a 1:10 dilution of primary antibodies in 1X TBST with 2% BSA for two hours, and washed twice for 30 min in 1X TBST. Secondary antibody incubation was one hour in a 1:20 dilution, and gels were washed twice for 30 min in 1X TBST and dried in a gentle nitrogen stream. Gels were imaged using a fluorescence microarray scanner (Genepix 4300A, Molecular Devices) with an Alexa-Fluor 555 filter (532 laser excitation, 500 PMT), and an Alexa-Fluor 647 filter (647 laser excitation, 600 PMT). For each reported separation condition, at least three technical replicates of EP cytometry were performed (on separate devices).

Image analysis and quantitation. Single-cell protein separation performance was characterized using custom analysis scripts in MATLAB R2016b, as previously described (and summarized briefly here)[67]. Images of the array were segmented, and intensity profiles of individual protein peaks were fit to Gaussian functions, with peak width and location determined from fit parameters for peaks which had a fit r-squared value of at least 0.7. Area-under-the curve (AUC) analysis was performed by summing the background-subtracted intensity profile over the pixels ± 2 peak widths from the peak center. Separation resolution calculations utilized the Gaussian peak fit parameters for peak center locations to calculate center-to-center distances (Δx), and peak width (MATLAB fit function 'Gauss1' sigma parameter divided by the square root of two). Images were median filtered in Fiji using the "Remove Outliers" macro with a radius of 2 pixels and threshold brightness of 50 AFU to remove punctate noise from adsorbed fluorescent antibodies. We determined the filtering process did not markedly change the peak width, location or area-under-the-curve. Statistical analysis of area-under-the-curve (AUC) levels was performed using the MATLAB function ranksum (which performs a Mann-Whitney U-test).

Numerical simulation and experimental measurement of diffusive protein losses. A COMSOL Multiphysics 4.2a diffusion simulation was performed with 2D-axisymmetry. In-gel diffusion coefficient estimates were generated according to the experimentally derived expression[87]:

$$\frac{D_{gel}}{D_{solution}} = e^{-3.03 R_H^{0.59} \%T^{0.94}} \qquad \text{Eq. 6.2}$$

where D_{gel} is the in-gel diffusivity, $D_{solution}$ is the Stokes-Einstein diffusivity calculated in the main text, R_H is the hydrodynamic radius of the protein in angstroms, and $\%T$ is the total acrylamide monomer concentration (in g/mL, 0.08 for the present study). As in the main text, we used the experimentally reported GFP hydrodynamic radius of 28.2 angstroms[203]. Accordingly, we found $\frac{D_{gel}}{D_{solution}}$ was 0.13 for GFP in an 8%T gel. The model geometry utilized square meshing (2 µm elements) with the specified dimensions of the protein band (15 µm initial width), gel (36 µm height), and buffer layer (250 µm height). Fick's law was solved over the entire geometry using time-dependent Transport of Dilute Species with no convection (model is performed in the reference frame of the electrophoresing protein band), and an initial protein concentration of 1×10^{-6} mol/m^3. The in-solution diffusivities are a function of time for each model, and summarized in Table 6-1, Table 6-2 and Table 6-3 below. The time-dependent diffusivity is input in the model as an exponential function, which was a fit of the time versus solution diffusivity (see Table 6-1,

Table 6-2 and Table 6-3). The in-gel diffusivity was input as the solution diffusivity function multiplied by the ratio 0.13, as described in the section above.

The number of protein molecules was summed in the gel (using a surface integration calculating the volume integral of the axisymmetric model) and normalized to the starting number of molecules to determine the quantity of protein retained in the gel as a function of time.

Table 6-1: Time-dependent diffusivities used in the numerical simulation of diffusive losses during EP corresponding with the parameters of the validation experiment (Figure 6.4B; 4 °C bifunctional lysis/EP buffer, with temperature elevating to 9 °C during the 25s lysis of the U251 GFP cells, and a temperature rise of 0.9 °C/s with an applied E-field of 50 V/cm). Diffusivity versus time exponential fit function was $y = 6E\text{-}11e^{0.0207t}$, with $R^2 = 0.9995$.

Time (s)	Temperature (°C)	$D_{solution}$ GFP (m^2/s)
0	9	6.12713E-11
1	9.9	6.26649E-11
2	10.8	6.40816E-11
3	11.7	6.55218E-11
4	12.6	6.69857E-11
5	13.5	6.84734E-11
6	14.4	6.99852E-11
7	15.3	7.15213E-11
8	16.2	7.30821E-11
9	17.1	7.46676E-11
10	18	7.6278E-11
11	18.9	7.79138E-11
12	19.8	7.9575E-11
13	20.7	8.12618E-11
14	21.6	8.29746E-11
15	22.5	8.47135E-11
16	23.4	8.64787E-11
17	24.3	8.82706E-11
18	25.2	9.00892E-11

19	26.1	9.19349E-11
20	27	9.38078E-11
21	27.9	9.57081E-11
22	28.8	9.76362E-11
23	29.7	9.95922E-11
24	30.6	1.01576E-10
25	31.5	1.03589E-10
26	32.4	1.0563E-10
27	33.3	1.077E-10
28	34.2	1.09799E-10
29	35.1	1.11927E-10
30	36	1.14084E-10

Table 6-2: Time-dependent diffusivities used in the numerical simulation of diffusive losses during EP corresponding with EP cytometry in 55 °C bifunctional lysis/EP buffer (Figure 6.4C; 55 °C bifunctional lysis/EP buffer, which cools to 40 °C during 25 s lysis, and elevates at 0.9 °C/s with an applied E-field of 50 V/cm). Diffusivity versus time exponential fit function was $y = 1E\text{-}10e^{0.0172t}$, with $R^2 = 0.9996$.

Time (s)	Temperature (°C)	$D_{solution}$ GFP (m^2/s)
0	40	1.24036E-10
1	40.9	1.26358E-10
2	41.8	1.28711E-10
3	42.7	1.31095E-10
4	43.6	1.3351E-10
5	44.5	1.35956E-10
6	45.4	1.38435E-10
7	46.3	1.40945E-10
8	47.2	1.43488E-10
9	48.1	1.46063E-10

10	49	1.4867E-10
11	49.9	1.51311E-10
12	50.8	1.53984E-10
13	51.7	1.5669E-10
14	52.6	1.5943E-10
15	53.5	1.62204E-10
16	54.4	1.65012E-10
17	55.3	1.67853E-10
18	56.2	1.70729E-10
19	57.1	1.7364E-10
20	58	1.76585E-10
21	58.9	1.79565E-10
22	59.8	1.8258E-10
23	60.7	1.8563E-10
24	61.6	1.88716E-10
25	62.5	1.91838E-10
26	63.4	1.94995E-10
27	64.3	1.98189E-10
28	65.2	2.01419E-10
29	66.1	2.04686E-10
30	67	2.07989E-10

Table 6-3: Time-dependent diffusivities used in the numerical simulation of diffusive losses during EP corresponding with EP cytometry in 4 °C run buffer (main text Figure 6.4C; 4 °C run buffer with an applied E-field of 50 V/cm). Diffusivity versus time exponential fit function was $y = 5E\text{-}11e^{0.005t}$ and $R^2 = 1$.

Time (s)	Temperature (°C)	$D_{solution}$ GFP (m^2/s)
0	4	5.39416E-11

1	4.2	5.42217E-11
2	4.4	5.45028E-11
3	4.6	5.4785E-11
4	4.8	5.50683E-11
5	5	5.53527E-11
6	5.2	5.56381E-11
7	5.4	5.59247E-11
8	5.6	5.62123E-11
9	5.8	5.6501E-11
10	6	5.67909E-11
11	6.2	5.70818E-11
12	6.4	5.73738E-11
13	6.6	5.76669E-11
14	6.8	5.79612E-11
15	7	5.82565E-11
16	7.2	5.85529E-11
17	7.4	5.88505E-11
18	7.6	5.91492E-11
19	7.8	5.9449E-11
20	8	5.97499E-11
21	8.2	6.00519E-11
22	8.4	6.03551E-11
23	8.6	6.06594E-11
24	8.8	6.09648E-11
25	9	6.12713E-11
26	9.2	6.1579E-11
27	9.4	6.18878E-11
28	9.6	6.21978E-11
29	9.8	6.25089E-11

30	10	6.28211E-11

Model validation was performed experimentally, imaging protein EP with U251-GFP cells as described in the EP cytometry protein separation section, except using 4 °C bifunctional lysis/EP buffer (to prevent complete signal loss by denaturation of GFP in elevated temperature buffer). EP was carried out in a custom glass-bottom chamber for imaging EP, with the buffer volume corrected to maintain a 1.8 mm height, and voltage adjusted to yield a 50 V/cm electric field. The EP process was imaged with time-lapse epi-fluorescent microscopy using Metamorph software (Molecular Devices) and an Olympus IX50 inverted epifluorescence microscope, a CCD camera (Photometrics Coolsnap HQ^2), motorized stage (ASI), a mercury arc lamp (X-cite, Lumen Dynamics) and an XF100-3 filter (Omega Optical). Imaging was performed through a 10× magnification objective (Olympus UPlanFLN, NA 0.45) with 900 ms exposure times, 1 s time intervals, and 1x pixel binning.

GFP AUC analysis was performed as described above, and the AUC at each time point was normalized to the initial injected AUC to determine the quantity of protein retained in the gel.

6.3 Results and Discussion

To understand physical limitations on separation performance we first quantitatively characterized Joule heating and its impact on protein diffusivity and separation performance in the bifunctional lysis/EP buffer and a more conventional EP run buffer. Design of a buffer exchange process allowed complete cell lysis and protein solubilization in a lysis buffer, and reduction of Joule heating-based band dispersion during the separation in an EP run buffer. We developed an analytical model of separation resolution accounting for Joule heating to predict separation performance as a function of EP time in both the bifunctional lysis/EP buffer and in the buffer exchange to run buffer. In EP cytometry, EP time is limited owing to diffusion of protein out of the separation gel into the surrounding buffer, and thus we also describe a numerical simulation to understand the tradeoff between analytical sensitivity and separation performance. To evaluate separation performance, we performed a model separation of GAPDH (36 kDa) and phospho-S6 (PS6, 32 kDa), which differ by only ~4 kDa or 12% (as relevant to exon skipping splice isoforms). As shown in Figure 6.1B, the two targets were poorly separated, motivating our efforts to explore the role of Joule heating on separation performance.

Joule heating theory applied to EP cytometry. Efficient cell lysis and protein solubilization during the rapid assay timescales required to maintain sufficiently high local concentration of protein from the single-cell lysates necessitates the use of lysis/EP buffer at elevated temperature (around 55 °C)[24,67] . We anticipated that the elevated temperature enhances protein diffusion. Analyte diffusivity is linear with temperature and inversely proportional to the viscosity (which is also temperature-dependent) by the Stokes-Einstein relation:

$$D_{eff} = \frac{kT}{6\pi\mu R} \qquad \text{Eq. 6.3}$$

where k is Boltzmann's constant, μ is the viscosity and R is the radius of the diffusing species. The viscosity exponentially decreases with temperature and has been found to follow the expression below for water:

$$\mu = 2.7 \times 10^{-3} e^{\left(\frac{1713}{T}\right)} \qquad \text{Eq. 6.4}$$

where T is the temperature in Kelvin[196]. As schematized in Figure 6.1B, increased diffusivity yields enhanced diffusive band broadening of protein peaks during EP as the initial injected peak width (σ_0) increases with time (t) due to molecular diffusion:

$$\sigma(t) = \sqrt{\sigma_0^2 + 2D_{eff}t} \qquad \text{Eq. 6.5}$$

Diffusive band broadening negatively impacts separation performance, as the separation resolution for separating two protein species is given as the ratio of the peak center-to-center distance (Δx) to average peak width (σ):

$$R_s = \frac{\Delta x}{\frac{1}{2}(4\sigma_1 + 4\sigma_2)} \qquad \text{Eq. 6.6}$$

The temperature of the bifunctional lysis/EP buffer further increases owing to Joule heating throughout the EP separation, which enhances diffusive band broadening.

Specifically, we hypothesized Joule heating would be exacerbated due to the conductivity of the bifunctional lysis/EP buffer, resulting in reduced separation performance. We measured the conductivity of the bifunctional lysis/EP buffer and a typical run buffer for SDS-polyacrylamide gel EP of proteins (containing 0.5X Tris glycine and 0.1% SDS, which is just above the critical micelle concentration for SDS in Tris glycine[204]). The ~3-fold higher conductivity of the bifunctional lysis/EP buffer (0.90 ± 0.01 compared to 0.32 ± 0.01 mS/cm in run buffer) is due to higher concentrations of ionic detergents in the bifunctional lysis/EP buffer, which are critically important to lyse the cell membrane, solubilize[67] and coat the proteins with SDS for accurate sizing by SDS-polyacrylamide gel EP[205]. Given the linear relation between Joule heating flux, and conductivity in Eq. 6.1, the 3-fold higher conductivity of the bifunctional lysis/EP buffer compared to conventional run buffer should yield ~a 3-fold increase in Joule heating. Thus, owing to the conductivity of the bifunctional lysis/EP buffer, we expected Joule heating would substantially elevate temperature during EP.

Joule heating estimated to reduce separation resolution ~2-fold in EP cytometry. To quantitatively characterize Joule heating during EP cytometry, we sought to directly measure buffer temperature increases in an EP cytometry chamber. In enclosed capillary or microchannel EP, a variety of methods have been employed for temperature measurements such as quantifying changes in conductivity[206], electoosmotic mobility[207], or fluorescence[208] and absorbance of temperature-sensitive materials[209]. In contrast, due to the open geometry of the EP cytometry device, buffer temperature is readily accessible for measurement with a variety of conventional temperature sensors. While thermocouples are commonly used for temperature measurements, we required an electrically insulated probe, which yielded too long a time constant for accurate temperature measurements. Thus, we used pre-calibrated commercially available liquid crystal temperature sensors, which instead contain material with temperature-varying visible light absorbance (yielding a color change), and time constants on the order of 1-100 ms[210,211]. The

liquid crystal temperature sensor was completely submerged at the bottom of the EP chamber containing 12 mL of buffer (where the microwell array gel is typically placed) for accurate estimate of buffer temperatures within the polyacrylamide gel during EP (as shown in Figure 6.2A).

We measured remarkable Joule heating in the bifunctional lysis/EP buffer compared with the standard EP run buffer. Buffer was poured into the chamber (conductor height of ~1.8 mm, the minimum required to ensure buffer contacts the electrodes and covers the gel surface) and 25 s passed before applying voltage (to simulate single-cell lysis, which is typically performed in 55 ℃ buffer for 15-25 s). Under an applied electric field of 50 V/cm (initial current ~200 mA in lysis/EP buffer and ~30 mA in run buffer; see SI for current as a function of time), we observed a nearly 20 ℃ temperature increase during a typical EP time of ~20 s, as shown in Fig. 2B. A linear fit of the temperature readings in Figure 6.2B reveals a temperature rise of 0.90 ± 0.15 ℃/s (which is in good agreement with an estimate of 0.81 ± 0.11 ℃/s found by imaging GFP EP in gels of different density and performing exponential fits to the EP velocity versus time curves[106]). As expected, the run buffer with 3-fold lower conductivity than the bifunctional lysis/EP buffer gave a nearly 3-fold lower heating rate of 0.20 ± 0.01 ℃/s.

In an open microfluidic format, the constant temperature rise observed during EP cytometry differs from the behaviors observed in capillary and microchannel EP formats. In open formats,

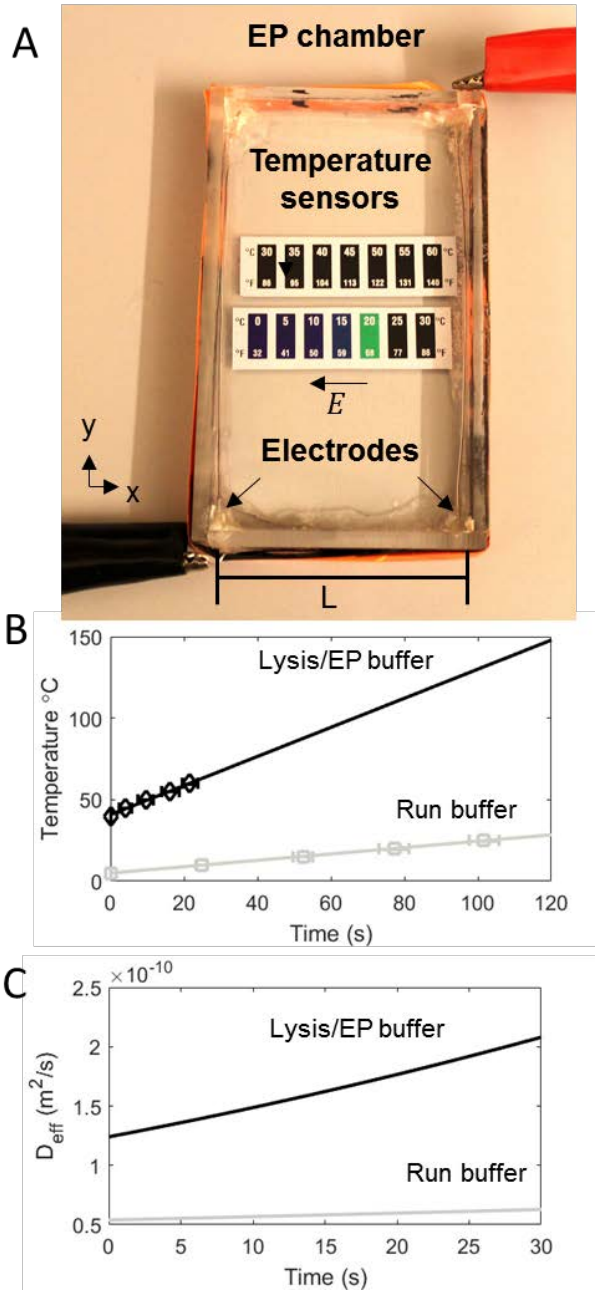

Figure 6.2: Joule heating-induced temperature rise in open microfluidic electrophoresis results in ~4-fold higher protein diffusivity. (A) Top-down image of liquid crystal temperature sensors in the EP chamber (location of the separation gel). (B) Quantitation of Joule heating as a function of EP time (E=50 V/cm) in 55 ℃ bifunctional lysis/EP buffer (black diamonds, n=3 measurements, error bar is standard deviation) and 4 ℃ 0.5 X Tris glycine with 0.1% SDS (run buffer, grey squares, n=5 runs). Measurement of the temperature rise in the bifunctional buffer is limited to the first 30s of EP because the power supply current limit is reached yielding a voltage drop (see SI). Linear fits (solid lines) give the temperature rise (0.90 ± 0.15 ℃/s for the bifunctional lysis/EP buffer, R^2=0.99; and 0.20 ± 0.01 ℃/s for the run buffer, R^2=0.99). (C) Estimates of increase in protein diffusivity during EP using Eq. 6.3 and Eq. 6.4, the hydrodynamic radius for GFP (2.82×10^{-9} m) and the rate of temperature rise measured in (B)

assuming a starting temperature of 40 ℃ for the bifunctional lysis/EP buffer (accounting for cooling from 55 ℃ to 40 ℃ during 25 s of simulated lysis, black line), and 4 ℃ for the run buffer (grey line).

large temperature rises increase buffer conductivity, which further raises the heat flux (by Eq. 6.1) giving way to the autothermal runaway phenomenon[212,213]. Utilizing a power supply in constant voltage mode yields increasing electrical current and, thus, power as the conductivity increases (Figure 6.3). However, in capillary electrophoresis the buffer conductivity is maintained as a constant, thus the buffer temperature is affected by increasing the applied voltage and power[196,207,214]. Heat dissipation in capillary and microchannel systems is so efficient that autothermal runaway is not observed even with ~100x higher applied electric fields and ~10x higher buffer conductivities than those in EP cytometry[200]. In capillary electrophoresis, preventing radial temperature gradients >1.5 degrees Kelvin achieves separation efficiencies unhindered by Joule heating[215]. In contrast, in EP cytometry the impact of temperature-rise from Joule heating-induced autothermal runaway have yet to be studied.

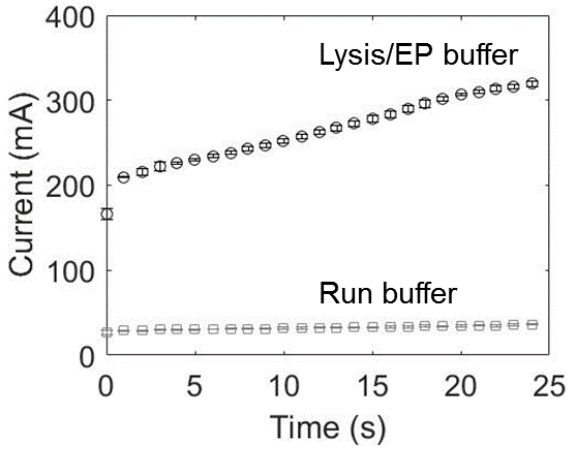

Figure 6.3: Quantitation of current increase as a function of EP time. EP is performed as described in the main text at 50 V/cm, with 12 mL of the specified buffer (55 ℃ bifunctional lysis/EP buffer, or 4 ℃ 0.5x tris glycine 0.1% SDS run buffer) present in the EP chamber.

To understand the impact of Joule heating on EP cytometry separation performance, we calculated the time-dependent protein diffusivity, and band broadening to approximate the scaling of separation resolution. We estimated the effect of increasing temperature during EP on protein diffusivity using Eq. 6.3 and Eq. 6.4 (assuming the buffer viscosity can be approximated with that of water) and temperatures derived from the measured rates of heating in the bifunctional lysis/EP buffer and the run buffer, as shown in Figure 6.2C. The diffusivity is estimated for GFP, which has a known hydrodynamic radius of ~2.82×10^{-9} m[203] and is in a similar molecular mass range as the PS6 and GAPDH used for the model separation in Fig. 1 (27 kDa versus 32 and 36 kDa respectively). Given the scaling of separation resolution with peak width and diffusivity (Eq. 6.5 and Eq. 6.6), the 2-4-fold increase in diffusivity due to heating in the bifunctional lysis/EP buffer versus run buffer would yield an up to 2-fold reduction in

separation resolution. Such reductions in separation performance currently prevent the separation of alternatively spliced protein isoforms in EP cytometry size-based separations.

Diffusive loss of protein out of the open microfluidic device into the buffer reservoir limits separation time in EP cytometry. A unique consequence of increased diffusivity in open microfluidics is enhanced diffusive loss of analyte out of the device, which reduces analytical sensitivity. This is a tremendous challenge when handling protein quantities present in single cells. To assess the effect of Joule heating on protein losses from the gel during EP, we performed numerical simulations of 2D diffusion of protein out of the gel. Using COMSOL Multiphysics 4.2a, we solve Fick's law, again utilizing the time and temperature-dependent GFP diffusivities from Figure 6.2 and assuming an in-gel diffusion coefficient that is 0.13 time the solution diffusivity (see SI for model parameters). We validated the model by comparing directly with experimental EP data collected by imaging EP of GFP from single U251-GFP expressing cells (in 4 ℃ lysis/EP buffer to maintain GFP fluorescence before adjusting model parameters to reflect elevated temperature buffer used for solubilizing endogenous proteins), as shown in Figure 6.4A. The AUC at each EP time point is normalized to the initial injected AUC and plotted in Figure 6.4B. The number of in-gel protein molecules as a function of time in the model is normalized to the initial in-gel protein molecules, and plotted in Figure 6.4B showing good agreement with the experimental data (with a GFP diffusivity corresponding to a temperature of 9 ℃ initially, the typical temperature after 25 s of lysis, and a Joule heating temperature rise of 0.9 ℃/s). We hypothesize detergent denaturation of GFP yields signal loss that causes deviation between the experiment and the model.

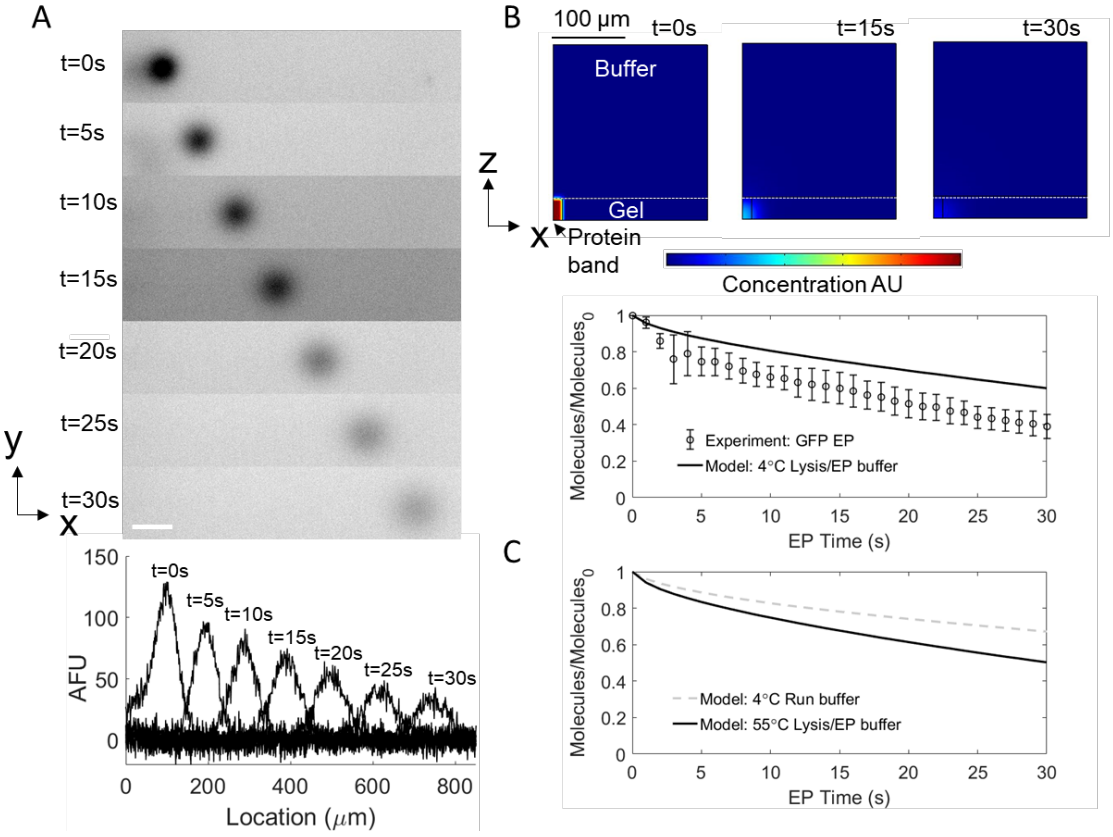

Figure 6.4: Joule heating yields significant diffusive losses in EP cytometry, limiting EP time. (A) Montage of inverted grayscale micrographs and intensity profiles depicting reduction in GFP signal due to diffusion during EP. Analyte is GFP from U251-GFP cells (performed in 4 ℃ bifunctional lysis/EP buffer at 50 V/cm). Scale bar is 100 μm. (B) Concentration heat maps from simulation of diffusive losses during EP and quantitation of the normalized retained signal in the gel as a function of time from the simulation (solid line) and the EP experiment in A (n=5 cells, error bars are standard deviations). (C) Simulation quantitation of diffusive losses with model parameters adjusted for the 55 ℃ bifunctional lysis/EP buffer used for EP cytometry (solid line), and with a 4 ℃ 0.5X Tris glycine 0.1% SDS run buffer (dashed grey line).

Having observed reasonable agreement between the model and validation EP data, we applied the model to quantify protein losses during typical EP cytometry separations in the elevated temperature bifunctional lysis/EP buffer. Additionally, we sought to understand how significantly diffusive losses would be mitigated if EP cytometry were performed in the low conductivity run buffer (4 °C 0.5X Tris glycine 0.1% SDS run buffer). A plot of protein molecules in the gel (normalized to initial molecules in gel) versus time (Figure 6.4C) reveals over 50% loss of protein in typical EP times in heated bifunctional lysis/EP buffer compared with only 30% loss of protein electrophoresed in cold run buffer. Such protein loss accounts for one of the highest losses of any step in the EP cytometry assay, as the estimated diffusive loss from the microwell during lysis is ~40-90%[65] and immobilization for proteins between 21 and 116 kDa yields only ~10-30% loss[70]. In contrast, in enclosed microchannel or capillary EP, little-to-no mass is lost during the separation. In such systems, scaling of signal with time due to diffusive band broadening, and the dependence of dimensionless signal-to-noise ratio on system parameters has been characterized[96]. Given variation in signal-to-noise ratio[126] in EP cytometry from heterogeneity of protein expression in individual cells (biological variation), validating with a model of signal-to-noise ratio as a function of time is not appropriate.

The quantitation of protein loss gives context to estimates of analytical sensitivity of EP cytometry separations. The reported analytical sensitivity of ~27,000 copies of protein in-gel corresponds with the starting concentration of approximately a median-range expressed protein (~170,000 copies of protein per cell)[26]. Lower abundance proteins would be detectable by reducing diffusive losses during EP (reducing Joule heating, and using higher electric fields to achieve more rapid separations). Designing separations of low-abundance, small molecular mass difference species remains a measurement challenge given the tradeoff between analytical sensitivity and separation performance in EP cytometry. Clearly, it would be preferable to perform EP cytometry separations in lower conductivity buffers to reduce diffusive losses of analyte. Using assay stage-optimized buffers requires rapid replacement of the lysis buffer without reducing protein levels below the in-gel immunoassay limit of detection.

Buffer exchange to a run buffer with lower Joule heating does not result in appreciable protein loss from the gel. We designed a buffer exchange procedure to switch from the bifunctional lysis/EP buffer to a lower-conductivity EP buffer to directly measure the impact of lowering Joule heating in EP cytometry. We aimed to perform the buffer exchange in a manner that limited loss of the single-cell protein lysate from the open microwell array into the surrounding buffer. Previously, we determined that recirculating flow in the microwells generated from pouring lysis buffer over the gel yielded loss of ~40% of protein during lysis[65]. Thus, we instead electrophoretically injected the protein into the gel prior to the buffer exchange, since diffusion in the gel is hindered relative to diffusion in solution in the microwell[82,87]. For

example, GFP diffusivity in an 8%T gel is ~0.13 times the diffusivity in the microwell. As shown in Figure 6.5, we carried out the buffer exchange, after 4 s of EP for the low molecular mass GAPDH and PS6 model separation, stopping the E-field and removing the bifunctional lysis/EP buffer from chamber before adding 4 ℃ 0.1% SDS 0.5X Tris glycine run buffer and resuming EP. The protein injection time must be adjusted based on the EP mobilities of the proteins of interest (which will be a function of the protein size and percent T of the gel)[85]. The entire process of exchanging buffers takes ~10 s when performed manually, but future designs could incorporate more rapid automated buffer delivery to maximize retention of protein in the gel.

To ensure that the buffer exchange did not result in substantial loss of protein, we quantified the PS6 protein expression levels in EP cytometry with and without buffer exchange. In both the buffer exchange and EP in the bifunctional lysis/EP buffer, the total EP time was 16 s, allowing direct comparison of the protein levels in the immobilized PS6 protein bands. We quantified area under-the-curve (AUC) in the bifunctional lysis/EP buffer only (n=58 cells) and buffer exchange gel (n=75 cells). The AUC distributions completely overlapped, and thus we find a Mann Whitney U-test p-value of 0.39 (Figure 6.5B). Thus, there was no detectable loss of protein upon buffer exchange.

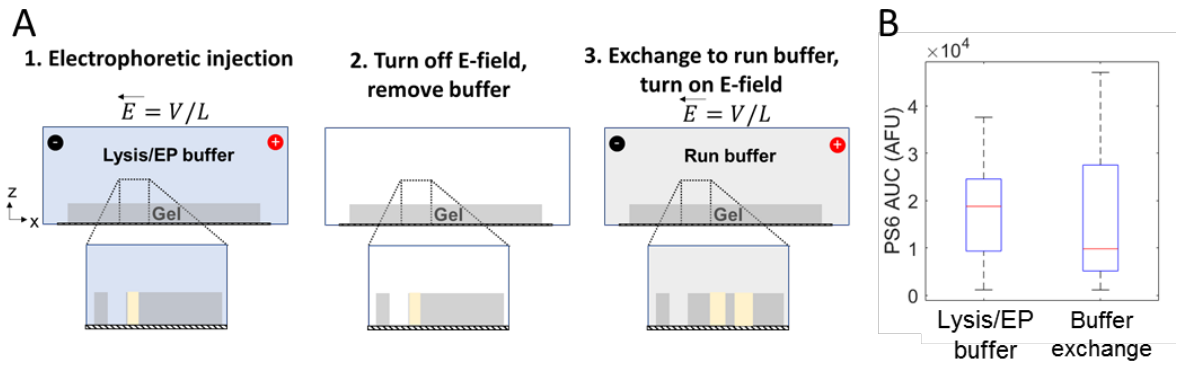

Figure 6.5: Buffer exchange in open microfluidic EP cytometry does not result in significant protein loss from the ultra-thin separation gel, allowing for direct comparison of separation performance in buffers that yield different levels of Joule heating. (A) Schematic workflow of the buffer exchange performed by initially lysing the cell in the lysis/EP buffer, and electrophoretically injecting protein into the gel (50 V/cm). The E-field is turned off and buffer is removed and replaced (within ~10 s) with 4 ℃ 0.5X Tris glycine with 0.1% SDS, and the E-field is turned back on to perform the protein separation. (B) Quantitation of PS6 area-under-the-curve AUC (in arbitrary fluorescence units, AFU) demonstrates that buffer exchange (n=75 cells) does not yield measurable losses of protein compared to the bifunctional lysis/EP buffer (n=58) control (16 s total EP at 50 V/cm for both conditions, Mann-Whitney p-value=0.39).

Buffer exchange increases separation resolution while decreasing separation resolution variation. We applied the buffer exchange to optimize single cell separations of endogenous GAPDH (36 kDa) and PS6 (32 kDa) with a 4 kDa (12%) molecular mass difference (Figure 6.6A). Interestingly, the separation resolution distribution is non-normal, as is apparent from the distribution skew in Figure 6.6B (and shown with QQ plots in Figure 6.7). Thus, we compare the median separation resolution values upon electromigrating the PS6 protein near the end of the

separation lane (~1300-1400 μm from the well) for the bifunctional lysis/EP buffer (25s EP) versus buffer exchange (75s EP). The median separation resolution is 0.77 and 0.49 for buffer exchange and bifunctional lysis/EP buffer respectively (Mann Whitney p-value=0.0013). This corresponds to a 1.6-fold increase in separation resolution, which is in reasonable agreement with the anticipated 2-fold increase in separation resolution estimated by scaling relations earlier in the present work. The nearly fully-resolved separations or proteins with a 12% molecular mass difference represents the smallest size separation achieved in size-based EP cytometry to date (previously limited to 33% molecular mass differences).

Application of EP cytometry to elucidate cancer progression via protein profiling of circulating tumor cells from cancer patients[24] requires separations with low technical variation, as observed in the buffer exchange here. Notably, we observe marked decreases in lane-to-lane variation in separation resolution upon performing the buffer exchange, as demonstrated in Figure 6.6C. Given the non-normal separation resolution distributions, instead of characterizing variation with a coefficient of variation, we utilize the coefficient of quartile variation, CQV[165]. The CQV is defined as:

$$CQV = \frac{Q_3 - Q_1}{Q_3 + Q_1} \qquad \text{Eq. 6.7}$$

where Q3 is the 75th percentile value, and Q1 is the 25th percentile value for the distribution. We observe CQV values ~50% for the bifunctional lysis/EP buffer, and only ~20% for the buffer exchange. The high variation in separation resolution in the bifunctional lysis/EP buffer was also observed in EP cytometry separations of proteins 25-44 kDa in 8%T gels[106]. The underlying mechanisms contributing to high separation resolution variation in EP cytometry employing bifunctional lysis/EP buffer is not yet understood. We learn here that lowering the buffer conductivity and temperature reduces separation resolution variation, which is a valuable first step towards understanding sources of technical variation in EP cytometry separations. The reduced variation in separation resolution upon buffer exchange is invaluable when working with rare cell samples (e.g., circulating tumor cells from cancer patients in which only ~1-10 cells may be isolated[24]). Thus, we anticipate that the buffer exchange method demonstrated here will be applied for EP cytometry analysis of rare cells.

The demonstrated separation performance is relevant to isoform detection resulting from alternative splicing (molecular mass differences of ~4 kDa). We note that given the similarity in length of many exons, when deletions of various exons occur, the molecular mass differences between alternatively spliced isoforms can be 1 kDa or smaller[216]. However, recent analysis of peptide data from large-scale proteomics databases supports a hypothesis that the majority of genes express only one main isoform[217]. For such smaller molecular mass difference separations, potentially longer separation times may be employed, but this requires careful consideration of the tradeoff between separation performance and analytical sensitivity in EP cytometry.

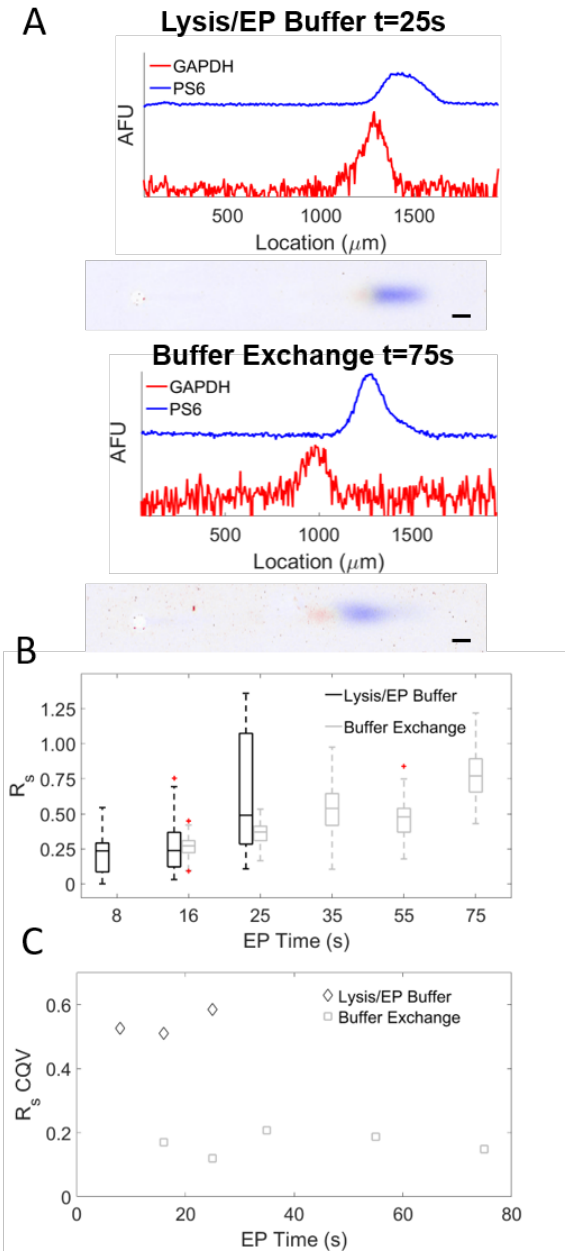

Figure 6.6: Buffer exchange yields higher separation resolution and decreased variation in separation resolution compared with the bifunctional lysis/EP buffer for separations of GAPDH and PS6 from single cells. (A) Representative offset intensity profiles and false-color micrographs of separations of GAPDH (red) and PS6 (blue) from MCF-7 cells upon performing EP for the specified buffer and time at 50 V/cm. The separation times shown correspond with PS6 electrophoresis to ~1300-1400 μm from the well (nearing the end of the separation lane). Scale bar is 100 microns. (B) Quantitation of separation resolution in lysis/EP buffer (black boxes) versus buffer exchange to run buffer (grey boxes). For the run buffer experiment points, n=129, n=76, n=84, n=103 and n=129 for the 16 s, 25 s, 35 s, 55 s, and 75 s EP times respectively. In the bifunctional lysis/EP buffer control, n=106, n=86 and n=66 for the 8, 16 and 25 s EP times respectively. With PS6 migration to the end of the separation lane (25s EP in

lysis/EP buffer and 75s EP in buffer exchange, as in A), median separation resolution is 1.6 times higher in the buffer exchange compared with bifunctional lysis/EP buffer (Mann-Whitney p-value=0.0013). (C) Quantitation of the coefficient of quartile variation, CQV, of separation resolution for the data shown in B with lysis/EP buffer (black diamonds) and buffer exchange (grey squares).

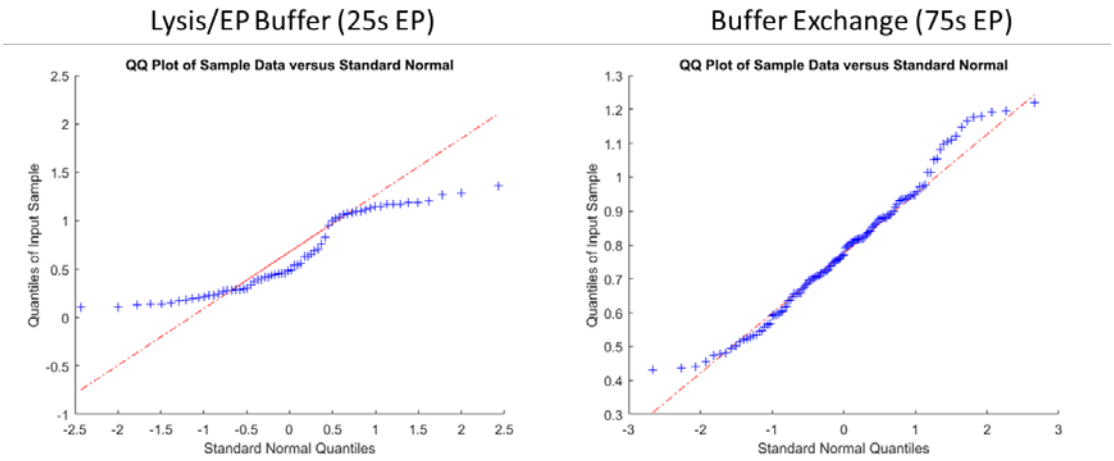

Figure 6.7: Separation resolution distribution displays non-normality in EP cytometry. QQ plots for the measured separation resolution distribution versus a standard normal distribution (data from Figure 6.6). Significant non-linearity particularly for the bifunctional lysis/EP buffer (left) indicates the data are not normally distributed.

Separation resolution analytical model employing Joule-heating induced increased diffusivity guides optimization of separation. We sought to develop an analytical model to predict separation performance while tuning separation parameters for optimized EP cytometry separations with buffer exchange. We re-cast the separation resolution expression (Eq. 6.6) in terms of the diffusivities, initial peak widths, and the peak center distance:

$$R_s = \frac{\Delta\mu_{EP} E t}{\frac{1}{2}\left(4\sqrt{\sigma_{0,1}^2 + 2D_{eff,1}t} + 4\sqrt{\sigma_{0,2}^2 + 2D_{eff,2}t}\right)} \qquad \text{Eq. 6.8}$$

where $\Delta\mu_{EP}$ is the difference in EP mobility between the two proteins. We utilized the estimates of EP time-dependent (i.e., temperature-dependent) protein diffusivity from Figure 6.2, modifying the diffusivity by a factor of 0.13 to account for the lower diffusivity in gel compared to solution. We assumed an initial injected peak width in the model of ~50 μm for each protein (in line with measured PS6 peak widths at short electrophoresis times). Finally, we required an estimate of $\Delta\mu_{EP}$, which can be determined by performing three initial EP cytometry separations with different EP times, and quantifying change in peak location versus time (velocity, *U*), as $U=\mu_{EP}E$, for each protein. As shown in Figure 6.8, EP cytometry separations were performed with the buffer exchange to run buffer and varying EP times (with 16, 25 and 35 s separations used to seed the $\Delta\mu_{EP}$ model parameter in Eq. 6.8). In the bifunctional lysis/EP buffer, PS6 approaches the end of the separation lane in only 25s. At the same time, the current limit is reached for the power supply used. Thus, the model cannot be used to extrapolate how separation performance will improve with longer separations because the electric field is not constant, and longer separation lanes would be required. We observed a relatively linear relation between peak location and time (R^2 values>0.94; U=23.31 μm/s for PS6, and 20.11 μm/s for GAPDH). Fits of peak location versus time in the bifunctional lysis/EP buffer attained R2 values>0.97 with U=51.9 and 45.6 μm/s for PS6 and GAPDH, respectively.

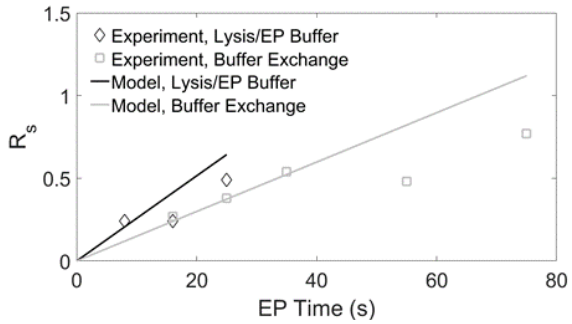

Figure 6.8: Impact of Joule heating-induced peak dispersion on operation of open microfluidic EP cytometry. Experimentally determined median separation resolution from boxplots in Figure 5B for lysis/EP buffer (black diamonds) and buffer exchange to run buffer (grey squares) is plotted versus electrophoretic separation time. Numerical model of separation resolution for lysis/EP buffer (black line), and buffer exchange (grey line) accounts for increased protein diffusivity owing to Joule heating throughout the separation.

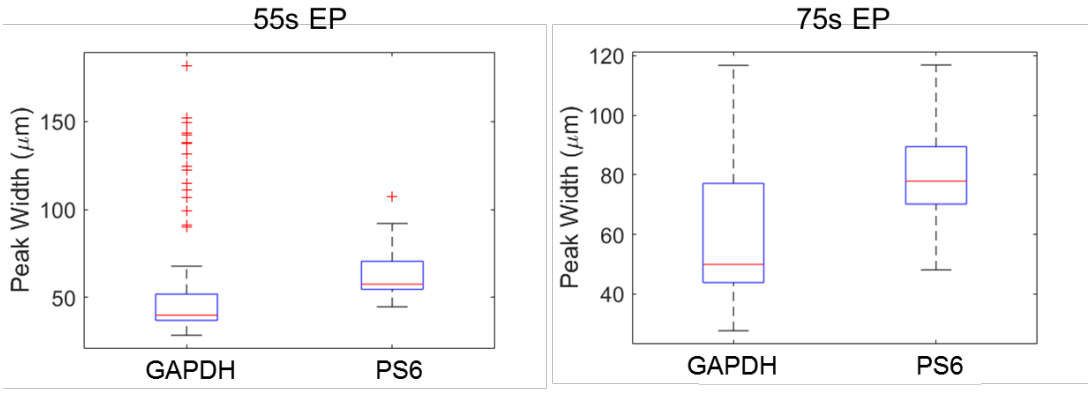

Figure 6.9: Quantitation of protein peak width for GAPDH and PS6 in the buffer exchange 55 and 75 s EP separation conditions from Figure 6.6 (n=129 cells). A number of outliers are observed for GAPDH in the 55 s EP condition, which contribute to the measured reduced separation resolution. The PS6 peak width deviates significantly from the anticipated peak width from diffusive band broadening alone at the 75 s time point (~51 microns estimated, versus a median of 78.9 microns measured experimentally).

We observe reasonable agreement between the model and separation data for the bifunctional lysis/EP buffer condition, and for initial time points for the exchange to run buffer condition data and model. At the longest separation times, divergence between the separation model and experimental data occurs in the buffer exchange because the measured peak widths deviate from the widths anticipated by diffusive band broadening alone (see Figure 6.9). One possible explanation for this observation is that following the buffer exchange (from a 0.5% SDS to 0.1% SDS buffer), SDS begins unbinding from the protein resulting in partial refolding of the denatured protein, which would alter the electrophoretic mobility and broaden the peak. Others have reported partial unbinding of SDS from proteins within 30 s of introducing SDS-saturated proteins into solutions containing lower concentrations of SDS[204]. Thus, further studies investigating the use of intermediate concentrations of SDS, and balancing the tradeoff of

increased Joule heating versus potential SDS unbinding-based dispersion, may be warranted. Such investigation may allow separation performance with a buffer exchange to approach the separation resolution predicted by the model. Finally, we note the agreement between the separation resolution models and early EP time points supports the hypothesis that separation performance in EP cytometry can be accounted for by Joule heating-induced increased diffusivity alone. In contrast, capillary EP separation performance is explained by differences in mobility and diffusivity arising from thermal gradients from the glass wall to the capillary center[200]. Thus, optimization of open microfluidic EP separations will seek to mitigate constant increases in diffusivity as opposed to addressing thermal gradients.

6.4 Conclusions

We report on the effects of Joule heating on separation performance and analytical sensitivity in open microfluidic devices, here for EP cytometry. Given the open device geometry, the separation time is inherently limited by out-of-plane diffusive losses during EP. We conduct experiments and numerical simulations to quantify diffusive losses during EP, and find up to 50% loss of protein during typical separation times, which limits detection to proteins expressed at median copy numbers or higher for mammalian proteomes. To mitigate analyte losses and band dispersion, we designed a lysis-run buffer exchange that (i) completes rapid cell lysis (< 30 s) under a high-temperature, high concentration ionic detergent solution and (ii) gel electrophoresis of each cell lysate in a lower temperature and conductivity run buffer. By electrophoretically injecting protein in the dense separation gel prior to buffer exchange, single cell lysate protein concentrations are maintained above the in-gel immunoassay limit of detection. A separation model estimates the EP duration necessary for a desired separation resolution and is in good agreement with empirical observations. We do not consider peak dispersion arising from dissociation of SDS from protein during EP. With buffer exchange, EP cytometry resolves endogenous GAPDH and PS6 (36 and 32 kDa, respectively) in lysate from single MCF-7 breast cancer cells. This 4 kDa (12%) molecular mass difference is the smallest protein mass difference resolved by size-based EP cytometry separations to date, with notable decreases in separation resolution variation. In future work, the demonstrated separation performance will be utilized for first-in-kind measurements of cancer-driving exon skipping protein isoforms of rare cell samples.

Chapter 7.

Electrophoretic cytometry complex fractionation isolates actin cytoskeletal complexes from single cells

This work was performed in collaboration with Ryo Higuchi-Sanabria, Andrew Dillin and Yizhe Zhang. Portions of this chapter are reproduced with permission from J. Vlassakis and A.E. Herr, "Electrophoretic cytometry reveals heterogeneity in cytoskeletal molecular states of cancer cells", *Proceedings of the 21st International Conference on Miniaturized Systems for Chemistry and Life Sciences (MicroTAS),* 2017.

7.1 Introduction

The cytoskeletal protein actin has critical functions in cell motility, proliferation and differentiation[218]. For example, cytoskeletal rearrangements are thought to impact neuronal guidance in axonal growth cones, where actin polymerization kinetics determine cellular motility[219] Actin exists in a monomeric form (G-actin, ~42 kDa) in the cytoplasm of the cell, but polymerizes into long actin filaments (F-actin)[220] in a highly dynamic process[221,222]. Regulation of actin polymerization and depolymerization, is carried out by over 100 binding proteins that complex with monomeric actin (G-actin, 42 kDa) and filamentous actin (F-actin, up to 100s of monomers)[220,223].

Changes in molecular interactions, like those governing actin polymerization, underpin disease and drug treatment alike. In cancer progression, actin polymerization is disrupted, impacting numerous essential cellular processes (from cell motility to proliferation[218]). Consequently, oncology drugs targeting stabilization of F-actin filaments have been studied[224]. Single-cell resolution of actin polymerization state and binding protein complexes would inform drug development but is currently unfeasible.

Given the numerous aspects of cell biology influenced by actin cytoskeletal organization, various methods for measuring F and G-actin have been developed. One major class of measurements is fluorescence microscopy or cytometry-based quantitation of actin structures. Fluorescent reporters such as EGFP actin were used to visualize G actin in cells[225,226], or in non-transfectable cells, small peptide staining of F-actin has also been demonstrated[227]. Also, labeling of F-actin with fluorescent phalloidin, and G-actin by vitamin D binding protein, or DNaseI[226,228–230] has been performed. With such techniques, groups have successfully quantified the spatial localization of G actin (and F to G ratios) in the leading edge of neuronal growth cones[226]. Furthermore, flow cytometry of F-actin stained cells showed that the F-actin levels were higher in aged lymphocytes compared to young ones[228]. However, the measured F to G-actin ratio is highly sensitive to the permeabilization and fixative method (with Triton X-100 eliminating the

fluorescence staining of G-actin)[226,230]. Thus, fixation artifacts can hinder accurate quantitation, despite the excellent spatial information about actin cytoskeletal organization from fluorescent reporters. Furthermore, actin binding proteins and oncology drugs compete with small-molecule stains for actin binding sites. For example, the drug jasplakinolide, demonstrated as a promising therapy for prostate cancer[224], has been shown to prevent accurate F-actin staining[231]. Thus gold-standard F and G-actin stains have limited utility in cancer studies of actin polymerization and binding protein complexation[231]. Furthermore, staining is rarely used as a quantitative method, and few cells are imaged, preventing identification of cellular subpopulations.

Another class of measurements of actin utilize mild lysis reagents and F-actin stabilization buffers to solubilize G-actin and preserve F-actin prior to ultracentrifugation, and downstream Western blotting (or DNase assay quantitation) of the actin fractions[172,232]. In such approaches, the formulation of the stabilization buffer is crucial in maintaining the F-actin filaments in the first assay step, and depolymerizing buffer disrupts the F-actin prior to western blotting. Though widely used in biochemical studies of actin organization[233], this method requires approximately 10^7 cells, making it unfeasible for the study of single or small numbers of cells.

We have developed a micro-scale electrophoretic cytometry assay that preserves chemical interactions to separate and detect molecular complexes in up to 1000s of single-cells. As a first demonstration, we fractionate F and G-actin from single cancer cells in a microwell array patterned in polyacrylamide gel. We use gel lid fluidics[132] to introduce a series of lysis buffers, first containing non-ionic detergents to preserve interactions, followed by a depolymerization buffer. G-actin is electrophoresed in interaction-stabilizing lysis buffer and immobilized in the gel, while F-actin is size-excluded from the gel. Upon delivery of depolymerization buffer, F-actin is electrophoresed in the opposite direction of the G-actin and immobilized. Antibody detection of the actin species yields quantitation of previously unmeasured heterogeneity in F and G actin at the single-cell level.

7.2 Materials and Methods

Chemicals

Tetramethylethylenediamine (TEMED, T9281), 40% T, 3.4% C acrylamide/bis-acrylamide (29:1) (A7802), N,N,N′,N′-, ammonium persulfate (APS, A3678), sodium deoxycholate (NaDOC, D6750), sodium dodecyl sulfate (SDS, L3771), bovine serum albumin (BSA, A7030), and triton X-100 (X100), were acquired from Sigma Aldrich. An Ultrapure Millipore filtration system provided deionized water (18.2 MΩ). PharmAgra Laboratories custom-synthesized N-[3-[(3-Benzoylphenyl)- formamido]propyl] methacrylamide (BPMAC). Phosphate buffered saline was purchased from VWR (10X PBS, 45001−130). Tris glycine (10X) buffer was attained from Bio-Rad (25 mM Tris, pH 8.3; 192 mM glycine, #1610734).

Cell culture

BJ fibroblasts and U20s RFP-LifeAct cells were maintained in DMEM (11965, Life Technologies) supplemented with 10% FBS, 1% penicillin/streptomycin, and 1% non-essential amino acids, while MDA-MB-231 GFP actin cells were maintained in the same media minus the

1% non-essential amino acids. All cells were cultivated in a humidified incubator in 5% CO_2 kept at 37 °C (except for heat shocked cells which were briefly incubated at 45 °C).

Adherent cell device fabrication and cell culture

A base layer (80 micron thick) of 8%T polyacrylamide containing 10 μg/mL fibronectin was photopolymerized (60s UV exposure at 20 mW/cm^2 with 0.25% LAP) on top of silanized glass. An 8%T polyacrylamide precursor was incubated 15 min with the base layer on top of a SU-8 on glass micropost mold (post diameters were 100 microns). The gel was photopolymerized for 5 minutes (20 mW/cm^2) and rehydrated with water for several minutes before being peeled from the mold. The microwell gel was sterilized in 100% ethanol for 30 minutes and rinsed in 1X PBS for at least 10 minutes. BJ fibroblasts were trypsinized and introduced to the microwell array in cell media. After ~75 minutes, excess cells were vigorously washed off the gel surface with media. Cells were then cultured overnight (~18 hours) at 37 °C. The detailed protocol is provided in the Appendix.

EP cytometry complex fractionation assay

The complete assay protocol is provided in the Appendix and summarized briefly here.

Buffers and gel lid incubation: F-actin stabilization lysis buffer used was 10 mM Tris-HCl, 1% Triton X-100, 2 mM $MgCl_2$, and 0.5 mM DTE (titrated to pH=7.4). The DTE was added at the time of a given experiment. The depolymerization buffer was prepared as a 1.56x RIPA buffer such that upon addition of 8 M urea, the final buffer composition was 0.5x Tris glycine, 0.5% SDS, 0.25% sodium deoxycholate, 0.1% Triton X-100, 8 M urea, pH=8.3. Urea was added fresh at the time of the experiment. Gel lids (15%T 3.3% C) were photopolymerized as previously described[132], and incubated overnight in either the F-actin stabilization or the depolymerization buffer (before urea or DTE addition). Upon preparation of the urea or DTE containing buffer, the complete buffers were introduced to the gel lids in a water bath set to 75 °C and incubated for ~30 minutes before beginning the experiments. Gel lids and buffers were only stored for up to 2 weeks, and buffer solution was never re-used.

Fractionation gels (8%T and 3.3%C with 3 mM BPMAC incorporated) were prepared as described elsewhere[67], and trypsinized cells were introduced to the microwell array in 1X PBS solution. In the optimized suspension cell protocol, trypsinization was performed for 3 minutes, and cells in PBS settled in the microwell array for 10 minutes. Each replicate experiment was run with a different petri dish of freshly trypsinized cells in suspension.

For the fractionation separation, the fractionation gel device was pre-incubated in 10 mM Tris-HCl (pH=7.5) briefly before the glass slide was superglued to the surface of a custom 3D printed electrophoresis chamber[132]. The F-actin stabilization gel lid was then applied to the array and cell lysis proceeded for 45s before the electric field was applied (30 V/cm, 45s for 42 kDa actin in fibroblasts, or 60s for 69 kDa GFP-actin from the GFP-actin cells). UV photoimmobilization of protein by covalent bonding to BPMAC in the gel was performed (Lightningcure LC5, Hamamatsu, 100% power, 45 s). The gel lid was then removed, the electrode terminals were

reversed, and the gel lid was replaced with the depolymerization buffer gel lid for 45s. EP was performed for the same duration in the opposite direction before a final UV photoimmobilization step (same UV power and duration). The glass slide was peeled from the electrophoresis chamber, and the fractionation gel was washed in 1X TBST for at least 30 min to overnight prior to immunoprobing.

Immunoprobing was performed as previously described[67], utilizing a rabbit anti-GFP antibody for GFP-actin (Abcam Ab290), mouse anti-actin monoclonal antibody (Millipore MAB1501), rabbit anti-actin polyclonal antibody (Cytoskeleton Inc. AAN01), rhodamine-labeled anti-actin Fab (Biorad 12004164) and rabbit anti-vinculin monoclonal antibody for vinculin (Cell Signaling Technologies E1E9V). Gels were incubated with 1:10 dilution of the stock primary antibody for two hours and then washed 2x for 30 minutes in 1X TBST. Donkey Anti-Rabbit IgG (H+L) Cross-Adsorbed Secondary Antibody, Alexa Fluor 647-labeled (A31573, Thermo Fisher Scientific) and Donkey Anti-Mouse IgG (H+L) Cross-Adsorbed Secondary Antibody, Alexa Fluor 647-labeled (A31571, Thermo Fisher Scientific) were used at a 1:10 dilution with a one-hour incubation. Two more 30-min TBST washes were performed prior to drying the gels in a N_2 stream and imaging with a laser microarray scanner (Genepix 4300A, Molecular Devices).

Images were analyzed using the analysis scripts described earlier in this dissertation and elsewhere[67]. Briefly, the images were median filtered utilizing the "Remove Outliers" macro in Fiji (pixel radius=2 and threshold=50 AFU). The images were then segmented, intensity profiles were generated for each separation lane by averaging along the transverse axis, background subtraction was performed and each peak was fit to a Gaussian curve. For fits with an $R^2>0.7$ and peaks with an SNR>3, user-based quality control is performed, and area under the curve is calculated within two peak widths from the center on the background subtracted profile. Image analysis and statistical analysis were performed in MATLAB R2016b.

Fluorescence imaging of lysis and electrophoresis

Imaging was performed via time-lapse epi-fluorescence microscopy on an Olympus IX50 inverted epifluorescence microscope. The microscope was controlled using Metamorph software (Molecular Devices) and images were recorded with a CCD camera (Photometrics Coolsnap HQ^2). The imaging setup included a motorized stage (ASI), a mercury arc lamp (X-cite, Lumen Dynamics) and an XF100-3 filter for GFP (Omega Optical) and an XF111-2 filter for RFP (Omega Optical). Imaging was performed with a 10× magnification objective (Olympus UPlanFLN, NA 0.45) and 900 ms exposures (1 s time intervals, and 1x pixel binning). Exposure times were lowered for lysis imaging to 600 ms.

F-actin cell staining with phalloidin and Latrunculin A and Jasplakinolide drug treatment

Latrunculin A (Cayman Chemicals *10010630)* was dissolved in DMSO by first using a gently nitrogen stream to evaporate the ethanol the LatA was supplied in, and then 2 mM stock solution was prepared and stored at -20 °C until use. Jasplakinolide (Millipore-Sigma, 420107) was reconstituted in DMSO and stored at -20 °C for up to 3 months. Cells were incubated in the drug

solution at the concentration and for the time listed in the main text. The DMSO control cells were exposed to 0.1% DMSO in cell culture media for the same time as the drug treated cells.

Cells were fixed with 3.7% paraformaldehyde in 1X PBS, and permeabilized with 0.1% Triton X-100 and stained with Alexa Fluor 647-labeled phalloidin (ThermoFisher Scientific, A22287) as described in the protocol in the Appendix.

7.3 Results and Discussion

To measure actin molecular heterogeneity in single cancer cells, we describe a first-in-kind microfluidic cytometry assay that fractionates F and G-actin molecules (Figure 7.1). In a unique layered microdevice, we perform single-cell electrophoresis to separate large F-actin polymers from G-actin monomers. Through microfluidic integration, we perform single-cell settling in a polyacrylamide gel microwell array, delivery of selective lysis reagents, physical separation and blotting (immobilization) of F and G-actin and antibody detection. We interface gel-lid fluidics[132] with a cell-laden microwell array for differential detergent fractionation of the two molecular forms of actin (Figure 7.1). The gel-lid fluidics sequentially deliver F-actin stabilization lysis buffer and depolymerizing buffers commonly used in bulk cell actin ultracentrifugation (Figure 2A). Without complex pneumatics or interfacing, gel-lid fluidics provide facile exchange of buffer chemistries in thousands of cell-laden microwells. Rapid chemical transfers prevent single-cell lysate dilution that would make the measurement otherwise impossible. Our novel microscale assay utilizes reaction volumes 10^8-fold smaller than bulk ultracentrifugation. Short diffusive length scales for detergent micelles from the gel-lid to the microwell array yields lysis of GFP-actin expressing cells within ~45s.

In the following sections, assay design principles that govern EP cytometry complex fractionation are discussed in detail. First, the choice of a selective assay chemistry to lyse cells while maintaining complexes, and to support electrophoresis is described. We confirm that the selected buffer and design of gel lids with high surface area-to-volume ratios for efficient heat dissipation prevent appreciable heating. By visualizing EP with fluorescent actin expressing cells we validate that F-actin is fractionated in the EP cytometry microwell. Next, we describe further assay optimization for achieving uniform E-fields across the EP cytometry device interfaced with gel lid fluidics, and for rapidly depolymerizing F-actin to minimize injection dispersion. The complete bi-directional separation assay rapidly isolates GFP F and GFP G-actin from 100s of single cells in minutes. We validate the assay by completing separations on cells treated with an F-actin destabilizing drug and observe that GFP-actin is not susceptible to the drug, while endogenous F-actin levels decrease in BJ fibroblasts upon drug treatment. Investigation of three applications for EP cytometry complex fractionation are described: i) quantifying F-actin levels in cells treated with a drug that appears to have different effects from in vitro polymerization experiments and phalloidin staining; ii) measurement of other actin protein complexes with a focus on the focal adhesion protein vinculin; iii) introduction of a version of the assay for adherent cells towards assaying the effects of cell stresses (e.g., heat shock) and mechanical microenvironment on actin polymerization at the single cell level. Finally, we explore an

intriguing result that native G-actin immunoprobe signal is lacking with various typical actin antibodies, and demonstrate that immunoprobing is feasible with an anti-actin Fab fragment probe.

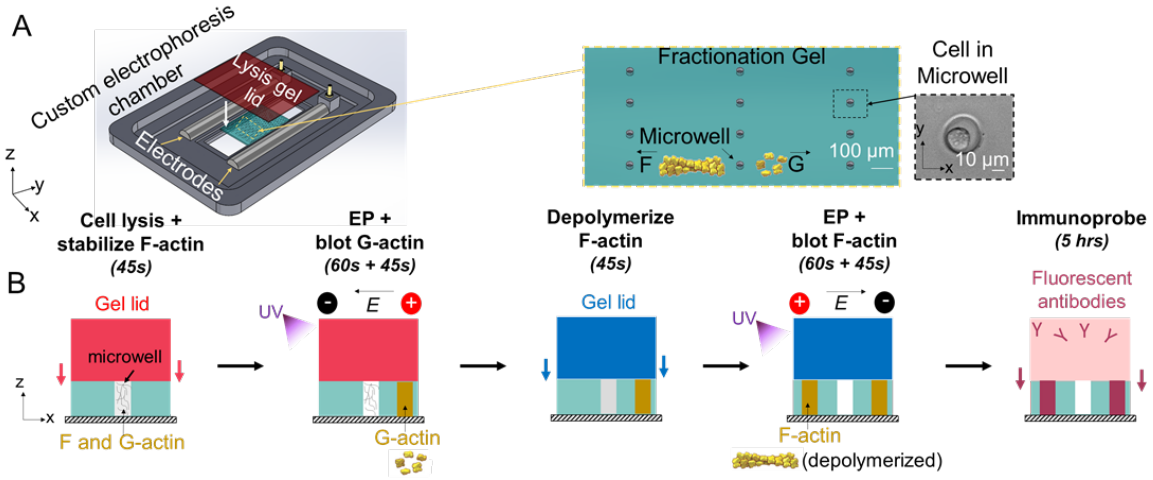

Figure 7.1: Electrophoretic fractionation cytometry integrates on-chip sample preparation, electrophoresis and detection of actin complexes from hundreds of single-cells. (A) Three-dimensional rendering of the fractionation cytometry device and brightfield image of a cell in a microwell patterned in the polyacrylamide fractionation gel. (B) The complex fractionation assay is completed in steps comprising gel lid delivery of F-actin stabilization lysis buffer to the array, electrophoresis (EP) of G-actin monomers, UV-immobilization of G-actin in the gel, gel lid delivery of depolymerization buffer, EP of depolymerized F-actin filaments in the opposite direction of G-actin, UV immobilization and antibody detection.

Selection of buffer for preserving protein-protein interactions and performing electrophoresis

As in the bulk ultracentrifugation assay, a critical feature of EP cytometry complex fractionation is the capability to lyse cells while minimally perturbing protein complexes. Of note, the interactions between individual actins is enhanced by cooperativity of binding[234]. Van der Waals forces and hydrogen bonding confer strong molecular recognition between 20-30 angstrom cross-sectional areas of two actins, while hydrophobic interactions contribute most significantly to the thermodynamic stability of the polymer[234], as in other protein-protein interactions[235]. No buffer will completely maintain the actin distribution present prior to lysis. Consequently, as with the ultracentrifugation assay, the assay is intended to provide information regarding relative shifts in F-actin ratios (e.g., comparing control to a drug treatment)[172]. Still, we aim to minimize the effects of the buffer such that we can leverage the rapid electrophoresis handling steps to attain a more accurate measurement of cellular F and G actin levels.

The typical components of F-actin stabilization buffers are summarized below:

1. Detergents:

Lysis buffers capable of largely maintaining F-actin filaments typically utilize Triton X-100, non idet P40 (NP-40) or both[172,236]. Triton X-100 and NP-40 are both non-ionic detergents, and have been shown to minimally alter in vitro polymerization rates of actin around concentrations of approximately 0.1%[237]. In cell lysates, the addition of 2 mM $MgCl_2$ mitigated actin depolymerization in Triton X-100-containing lysis buffer[172].

2. Buffering species:

Maintenance of F-actin requires near-physiological pH for the buffering species. Consequently, Tris-HCl and PIPES buffers (pKa of 8.08 and 6.76 respectively) have both been used in lysis/stabilization buffers. It has been shown that denaturation of F-actin incubated for extensive time periods (e.g. 1 week or greater) in buffers of varying pH occurs at a relatively constant rate in the pH=6-8 range[238].

3. Cations and ionic strength:

Actin polymerization and depolymerization rates and structural stability depend heavily on the presence of specific cations and the ionic strength of the environment[239]. An increase in sodium chloride from 30 to 80 mM has been shown to reduce the actin critical concentration by almost two-fold[240] (concentration of actin at which polymerization begins), thermodynamically stabilizing actin filaments. However, potassium salt concentrations above physiological conditions yields actin depolymerization[241], indicating the importance of electrostatic interactions in filament stability. Salt-induced stabilization arises from ion screening of actin monomer charge[242], and more predominantly, binding of divalent cations to specific sites of the actin protein[243]. For example, two binding sites for magnesium have been identified in actin monomers and filaments. The first binding site yields a conformation change that promotes filament polymerization[244], while the second binding site overlaps at several amino acid residues with inter-subunit contacts between adjacent actins[239].

Studies have investigated actin polymerization rates with different ionic components and concentrations. Fluorescence spectroscopy of pyrene labeled actin polymerization kinetics indicated that 2 mM $MgCl_2$ yielded relatively constant polymerization rates across a wide range of potassium chloride concentrations (even well below physiological concentrations)[237]. Previously, it was demonstrated that 2 mM $MgCl_2$ prevented depolymerization of F-actin or polymerization of G-actin in the presence of Triton-X 100[172].

4. ATP

Unlike other components, discussion of the addition of ATP and the concentration used was omitted in publications that use ATP[245–248]. However, when it is included, it is typically in the 0.2 mM to 1 mM concentration range. ATP plays a role in polymerization and depolymerization of actin. Actin monomers are bound to ATP and profilin and are recruited to Arp2/3 complexes to polymerize into filaments. When ATP on actin is hydrolyzed, severing proteins (such as ADF and cofilin) bind to the ADP actin filaments and cause depolymerization.

Examples of several buffer compositions from the literature are given below. While numerous buffers have been utilized, the Heacock et al. formulation was more extensively quantitatively characterized. For example, in the Heacock et. al. buffer, the long-term stability of the F-actin pellet was quantified by the DnaseI inhibition assay (Figure 7.2). Notably, for the first several minutes after cell lysis, F-actin levels remain relatively constant. However, over the 30-60 min time frame typically employed to pellet all F-actin via ultracentrifugation, up to 40% of the actin depolymerizes. These results highlight the role that rapid electrophoretic separations can play in attaining more accurate quantitative information regarding actin polymerization state. Because of the availability of the quantitative characterization of the Heacock buffer, this buffer formulation was selected for the EP cytometry complex fractionation assay.

Table 7-1: Carlsson et al.[249] F-actin stabilization buffer.

Lysis and F-actin stabilization buffer component	**Concentration**
Tris HCl, pH=7.4	10 mM
Dithioerythritol	0.5 mM
MgCl2	2 mM
Triton X-100	1%
EGTA	2 mM
ATP	0.2 mM

Table 7-2: Srivastava and Barber[246] F-actin stabilization buffer. This buffer recipe is for in vitro protein-protein interaction measurement. In vitro polymerized actin is incubated with actin binding proteins in the specified buffer for one hour at room temperature prior to ultracentrifugation and SDS-PAGE of the supernatant and pellet. Authors indicate buffer components should be tuned based on protein interaction to be preserved.

F-actin binding protein stabilization buffer component	**Concentration**
Tris HCl, pH=7.0	10 mM
DTT	0.2 mM
MgCl2	2 mM
CaCl2	0.1 mM
EGTA	1 mM
ATP	1 mM

Table 7-3: Wu and Parsons[247] F-actin stabilization buffer. Used buffer to co-sediment F-actin from lysates of chick embryos w/ cortactin binding protein. Cells were lysed first in ice-cold buffer containing 2 mM Tris HCl, pH=8, 0.2 mM ATP, 0.5 mM DTT and 0.2 mM $CaCl_2$.

F-actin binding protein stabilization buffer component	**Concentration**
Tris HCl, pH=8.0	2 mM
DTT	0.2 mM
MgCl2	2 mM
CaCl2	0.2 mM
KCl	50 mM
ATP	1 mM

Table 7-4: F-actin stabilization buffer as prepared by Heacock[172].

Component	**MW (g/mol)**	**stock conc. (v/v%)**	**final conc. (M)**	**conc. v/v%**	**Amount, 500 mL buffer**	**unit**
Tris HCl (pH=7.5)	302.37	1 M	10 mM		5	mL
$MgCl_2$	95.211		0.002		0.0952	g
Triton X-100		100		1	5	mL
DTE	154.253		0.0002*		Add fresh to aliquot prior to assay	g
Water					490	mL

*EP cytometry fractionation assay typically uses 0.5 mM instead of 0.2 mM DTE (which is added to the buffer immediately before beginning an experiment as DTE is known to degrade in solution over time). pH is titrated to 7.4 upon buffer preparation.

In order to test the efficacy of the Heacock et. al. lysis buffer for EP cytometry complex fractionation, the lysis of MDA-MB-231 GFP actin cells upon gel lid-delivery of the buffer was imaged with fluorescence microscopy (Figure 7.3). GFP signal is lost from the microwell upon lysis owing to diffusion out of the open microfluidic device into the fluid layer between the separation gel and gel lid. Additionally, photobleaching will occur during imaging that contributes to fluorescence loss. However, substantial fluorescence is retained even up to 60s after lysis.

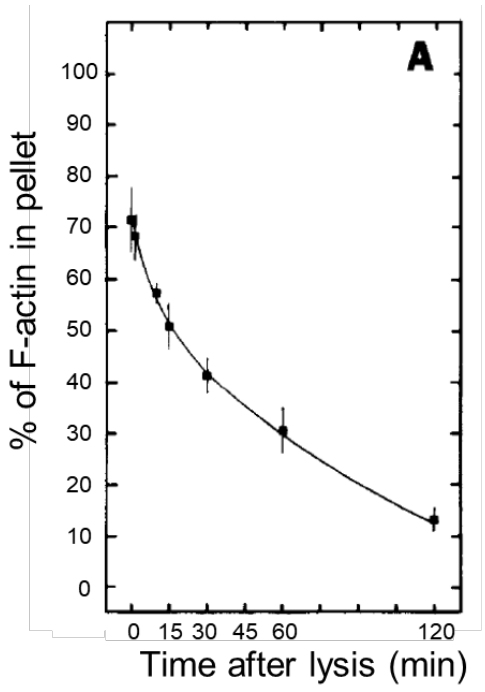

Figure 7.2: Quantifying F-actin levels upon lysis in an F-actin stabilizing buffer. Reprinted from Analytical Biochemistry, 135, C. S. Heacock and J. R. Bamburg, "*The quantitation of G- and F-actin in cultured cells*", 22-36 (1983)[172] with permission from Elsevier.

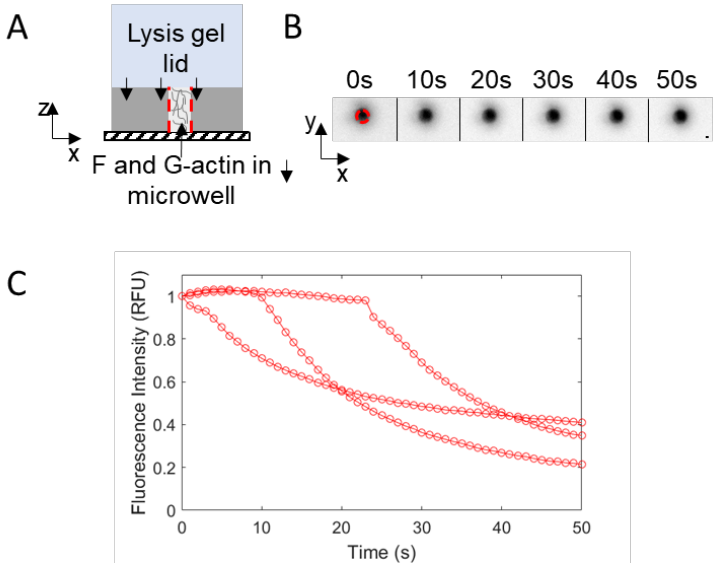

Figure 7.3: Cell lysis in an F-actin stabilization buffer. (A) Side-view schematic of gel lid delivery of the F-actin stabilization lysis buffer. (B) False-color fluorescence micrographs of single MDA GFP-actin cells in microwells (red dashed outline) upon lysis with an F-actin

stabilization buffer (lyses cell but retains F-actin). Scale bar is 10 microns. (C) Total fluorescence in the microwell normalized to initial in-well fluorescence as a function of lysis time for n=3 cells.

While the first stage of the assay requires stabilization of complexes, prior to electrophoretic fractionation, ultimately to quantify the F-actin levels, the complexes must be rapidly disrupted. In the bulk version of the assay, the time requirements of F-actin disruption are relaxed. However, to prevent substantial diffusive losses during a slow F-actin depolymerization step, and to mitigate injection dispersion owing to incomplete depolymerization prior to electrophoresis, a potent depolymerization buffer is needed.

We sought to identify specific detergents or denaturants that could drive rapid depolymerization. Notably, while several detergents can actually increase actin polymerization rates, CHAPS increases actin depolymerization rates several-fold[237]. Interestingly, the authors noted that at 3% CHAPS, they observed possible crosslinking of actin facilitated by the CHAPS detergent. Thus, formulations of a typical EP cytometry RIPA buffer containing 0.5% CHAPS were prepared. Furthermore, the technical datasheet for a commercially available bulk F/G actin assay states that the depolymerization buffer contains urea. Therefore, RIPA buffer containing 6.7 M urea was also tested. For this set of experiments, cells are lysed directly in the depolymerization buffer, and bidirectional EP was still performed.

The results of the RIPA control single-cell actin measurements with the modified buffers is shown in Figure 7.4, below. Interestingly, the CHAPS-containing lysis buffer yielded reduced injection dispersion but multiple actin bands were observed, potentially as a result of previously described actin crosslinking in CHAPS[237]. Finally, the urea-containing lysis buffer did in fact improve actin solubilization, with one clear actin band and a “shoulder”, which became less distinct with longer lysis time. Based on this experiment, we ultimately found the following buffer preparation was most effective at depolymerizing F-actin: RIPA control buffer is prepared at approximately 1.5x concentration (and stored for up to 2 weeks), such that urea can be added to buffer aliquots fresh immediately prior to the start of the experiment to yield a 1X RIPA (0.5% SDS, 0.25% sodium deoxycholate) with 8 M urea.

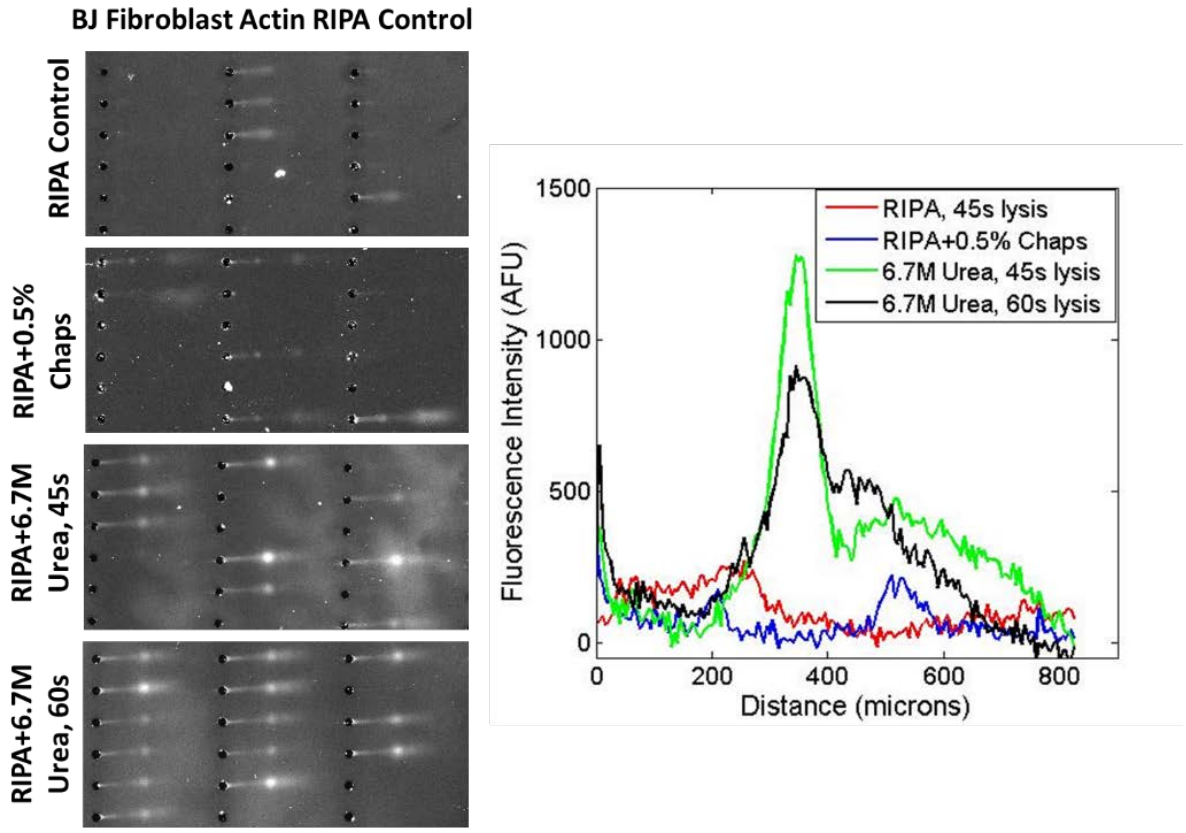

Figure 7.4: Representative fluorescence images and intensity profiles for actin from single BJ fibroblasts lysed with the specified buffer composition (via gel lid). Cells were lysed for 35s at 37C with a gel lid pre-incubated overnight in the specified buffer, electrophoresis was performed for 45s (30 V/cm), protein was photocaptured for 45s, the E-field was reversed and applied for 45s (30 V/cm), and protein was photocaptured again for 45s. Immunoprobing with a pan-actin antibody was conducted as described in the methods section.

Design of electrophoretic fractionation of F and G actin

A major technical challenge for EP cytometry complex fractionation is that the buffers that stabilize complexes are not inherently suitable for electrophoresis. The Heacock et. al. buffer formulation, in fact, has a buffer conductivity of 1.3 mS/cm, which is ~1.4-fold higher than the typical lysis buffer employed in EP cytometry[125]. Given the dependence of the heat flux ($\dot{Q}$) on conductivity (σ_c), more substantial Joule heating is expected in the F-actin stabilization lysis buffer:

$$\dot{Q} = \frac{(IR)^2}{L^2}\sigma_c H \qquad \text{Eq. 7.1}$$

where I is the current, R is the resistance, L is the distance between electrodes and H is the cross-sectional height of the conductor (in this case the separation gel and gel lid assembly height, Figure 7.5). One implication of Joule heating in this context is that protein complexes including

microtubules have been shown to disassemble above 45 °C[250]. Unsurprisingly, actin depolymerization rates also increase with temperature[251].

Thus, to offset the increase in conductivity and attempt to mitigate heating, the gel lid thickness is set to 0.5 cm (or ~4-fold lower than the typical cross-sectional height of the buffer layer in EP cytometry)[125]. Thus, upon measuring temperature during electrophoresis with a gel lid pre-incubated in F-actin stabilization lysis buffer, we find no autothermal runaway heating and the system remains stably near room-temperature (Figure 7.5).

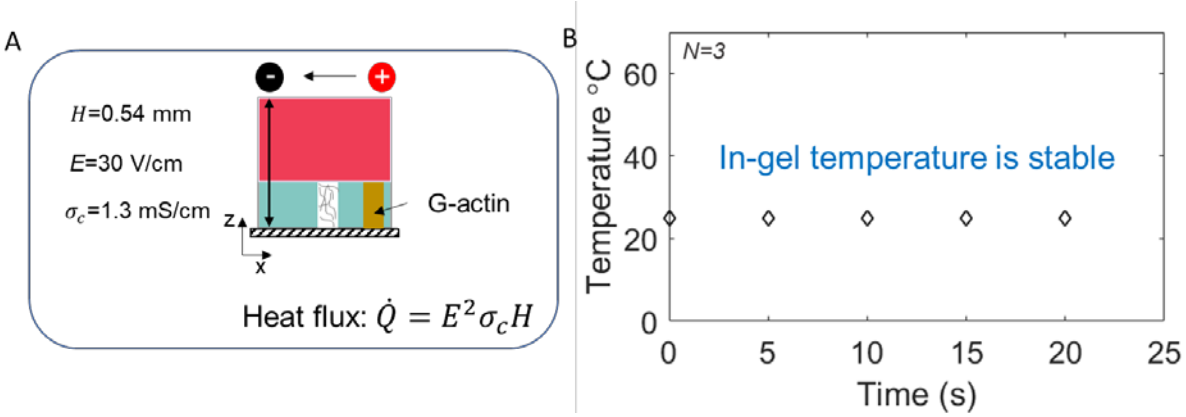

Figure 7.5: Heat is efficiently dissipated due to the high surface area-to-volume ratio of the gel lid assembly used in EP cytometry complex fractionation. (A) Side-view schematic of the EP cytometry device interfaced with the gel lid and parameters of the heat flux equation for the fractionation step. (B) Measurement of temperature as a function of electrophoresis time in the F-actin stabilization lysis buffer gel lid. The gel lid was interfaced with a liquid crystal temperature sensor, which indicated a constant temperature during electrophoresis at 30 V/cm.

We next aimed to test the hypothesis that F-actin could be electrophoretically fractionated from monomeric, G actin in a polyacrylamide gel. The average F-actin complex is ~2700 kDa. Previous native-PAGE experiments electrophoresing proteins of similar size in an 8%T gel at 35 V/cm yielded negligible electrophoretic mobilities[252]. Though actin oligomers of various sizes exist, the subunit unbinding rates are many orders of magnitude higher for dimers and trimers[253]. Consequently, dimers and trimers are expected to be present at very low levels at any given time in the cell. In order to assess the actin species fractionated in EP cytometry complex fractionation we performed fluorescence microscopy during electrophoresis of single cell lysates from MDA-MB-231 GFP-actin cells and U20s RFP-LifeAct cells (Figure 7.6). In the former, all beta actin is GFP-tagged (whether F or G-actin), while in the latter, the RFP-LifeAct peptide binds only to F-actin[227]. While some GFP-actin electrophoretically injects into the 8%T fractionation gel, a substantial proportion of actin remains in the microwell. We hypothesized this species was F-actin and repeated the imaging experiment during electrophoresis of the F-actin fluorescent U20s RFP-LifeAct cells (Figure 7.6). In contrast, no fluorescent actin (F-actin in this case) enters the gel, but rather it electromigrates to the microwell edge. Thus, we confirm that F-actin is selectively retained in the microwell and electrophoretically fractionated from monomeric G-actin. We also provide further evidence that supports

As an additional consideration for attaining reproducible electrophoretic fractionation with minimal intra assay variation in electromigration, we assessed methods for pre-equilibrating the fractionation gel in buffering species before interfacing the gel lid for electrophoresis (Figure 7.8). In the first method, a small volume of buffer is pipetted over the top of the array, while in the second, the entire gel is briefly submerged in buffering species (in both cases the buffer does not contain any detergents and exposure is ~30s before introducing the gel lid). In both approaches, injected GFP-actin peaks are visualized. Quantifying the peak widths and locations across replicates, we find that pipetting the buffer on the surface resulted in run-to-run variation in peak location (Figure 7.8), while higher intra-assay variation in peak location occurs with submerging the array. Given that the complex fractionation assay is intended to compare actin levels in control cells versus cells subjected to stimuli, minimal run-to-run variation is critical, and thus we employ the submerging method to pre-equilibrate the array in buffering species prior to gel lid interfacing.

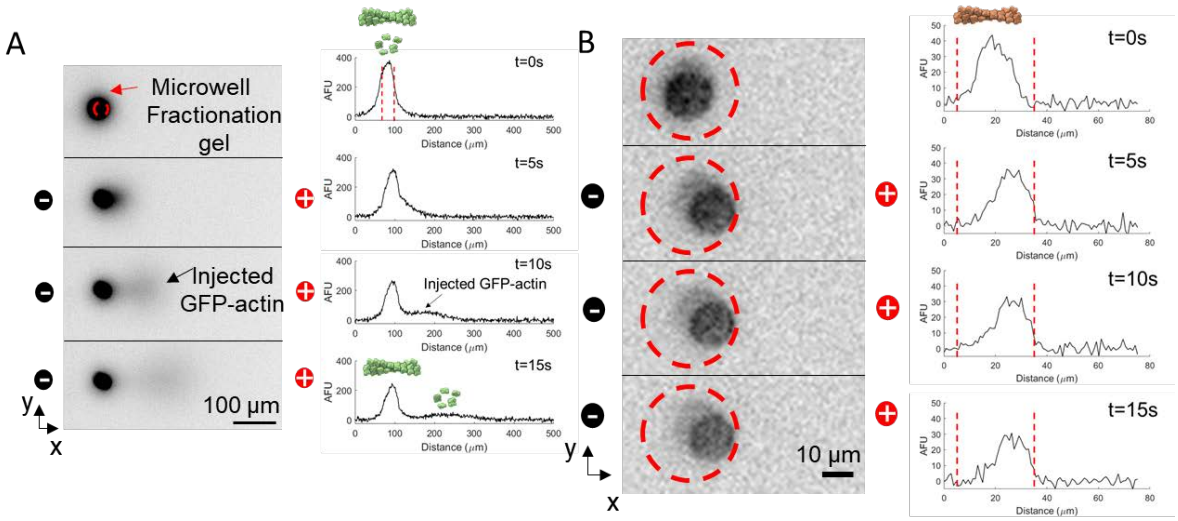

Figure 7.6: Imaging fluorescent actin species during electrophoresis confirms that F-actin is fractionated in the microwell during electrophoresis in F-actin stabilization buffer. (A) False-color fluorescence micrographs and corresponding intensity profiles during electrophoresis (30 V/cm) of MDA GFP-actin cell lysates (all actin is fluorescent) in F-actin stabilization buffer. (B) False-color fluorescence micrographs and corresponding intensity profiles during electrophoresis (30 V/cm) of U20s RFP-Lifeact cell lysates (only F-actin is fluorescent) in F-actin stabilization buffer.

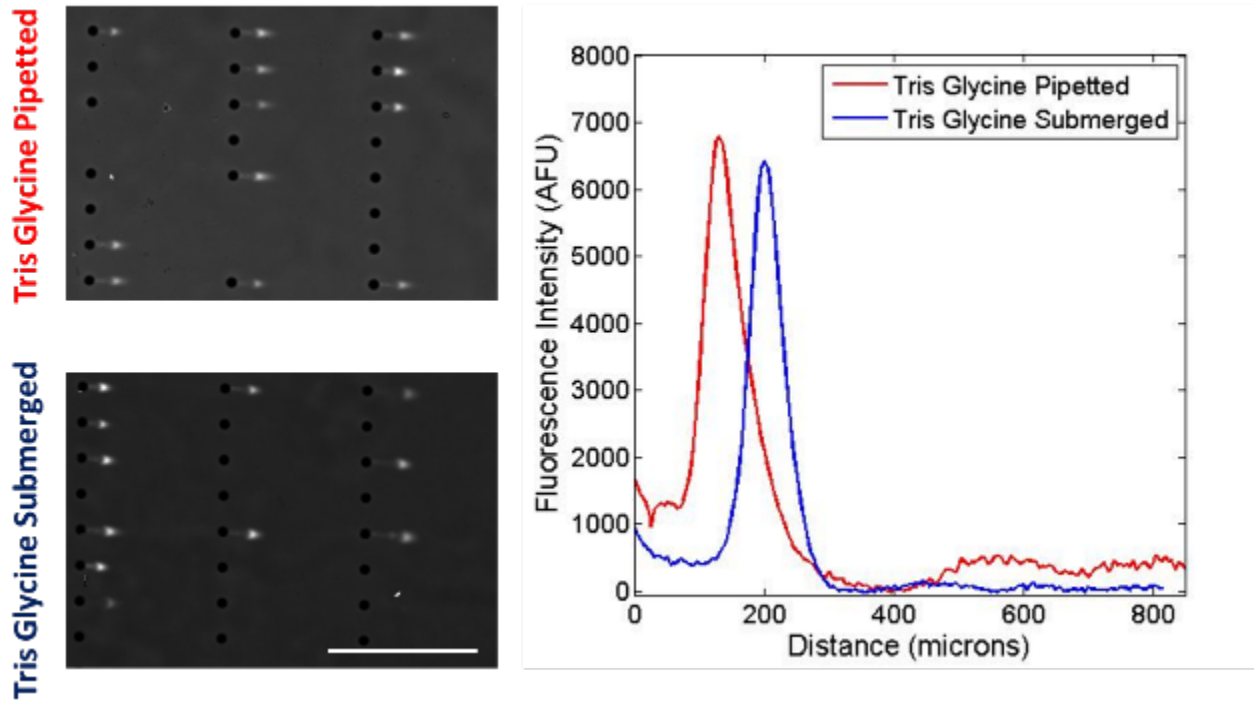

Figure 7.7: Fluorescence micrographs and representative intensity profiles of MDA GFP-actin cells lysed for 30s by 0.5% RIPA gel lid, followed by electrophoresis at 30 V/cm (1 min), UV photocapture, electrophoresis in the opposite direction at 30 V/cm (1 min) and UV photocapture. Two methods for exchanging PBS with tris glycine before gel lid interfacing with the separation gel are assessed (tris glycine pipetted over separation gel, or separation gel briefly submerged in a dish of tris glyine). Scale bar is 1 mm.

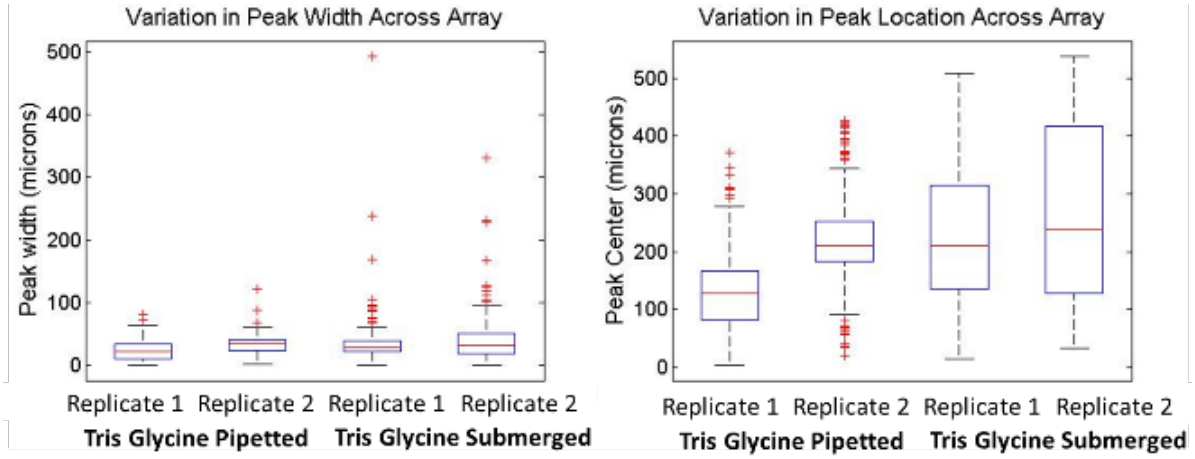

Figure 7.8: Quantitation of peak width and peak location with two strategies for rapid buffer removal of PBS with the separation buffer prior to gel lid introduction (tris glycine pipetted over separation gel, or separation gel briefly submerged in a dish of tris glyine). Peak width for tris-glycine pipetted gels (n=190, 2 outliers, replicate 2: n=299, 3 outliers). Peak width for tris-

glycine submerged gels (replicate 1: n=197, 17 outliers, replicate 2: n=127, 11 outliers). Peak location for tris-glycine pipetted gels (replicate 1: n=190, 9 outliers, replicate 2: n=299, 36 outliers). Peak Location for tris-glycine submerged gels (replicate 1: n=197, 0 outliers, replicate 2: n=127, 0 outliers).

EP cytometry complex fractionation assay integration and validation

Integrating the gel lid delivery, bi-directional separations, photoimmobilization and immunoprobing for GFP-actin, we demonstrate the capability to isolate and detect complexes versus monomeric protein in hundreds of single cells (Figure 7.9). We achieve high assay throughput and quantitative accuracy that does not suffer from challenges associated with cell segmentation as in staining-based methods.

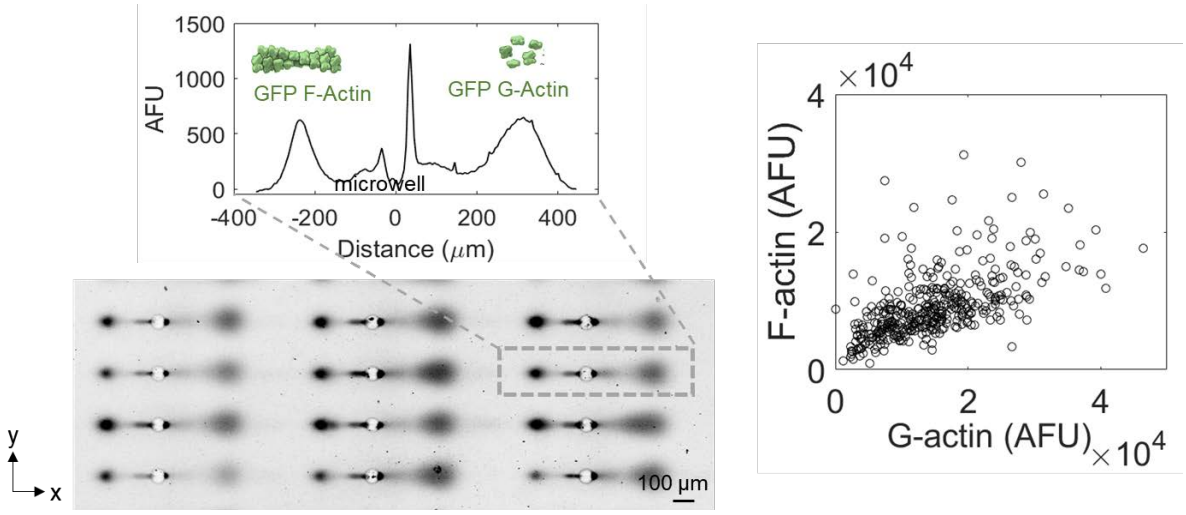

Figure 7.9: Actin complexes can be stabilized, fractionated, and quantified in a single micro-scale device. Left: representative false-color fluorescence micrographs and intensity profiles of GFP F and GFP G-actin from single MDA-MB-231 GFP-actin cells (scale bar is 100 microns). Right: scatter plot of F and G actin from hundreds of single-cell protein complex separations.

In order to further validate the assay, we sought to quantify F-actin levels upon drug treatment with Latrunculin A (LatA), which destabilizes F-actin[254]. Previously, others reported the ratio of F versus G actin fluorescence reduced by a factor of two upon LatA (1 μM, 60 min) treatment by quantitative imaging of F-actin staining (by phalloidin) and G-actin staining (by DnaseI) in lymphocytes [255]. Neurons treated with LatA for 24 hrs, and then allowed to recover for 24 hours display re-polymerization of F-actin[256], and thus LatA treatment is reversible. However, there is little information recovery on the timescale relevant EP cytometry (~30 min potential recovery time during trypsinization and cell settling). Thus, we included experimental conditions that mimic EP cytometry in a staining study. We qualitatively assessed the effect of LatA on the MDA-MB-231 GFP-actin cells by treating the cells with the drug and then fixing, permeabilizing and staining the cells with fluorescently-labeled phalloidin (a small molecule that binds to F-

actin). Cells were stained either as adherent cells (Figure 7.10) or in suspension (Figure 7.11) in attempts to mimic the cell handling for the EP cytometry complex fractionation assay. In both instances, treatment with 2 μM LatA led to reduced F-actin fluorescence.

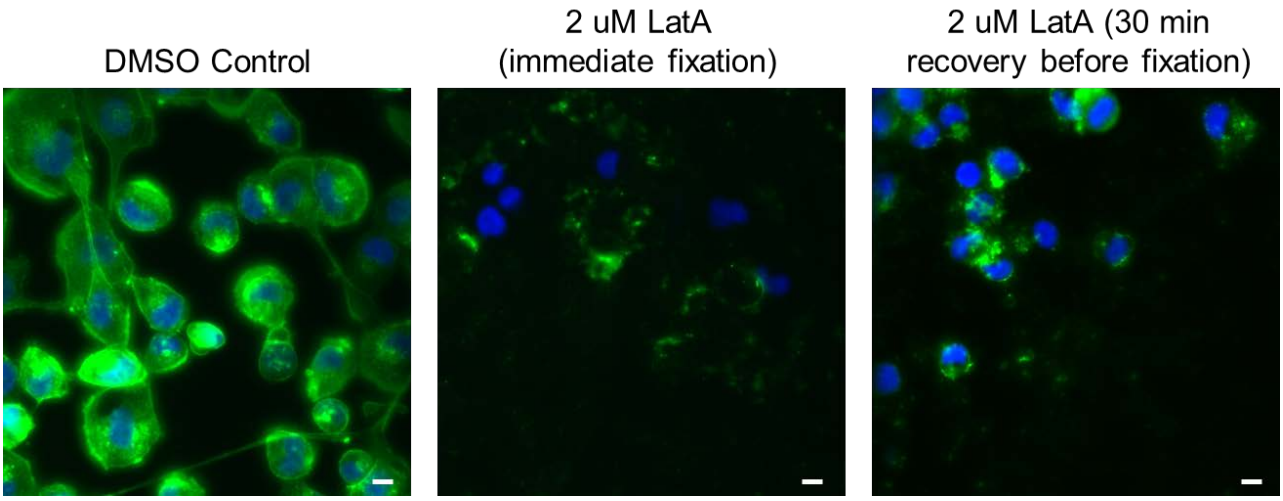

Figure 7.10: False-colored fluorescence micrographs of adherent MDA-MB-231 GFP-actin cells treated with the indicated reagents, fixed, permeabilized and stained for Hoescht (blue, nucleus) and phalloidin (green, F-actin). All cells were incubated for 30 min in either 0.1% DMSO (DMSO control) or 2 μM LatA in 0.1% DMSO. Cells were either immediately fixed after treatment (DMSO control and immediate fixation), or after 30 min of recovery in cell media in the humidified, heated incubator (30 min recovery before fixation). Scale bar is 10 microns. All images are contrasted identically and were collected with a 40x objective (200 ms exposure for the Hoescht image, and 800 ms for the phalloidin channel).

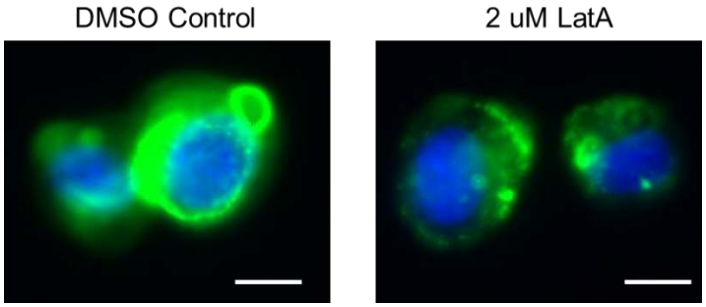

Figure 7.11: Representative false-colored fluorescence micrographs of MDA-MB-231 GFP-actin cells in-suspension treated with the indicated reagents (30 min in incubator, while cells were adherent), trypsinized, incubated 30 min in 1X PBS at room temperature, fixed, permeabilized (mimics cell handling prior to the single-cell actin separations) and stained for Hoescht (blue, nucleus) and phalloidin (green, F-actin). Scale bar is 10 microns.

Having established that the drug treatment results in appreciable loss of F-actin from the staining experiments even with cells in suspension, we carried out EP cytometry complex fractionation

with the GFP-actin cells. As shown in Figure 7.12, the F-actin ratios were highly similar in the drug treated cells versus the 0.1% DMSO vehicle control-treated cells (Mann-Whitney U-test p-value of 0.4274). This lack of a difference between the drug treated and control cells was surprising given the observed staining results and literature precedent. One hypothesis that explains the disagreement between the staining and separation data is that the cells express both GFP-actin and untagged actin, and that the drug is binding to the untagged actin, resulting in staining images that reflect the effect of the drug on the untagged actin, while the separations specifically show the GFP-actin fractions (since GFP immunoprobing for GFP-actin is performed). The GFP-expressing cells were generated by zinc finger nuclease editing that results in a GFP fusion on beta actin, as described previously by the Drubin lab[257]. Furthermore, not all beta actin may be fused to GFP, as has been described by other groups (in which the GFP-expressing proteins were present at levels ~1000-fold lower than typical endogenous actin)[258].

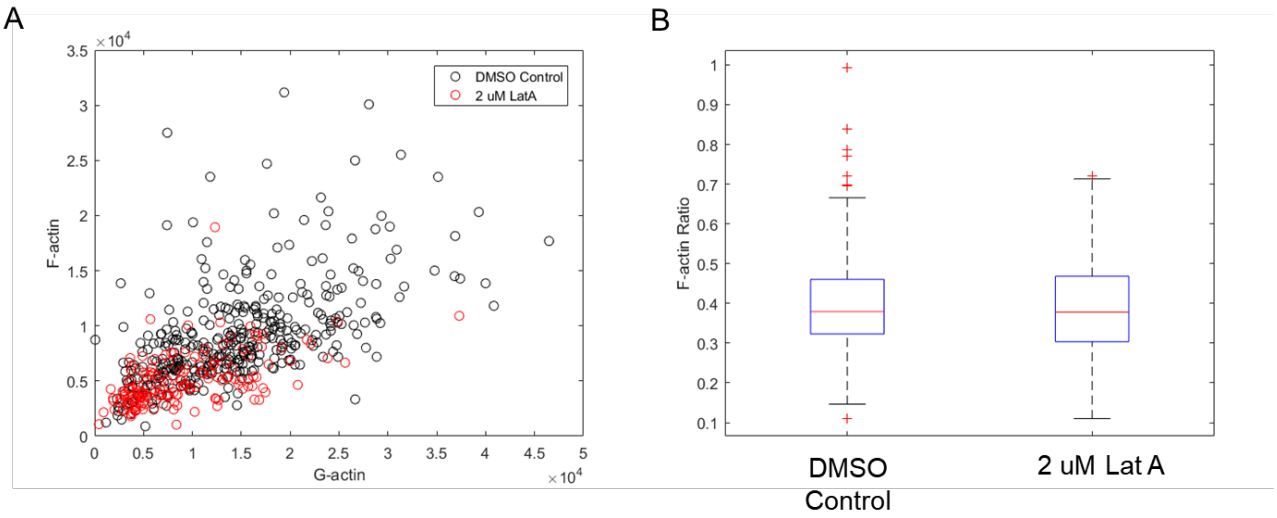

Figure 7.12: Quantifying F and G actin in single-cell F and G actin separations of MDA-MB-231 GFP-actin cells treated with either 2 μM LatA or DMSO vehicle control (0.1% DMSO). (A) Scatter plot of F-actin vs. G-actin in n=383 single-cells for the DMSO control, and n=162 cells for LatA-treated cells. (B) Quantification of the F-actin ratio (F-actin divided by total actin from each single-cell). P-value for the Mann-Whitney U-test is 0.4274.

In order to mitigate potentially confounding effects of performing the validation drug treatment with the GFP-actin cells, the staining (Figure 7.13 and Figure 7.14) and separations (Figure 7.15) were repeated with BJ fibroblasts that express unmodified actin. Again, the staining qualitatively suggests substantial F-actin destabilization. Furthermore, from the separations, we observe a statistically significant decrease in the F-actin levels upon LatA treatment (Mann-Whitney U-test p-value=0.005). Consequently, we anticipate being able to assess the effect of other stimuli with unknown effects on F-actin complexes with EP cytometry complex fractionation.

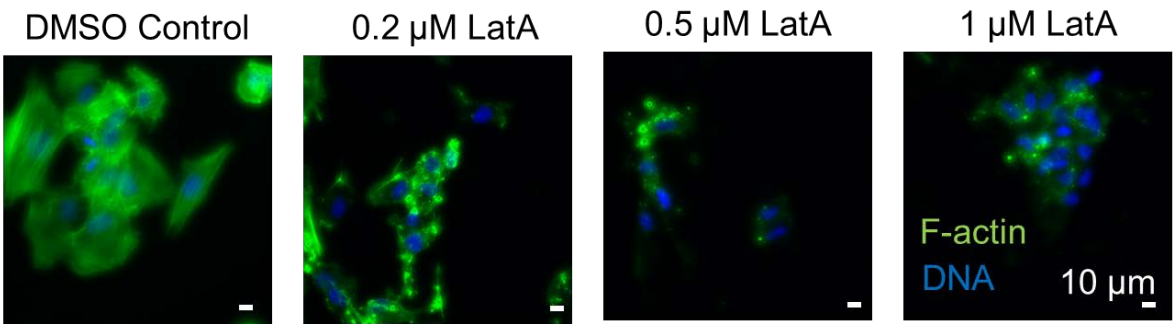

Figure 7.13: Visualizing F-actin destabilization in Latrunculin A (LatA). False-color fluorescence micrographs of BJ fibroblast cells phalloidin-stained for F-actin (green), and nuclear-stained (blue) in the presence of varying levels of LatA.

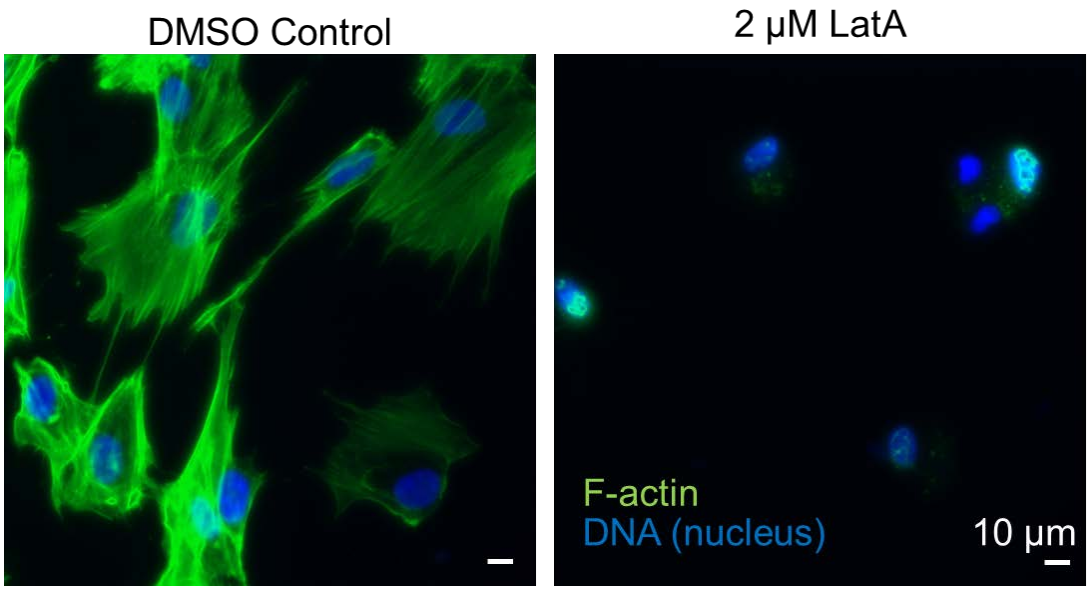

Figure 7.14: Visualizing F-actin destabilization at high LatA concentrations. False-color fluorescence micrographs of BJ fibroblast cells phalloidin-stained for F-actin (green), and nuclear-stained (blue) in the presence of varying levels of LatA. Cells were imaged with a 40x objective.

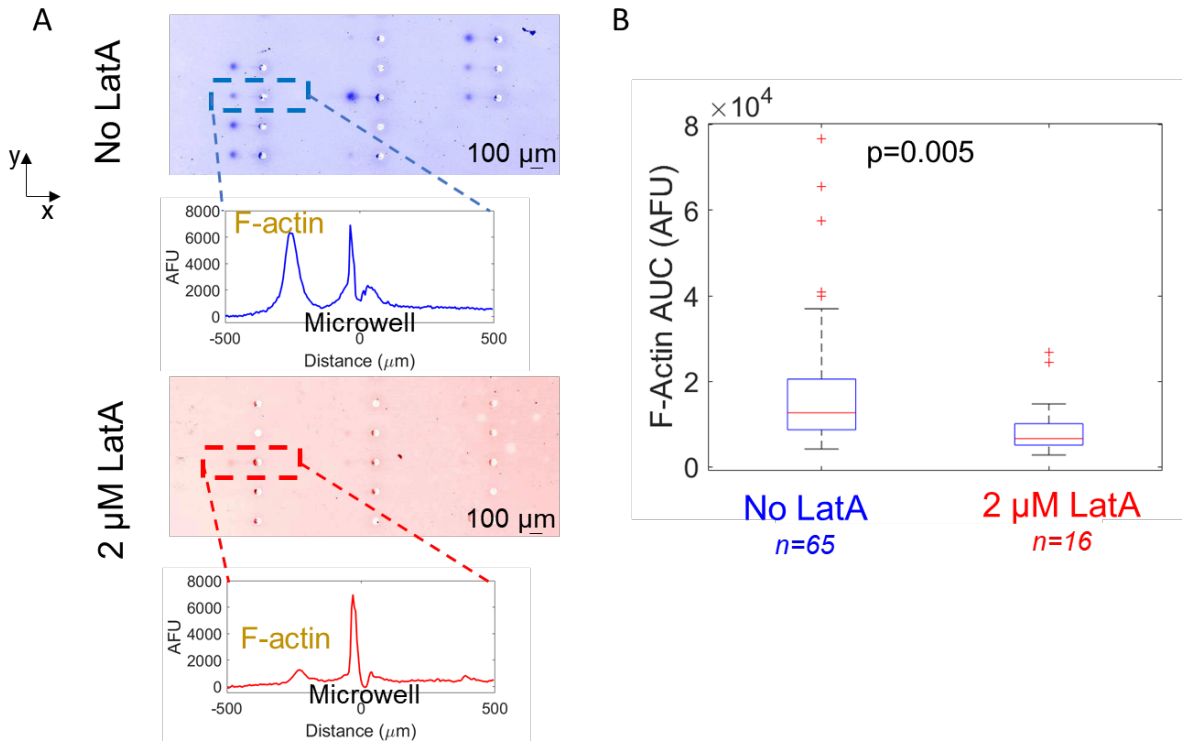

Figure 7.15: F-actin destabilizing drug treatment with LatA validates EP cytometry complex fractionation assay. (A) False-color fluorescence micrographs and representative intensity profiles of EP cytometry complex fractionation with cells treated with LatA or DMSO vehicle control. Depolymerized F-actin is electromigrated left of the microwell. (B) Box plots quantifying the F-actin area-under-the-curve. Mann-Whitney U-test p-value=0.005.

EP cytometry complex fractionation assesses effects of a drug known to compete with phalloidin for F-actin binding

As F-actin maintenance is a goal for novel cancer therapeutics aimed at altering migratory behavior of invasive cells, assays capable of determining the effects of such drugs on F-actin in subpopulations of cells are needed. In vitro, the drug Jasplakinolide was shown to stabilize F-actin, while staining with phalloidin resulted in apparent lower levels of F-actin. Bulk biochemical assays supported the in vitro findings as a significant increase in F-actin resulted upon incubation of 0.1 µM jasplakinolide with HEK293 cells for 30 min[259], and 10 min incubation of 0.3-1 µM jasplakinolide with MCF7 cells (as determined by a bulk F to G-actin ratio assays)[260]. Bubb et al. showed that jasplakinolide competitively binds with phalloidin for F-actin using in vitro biochemical assays of phalloidin fluorescence upon incubation with F-actin and varying levels of Jasplakinolide. The measured K_D was ~15 nM for jasplakinolide versus ~40 nM for phalloidin[231]. There was no evidence that phalloidin and jasplakinolide competed for the same binding site. In a later publication, Bubb et al. argue that changes in cellular architecture (not just phalloidin fluorescence) could not be explained by competitive binding. Detailed biochemical assays determined that jasplakinolide lowers the number of actin subunits

in an oligomer for filament nucleation from 4 to 3, and the authors suggested this might result in disordered aggregates[261]. Therefore, there is substantial disagreement in the literature regarding the effect of jasplakinolide on F-actin levels. We aimed to address the discrepancy in previous findings with EP cytometry complex fractionation.

Drug treatment effects on F-actin were assessed both by staining (Figure 7.16) and EP cytometry complex fractionation (Figure 7.17). Both result in decreased F-actin levels, with a Mann-Whitney U-test p-value = $3x10^{-10}$ from the quantified F-actin area under the curve from EP cytometry complex fractionation. Thus, the results attained here corroborate the staining (in spite of competitive binding artifacts) and support the work of Bubb et al. in which the authors argue that filament nucleation is altered with jasplakinolide treatment. Consequently, the assay presented here can provide additional quantitative insight when staining results alone are confounded.

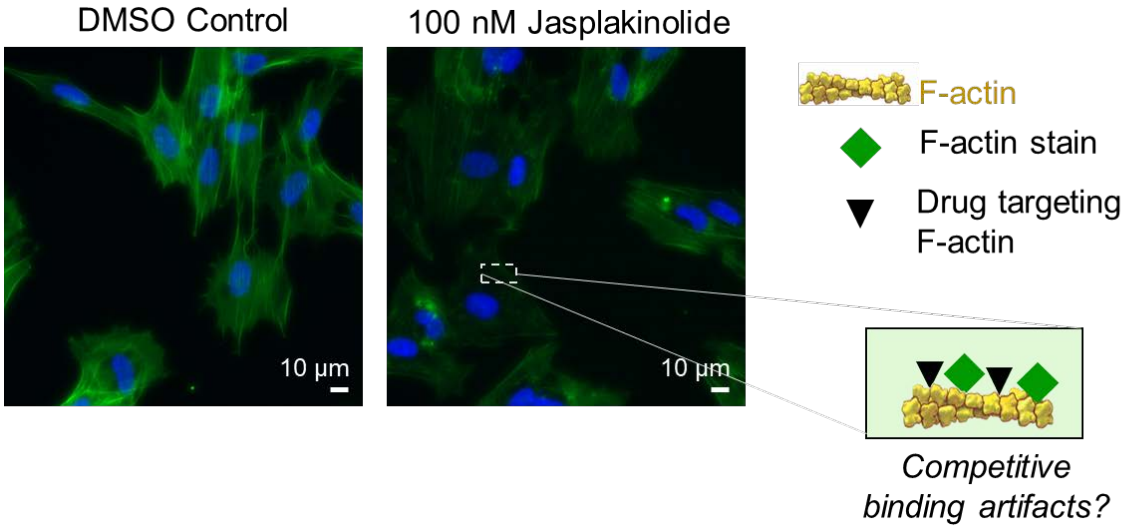

Figure 7.16: False-color fluorescence micrographs of BJ fibroblasts stained with phalloidin after treatment with 100 nM Jasplakinolide (2 hours at 37 °C) or control (addition of 0.1% DMSO to cell media at 37 °C. Right: schematic diagram of competitive binding between the drug and phalloidin that may explain lower F-actin fluorescence in drug-treated cells.

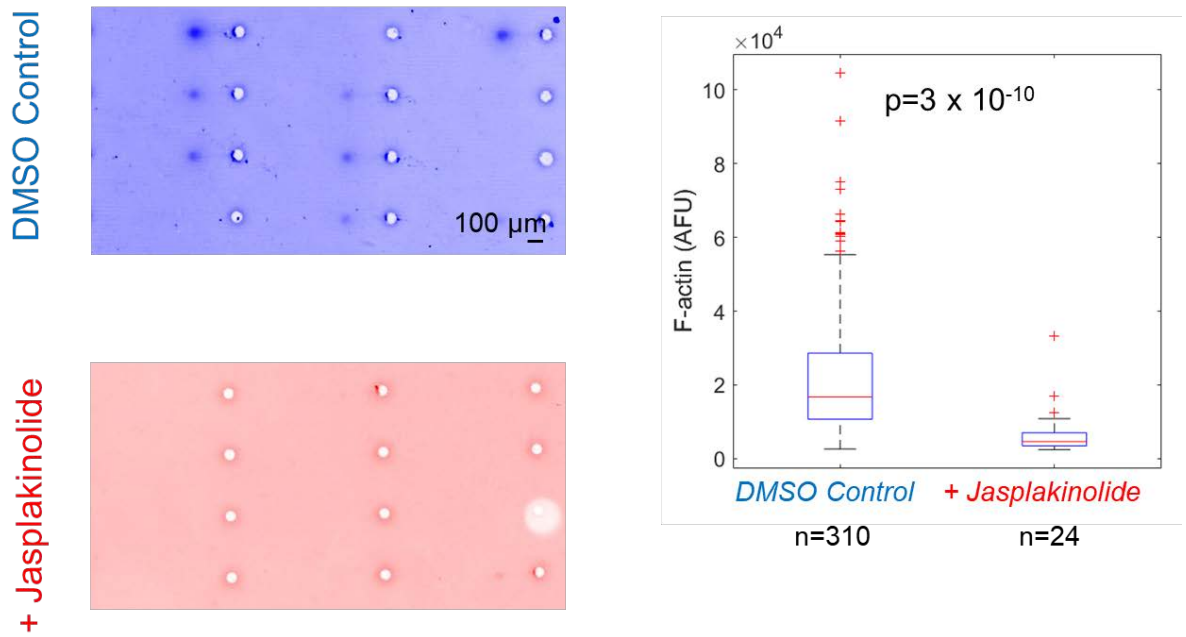

Figure 7.17: False-color fluorescence micrographs and boxplots of F-actin area-under-the-curve for BJ fibroblasts that were with jasplakinolide (100 nM for 2 hours). Mann-Whitney U-test p-value=$3x10^{-10}$.

Extending EP cytometry complex fractionation to other actin protein complexes

Over 160 actin binding proteins regulate the dynamic polymerization and depolymerization of actin in the cell (not including isoforms)[223]. Assessment of binding protein function is generally performed with bulk sedimentation assays or fluorescence imaging (where binding is inferred by colocalization), neither of which is well suited for high-throughput single-cell analysis. Thus, we sought to demonstrate that the fractionation assay can be adapted to measure actin binding proteins. F-actin binding proteins were considered based on their cellular localization (cytoplasmic according to UniProt) and expression levels to be detectable by EP cytometry[26] (many are present at ~1,000,000 copies or higher per cell). For proof-of-principle, we detect the level of F-actin bound vinculin, a focal adhesion protein (Figure 7.19). Run-to-run variation in the F-actin bound fraction of vinculin may be attributable to variable injection of the unbound vinculin (to the left of the microwell). Thus, further optimization of separation conditions are required before being able to assess the correlation between the bound fraction and the F-actin levels in the cell. Finally, as vinculin is involved in focal adhesions, questions arise as to whether the sample preparation employed here would appreciably maintain vinculin complexes, as we trypsinize the cells.

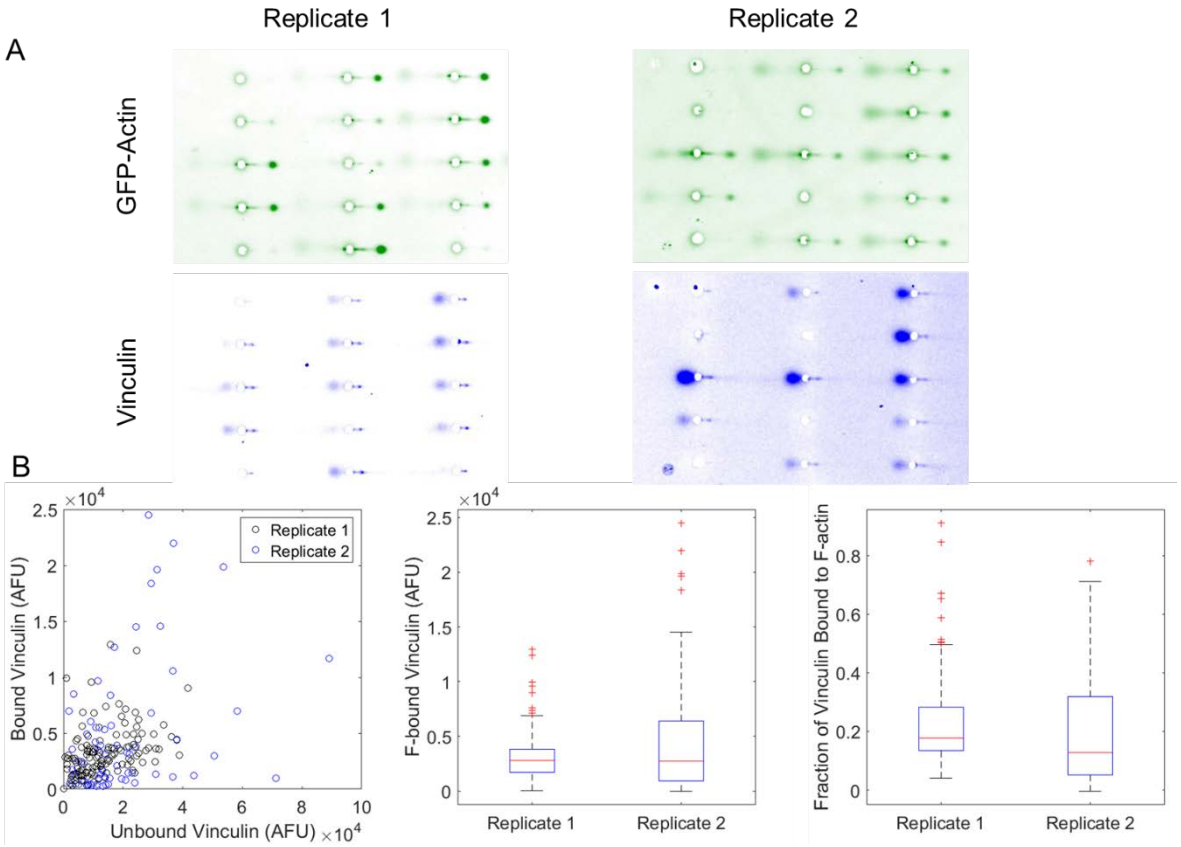

Figure 7.18: Quantifying F-actin binding protein complexes from single cells. (A) False-colored fluorescence micrographs of two replicate separations of GFP-F/G actin (green) and vinculin (F-actin binding protein, ~120 kDa; blue) from MDA-MB-231-GFP actin cells. Cells were lysed for 45s with F-actin stabilization lysis buffer, EP was performed for 75s at 30 V/cm, and G-actin was UV-immobilized for 45s. F-actin was then depolymerized in-well for 45s in RIPA+8M urea depolymerization buffer (EP and UV performed as for the G-actin with EP in the opposite direction for 75s (30 V/cm). The F-actin bound fraction is located right of the microwell. (B) Left: scatter plot of the bound versus unbound vinculin. Middle: boxplot of the F-actin-bound vinculin fraction (Mann-Whitney p-value 0.7186). Right: boxplot of fraction of vinculin bound to F-actin (Mann-Whitney p-value is 0.0094).

Altering the cellular microenvironment: effects of trypsinization and stress

Given the sensitivity of actin remodeling to chemical environment, it is important to evaluate whether steps in our assay such as cell trypsinization and settling in suspension dramatically alter the distribution of F/G actin. One study found that trypsinization did not lead to changes in total phalloidin-stained F-actin fluorescence, but introducing Ca^{2+} containing media led to 4-fold decreases in F-actin fluorescent signal (in XTH-2 cells).[262] In contrast, another group found that trypsinization led to a 25% increase in the ratio of F-actin (FITC-phalloidin staining) to G-actin (rhodamine-DNAse I fluorescence) in HGF and HPLF cells even accounting for changes in cell area upon trypsinization[230]. The effects of long-term suspension of adherent cells were studied and found to increase F-actin (Alexa-546 phalloidin stained) measured when adherent CHO cells

were cultured in suspension (approximately 2-fold higher F-actin)[263]. Additionally, trypsin is known to disrupt stress fibers[264].

Results of separations performed with replicates at specific cell settling times support the hypothesis that the amount of time post-trypsinization prior to lysis impacts the measured F-actin ratio. Experiments should be performed with constant cell handling times (e.g. trypsinization, and cell settling), minimizing the cell settling time. A set of replicates with only 10 minutes of cell settling time yielded consistent F and G actin levels upon performing separations, but varied as function of time post-trypsinization, as shown in Figure 7.19, below.

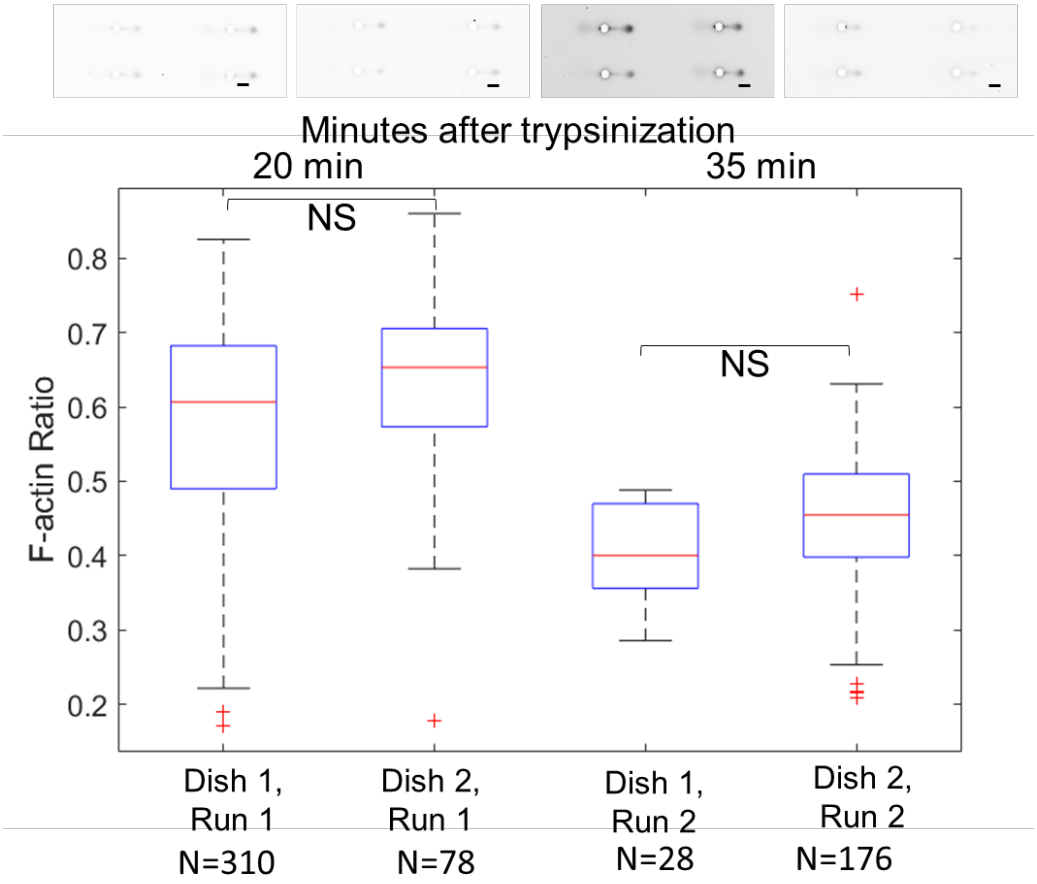

Figure 7.19: Quantitation of the F-actin ratio (F/F+G) and representative micrographs for MDA-MB-231 GFP actin for replicates performed from two dishes of cells with two runs (1st run was 20 min after trypsinization, 2nd run was 35 min after trypsinization). Kruskall-Wallis p-value $3.3e^{-38}$; Dunn's post-hoc test p-values were 0.089 (Dish 1 run 1 and Dish 2 run 1), 0 (Dish 1 run 1 and Dish 1 run 2), 0 (Dish 1 run 1 and dish 1 run2), 0 (Dish 2 run 1 and Dish 1 run 2), 0 (Dish 2 run 1 and Dish 1 run2) and 0.31 (Dish 1 run 2 and Dish 2 run 2). NS=not statistically significant.

Cytoskeletal reorganization is a hallmark of disease states[218], aging and cellular stress[265], and thus we aim to investigate the effect of heat shock on relative levels of F and G actin with EP cytometry complex fractionation. Through initial cell staining experiments (Figure 7.20 and Figure 7.21) we sought to identify a heat shock condition that would dramatically alter the F-actin levels in the cell and selected a 90-minute heat shock at 45 °C. However, we found that the heat shocked cells displayed marked changes in morphology that would prevent the cells from being settled into microwells (Figure 7.22). Consequently, we investigated altering the EP cytometry fractionation protocol to be able to assay adherent cells that could be heat shocked directly in the microwell.

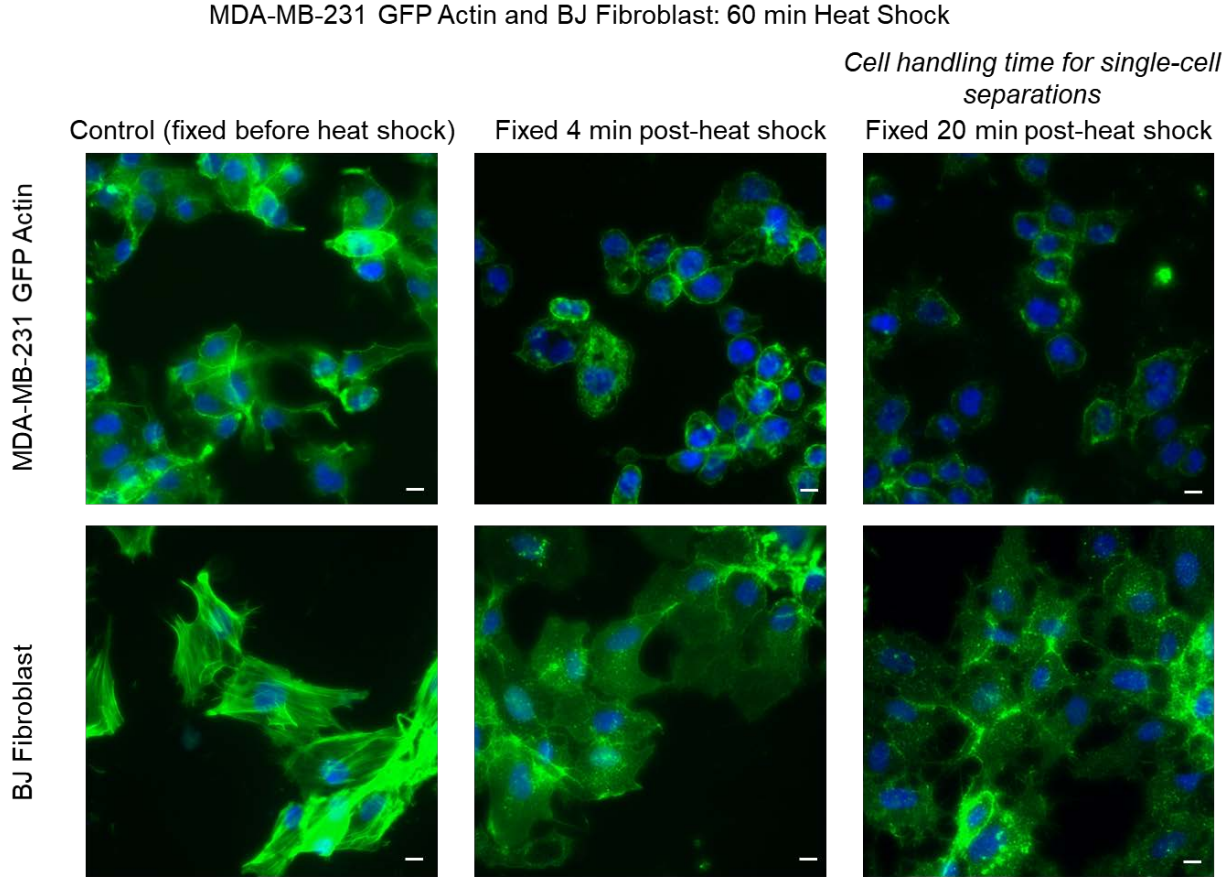

Figure 7.20: False-color fluorescence micrographs of adherent MDA-MB-231 GFP-actin and BJ fibroblast cells fixed and stained for F-actin (phalloidin, green) and the nucleus (Hoescht, blue) before or after heat shock (45C for 60 min). Scale bar is 10 microns.

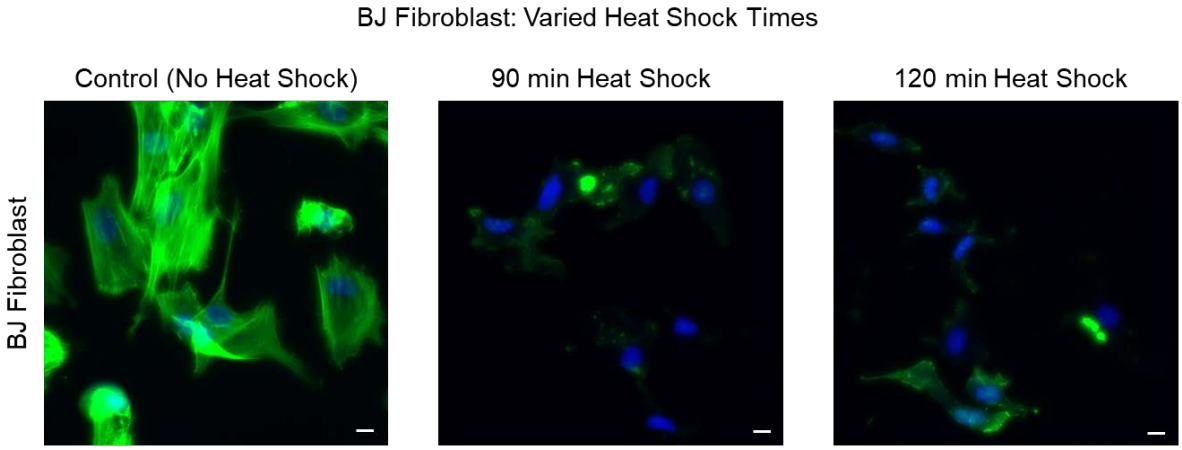

Figure 7.21: False-color fluorescence micrographs of adherent BJ fibroblast cells fixed and stained for F-actin (phalloidin, green) and the nucleus (Hoescht, blue) with varying heat shock (45 C) times. Scale bar is 10 microns.

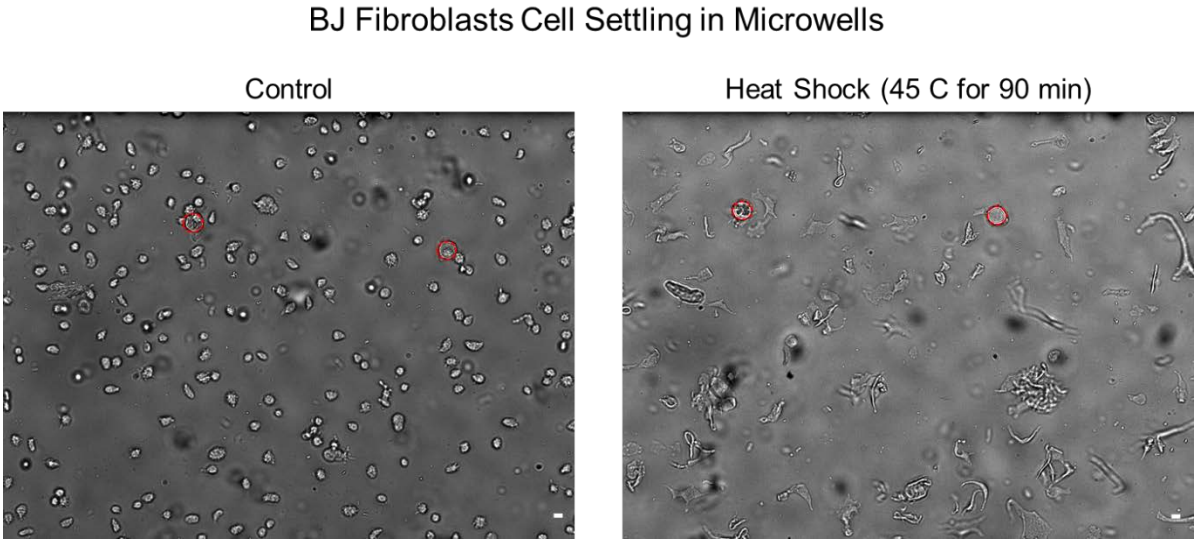

Figure 7.22: Dramatic morphology changes visible by brightfield microscopy upon heat shock prevents settling of cells in microwells. Left: Control BJ fibroblast cells in suspension on a microwell array (wells outlined in red) in polyacrylamide gel. Cells were kept at 37C prior to trypsinization and 10 min of settling. Right: Heat shocked BJ fibroblast cells in suspension (45C for 90 min) prior to trypsinization and 10 min of settling. While cell debris settles in cells, the elongated morphologies prevent cell setting in the microwells. Cells are imaged at 4x.

Towards controlling the cellular microenvironment: adherent cell complex fractionation

In order to eliminate F-actin re-organization from trypsinization, measure heat shocked cells, and understand how vinculin binding relates to F-actin levels, we sought to establish EP cytometry complex fractionation of adherent cells. We modified existing protocols for patterning cells on polyacrylamide substrates[266], in order to fabricate a base layer of polyacrylamide with the

extracellular matrix protein fibronectin in the gel. On top of the base layer, we then fabricate the microwell array in polyacrylamide gels. Using this protocol, we attain cells with spread morphology and distinct F-actin networks upon culturing the cells overnight on the base polyacrylamide layer with fibronectin (Figure 7.23). In a proof-of-concept demonstration, cells were settled into large 100-micron diameter wells (resulting in some multi-cell wells), and allowed to adhere and culture overnight. We then carried out the EP cytometry complex fractionation assay and observed distinct F-actin bands from the wells that contained cells. In the future, this protocol will be further optimized to attain high single-cell well occupancy by lowering the starting seeding density of cells and decreasing the microwell diameter.

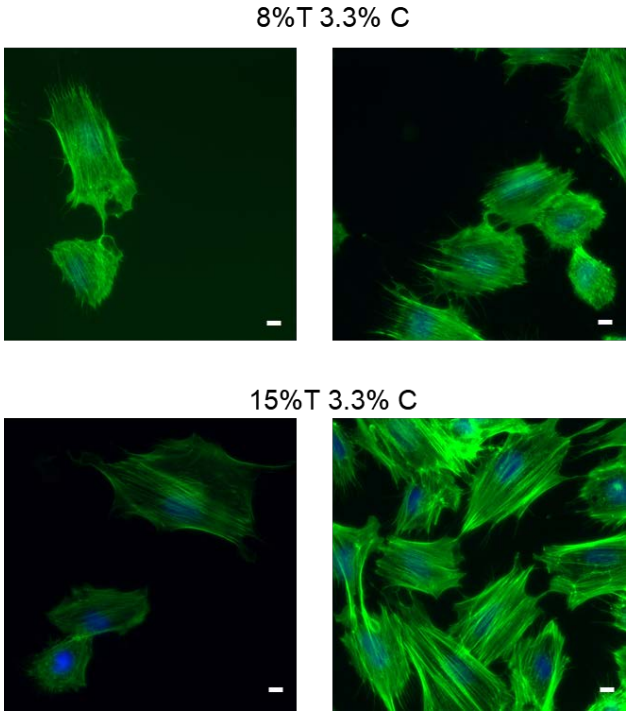

Figure 7.23: False-color fluorescence images of phalloidin (F-actin) staining of BJ fibroblasts on polyacrylamide gel of the specified densities. Thin (80-micron) gels were photopolymerized on top of silanized glass with precursor containing 10 μg/mL fibronectin and 3 mM BPMAC. Gels were sterilized with ethanol (30 min) and incubated in 1X PBS before trypsinized cells were added to the gel, allowed to attach for 1 hour and rinsed in media before overnight culture (~17 hours). Cells were fixed in 3.7% PFA, permeabilized with 0.1% Trition X-100 and stained with Alexa-fluor 647 phalloidin. Images were collected with a 40X objective through a glass slide (with the PA gel with cells placed gel-side down on the glass slide). Scale bar is 10 microns.

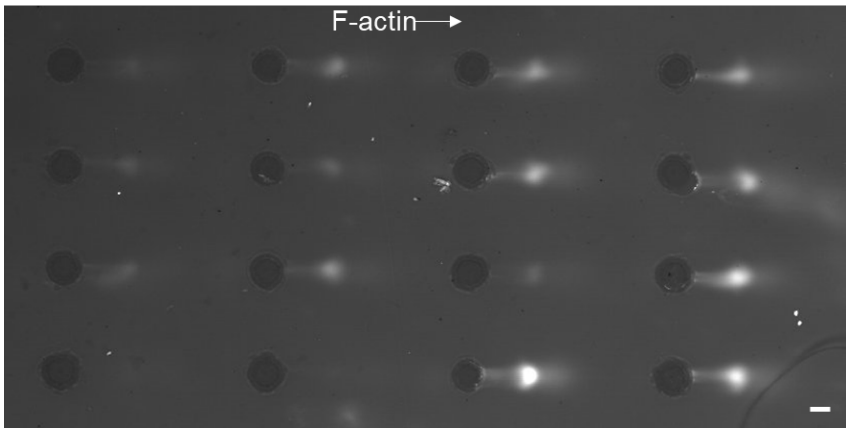

Figure 7.24: False-color fluorescence micrograph of separations of actin from BJ fibroblasts cultured in the 100-micron diameter wells. Immediately prior to beginning the complex fractionation assay, the gel was rinsed in PBS, followed by 1X Tris HCl. Cells were lysed by gel lid delivery of F-actin stabilization lysis buffer (45s), EP was performed for 45s at 30 V/cm, and protein was photo-immobilized. The gel lid was replaced with a lid containing RIPA+8M urea for 45s of F-actin depolymerization prior to 45s EP in the opposite direction and UV immobilization. The separation gel was washed overnight in 1X TBST, and immunoprobed for 4 hours with a 1:5 dilution of rhodamine-labeled anti-actin Fab before two 30-min washes in 1X TBST. Scale bar is 100 microns.

Detection of native endogenous G-actin by immunoprobing

In the data presented thus far, there is a surprising lack of G-actin signal upon separations of endogenous actin (i.e., not GFP-actin). Two hypotheses could account for the lack of G-actin signal: i) the G-actin fraction not sufficiently abundant for detection; and ii) the antibody binding epitope is not accessible when G-actin immobilized in gel in native state (either due to protein conformation or association with binding proteins).

Considering the first hypothesis, literature estimates, coupled with our knowledge of approximate losses of protein during various stages of the assay suggest there should be sufficient G-actin for detection. First, previous reports found for mouse embryonic fibroblast the G/F ratio ~0.6, so ~30% of the total actin is G-actin.[267] If we conservatively assume only 10% of the actin is G-actin and consider that the starting G-actin concentration in the cell is ~10 μM, then with only ~1 μM after lysis, 500 nM after EP, and ~250 nM in gel after photocapture[65], then this concentration is well above our limit of detection of ~0.6 nM in gel[126]. Thus, there is poor support for the hypothesis that the G-actin concentration is too low to be detected.

In order to test the second hypothesis, we attempted a sample preparation strategy that allows the native G-actin to be denatured prior to photoimmobilization. Actin was detected either with a monoclonal actin antibody or with the G-actin-specific DnaseI. As shown in Figure 7.25, interestingly no actin signal is observed at all with in-gel denaturation of the G-actin. Strikingly, the Dnase I detects a peak in the control (in which all actin is depolymerized prior to electrophoresis). However, this peak does not align with the actin peak that was detected by

antibody. Thus, it is unclear if the Dnase I is binding to actin or non-specifically with some other species. Crystallography studies indicate that Dnase I binds largely with amino acids 39-63 of monomeric actin[268], while the clone C4 antibody binds in the vicinity of amino acids 50-70. Thus, it is reasonable that if the antibody binding epitope is inaccessible for the native G-actin in the gel, then the DNase I would also be unable to bind. As a result, the epitope unavailability hypothesis was still valid based on the results.

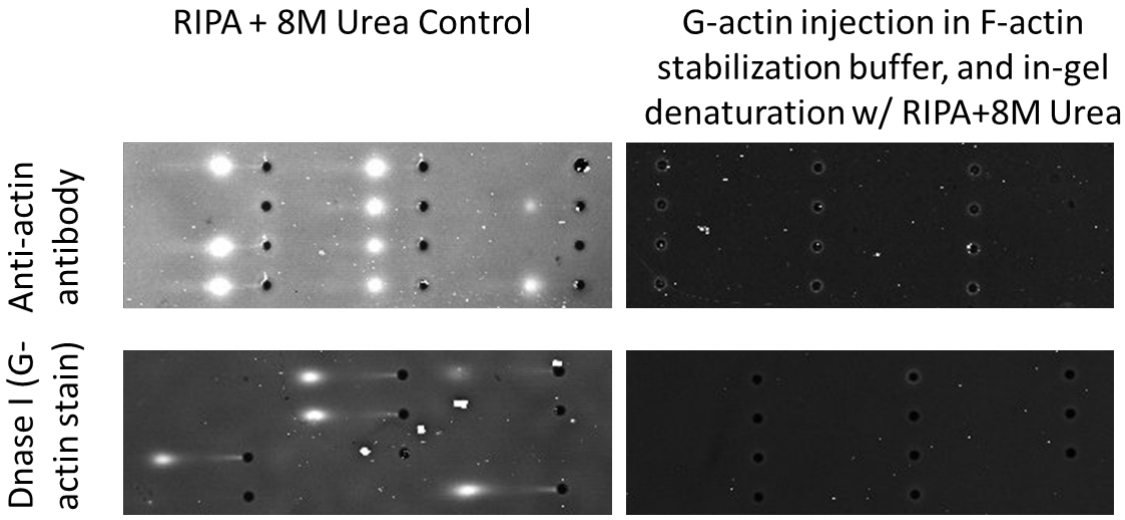

Figure 7.25: False-color micrographs show G-actin signal is not recovered by in-gel denaturation with RIPA + 8M urea prior to photocapture and probing. Left: BJ fibroblasts were settled in 8%TPA gels and lysed by applying a gel lid in RIPA + 8M urea for 45s. Depolymerized actin was electrophoretically injected in the gel (45s, 30 V/cm), and photocaptured. Actin is detected using either anti-actin antibodies (C4 clone), or AF-488 Dnase I stain (binds to G-actin). Right: Cells were lysed in F-actin stabilization buffer and EP was performed for 45s at 30 V/cm. The gel lid was replaced with the RIPA + 8M urea gel lid for 45s prior to photocapture. No actin signal is observed in this condition.

Given the prevalence of actin antibodies, we sought alternative immunoprobe reagents for actin detection, considering factors such as the clonality, site of the epitope and valid applications for the antibody (see Table 7-5, below). We then carried out the bi-directional EP cytometry complex fractionation assay and determined whether native G-actin could be detected from the BJ fibroblasts. As the table indicates, we identified one anti-actin Fab fragment reagent that resulted in detectable G-actin signal (Figure 7.26). Though further optimization of immunoprobing is required (as the F-actin fractions are higher than anticipated owing to the low G-actin signal), the identification of this selective immunoreagent for measuring both F and G actin increases the information gleaned from each fractionation assay.

Table 7-5: Screen of antibodies for detection of both F and G-actin upon bidirectional separation from BJ fibroblasts in EP cytometry complex fractionation.

Vendor	Product #	Clonality	Epitope Info	Valid Applications	Separation results
Millipore	MAB1501	Monoclonal (clone c4)	a.a. 50-70 (Chicken gizzard actin)	ELISA, IC, IF, IH, IH(P) & WB	F-actin band only (fibroblasts)
CST	8456S	Monoclonal	C-terminus of beta actin (synthetic peptide)	WB, IF, IHC	F-actin band only (fibroblasts)
CST	4968S	Polyclonal	Residues arounds Asp244 (synthetic peptide)	WB, IHC	F-actin band only (fibroblasts)
Abcam	ab1801	Polyclonal	~residues 350-Cterminus (peptide)	WB, IHC	No signal (fibroblasts)
Cytoskeleton Inc.	AAN01	Polyclonal	synthetic peptide 11 C-terminal amino acids of actin	WB, ICC, ELISA	F-actin band only (fibroblasts)
ThermoFisher	MA5-11869	Monoclonal (clone c4)	Chicken gizzard actin	IF, IH(P), WB, IP	F-actin band only (fibroblasts)
Biorad	12004164	Unspecified; rhodamine-labeled Fab	Recombinant human beta actin expressed in e. Coli	WB	F-actin band and faint G-actin band (fibroblasts)

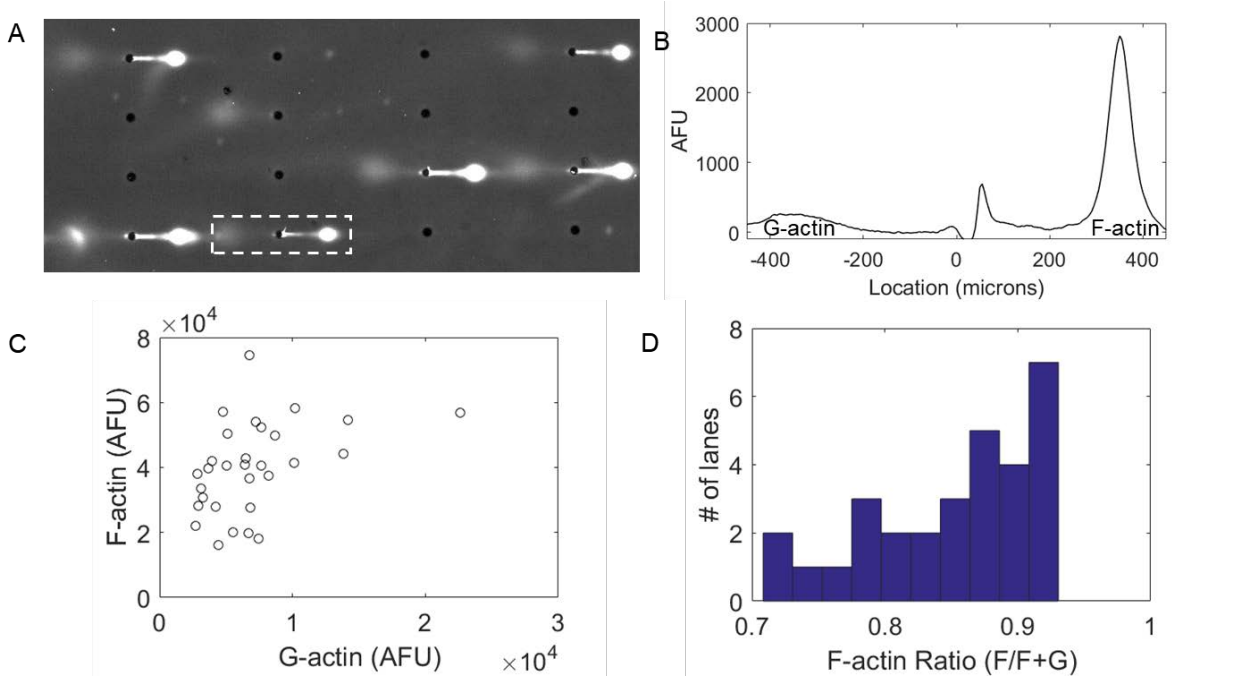

Figure 7.26: Quantifying endogenous F and G actin from BJ fibroblasts via rhodamine-labeled anti-actin Fab detection. (A) False-colored fluorescence micrographs of a bi-directional separation of endogenous F and G actin from BJ fibroblasts. Cells were lysed for 45s with F-actin stabilization lysis buffer (by gel lid). Electrophoresis was performed for 45s at 30 V/cm prior to 45s of UV immobilization. Depolymerization buffer (RIPA+8M urea) was applied to the

array (by gel lid) for 45s before 45s of EP in the opposite direction (30 V/cm) and 45s of UV. Gels were washed overnight in 1X TBST and probed with a 1:10 dilution of Biorad Hfab rhodamine-labeled anti-actin primary for two hours, and washed twice for 30 min each in 1X TBST before imaging on Genepix (532 laser, 100% power and 450 gain w/ AF555 filter). (B) Representative intensity profile of the separation outlined in A. (C) Scatter plot of F vs. G actin quantified from the image in A (n=30 cells). (D) Histogram of the F-actin ratio calculated from the quantified F and G actin levels from each separation lane.

7.4 Conclusions

Protein complexes drive critical cell processes, but methods for selective detection of complexes at the single-cell level have limited throughput and suffer from competitive binding artefacts. We sought to address these challenges by introducing a single-cell electrophoretic fractionation assay that isolates complexes from monomeric proteins. The cytoskeletal protein actin was selected as an intriguing yet challenging model protein owing to its key function as a structural protein that dynamically polymerizes to influence cell motility and signaling. We demonstrate selective cell lysis that maintain filamentous F-actin complexes while efficiently solubilizing monomeric actin. Electrophoretic fractionation is possible because the fractionation gel composition is tuned to size-exclude the large F-actin complexes. Upon cell treatment with F-actin destabilizing drugs, the EP cytometry complex fractionation assay detects lower F-actin levels in individual fibroblast cells. We further apply the assay to assess the effect of the drug jasplakinolide on F-actin levels given confounded results from staining and in vitro measurements. The broader applicability of the assay is demonstrated as we detected the F-actin binding protein vinculin, which is a component of focal adhesions that are key mediators of cell interaction with the micro-environment. Finally, we established proof-of-concept for a version of the assay in which the protein measurement is performed directly on adherent cells to minimize impacts of cell handling on actin polymerization.

We anticipate this measurement will have far-reaching applications both in the study of actin protein complexes and other protein complexes. The ability to measure many proteins from a single cell via chemical stripping and re-probing in EP cytometry assays could be employed to study the network of actin binding protein regulating actin polymerization and depolymerization. Furthermore, with the optimization of the adherent cell version of the assay, new possibilities for quantitatively elucidating the role of the cellular microenvironment on actin protein complexes emerge. Initial studies could determine how cell confinement (e.g., microwell diameter) impacts the F-actin levels and focal adhesion vinculin protein complexes, and the role of substrate stiffness in determining F-actin polymerization.

The method described here can be adapted for smaller homo-oligomeric proteins or interacting proteins. If the size exclusion mechanism is to be used for smaller proteins, the decrosslinking hydrogels described earlier in this dissertation will be necessary. Alternatively, uni-directional native separations may be utilized instead of size-exclusion based fractionation. In all cases, the

gel density may be tuned for the protein species of interest, and gradient gels[269] can be employed for multi-scale protein complexes.

Chapter 8.

Conclusions and future directions

Through several chapters of this dissertation, we explored the fundamental tradeoffs between separation performance and analytical sensitivity of the in-gel immunoassay in EP cytometry. The mechanism of loading dehydrated hydrogels with limiting volumes of detection antibodies is one solution presented in this work. Of note, this method has not been tested on higher density gels, and thus substantial open questions remain regarding the utility of the approach for separations requiring smaller pore-size gels. While decrosslinkable hydrogels are an intriguing avenue to further investigate to balance this tradeoff, the surface-constrained hydrogel swelling-induced buckling[176] limits the utility of decrosslinking gels in the present form factor (i.e., attached to a glass slide). The main constraint requiring the use of a glass substrate is the gel imaging modality, which is a microarray scanner for glass slides in which hydrated gels cannot be introduced. An alternative imaging setup that maintains the capabilities of rapid widefield imaging (e.g., scanning a half-slide in minutes) at ~5-micron pixel resolution with laser excitation to maximize signal[67], while allowing the hydrogel to be hydrated and not attached to a solid substrate would address this issue.

On the other hand, balancing the design goals for the orthogonal metrics of separation performance and analytical sensitivity may require radical re-thinking of the EP cytometry approach to push capabilities for the most challenging separations and lowest abundance protein species. Transfer of protein or other biomolecules out of the EP cytometry device may open up substantial additional analytical capabilities. A concept and preliminary data related to transferring biomolecule-collecting microparticles from EP cytometry microwells out of the device is described in the Appendix.

If EP cytometry is to stay within a single device, changes to the separation method may be necessary. Currently, we rely on the separation afforded by the retarding properties of the relatively inert polyacrylamide gel. However, alternatives that leverage either electrostatic[270] or hydrophobic interactions[271] between the analyte and sieving matrix have already been demonstrated in other chromatography approaches. One could imagine designing the separation material to have pendant groups that would result in interactions that differentially retard proteins. If such groups interfere with the immunoassay (by increasing background due to antibody interactions, or lower antibody loading due to negative interactions), the chemical modifications could be releasable. However, separations that employ electrostatic or hydrophobic interactions are not inherently sizing. Alternative nanopatterned sieving matrices[272,273] can still separate proteins while following the Ogston model, making such matrices an intriguing controllable separation medium. Such nanopatterned sieving matrices limit “pore” size variation, and thus we can hypothesize that potential contributors to

immunoassay background signal such as entropic trapping[274,275] could be better mitigated. Protein peak dispersion should also be minimized in a uniform-"pore" sieving matrix, resulting in reduced variation in the area-under-the-curve quantification.

The need for accurate quantitation of biological and technical variation in single-cell analysis cannot be overstated. Answering whether heterogeneity is functionally significant begins with establishing if it is even statistically significant. The early-stage approaches for assessing technical variation of protein expression and peak location (e.g., to determine if a given protein peak is in fact a proteoform of importance) described in this dissertation are just first-generation iterations of the types of analyses needed. More sophisticated reference standards that allow for normalization of protein levels of a given cell could address intra-device variation. Yet, we also must consider the sample pre-treatment, as it would be naïve to assume that the heterogeneity of the initial cell suspension is the de facto heterogeneity of a relevant in-vivo analogue (e.g., cancer cells in suspension, or even dissociated tissue may not represent a tumor given dissociation artifacts[276]). Contributing to this premise, emerging evidence suggests that cellular microenvironment and signaling may contribute substantially to cell-to-cell variation, and much of the observed heterogeneity disappears if cells are stratified based on the profiles of neighboring cells[277].

Numerous advances could further our understanding of the function of cellular heterogeneity and the technical variation that can mask insight. Approaches to barcode cells or preserve cellular context will be key. Assessing protein signaling that accounts for the levels of neighboring cell protein expression may explain events that give rise to outlier cells such as circulating tumor cells.

Clearly, the work in this dissertation also points to major questions regarding the impact of upstream sample-handling (e.g., trypsinization changing measured F-actin) on the measured protein levels. Careful quantitative analysis to understand how chemical processes such as trypsinization and tissue dissociation impact cell signaling will be critical.

Also, at the heart of any question in single-cell analysis is another important question: how many cells are needed to understand the sub-populations that are present? Towards this point, both assay and algorithm design-based approaches for increasing throughput (number of single cells measured) are needed. In collaboration with researchers in the Doerge lab, we are beginning to address algorithmic limitations to throughput by introducing machine learning-based quality control and image segmentation. The latter is useful because the current approach to generating a 1-D intensity profile collapses noise sometimes not in the peak region into the intensity profile, which prevents accurate quantitation.

As our quantitative approaches mature, large-parameter space data incorporating multiple biological molecules in the same measurement may give a global view of cellular function. Multi-omics has emerged in single-cell analysis in the past several years[189,278–280]. However, more is not always more; and integration projects require careful consideration of how the orthogonal types of information will be interpreted. In the Appendix, some early-stage progress

towards dual RNA and protein measurements is described. Finally, we should consider what other quantitative information we can extract from EP cytometry images. For example, can we discerning the meaning of disperse or non-Gaussian profiles as an indicator of specific chemical interactions not dealt with by sample preparation?

A key innovation presented in this dissertation leverages selective sample preparation chemistries to preserve and quantify protein-protein interactions. Sample preparation is the unglamorous, but pivotal initial assay step that dictates the information that can be derived from an experiment. About no individual's data in particular, Amy wisely says "garbage in, garbage out." Interestingly, at this early stage of understanding the role of sample preparation on EP cytometry, we arguably do not yet understand whether any dispersion is inherently garbage. In fact, the intriguing result presented in our work with circulating tumor cells[24] that primary circulating tumor cells were more difficult to lyse and protein was poorly solubilized could shed tremendous insight into the chemical and biophysical properties of circulating tumor cells. What we lack is the fundamental knowledge that links the observed EP cytometry intensity profile (when not a perfect Gaussian) to its chemical and physical underpinnings.

The future of EP cytometry sample preparation holds unbounded potential to revolutionize our understanding of molecular profiles of individual cells. As a first goal, the actin protein complex measurements can be expanded to non-cytoskeletal protein complexes. Also, protein-protein interaction mediated signaling networks (e.g. actin binding protein regulation of actin polymerization/depolymerization), must be fully measured to shed insight on how such signaling events determine the structural and biophysical properties of the cell (in the case of actin). Furthermore, proteins interact with numerous other biomolecules, and thus nucleic acid binding proteins and their effects on downstream protein signaling events can elucidate entire protein pathways. Finally, an elusive yet tantalizing goal for single-cell sample preparation would be the capability to assay proteoforms directly from banked fixed clinical samples. Chemical crosslinking of proteins[281] that arises during fixation is a striking analytical roadblock to working with fixed cells in EP cytometry. Some preliminary efforts towards this goal are briefly summarized in the Appendix. The blue-sky future for EP cytometry may actually change the goal of the assay from integrated sample preparation to detection of a dozen proteins in a single device, towards thorough sample preparation prior to downstream analysis off-chip measuring the entire proteome of the cell. Research that integrates physical and chemical fundamentals with engineering and algorithm design can push EP cytometry towards this future.

References:

1. Toriello, N. M. *et al.* Integrated microfluidic bioprocessor for single-cell gene expression analysis. *Proc. Natl. Acad. Sci. U. S. A.* **105,** 20173–8 (2008).

2. Kang, C.-C. *et al.* Electrophoretic cytopathology resolves ERBB2 forms with single-cell resolution. *npj Precis. Oncol.* **2,** 10 (2018).

3. Yu, M. *et al.* Circulating breast tumor cells exhibit dynamic changes in epithelial and mesenchymal composition. *Science* **339,** 580–4 (2013).

4. Marcus, J. S., Anderson, W. F. & Quake, S. R. Microfluidic single-cell mRNA isolation and analysis. *Anal. Chem.* **78,** 3084–9 (2006).

5. Bose, S. *et al.* Scalable microfluidics for single cell RNA printing and sequencing. *Genome Biol.* **16,** 120 (2015).

6. Fan, H. C., Fu, G. K. & Fodor, S. P. A. Combinatorial labeling of single cells for gene expression cytometry. *Science (80-.).* **347,** 1258367–1258367 (2015).

7. White, A. K. *et al.* High-throughput microfluidic single-cell RT-qPCR. *Proc. Natl. Acad. Sci. U. S. A.* **108,** 13999–4004 (2011).

8. Streets, A. M. *et al.* Microfluidic single-cell whole-transcriptome sequencing. *Proc. Natl. Acad. Sci. U. S. A.* **111,** 7048–53 (2014).

9. Wang, J., Fan, H. C., Behr, B. & Quake, S. R. Genome-wide single-cell analysis of recombination activity and de novo mutation rates in human sperm. *Cell* **150,** 402–12 (2012).

10. Yu, M. *et al.* RNA sequencing of pancreatic circulating tumour cells implicates WNT signalling in metastasis. *Nature* **487,** 510–3 (2012).

11. Vogel, C. *et al.* Sequence signatures and mRNA concentration can explain two-thirds of protein abundance variation in a human cell line. *Mol. Syst. Biol.* **6,** 1–9 (2010).

12. Taniguchi, Y. *et al.* Quantifying E. coli proteome and transcriptome with single-molecule sensitivity in single cells. *Science* **329,** 533–8 (2010).

13. Luck, K., Sheynkman, G. M., Zhang, I. & Vidal, M. Proteome-Scale Human Interactomics. *Trends in Biochemical Sciences* **42,** 342–354 (2017).

14. Yerbury, J. J. *et al.* Walking the tightrope: proteostasis and neurodegenerative disease. *J. Neurochem.* **137,** 489–505 (2016).

15. Burry, R. W. Controls for immunocytochemistry: an update. *J. Histochem. Cytochem.* **59,** 6–12 (2011).

16. Ng, A. H. C., Dean Chamberlain, M., Situ, H., Lee, V. & Wheeler, A. R. Digital

microfluidic immunocytochemistry in single cells. *Nat. Commun.* **6,** 7513 (2015).

17. Perfetto, S. P., Chattopadhyay, P. K. & Roederer, M. Seventeen-colour flow cytometry: unravelling the immune system. *Nat. Rev. Immunol.* **4,** 648–655 (2004).

18. Shapiro, H. M. *Overture -- Practical Flow Cytometry*. *Practical Flow Cytometry* (2003). doi:10.1002/0471722731.ch1

19. Bandura, D. R. *et al.* Mass Cytometry: Technique for Real Time Single Cell Multitarget Immunoassay Based on Inductively Coupled Plasma Time-of-Flight Mass Spectrometry. *Anal. Chem.* **81,** 6813–6822 (2009).

20. Fredriksson, S. *et al.* Protein detection using proximity-dependent DNA ligation assays. *Nat. Biotechnol.* **20,** 473–477 (2002).

21. Shi, Q. *et al.* Single-cell proteomic chip for profiling intracellular signaling pathways in single tumor cells. *Proc. Natl. Acad. Sci. U. S. A.* **109,** 419–424 (2012).

22. Lu, Y. *et al.* High-throughput secretomic analysis of single cells to assess functional cellular heterogeneity. *Anal. Chem.* **85,** 2548–2556 (2013).

23. Sachs, K., Perez, O., Pe'er, D., Lauffenburger, D. A. & Nolan, G. P. Causal protein-signaling networks derived from multiparameter single-cell data. *Science* **308,** 523–9 (2005).

24. Sinkala, E. *et al.* Profiling protein expression in circulating tumour cells using microfluidic western blotting. *Nat. Commun.* **8,** 14622 (2017).

25. Bruggner, R. V., Bodenmiller, B., Dill, D. L., Tibshirani, R. J. & Nolan, G. P. Automated identification of stratifying signatures in cellular subpopulations. *Proc. Natl. Acad. Sci.* (2014). doi:10.1073/pnas.1408792111

26. Li, J. J., Bickel, P. J. & Biggin, M. D. System wide analyses have underestimated protein abundances and the importance of transcription in mammals. *PeerJ* **2,** e270 (2014).

27. Stack, E. C., Wang, C., Roman, K. A. & Hoyt, C. C. Multiplexed immunohistochemistry, imaging, and quantitation: A review, with an assessment of Tyramide signal amplification, multispectral imaging and multiplex analysis. *Methods* **70,** 46–58 (2014).

28. Gerdes, M. J. *et al.* Highly multiplexed single-cell analysis of formalin-fixed, paraffin-embedded cancer tissue. *Proc. Natl. Acad. Sci. U. S. A.* **110,** 11982–11987 (2013).

29. Bendall, S. C., Nolan, G. P., Roederer, M. & Chattopadhyay, P. K. A deep profiler's guide to cytometry. *Trends Immunol.* **33,** 323–332 (2012).

30. Giesen, C. *et al.* Highly multiplexed imaging of tumor tissues with subcellular resolution by mass cytometry. *Nat. Methods* **11,** 417–422 (2014).

31. Lu, Y. *et al.* Highly multiplexed profiling of single-cell effector functions reveals deep functional heterogeneity in response to pathogenic ligands. *Proc. Natl. Acad. Sci.* (2015).

32. Leuchowius, K.-J., Weibrecht, I. & Söderberg, O. In situ proximity ligation assay for

microscopy and flow cytometry. *Curr. Protoc. Cytom.* **Chapter 9,** Unit 9.36 (2011).

33. Söderberg, O., Gullberg, M. & Jarvius, M. Direct observation of individual endogenous protein complexes in situ by proximity ligation. *Nat. …* **3,** 995–1000 (2006).

34. Srivastava, N. *et al.* Fully integrated microfluidic platform enabling automated phosphoprofiling of macrophage response. *Anal. Chem.* **81,** 3261–9 (2009).

35. Bexheti, D., Anderson, E. I., Hutt, A. J. & Hanna-Brown, M. Evaluation of multidimensional capillary electrophoretic methodologies for determination of amino bisphosphonate pharmaceuticals. *J. Chromatogr. A* **1130,** 137–144 (2006).

36. Zhang, H. & Tian, S. Advances in immunoanalysis of single cells with capillary electrophoresis. *Anal. Bioanal. Chem.* **387,** 21–23 (2007).

37. Huang, B. *et al.* Counting low-copy number proteins in a single cell. *Science* **315,** 81–4 (2007).

38. Mellors, J. S., Jorabchi, K., Smith, L. M. & Ramsey, J. M. Integrated microfluidic device for automated single cell analysis using electrophoretic separation and electrospray ionization mass spectrometry. *Anal. Chem.* **82,** 967–973 (2010).

39. Stadler, C. *et al.* Immunofluorescence and fluorescent-protein tagging show high correlation for protein localization in mammalian cells. *Nat. Methods* **10,** 315–323 (2013).

40. Bates, M., Huang, B., Dempsey, G. T. & Zhuang, X. Multicolor super-resolution imaging with photo-switchable fluorescent probes. *Sci. Pap. Ed.* **317,** 1749–1753 (2007).

41. Huang, B., Bates, M. & Zhuang, X. Super-Resolution Fluorescence Microscopy. *Annu. Rev. Biochem.* **78,** 993–1016 (2009).

42. Tsurui, H. *et al.* Seven-color fluorescence imaging of tissue samples based on Fourier spectroscopy and singular value decomposition. *J. Histochem. {&} Cytochem.* **48,** 653–662 (2000).

43. Brock, R. R., Hamelers, I. H. I. H. & Jovin, T. M. T. M. Comparison of fixation protocols for adherent cultured cells applied to a GFP fusion protein of the epidermal growth factor receptor. *Cytometry* **35,** 353–362 (1999).

44. Schnell, U. U., Dijk, F. F., Sjollema, K. A. K. A. & Giepmans, B. N. G. B. N. Immunolabeling artifacts and the need for live-cell imaging. *Nat. Methods* **9,** 152–158 (2012).

45. Wang, L. *et al.* Human CD4+ lymphocytes for antigen quantification: Characterization using conventional flow cytometry and mass cytometry. *Cytometry* **81A,** 567–575 (2012).

46. Angelo, M. *et al.* Multiplexed ion beam imaging of human breast tumors. *Nat. Med.* 1–9 (2014).

47. Shin, Y. S. *et al.* Chemistries for patterning robust DNA microbarcodes enable multiplex assays of cytoplasm proteins from single cancer cells. *ChemPhysChem* **11,** 3063–3069 (2010).

48. Söderberg, O. *et al.* Direct observation of individual endogenous protein complexes in situ by proximity ligation. *Nat. Methods* **3,** 995–1000 (2006).

49. Gustafsdottir, S. M. *et al.* In vitro analysis of DNA-protein interactions by proximity ligation. *Proc. Natl. Acad. Sci. U. S. A.* **104,** 3067–72 (2007).

50. Leuchowius, K.-J. *et al.* Parallel visualization of multiple protein complexes in individual cells in tumor tissue. *Mol. Cell. Proteomics* **12,** 1563–71 (2013).

51. Weibrecht, I. *et al.* Proximity ligation assays: a recent addition to the proteomics toolbox. *Expert Rev. Proteomics* **7,** 401–409 (2010).

52. Weibrecht, I. *et al.* In situ detection of individual mRNA molecules and protein complexes or post-translational modifications using padlock probes combined with the in situ proximity ligation assay. *Nat. Protoc.* **8,** 355–72 (2013).

53. Clausson, C.-M. *et al.* Increasing the dynamic range of in situ PLA. *Nat. Methods* **8,** 892–3 (2011).

54. Perez, O. D. & Nolan, G. P. Simultaneous measurement of multiple active kinase states using polychromatic flow cytometry. *Nat. Biotechnol.* **20,** 155–162 (2002).

55. Wu, M. & Singh, A. K. Single-cell protein analysis. *Curr. Opin. Biotechnol.* **23,** 83–8 (2012).

56. Srivastava, N. *et al.* Fully Integrated Microfluidic Platform Enabling Automated Phosphoprofiling of Macrophage Response. **81,** 3261–3269 (2009).

57. Perroud, T. D. *et al.* Microfluidic-based cell sorting of Francisella tularensis infected macrophages using optical forces. *Anal. Chem.* **80,** 6365–6372 (2008).

58. Maecker, H. T. & Trotter, J. Flow cytometry controls, instrument setup, and the determination of positivity. *Cytom. Part A* **69,** 1037–1042 (2006).

59. Dickinson, A. J., Armistead, P. M. & Allbritton, N. L. Automated capillary electrophoresis system for fast single-cell analysis. *Anal. Chem.* **85,** 4797–4804 (2013).

60. Aebersold, R. & Mann, M. Mass spectrometry-based proteomics. *Nature* **422,** 198–207 (2003).

61. Romanova, E. V, Rubakhin, S. S., Monroe, E. B. & Sweedler, J. V. Single cell mass spectrometry. *Single Cell Anal. Technol. Appl.* 109–133 (2009).

62. Begley, C. G. & Ellis, L. M. Drug development: Raise standards for preclinical cancer research. *Nature* **483,** 531–3 (2012).

63. Egelhofer, T. A. *et al.* An assessment of histone-modification antibody quality. *Nat. Struct. Mol. Biol.* **18,** 91–3 (2011).

64. Delom, F. & Chevet, E. Phosphoprotein analysis: from proteins to proteomes. *Proteome Sci.* **4,** 15 (2006).

65. Hughes, A. J. *et al.* Single-cell western blotting. *Nat. Methods* **11,** 749–55 (2014).

66. Kang, C.-C., Lin, J.-M. G., Xu, Z., Kumar, S. & Herr, A. E. Single-Cell Western Blotting after Whole-Cell Imaging to Assess Cancer Chemotherapeutic Response. *Anal. Chem.* **86,** 10429–10436 (2014).

67. Kang, C.-C. *et al.* Single cell–resolution western blotting. *Nat. Protoc.* **11,** 1508–1530 (2016).

68. Dormán, G. & Prestwich, G. D. Benzophenone photophores in biochemistry. *Biochemistry* **33,** 5661–5673 (1994).

69. Hughes, A. J., Lin, R. K. C., Peehl, D. M. & Herr, A. E. Microfluidic integration for automated targeted proteomic assays. *Proc. Natl. Acad. Sci. U. S. A.* **109,** 5972–7 (2012).

70. Hughes, A. J. & Herr, A. E. Microfluidic Western blotting. *Proc. Natl. Acad. Sci. U. S. A.* **109,** 21450–5 (2012).

71. Dormán, G., Nakamura, H., Pulsipher, A. & Prestwich, G. D. The Life of Pi Star: Exploring the Exciting and Forbidden Worlds of the Benzophenone Photophore. *Chemical Reviews* **116,** 15284–15398 (2016).

72. Probstein, R. F. *Physicochemical Hydrodynamics: An Introduction*. (John Wiley & Sons, 2005).

73. Smithies, O. Zone electrophoresis in starch gels: group variations in the serum proteins of normal human adults. *Biochem. J.* **61,** 629–641 (1955).

74. Ferguson, K. A. Starch-gel electrophoresis—Application to the classification of pituitary proteins and polypeptides. *Metabolism* **13,** 985–1002 (1964).

75. Hughes, A. J. & Herr, A. E. Quantitative enzyme activity determination with zeptomole sensitivity by microfluidic gradient-gel zymography. *Anal. Chem.* **82,** 3803–11 (2010).

76. Rodbard, D., Kapadia, G. & Chrambach, A. Pore gradient electrophoresis. *Anal. Biochem.* **40,** 135–157 (1971).

77. Schagger, H., Cramer, W. A. & Vonjagow, G. Analysis of Molecular Masses and Oligomeric States of Protein Complexes by Blue Native Electrophoresis and Isolation of Membrane Protein Complexes by Two-Dimensional Native Electrophoresis. *Analytical Biochemistry* **217,** 220–230 (1994).

78. Otzen, D. E. Protein unfolding in detergents: effect of micelle structure, ionic strength, pH, and temperature. *Biophys. J.* **83,** 2219–30 (2002).

79. Bhuyan, A. K. On the mechanism of SDS-induced protein denaturation. *Biopolymers* **93,** 186–99 (2010).

80. Otzen, D. Protein-surfactant interactions: a tale of many states. *Biochim. Biophys. Acta* **1814,** 562–91 (2011).

81. Gehrke, S. H., Fisher, J. P., Palasis, M. & Lund, M. E. Factors determining hydrogel

permeability. *Ann. N. Y. Acad. Sci.* **831,** 179–207 (1997).

82. Tong, J. & Anderson, J. L. Partitioning and diffusion of proteins and linear polymers in polyacrylamide gels. *Biophys. J.* **70,** 1505–1513 (1996).

83. Ogston, A. G. The spaces in a uniform random suspension of fibres. *Trans. Faraday Soc.* (1958). doi:10.1039/tf9585401754

84. Jøssang, T., Feder, J. & Rosenqvist, E. Photon correlation spectroscopy of human IgG. *J. Protein Chem.* **7,** 165–171 (1988).

85. Holmes, D. L. & Stellwagen, N. C. Estimation of polyacrylamide gel pore size from Ferguson plots of linear DNA fragments. II. Comparison of gels with different crosslinker concentrations, added agarose and added linear polyacrylamide. *Electrophoresis* **12,** 612–619 (1991).

86. Brinkman, H. C. A calculation of the viscous force exerted by a flowing fluid on a dense swarm of particles. *Appl. Sci. Res.* **1,** 27–34 (1949).

87. Park, I. H., Johnson, C. S. & Gabriel, D. A. Probe diffusion in polyacrylamide gels as observed by means of holographic relaxation methods: search for a universal equation. *Macromolecules* **23,** 1548–1553 (1990).

88. Chiari, M. & Righetti, P. G. New types of separation matrices for electrophoresis. *Electrophoresis* **16,** 1815–1829 (1995).

89. Wenisch, E., de Besi, P. & Righetti, P. G. Conventional isoelectric focusing and immobilized pH gradients in ‘macroporous’ polyacrylamide gels. *Electrophoresis* **14,** 583–590 (1993).

90. Squires, T. M., Messinger, R. J. & Manalis, S. R. Making it stick: convection, reaction and diffusion in surface-based biosensors. *Nat. Biotechnol.* **26,** 417–26 (2008).

91. Burnette, W. N. “Western Blotting”: Electrophoretic transfer of proteins from sodium dodecyl sulfate-polyacrylamide gels to unmodified nitrocellulose and radiographic detection with antibody and radioiodinated protein A. *Anal. Biochem.* **112,** 195–203 (1981).

92. Righetti, P. G. & Caravaggio, T. Isoelectric points and molecular weights of proteins. *J. Chromatogr. A* **127,** 1–28 (1976).

93. Herr, A. E. & Singh, A. K. Photopolymerized cross-linked polycrylamide gels for on-chip protein sizing. *Anal. Chem.* **76,** 4727–4733 (2004).

94. Jin, S. *et al.* Multiplexed Western Blotting Using Microchip Electrophoresis. *Anal. Chem.* **88,** 6703–6710 (2016).

95. Anderson, G. J., M Cipolla, C. & Kennedy, R. T. Western blotting using capillary electrophoresis. *Anal. Chem.* **83,** 1350–5 (2011).

96. Bharadwaj, R., Santiago, J. G. & Mohammadi, B. Design and optimization of on-chip capillary electrophoresis. *Electrophoresis* **23,** 2729–44 (2002).

97. Gassmann, M., Grenacher, B., Rohde, B. & Vogel, J. Quantifying Western blots: Pitfalls of densitometry. *Electrophoresis* **30,** 1845–1855 (2009).

98. Duncombe, T. A. & Herr, A. E. Photopatterned free-standing polyacrylamide gels for microfluidic protein electrophoresis. *Lab Chip* **13,** 2115–23 (2013).

99. Pan, Y. *et al.* Determination of equilibrium dissociation constants for recombinant antibodies by high-throughput affinity electrophoresis. *Sci. Rep.* **6,** 39774 (2016).

100. Gutzweiler, L. *et al.* Open microfluidic gel electrophoresis: Rapid and low cost separation and analysis of DNA at the nanoliter scale. *Electrophoresis* **38,** 1764–1770 (2017).

101. Wood, D. K., Weingeist, D. M., Bhatia, S. N. & Engelward, B. P. Single cell trapping and DNA damage analysis using microwell arrays. *Proc. Natl. Acad. Sci. U. S. A.* **107,** 10008–13 (2010).

102. Tentori, A. M., Yamauchi, K. A. & Herr, A. E. Detection of Isoforms Differing by a Single Charge Unit in Individual Cells. *Angew. Chemie - Int. Ed.* **55,** 12431–12435 (2016).

103. Shackman, J. G., Watson, C. J. & Kennedy, R. T. High-throughput automated post-processing of separation data. *J. Chromatogr. A* **1040,** 273–282 (2004).

104. Weingeist, D. M. *et al.* Single-cell microarray enables high-throughput evaluation of DNA double-strand breaks and DNA repair inhibitors. *Cell Cycle* **12,** 907–915 (2013).

105. Peng, R. D. Reproducible research in computational science. *Science (80-.).* **334,** 1226–1227 (2011).

106. Duncombe, T. A. *et al.* Hydrogel Pore-Size Modulation for Enhanced Single-Cell Western Blotting. *Adv. Mater.* **28,** 327–334 (2015).

107. Giddings JC. Unified Separation Science. *John Wiley sons New York* 97–101 (1991).

108. Glantz, S. *Primer of Biostatistics*. (2005).

109. Caballero, R. D., Garcıa-Alvarez-Coque, M. C. & Baeza-Baeza, J. J. Parabolic-Lorentzian modified Gaussian model for describing and deconvolving chromatographic peaks. *J. Chromatogr. A* **954,** 59–76 (2002).

110. Kang, C.-C. *et al.* Single cell-resolution western blotting. *Nat. Protoc.* **11,** 1508–1530 (2016).

111. Mitra, D. *et al.* An oncogenic isoform of HER2 associated with locally disseminated breast cancer and trastuzumab resistance. *Mol. Cancer Ther.* **8,** 2152–62 (2009).

112. Solakidi, S., Psarra, A.-M. G., Nikolaropoulos, S. & Sekeris, C. E. Estrogen receptors alpha and beta (ERalpha and ERbeta) and androgen receptor (AR) in human sperm: localization of ERbeta and AR in mitochondria of the midpiece. *Hum. Reprod.* **20,** 3481–7 (2005).

113. Okoro, D. R., Rosso, M. & Bargonetti, J. Splicing up mdm2 for cancer proteome

diversity. *Genes Cancer* **3,** 311–9 (2012).

114. Rajan, P., Elliott, D. J., Robson, C. N. & Leung, H. Y. Alternative splicing and biological heterogeneity in prostate cancer. *Nat. Rev. Urol.* **6,** 454–460 (2009).

115. Kim, J. J., Sinkala, E. & Herr, A. E. High-selectivity cytology via lab-on-a-disc western blotting of individual cells. *Lab Chip* **17,** 855–863 (2017).

116. Shadle, S. E. *et al.* Quantitative analysis of electrophoresis data: Novel curve fitting methodology and its application to the determination of a protein-DNA binding constant. *Nucleic Acids Res.* **25,** 850–860 (1997).

117. Amir, E. D. *et al.* visNe enables visualization of high dimensional single-cell data and reveals phenotypic heterogeneity of leukemia. *Nat. Biotechnol.* **31,** 545–552 (2013).

118. Powell, A. A. *et al.* Single cell profiling of Circulating tumor cells: Transcriptional heterogeneity and diversity from breast cancer cell lines. *PLoS One* **7,** e33788 (2012).

119. Arzalluz-Luque, Á., Devailly, G., Mantsoki, A. & Joshi, A. Delineating biological and technical variance in single cell expression data. *Int. J. Biochem. Cell Biol.* **90,** 161–166 (2017).

120. Jiang, L. *et al.* Synthetic spike-in standards for RNA-seq experiments. *Genome Res.* **21,** 1543–1551 (2011).

121. Islam, S. *et al.* Quantitative single-cell RNA-seq with unique molecular identifiers. *Nat. Methods* **11,** 163–166 (2014).

122. Perfetto, S. P., Ambrozak, D., Nguyen, R., Chattopadhyay, P. K. & Roederer, M. Quality assurance for polychromatic flow cytometry using a suite of calibration beads. *Nat. Protoc.* **7,** 2067–2079 (2012).

123. Schwartz, A., Marti, G. E., Poon, R., Gratama, J. W. & Fernández-Repollet, E. Standardizing flow cytometry: A classification system of fluorescence standards used for flow cytometry. *Cytometry* **33,** 106–114 (1998).

124. Hu, S., Zhang, L., Cook, L. M. & Dovichi, N. J. Capillary sodium dodecyl sulfate-DALT electrophoresis of proteins in a single human cancer cell. *Electrophoresis* **22,** 3677–3682 (2001).

125. Vlassakis, J. & Herr, A. E. Joule Heating-Induced Dispersion in Open Microfluidic Electrophoretic Cytometry. *Anal. Chem.* **89,** 12787–12796 (2017).

126. Vlassakis, J. & Herr, A. E. Effect of Polymer Hydration State on In-Gel Immunoassays. *Anal. Chem.* **87,** 11030–8 (2015).

127. Taniguchi Tomoharu Kajiyama & Hideki Kambara, K. Quantitative analysis of gene expression in a single cell by qPCR. *Nat. Methods* **6,** 503–506 (2009).

128. Molloy, M. P., Brzezinski, E. E., Hang, J., McDowell, M. T. & VanBogelen, R. A. Overcoming technical variation and biological variation in quantitative proteomics. *Proteomics* **3,** 1912–1919 (2003).

129. Shapiro, A. L., Viñuela, E. & V. Maizel, J. Molecular weight estimation of polypeptide chains by electrophoresis in SDS-polyacrylamide gels. *Biochem. Biophys. Res. Commun.* **28,** 815–820 (1967).

130. David, C. J. & Manley, J. L. Alternative pre-mRNA splicing regulation in cancer: pathways and programs unhinged. *Genes Dev.* **24,** 2343–64 (2010).

131. Los, G. V. *et al.* HaloTag: A novel protein labeling technology for cell imaging and protein analysis. *ACS Chem. Biol.* **3,** 373–382 (2008).

132. Yamauchi, K. & Herr, A. Sub-cellular western blotting of single cells. *Microsystems & Nanoengineering* **3,** 16079 (2017).

133. Sakharkar, M., Passetti, F., de Souza, J. E., Long, M. & de Souza, S. J. ExInt: an Exon Intron Database. *Nucleic Acids Res.* **30,** 191–4 (2002).

134. Peppas, N. a., Hilt, J. Z., Khademhosseini, a. & Langer, R. Hydrogels in Biology and Medicine: From Molecular Principles to Bionanotechnology. *Adv. Mater.* **18,** 1345–1360 (2006).

135. Gupta, P., Vermani, K. & Garg, S. Hydrogels: from controlled release to pH-responsive drug delivery. *Drug Discov. Today* **7,** 569–579 (2002).

136. Hitzbleck, M. & Delamarche, E. Reagents in microfluidics: an 'in' and 'out' challenge. *Chem. Soc. Rev.* **42,** 8494 (2013).

137. Hoffman, A. S. Hydrogels for biomedical applications. *Adv. Drug Deliv. Rev.* **54,** 3–12 (2002).

138. Appleyard, D., Chapin, S. & Doyle, P. Multiplexed protein quantification with barcoded hydrogel microparticles. *Anal. Chem.* **83,** 193–199 (2010).

139. Li, H., Leulmi, R. F. & Juncker, D. Hydrogel droplet microarrays with trapped antibody-functionalized beads for multiplexed protein analysis. *Lab Chip* **11,** 528–34 (2011).

140. de Lange, V., Binkert, A., Vörös, J. & Bally, M. Microarrays made easy: biofunctionalized hydrogel channels for rapid protein microarray production. *ACS Appl. Mater. Interfaces* **3,** 50–7 (2011).

141. Gehrke, S. H., Uhden, L. H. & McBride, J. F. Enhanced loading and activity retention of bioactive proteins in hydrogel delivery systems. *J. Control. Release* **55,** 21–33 (1998).

142. Sivars, U. & Tjerneld, F. Mechanisms of phase behaviour and protein partitioning in detergent/polymer aqueous two-phase systems for purification of integral membrane proteins. *Biochim. Biophys. Acta - Gen. Subj.* **1474,** 133–146 (2000).

143. Lewus, R. K. & Carta, G. Protein Transport in Constrained Anionic Hydrogels: Diffusion and Boundary-Layer Mass Transfer. *Ind. Eng. Chem. Res.* **40,** 1548–1558 (2001).

144. Albro, M. B. *et al.* Dynamic loading of deformable porous media can induce active solute transport. *J. Biomech.* **41,** 3152–7 (2008).

145. Shalaby, W. S. W., Abdallah, A. A., Park, H. & Park, K. Loading of Bovine Serum Albumin into Hydrogels by an Electrophoretic Process and Its Potential Application to Protein Drugs. *Pharm. Res.* **10,** 457–460 (1993).

146. Le Goff, G. C., Srinivas, R. L., Adam Hill, W. & Doyle, P. S. Hydrogel microparticles for biosensing. *Eur. Polym. J.* **72,** 386–412 (2015).

147. Moorthy, J., Burgess, R., Yethiraj, A. & Beebe, D. Microfluidic Based Platform for Characterization of Protein Interactions in Hydrogel Nanoenvironments. **79,** 5322–5327 (2007).

148. Chambers, I. *et al.* Nanog safeguards pluripotency and mediates germline development. *Nature* **450,** 1230–4 (2007).

149. Michel, M. C., Wieland, T. & Tsujimoto, G. How reliable are G-protein-coupled receptor antibodies? *Naunyn. Schmiedebergs. Arch. Pharmacol.* **379,** 385–8 (2009).

150. Scherer, G. W. Recent progress in drying of gels. *Journal of Non-Crystalline Solids* **147–148,** 363–374 (1992).

151. Gehrke, S. in *Responsive Gels: Volume Transitions II* 81–144 (1993). doi:10.1007/BFb0021130

152. Baselga, J., Hernández-Fuentes, I., Masegosa, R. M. & Llorente, M. A. Effect of crosslinker on swelling and thermodynamic properties of polyacrylamide gels. *Polym. J.* **21,** 467–474 (1989).

153. Toomey, R., Freidank, D. & Rühe, J. Swelling Behavior of Thin, Surface-Attached Polymer Networks. *Macromolecules* **37,** 882–887 (2004).

154. Yoon, J., Cai, S., Suo, Z. & Hayward, R. C. Poroelastic swelling kinetics of thin hydrogel layers: comparison of theory and experiment. *Soft Matter* **6,** 6004 (2010).

155. Mirsky, A. E. & Pauling, L. On the Structure of Native, Denatured, and Coagulated Proteins. *Proc. Natl. Acad. Sci. U. S. A.* **22,** 439–47 (1936).

156. Prestrelski, S. J., Tedeschi, N., Arakawa, T. & Carpenter, J. F. Dehydration-induced conformational transitions in proteins and their inhibition by stabilizers. *Biophys. J.* **65,** 661–71 (1993).

157. Carpenter, J. F., Crowe, J. H. & Arakawa, T. Comparison of Solute-Induced Protein Stabilization in Aqueous Solution and in the Frozen and Dried States. *J. Dairy Sci.* **73,** 3627–3636 (1990).

158. Daniel, R. M., Dunn, R. V, Finney, J. L. & Smith, J. C. The role of dynamics in enzyme activity. *Annu. Rev. Biophys. Biomol. Struct.* **32,** 69–92 (2003).

159. Flory, P. J. *Principles of Polymer Chemistry: Paul J. Flory*. (1953).

160. Scott, A. M., Wolchok, J. D. & Old, L. J. Antibody therapy of cancer. *Nat. Rev. Cancer* **12,** 278–87 (2012).

161. Schweizer, D., Serno, T. & Goepferich, A. Controlled release of therapeutic antibody formats. *Eur. J. Pharm. Biopharm. Off. J. Arbeitsgemeinschaft für Pharm. Verfahrenstechnik e.V* **88,** 291–309 (2014).

162. Yau, K. Y. F. *et al.* Affinity maturation of a V(H)H by mutational hotspot randomization. *J. Immunol. Methods* **297,** 213–24 (2005).

163. Batista, F. D. & Neuberger, M. S. Affinity Dependence of the B Cell Response to Antigen: A Threshold, a Ceiling, and the Importance of Off-Rate. *Immunity* **8,** 751–759 (1998).

164. Friedman, N., Cai, L. & Xie, X. S. Linking stochastic dynamics to population distribution: An analytical framework of gene expression. *Phys Rev Lett* **97,** 168302 (2006).

165. Bonett, D. G. Confidence interval for a coefficient of quartile variation. *Comput. Stat. Data Anal.* **50,** 2953–2957 (2006).

166. Fisher, R. A. Frequency Distribution of the Values of the Correlation Coefficient in Samples from an Indefinitely Large Population. *Biometrika* **10,** 507–521 (1915).

167. Rodbard, D. & Chrambach, A. Unified Theory for Gel Electrophoresis and Gel Filtration. *Proc. Natl. Acad. Sci.* **65,** 970–977 (1970).

168. Morris, C. J. & Morris, P. Molecular-sieve chromatography and electrophoresis in polyacrylamide gels. *Biochem. J.* **124,** 517–28 (1971).

169. Duncombe, T. A. *et al.* Hydrogel Pore-Size Modulation for Enhanced Single-Cell Western Blotting. *Adv. Mater.* **28,** 327–334 (2016).

170. Cano, M. L., Lauffenburger, D. A. & Zigmond, S. H. Kinetic analysis of F-actin depolymerization in polymorphonuclear leukocyte lysates indicates that chemoattractant stimulation increases actin filament number without altering the filament length distribution. *J. Cell Biol.* **115,** (1991).

171. Burlacu, S., Janmey, P. A. & Borejdo, J. Distribution of actin filament lengths measured by fluorescence microscopy. *Am J Physiol Cell Physiol* **262,** C569-577 (1992).

172. Heacock, C. S. & Bamburg, J. R. The quantitation of G- and F-actin in cultured cells. *Anal. Biochem.* **135,** 22–36 (1983).

173. Cooper, G. M. in *The Cell: A Molecular Approach. 2nd Ed.* (Sinauer Associates, 2000).

174. Cao, X. & Shoichet, M. S. Photoimmobilization of biomolecules within a 3-dimensional hydrogel matrix. *J. Biomater. Sci. Polym. Ed.* **13,** 623–636 (2002).

175. Hou, C. & Herr, A. E. Ultrashort separation length homogeneous electrophoretic immunoassays using on-chip discontinuous polyacrylamide gels. *Anal. Chem.* **82,** 3343–51 (2010).

176. Tanaka, T. *et al.* Mechanical instability of gels at the phase transition. *Nature* **325,** 796–798 (1987).

177. Guvendiren, M., Yang, S. & Burdick, J. a. Swelling-Induced Surface Patterns in Hydrogels with Gradient Crosslinking Density. *Adv. Funct. Mater.* **19,** 3038–3045 (2009).

178. Trujillo, V., Kim, J. & Hayward, R. C. Creasing instability of surface-attached hydrogels. *Soft Matter* **4,** 564 (2008).

179. Kim, J., Yoon, J. & Hayward, R. C. Dynamic display of biomolecular patterns through an elastic creasing instability of stimuli-responsive hydrogels. *Nat. Mater.* **9,** 159–164 (2010).

180. Li, B., Cao, Y.-P., Feng, X.-Q. & Gao, H. Mechanics of morphological instabilities and surface wrinkling in soft materials: a review. *Soft Matter* **8,** 5728 (2012).

181. Sharp, J. S. & Jones, R. A. L. Swelling-induced morphology in ultrathin supported films of poly (d , l − lactide). *Phys. Rev. E* **66,** 011801 (2002).

182. Schiller, L. R., Emmett, M., Santa Ana, C. A. & Fordtran, J. S. Osmotic effects of polyethylene glycol. *Gastroenterology* **94,** 933–941 (1988).

183. Denisin, A. K. & Pruitt, B. L. Tuning the Range of Polyacrylamide Gel Stiffness for Mechanobiology Applications. *ACS Applied Materials and Interfaces* **8,** 21893–21902 (2016).

184. De Schryver, F. C., Smets, G. & Van Thielen, J. Influence of the reaction medium on radical polymerization. II. *J. Polym. Sci. Part B Polym. Lett.* **6,** 547–550 (1968).

185. Gromov, V. F. & Khomikovskii, P. M. The Influence of the Solvent on the Rates of Chain Propagation and Termination Reactions in Radical Polymerisation. *Russ. Chem. Rev.* **48,** 1040–1054 (1979).

186. Zhuravleva, I. L., Zav'yalova, Y. N., Bogachev, Y. S. & Gromov, V. F. The radical polymerization of acrylamide in dimethyl sulfoxide-water mixtures. *Polym. Sci. U.S.S.R.* **28,** 976–981 (1986).

187. Kravchenko-Balasha, N., Shin, Y. S., Sutherland, A., Levine, R. D. & Heath, J. R. Intercellular signaling through secreted proteins induces free-energy gradient-directed cell movement. *Proc. Natl. Acad. Sci. U. S. A.* **113,** 5520–5 (2016).

188. Nemes, P., Rubakhin, S. S., Aerts, J. T. & Sweedler, J. V. Qualitative and quantitative metabolomic investigation of single neurons by capillary electrophoresis electrospray ionization mass spectrometry. *Nat. Protoc.* **8,** 783–99 (2013).

189. Rubakhin, S. S., Romanova, E. V, Nemes, P. & Sweedler, J. V. Profiling metabolites and peptides in single cells. *Nat. Methods* **8,** S20–S29 (2011).

190. Dolník, V., Liu, S. & Jovanovich, S. Capillary electrophoresis on microchip. *Electrophoresis* **21,** 41–54 (2000).

191. Kovarik, M. L., Lai, H.-H., Xiong, J. C. & Allbritton, N. L. Sample transport and electrokinetic injection in a microchip device for chemical cytometry. *Electrophoresis* **32,** 3180–3187 (2011).

192. Barkal, L. J. *et al.* Microbial metabolomics in open microscale platforms. *Nat. Commun.* **7,** 10610 (2016).

193. Pan, Y., Duncombe, T. A., Kellenberger, C. A., Hammond, M. C. & Herr, A. E. High-throughput electrophoretic mobility shift assays for quantitative analysis of molecular binding reactions. *Anal. Chem.* **86,** 10357–64 (2014).

194. Cargile, B. J., Bundy, J. L., Freeman, T. W. & Stephenson, J. L. Gel Based Isoelectric Focusing of Peptides and the Utility of Isoelectric Point in Protein Identification. *J. Proteome Res.* **3,** 112–119 (2004).

195. Wu, D., Qin, J. & Lin, B. Electrophoretic separations on microfluidic chips. *J. Chromatogr. A* **1184,** 542–559 (2008).

196. Knox, J. H. & McCormack, K. A. Temperature effects in capillary electrophoresis. 1: Internal capillary temperature and effect upon performance. *Chromatographia* **38,** 207–214 (1994).

197. Hjertén, S. Free zone electrophoresis. *Chromatogr. Rev.* **9,** 122–219 (1967).

198. Gaš, B. Axial temperature effects in electromigration. *J. Chromatogr. A* **644,** 161–174 (1993).

199. Coxon, M. & Binder, M. J. Radial temperature distribution in isotachophoresis columns of circular cross-section. *J. Chromatogr. A* **101,** 1–16 (1974).

200. Petersen, N. J., Nikolajsen, R. P. H., Mogensen, K. B. & Kutter, J. P. Effect of Joule heating on efficiency and performance for microchip-based and capillary-based electrophoretic separation systems: A closer look. *Electrophoresis* **25,** 253–269 (2004).

201. Moghadam, B. Y., Connelly, K. T. & Posner, J. D. Isotachophoretic Preconcenetration on Paper-Based Microfluidic Devices. *Anal. Chem.* **86,** 5829–5837 (2014).

202. Rosenfeld, T. & Bercovici, M. 1000-fold sample focusing on paper-based microfluidic devices. *Lab Chip* **14,** 4465–4474 (2014).

203. Terry, B. R., Matthews, E. K. & Haseloff, J. Molecular Characterization of Recombinant Green Fluorescent Protein by Fluorescence Correlation Microscopy. *Biochem. Biophys. Res. Commun.* **217,** 21–27 (1995).

204. Schneider, G. F., Shaw, B. F., Lee, A., Carillho, E. & Whitesides, G. M. Pathway for unfolding of ubiquitin in sodium dodecyl sulfate, studied by capillary electrophoresis. *J. Am. Chem. Soc.* **130,** 17384–93 (2008).

205. Reynolds, J. A. & Tanford, C. Binding of Dodecyl Sulfate to Proteins at High Binding Ratios. Possible Implications for the State of Proteins in Biological Membranes. *Proc. Natl. Acad. Sci.* **66,** 1002–1007 (1970).

206. Bello, M. S., Chiari, M., Nesi, M., Righetti, P. G. & Saracchi, M. Prediction of current-voltage dependence and electrochemical calibration for capillary zone electrophoresis. *J. Chromatogr. A* **625,** 323–330 (1992).

207. Burgi, D. S., Salomon, K. & Chien, R.-L. Methods For Calculating the Internal Temperature of Capillary Columns During Capillary Electrophoresis. *J. Liq. Chromatogr.* **14,** 847–867 (1991).

208. Ross, D., Gaitan, M. & Locascio, L. E. Temperature measurement in microfluidic systems using a temperature-dependent fluorescent dye. *Anal. Chem.* **73,** 4117–4123 (2001).

209. Wätzig, H. The measurement of temperature inside capillaries for electrophoresis using thermochromic solutions. *Chromatographia* **33,** 445–448 (1992).

210. Fergason, J. L. Liquid Crystals in Nondestructive Testing. *Appl. Opt.* **7,** 1729 (1968).

211. Ireland, P. T. & Jones, T. V. The response time of a surface thermometer employing encapsulated thermochromic liquid crystals. *J. Phys. E.* **20,** 008 (1987).

212. Gobie, W. A. & Ivory, C. F. Thermal model of capillary electrophoresis and a method for counteracting thermal band broadening. *J. Chromatogr. A* **516,** 191–210 (1990).

213. Nishikawa, T. & Kambara, H. Temperature profile of buffer-filled electrophoresis capillaries using air convection cooling. *Electrophoresis* **17,** 1115–1120 (1996).

214. Vinther, A. & Søeberg, H. Temperature elevations of the sample zone in free solution capillary electrophoresis under stacking conditions. *J. Chromatogr. A* **559,** 27–42 (1991).

215. Grushka, E., McCormick, R. M. & Kirkland, J. J. Effect of Temperature Gradients on the Efficiency of Capillary Zone Electrophoresis Separations. *Anal. Chem.* **61,** 241–246 (1989).

216. Sittler, A., Devys, D., Weber, C. & Mandel, J.-L. Alternative Splicing of Exon 14 Determines Nuclear or Cytoplasmic Localisation of FMR1 Protein Isoforms. *Hum. Mol. Genet.* **5,** 95–102 (1996).

217. Ezkurdia, I. *et al.* Most Highly Expressed Protein-Coding Genes Have a Single Dominant Isoform. *J. Proteome Res.* **14,** 1880–1887 (2015).

218. Rao, K. M. K. & Cohen, H. J. Actin cytoskeletal network in aging and cancer. *Mutat. Res.* **256,** 139–148 (1991).

219. Suter, D. M. & Forscher, P. An emerging link between cytoskeletal dynamics and cell adhesion molecules in growth cone guidance. *Curr. Opin. Neurobiol.* **8,** 106–116 (1998).

220. Masai, J., Ishiwata, S. & Fujime, S. Dynamic light-scattering study on polymerization process of muscle actin. *Biophys. Chem.* **25,** 253–269 (1986).

221. Condeelis, J. How is actin polymerization nucleated in vivo? *Trends Cell Biol.* **11,** 288–293 (2001).

222. Wegner, A. Treadmilling of actin at physiological salt concentrations. *J. Mol. Biol.* **161,** 607–615 (1982).

223. dos Remedios, C. G. *et al.* Actin binding proteins: regulation of cytoskeletal microfilaments. *Physiol. Rev.* **83,** 433–73 (2003).

224. Senderowicz, A. M. *et al.* Jasplakinolide's inhibition of the growth of prostate carcinoma cells in vitro with disruption of the actin cytoskeleton. *J. Natl. Cancer Inst.* **87,** 46–51 (1995).

225. Koestler, S. A. *et al.* F- and G-actin concentrations in lamellipodia of moving cells. *PLoS One* **4,** e4810 (2009).

226. Lee, C. W. *et al.* Dynamic localization of G-actin during membrane protrusion in neuronal motility. *Curr. Biol.* **23,** 1046–56 (2013).

227. Riedl, J. *et al.* Lifeact: a versatile marker to visualize F-actin. *Nat. Methods* **5,** 605–7 (2008).

228. Rao, K. M. K., Currie, M. S., Padmanabhan, J. & Cohen, H. J. Age-Related Alterations in Actin Cytoskeleton and Receptor Expression in Human Leukocytes. *J. Gerontol.* **47,** B37–B44 (1992).

229. Bear, J. E., Rawls, J. F. & Saxe, C. L. SCAR, a WASP-related Protein, Isolated as a Suppressor of Receptor Defects in Late Dictyostelium Development. *J. Cell Biol.* **142,** 1325–1335 (1998).

230. Knowles, G. C. & McCulloch, C. A. Simultaneous localization and quantification of relative G and F actin content: optimization of fluorescence labeling methods. *J. Histochem. Cytochem.* **40,** 1605–12 (1992).

231. Bubb, M. R., Senderowicz, A. M., Sausville, E. A., Duncan, K. L. & Korn, E. D. Jasplakinolide, a cytotoxic natural product, induces actin polymerization and competitively inhibits the binding of phalloidin to F-actin. *J. Biol. Chem.* **269,** 14869–71 (1994).

232. Fox, J. E. B., Dockter, M. E. & Phillips, D. R. An improved method for determining the actin filament content of nonmuscle cells by the DNase I inhibition assay. *Anal. Biochem.* **117,** 170–177 (1981).

233. Tu, Y., Wu, S., Shi, X., Chen, K. & Wu, C. Migfilin and Mig-2 Link Focal Adhesions to Filamin and the Actin Cytoskeleton and Function in Cell Shape Modulation. *Cell* **113,** 37–47 (2003).

234. Erickson, H. P. Co-operativity in protein-protein association. *J. Mol. Biol.* **206,** 465–474 (1989).

235. Chothia, C. & Janin, J. Principles of protein-protein recognition. *Nature* **256,** 705–8 (1975).

236. Bray, D. & Thomas, C. Unpolymerized actin in fibroblasts and brain. *J. Mol. Biol.* **105,** 527–544 (1976).

237. Ujfalusi-Pozsonyi, K. *et al.* The effects of detergents on the polymerization properties of actin. *Cytom. Part A* **9999A,** NA-NA (2010).

238. Ikeuchi, Y., Iwamura, K., Machi, T., Kakimoto, T. & Suzuki, A. Instability of F-actin in

the absence of ATP: a small amount of myosin destabilizes F-actin. *J. Biochem.* **111,** 606–13 (1992).

239. Kang, H., Bradley, M. J., Elam, W. A. & De La Cruz, E. M. Regulation of actin by ion-linked equilibria. *Biophys. J.* **105,** 2621–8 (2013).

240. Oda, T., Makino, K., Yamashita, I., Namba, K. & Maéda, Y. Distinct structural changes detected by X-ray fiber diffraction in stabilization of F-actin by lowering pH and increasing ionic strength. *Biophys. J.* **80,** 841–851 (2001).

241. Béla, N. & Jencks, W. P. Depolymerization of F-Actin by Concentrated Solutions of Salts and Denaturing Agents [1]. *J. Am. Chem. Soc.* **87,** 2480–2488 (1965).

242. Rouayrenc, J.-F. & Travers, F. The First Step in the Polymerisation of Actin. *Eur. J. Biochem.* **116,** 73–77 (1981).

243. Estes, J. E., Selden, L. A. & Gershman, L. C. Tight binding of divalent cations to monomeric actin. Binding kinetics support a simplified model. *J. Biol. Chem.* **262,** 4952–7 (1987).

244. Frieden, C., Lieberman, D. & Gilbert, H. R. A fluorescent probe for conformational changes in skeletal muscle G-actin. *J. Biol. Chem.* **255,** 8991–3 (1980).

245. Blikstad, I. & Carlsson, L. On the dynamics of the microfilament system in HeLa cells. *J. Cell Biol.* **93,** 122–128 (1982).

246. Srivastava, J. & Barber, D. Actin co-sedimentation assay; for the analysis of protein binding to F-actin. *J. Vis. Exp.* (2008). doi:10.3791/690

247. Wu, Hong and Parsons, T. Cortactin, an 80/85-Kilodalton Src substrate, is a filmanetous actin binding protein enriched in the cell cortex. *J. Cell Biol.* **120,** 1417–1426 (1993).

248. Eddy, R. J., Han, J. & Condeelis, J. S. Capping protein terminates but does not initiate chemoattractant-induced actin assembly in Dictyostelium. *J. Cell Biol.* **139,** 1243–53 (1997).

249. Carlsson, L., Markey, F., Blikstad, I., Persson, T. & Lindberg, U. Reorganization of actin in platelets stimulated by thrombin as measured by the DNase I inhibition assay. *Proc. Natl. Acad. Sci. U. S. A.* **76,** 6376–6380 (1979).

250. Turi, A. Lu, R.C. Lin, P.-C. Effect of heat on the microtubule disassembly and its relationship to body temperatures. *Biochem. Biophys. Res. Commun.* **100,** 584–590 (1981).

251. Wendel, H. & Dancker, P. Kinetics of actin depolymerization: influence of ions, temperature, age of F-actin, cytochalasin B and phalloidin. *Biochim. Biophys. Acta - Protein Struct. Mol. Enzymol.* **873,** 387–396 (1986).

252. Rodbard, D., Kapadiia, G. & Chrambach, A. Pore gradient electrophoresis. *Anal. Biochem.* **157,** 135–157 (1971).

253. Pollard, T. D. & Cooper, J. A. Actin, a central player in cell shape and movement. *Science*

(80-.). **326,** 1208–1212 (2009).

254. Coué, M., Brenner, S. L., Spector, I. & Korn, E. D. Inhibition of actin polymerization by latrunculin A. *FEBS Lett.* **213,** 316–318 (1987).

255. Lyubchenko, T. a, Wurth, G. a & Zweifach, A. The actin cytoskeleton and cytotoxic T lymphocytes: evidence for multiple roles that could affect granule exocytosis-dependent target cell killing. *J. Physiol.* **547,** 835–847 (2003).

256. Allison, D. W., Gelfand, V. I., Spector, I. & Craig, A. M. Role of Actin in Anchoring Postsynaptic Receptors in Cultured Hippocampal Neurons: Differential Attachment of NMDA versus AMPA Receptors. *J. Neurosci.* **18,** 2423–2436 (1998).

257. Dambournet, D., Hong, S. H., Grassart, A. & Drubin, D. G. in 139–160 (2014). doi:10.1016/B978-0-12-801185-0.00007-6

258. McDonald, D., Carrero, G., Andrin, C., de Vries, G. & Hendzel, M. J. Nucleoplasmic β-actin exists in a dynamic equilibrium between low-mobility polymeric species and rapidly diffusing populations. *J. Cell Biol.* **172,** (2006).

259. Diamond, M. I. *et al.* Subcellular localization and Ser-137 phosphorylation regulate tumor-suppressive activity of profilin-1. *J. Biol. Chem.* **290,** 9075–86 (2015).

260. Kiuchi, T., Nagai, T., Ohashi, K. & Mizuno, K. Measurements of spatiotemporal changes in G-actin concentration reveal its effect on stimulus-induced actin assembly and lamellipodium extension. *J. Cell Biol.* **193,** 365–80 (2011).

261. Bubb, M. R., Spector, I., Beyer, B. B. & Fosen, K. M. Effects of jasplakinolide on the kinetics of actin polymerization. An explanation for certain in vivo observations. *J. Biol. Chem.* **275,** 5163–70 (2000).

262. Bereiter-Hahn, J., Lück, M., Miebach, T., Stelzer, H. K. & Vöth, M. Spreading of trypsinized cells: cytoskeletal dynamics and energy requirements. *J. Cell Sci.* **96 (Pt 1),** 171–88 (1990).

263. Walther, C. G., Whitfield, R. & James, D. C. Importance of Interaction between Integrin and Actin Cytoskeleton in Suspension Adaptation of CHO cells. *Appl. Biochem. Biotechnol.* **178,** 1286–302 (2016).

264. Pollack, R. & Rifkin, D. Actin-containing cables within anchorage-dependent rat embryo cells are dissociated by plasmin and trypsin. *Cell* **6,** 495–506 (1975).

265. Baird, N. A. *et al.* HSF-1-mediated cytoskeletal integrity determines thermotolerance and life span. *Science* **346,** 360–3 (2014).

266. Su, E. J. & Herr, A. E. Electrophoretic cytometry of adherent cells. *Lab Chip* **17,** 4312 (2017).

267. Bunnell, T. M., Burbach, B. J., Shimizu, Y. & Ervasti, J. M. -Actin specifically controls cell growth, migration, and the G-actin pool. *Mol. Biol. Cell* **22,** 4047–4058 (2011).

268. Kabsch, W., Mannherz, H. G., Suck, D., Pai, E. F. & Holmes, K. C. Atomic structure of

the actin-DNAse-I complex. *Nature* **347,** 37–44 (1990).

269. Duncombe, T. A. *et al.* Hydrogel Pore-Size Modulation for Enhanced Single-Cell Western Blotting. *Adv. Mater.* **28,** 327–334 (2016).

270. Ståhlberg, J., Jönsson, B. & Horváth, C. Theory for electrostatic interaction chromatography of proteins. *Anal. Chem.* **63,** 1867–1874 (1991).

271. Queiroz, J. A., Tomaz, C. T. & Cabral, J. M. S. Hydrophobic interaction chromatography of proteins. *J. Biotechnol.* **87,** 143–159 (2001).

272. Doyle, P. S., Bibette, J., Bancaud, A. & Viovy, J. L. Self-assembled magnetic matrices for DNA separation chips. *Science (80-.).* **295,** 2237 (2002).

273. Fu, J., Yoo, J. & Han, J. Molecular sieving in periodic free-energy landscapes created by patterned nanofilter arrays. *Phys. Rev. Lett.* **97,** 018103 (2006).

274. Han, J., Turner, S. W. & Craighead, H. G. Entropic Trapping and Escape of Long DNA Molecules at Submicron Size Constriction. *Phys. Rev. Lett.* **83,** 1688–1691 (1999).

275. Liu, L., Li, P. & Asher, S. Entropic trapping of macromolecules by mesoscopic periodic voids in a polymer hydrogel. *Nature* 141–144 (1999).

276. Van Den Brink, S. C. *et al.* Single-cell sequencing reveals dissociation-induced gene expression in tissue subpopulations. *Nat. Methods* **14,** 935–936 (2017).

277. Goltsev, Y. *et al.* Deep profiling of mouse splenic architecture with CODEX multiplexed imaging. *bioRxiv* (2018).

278. Darmanis, S. *et al.* Simultaneous Multiplexed Measurement of RNA and Proteins in Single Cells. *Cell Rep.* **14,** 380–389 (2015).

279. Frei, A. P. *et al.* Highly multiplexed simultaneous detection of RNAs and proteins in single cells. *Nat. Methods* **13,** 269–275 (2016).

280. Albayrak, C. *et al.* Digital Quantification of Proteins and mRNA in Single Mammalian Cells. *Mol. Cell* **61,** 914–924 (2016).

281. Wolff, C., Schott, C., Porschewski, P., Reischauer, B. & Becker, K.-F. Successful protein extraction from over-fixed and long-term stored formalin-fixed tissues. *PLoS One* **6,** e16353 (2011).

282. Torsvik, A. *et al.* U-251 revisited: Genetic drift and phenotypic consequences of long-term cultures of glioblastoma cells. *Cancer Med.* **3,** 812–824 (2014).

283. Timerman, D. & Yeung, C. M. Identity confusion of glioma cell lines. *Gene* **536,** 221–2 (2014).

284. Madren, S. M. *et al.* Microfluidic device for automated synchronization of bacterial cells. *Anal. Chem.* **84,** 8571–8 (2012).

285. Na, S. *et al.* Rapid signal transduction in living cells is a unique feature of

mechanotransduction. *Proc. Natl. Acad. Sci. U. S. A.* **105,** 6626–6631 (2008).

286. Henjes, F. *et al.* Strong EGFR signaling in cell line models of ERBB2-amplified breast cancer attenuates response towards ERBB2-targeting drugs. *Oncogenesis* **1,** e16 (2012).

287. Sniadecki, N. J., Han, S. J., Ting, L. H. & Feghhi, S. Micropatterning on Micropost Arrays. *Cell Biol. Methods Cell Biol.* **121,** 61–73 (2014).

288. Yang, M. T., Fu, J., Wang, Y., Desai, R. A. & Chen, C. S. Assaying stem cell mechanobiology on microfabricated elastomeric substrates with geometrically modulated rigidity. *Nat. Protoc.* **6,** 187–213 (2011).

289. Bharadwaj, S., Thanawala, R., Bon, G., Falcioni, R. & Prasad, G. L. Resensitization of breast cancer cells to anoikis by Tropomyosin-1: role of Rho kinase-dependent cytoskeleton and adhesion. *Oncogene* **24,** 8291–8303 (2005).

290. Cramer, L. P., Briggs, L. J. & Dawe, H. R. Use of fluorescently labelled deoxyribonuclease I to spatially measure G-actin levels in migrating and non-migrating cells. *Cell Motil. Cytoskeleton* **51,** 27–38 (2002).

291. Deborah K. Wilkins *et al.* Hydrodynamic Radii of Native and Denatured Proteins Measured by Pulse Field Gradient NMR Techniques†. (1999). doi:10.1021/BI991765Q

292. Liu, W., Chen, D., Du, W., Nichols, K. P. & Ismagilov, R. F. SlipChip for immunoassays in nanoliter volumes. *Anal. Chem.* **82,** 3276–3282 (2010).

293. Cass, A. E. G. & Cass, T. *Immobilized Biomolecules in Analysis: A Practical Approach*. (Oxford University Press, 1998).

294. Cras, J. ., Rowe-Taitt, C. ., Nivens, D. . & Ligler, F. . Comparison of chemical cleaning methods of glass in preparation for silanization. *Biosens. Bioelectron.* **14,** 683–688 (1999).

295. Taylor, S. Impact of surface chemistry and blocking strategies on DNA microarrays. *Nucleic Acids Res.* **31,** 87e–87 (2003).

296. Lovatt, D. *et al.* Transcriptome in vivo analysis (TIVA) of spatially defined single cells in live tissue. *Nat. Methods* **11,** 190–6 (2014).

Appendix A.

EP cytometry protocol

This work was developed in collaboration with Dr. Chi-Chih Kang, Dr. Kevin Yamauchi, Dr. Elly Sinkala, Dr. Todd Duncombe and Dr. Amy Herr. The content is reproduced with permission from: C. Kang, K. A. Yamauchi, J. Vlassakis, E. Sinkala, T.A. Duncombe and A. E. Herr. Single-cell resolution western blotting (2016) *Nat. Prot.* **11**, 1508-1530.

REAGENTS

- Applicable cell line: The human U373 glioblastoma cell line (U373 MG) and U373-GFP cell line are used in this protocol. The U373-GFP is the U373 MG cells stably transduced with GFP by lentiviral infection (multiplicity of infection = 10). Both U373 MG and U373-GFP cell lines were kindly provided by Prof. S. Kumar's Laboratory[66]. In this protocol, we have shown both successful and failed scWB experiment performed using U373 MG cells. We have also demonstrated that scWB can be successfully applied in other mouse (i.e., mouse neural stem cell[65]) and human cell lines (i.e., breast cancer cell SKBR3[106] as well as clinical human breast cancer samples[106].
  ! CAUTION The "U373" human glioblastoma cell line used in this study is not the original U373, but a misidentified U251 human glioblastoma cell line. The "U373" is genetically non-distinct from the U251 based on ATCC, International Cell Line Authentication Committee and other references[282,283]. We employed the GFP protein in U373-GFP cells for system characterization only without any biological interpretation (i.e., real time in-well lysis and comparison of uniform and pore-gradient scWB).
  ! CAUTION Cell lines should be regularly checked to ensure that the cells are neither misidentified nor infected with mycoplasma.
- 3-(Trimethoxysilyl)propyl methacrylate (98%, Sigma-Aldrich, cat. no. 440159)
  !CAUTION 3-(Trimethoxysilyl)propyl methacrylate is combustible. Handle with gloves in a chemical fume hood.
- Acetic acid (ACS grade, ≥99.7%, Sigma-Aldrich, cat. no. 695092) **!CAUTION** Acetic acid is highly flammable and may cause severe skin burns and eye damage. Avoid contact with skin, eyes and clothing, and handle with gloves in a chemical fume hood.
- Methanol (ACS grade, ≥99.7%, Sigma-Aldrich, cat. no. 179337) **!CAUTION** Methanol is highly flammable and is toxic on inhalation, on contact with skin and if swallowed. Avoid contact with skin, eyes and clothing, and handle with gloves in a chemical fume hood.
- Tetramethylethylenediamine (TEMED; Sigma-Aldrich, cat. no. T9281) **!CAUTION** TEMED is highly flammable, corrosive and is toxic on inhalation, on contact with skin and if swallowed. Avoid contact with skin, eyes and clothing, and handle with gloves in a chemical fume hood.
- Ammonium persulfate (APS; Sigma-Aldrich, cat. no. A3678).

- β-mercaptoethanol (Sigma-Aldrich, cat. no. M3148) **!CAUTION** β-mercaptoethanol is toxic on inhalation, on contact with skin and if swallowed, and is hazardous to the aquatic environment. Avoid contact with skin, eyes and clothing, and handle with gloves in a chemical fume hood.
- 2,2-azobis[2-methyl-N-(2-hydroxyethyl) propionamide] (VA-086, Wako Chemical)
- *N,N'*-[(1-methylethylidene)bis(oxy-2,1-ethanediyl)]diacrylamide (abbreviated as diacrylamide ketal, DK) was synthesized in a one-step reaction and the procedure is described elsewhere[106].
- Acrylamide/bis-acrylamide, 30% solution (BioReagent, suitable for electrophoresis, 37.5:1, Sigma-Aldrich, cat. no. A3699) **!CAUTION** This material is highly toxic, carcinogenic and teratogenic. Avoid direct contact and review and understand all Material Safety Data Sheet (MSDS) information.
- Acrylamide/bis-acrylamide, 40% solution (BioReagent, suitable for electrophoresis, 29:1, Sigma-Aldrich, cat. no. A7802) **!CAUTION** This material is highly toxic, carcinogenic and teratogenic. Avoid direct contact and review and understand all Material Safety Data Sheet (MSDS) information.
- Acrylamide, 40% solution (for electrophoresis, Sigma-Aldrich, cat. no. A4058) **!CAUTION** This material is highly toxic, carcinogenic and teratogenic. Avoid direct contact and review and understand all Material Safety Data Sheet (MSDS) information.
- Triton X-100 (Fisher Scientific, cat. No.BP-151)
- Sodium dodecyl sulfate (SDS; BioReagent, suitable for electrophoresis, for molecular biology, ≥98.5% (GC), Sigma-Aldrich, cat. no. L3771) **!CAUTION** SDS is flammable solid and harmful if swallowed or inhaled. Avoid contact with skin and eyes, and handle with gloves.
- Sodium deoxycholate (≥97%, Sigma-Aldrich, cat. no. D6750) **!CAUTION** Sodium deoxycholate is harmful if swallowed or if inhaled. Avoid contact with skin and eyes, and handle with gloves.
- 0.5M Tris-HCl pH 6.8 (Teknova, cat no. T1568)
- 1.5M Tris-HCl pH 8.8 (Teknova, cat no. T1588)
- Premixed 25X Tris-Glycine transfer buffer (Novex, cat. no. LC3675)
- 10X Tris-CAPS Anode buffer (Boston BioProducts, cat. no. BP-192)
- Premixed 10X Tris-glycine electrophoresis buffer (25 mM Tris, pH 8.3, 192 mM glycine, BioRad, cat. no. 161-0734)
- Deionized water (ddH_2O, 18.2 MΩ, obtained using an Ultrapure water system from Millipore)
- BPMAC, N-[3-[(3-benzoylphenyl)formamido]propyl] methacrylamide can be custom synthesized by PharmAgra Labs (cat. no. PAL0603)[66,106,126] or a positional isomer (para-

form, N-[3-[(4-benzoylphenyl)formamido]propyl] methacrylamide) of the BPMAC was synthesized in-house[65,70].

- Tris Buffered Saline with Tween 20 (20X TBST, Santa Cruz Biotechnology, cat. no. sc-281695)
- Phosphate buffered saline (PBS, pH 7.4, Gibco, cat. no. 10010-023)
- Bovine Serum Albumin (BSA; heat shock fraction, protease free, fatty acid free, essentially globulin free, pH 7, ≥98%, Sigma-Aldrich, cat. no. A7030)
- Petroleum jelly (Cumberland Swan Petroleum Jelly cat. no. 18-999-1829)
- Gel Slick solution (Lonza, cat. co. 50640)
- Photoresist SU-8 2025 (MicroChem, cat. no. Y111069) **!CAUTION** SU-8 2025 is flammable and may cause severe skin and eye irritation. Avoid contact with skin, eyes and clothing, and handle with gloves in a chemical fume hood.
- SU-8 developer (MicroChem, cat. no.Y020100) **!CAUTION** SU-8 developer is slightly toxic, combustible flammable and may cause severe skin and eye irritation. Avoid contact with skin, eyes and clothing, and handle with gloves in a chemical fume hood.
- 75% (wt/vol) titanium diisopropoxide bis(acetylacetonate) in isopropanol. (Sigma-Aldrich, cat. no. 325252) **!CAUTION** Titanium acetylacetonate is flammable and has acute toxicity (oral, dermal, inhalation). Avoid contact with skin, eyes and clothing, and handle with gloves in a chemical fume hood.
- Isopropyl alcohol (Sigma-Aldrich, cat. no. W292907) **!CAUTION** Isopropyl alcohol is flammable and may cause skin and eye irritation. Avoid contact with skin, eyes and clothing, and handle with gloves in a chemical fume hood.
- Acetone (Sigma-Aldrich, cat. no. 320110) **!CAUTION** Acetone is flammable and may cause skin and eye irritation. Avoid contact with skin, eyes and clothing, and handle with gloves in a chemical fume hood.
- 36.5-38% w/w% Hydrochloric acid (Fisher Scientific cat. no. A144) **!CAUTION** Concentrated HCl is a strong acid and causes burns by all exposure routes. Use only under a chemical fume hood with proper personal protective equipment.

EQUIPMENT

- Standard cell culture equipment (laminar flow hood, humidified tissue culture incubator at 37 °C and 5% CO_2, water bath at 37 °C, fridge and freezer) to grow cells
- Standard cell culture disposables, including sterile tissue culture flasks and sterile serological pipettes, to grow cells
- 10 cm or 15 cm Petri dishes (VWR, cat. no. 25384-342)

- Bath sonicator (Bransonic 220; Branson Ultrasonics)
- Vacuum line and nitrogen gas line
- Centrifuge (Thermo Scientific, Sorvall ST 8 Small Benchtop Centrifuge, cat. no. 75007200)
- Centrifuge tubes, 15 ml (Thermo Scientific Nunc, 15ml Conical Sterile Polypropylene Centrifuge Tubes, cat. no. 339651)
- SU-8 Si mold for uniform gel and glass mold for pore-gradient microgel. The SU-8 glass mold fabrication details have been described previously[106] and detailed in the **PROCEDURE**. The mold is pre-coated with GelSlick prior to usage to increase the hydrophobicity.
- Gel electrophoresis chamber
- Rotator (Thermo Scientific, Compact Digital Waving Rotator, cat. no. 88880021)
- Razor blades (VWR, cat. nos. 55411-050) **!CAUTION** Razor blades are sharp. Handle with care.
- Plain glass slide (25 mm x 75 mm x 1 mm, VWR, cat. no. 16004-422)
- Diamond scribing pen (Ted Pella Inc., cat. no. 54468)
- Slide breaker (e.g., Fletcher's Running and Nipping Pliers for Glass & Acrylic, Fletcher-Terry Company LLC, cat. no. 06-111)
- Cell strainer (Falcon Tube with Cell Strainer Cap, 35 μm PET filter, BD, cat. no. 352235)
- Light microscope (MFL-06 Duo-scope Microscope)
- UV illumination system (Hamamatsu Lightning Cure LC5) **!CAUTION** UV light is hazardous. Appropriate personal protective equipment should be worn while using UV source.
- Imaging software (Metamorph)
- Power supply (Biorad Powerpac Basic)
- 4-well rectangular slide plate (Thermo Scientific NUNC, cat. no. 267061)
- 5- place slide mailer (Heathrow Scientific cat. no. HS159836)
- Fluorescence microarray scanner (i.e., Genepix 4300A)
- Epi-fluorescence microscope system, including microscope (Olympus IX71 inverted fluorescence microscope), CCD camera (Andor, iXon+ EMCCD camera), and mercury lamp light source (Lumen Dynamics, X-cite)
- Image analysis software (NIH Image J)
- Mini centrifuge (VWR, Galaxy mini centrifuge)
- Manual staining assembly - staining dish and rack handle (Thermo Scientific, cat.no.110)

Wheaton 900200 20 Slide Glass Staining Dish with Removable Slide Rack

- Microscope slide storage box (VWR, cat no. 82003)
- Chrome mask (aBeam Technologies, Hayward, California). The design and purchase of chrome mask have been described for fabricating pore-gradient microgel[106].
- Near UV light source (OAI, San Jose, California). An upward facing UV source is required to follow the alignment protocol described in this protocol.
- Long pass filter plastic sheet (390 nm, #39-426, Edmund Optics, Barrington, New Jersey)
- Spin coater (Brewer Science, Rolla, Missouri)
- Mask aligner (OAI Series 200 aligner, San Jose, California)
- 3-inch diameter silicon wafer (University Wafer, cat. no. 1196)
- 3-inch diameter glass wafer (University Wafer, cat. no. 1610)

REAGENT SETUP

- **10% (wt/vol) APS**. Dissolve 10 mg of APS in 100 µl ddH_2O. Store at 4 ^oC for short term (< 7 days) storage.

  ▲ **CRITICAL** Freshly prepare before use.

- **10% (vol/vol) TEMED**. Dissolve 10 µl of TEMED in 100 µl ddH_2O. Store at 4 ^oC for short term (< 7 days) storage.

  ▲ **CRITICAL** Freshly prepare before use.

- **5% (wt/vol) SDS**. Dissolve 0.5 g of SDS in 10 ml ddH_2O. Store at room temperature (20~25 ^oC). The maximum recommended storage time is 6 months.
- **5% (vol/vol) Triton X-100**. Dissolve 0.5 ml of Triton X-100 in 10 ml ddH_2O. Store at room temperature. The maximum recommended storage time is 6 months.
- **100 mM BPMAC**. Dissolve 70.048 mg of BPMAC in 2 ml DMSO. Aliquot into 100 µl per 0.65 ml Eppendorf tube. Store at -20 ^oC. Shield from light. Avoid freeze and thaw cycles. The maximum recommended storage time is 3 months.
- **1X TBST**. Washing buffer for in-gel immunoprobing steps. Add 50 ml of 20X TBST to 950 ml of ddH_2O to make a 1X TBST solution. Store the buffer solution at 4^oC. Final concentration of Tween 20 in 1X TBST is 0.05%. The maximum recommended storage time is 3 months.
- **2% (wt/vol) BSA/TBST**. Antibody dilution buffer for in-gel immunoprobing steps. Dissolve 2 g of BSA in 100 ml of 1X TBST. Store at 4 ^oC. The maximum recommended storage time is 3 months.
- **3% (wt/vol) VA-086 photo-initiator solution**. Dissolve 30 mg of VA-086 in 1 ml ddH_2O.

▲ **CRITICAL** Freshly prepare before use.

- **1X Tris-CAPS solution**. Add 50 ml of 10X Tris-CAPS to 450 ml of ddH_2O to make a 1X Tris-CAPS solution. Store the buffer solution at room temperature. The maximum recommended storage time is 3 months.
- **1% (vol/vol) HCl solution**. Add 5 ml of concentrated HCl (36.5-38% w/w%) to 495 ml of ddH_2O. Store the 1% HCl solution in a secondary container in the corrosive cabinet of the fume hood. The maximum recommended storage time is 6 months.
- **400 mM diacrylamide ketal solution**. Dissolve 108.1 mg of lyophilized diacrylamide ketal (270.32 Da) in 1 ml of 1X Tris-CAPS solution. Shake the solution until dissolved. Aliquot the solution into microcentrifuge tubes. Store the tubes in a dark environment at -20˚C for long term storage. The maximum recommended storage time is 3 months.
- **Silane solution**. For a 400 ml silane solution, add 80 ml of 3-(Trimethoxysilyl)propyl methacrylate and 120 ml of acetic acid to 200 ml of ddH_2O in a glass Erlenmeyer flask. Mix well and degas in the sonicator.

▲ **CRITICAL** Freshly prepare before use.

- **Lysis/electrophoresis buffer**. For a 500 ml lysis/electrophoresis buffer solution, add 25 ml of 10X Tris-glycine electrophoresis buffer (final concentration 0.5X), 2.5 g of SDS (final concentration 0.5% wt/vol), 1.25 g of sodium deoxycholate (final concentration 0.25% wt/vol), and 500 µl of Triton X-100 (final concentration 0.1% vol/vol) to 474.5 ml of ddH_2O in a 500 ml glass container. Dissolve and mix well before use. Store at 4 ^oC. The maximum recommended storage time is 3 months.
- **Harsh stripping buffer**. For a 100 ml harsh stripping buffer solution, add 12.5 ml of 0.5M Tris-HCl pH 6.8 buffer (final concentration 62.5 mM Tris-HCl), 2 g of SDS (final concentration 2% wt/vol), and 800 µl of β-mercaptoethanol (final concentration 0.8% vol/vol) to 87 ml of ddH_2O in a 100 ml glass container. Dissolve and mix well before use. Store at room temperature in the chemical fume hood. The maximum recommended storage time is 3 months.
- **Gel precursor solution**. For a 10%T, 2.7 %C gel precursor solution, add 25 µl of 1.5M Tris-HCl pH 8.8 buffer (final concentration 75 mM Tris-HCl), 166.7 µl of 30%T Acrylamide/bis-acrylamide solution, and 15 µl of 100 mM BPMAC (final concentration 3 mM) to 265.3 µl of ddH_2O in a 1.5 ml Eppendorf tube. Vortex to mix the solution. Spin down to remove solution from the cap of the Eppendorf tube by mini centrifuge, carefully puncture the cap of the Eppendorf tube with a syringe needle and attach a vacuum line to degas in a sonicator for 6 min. Add 10 µl of 5% SDS (final concentration 0.1 % vol/vol), 10 µl of 5 % Triton X-100 (final concentration 0.1 % vol/vol), 4 µl of 10% APS (final concentration 0.08 % vol/vol), and 4 µl of 10% TEMED (final concentration 0.08 % vol/vol) to the degassed gel precursor solution. Mix well without introducing bubbles and load immediately in between the glass slide and wafer.

▲ **CRITICAL** Freshly prepare before use.

- **Pore-gradient microgel precursor solution**. For a 11%T, 3.3%C pore-gradient precursor

solution, add 183.3 µl of 30%T Acrylamide/bis-acrylamide solution, 166.7 µl of 3% VA-086 (final concentration 1% wt/vol), and 15 µl of 100 mM BPMAC (final concentration 3 mM) to 135 µl of ddH_2O in a 1.5 ml Eppendorf tube. Vortex to mix the solution. Spin down to remove solution from the cap of the Eppendorf tube by mini centrifuge, carefully puncture the cap of the Eppendorf tube with a syringe needle and attach a vacuum line to degas in a sonicator for 6 min.

▲ **CRITICAL** Freshly prepare before use.

- **99:1 De-crosslinking gel precursor solution**. For a 12%T pore-gradient precursor solution with a molar crosslinker ratio of 99:1 diacrylamide ketal to methylene bisacrylamide, add 20 µl of 25X Tris-Glycine transfer buffer (1X final concentration), 138.4 µl of 40%T Acrylamide solution, 2.7 µl of 40%T Acrylamide/bis-acrylamide solution (233 nmol bisacrylamide), 166.7 µl of 3% VA-086 (final concentration 1% wt/vol), 57.6 µl of 400 mM diacrylamide ketal (23.1 µmol DK), and 15 µl of 100 mM BPMAC (final concentration 3 mM) to 99.6 µl of ddH_2O in a 1.5 ml Eppendorf tube. Vortex to mix the solution. Spin down to remove solution in the Eppendorf cap by mini centrifuge, carefully puncture the cap of the Eppendorf tube with a syringe needle and attach a vacuum line to degas in a sonicator for 6 min.

  ▲ **CRITICAL** A correct composition of the 99:1 De-crosslinking gel precursor solution is critical to the success of the experiments. Freshly prepare before use.

- **Adhesion primer**. The adhesion primer used here is 2% titanium acetylacetonate. Dilute the 75% (wt/vol) titanium diisopropoxide bis(acetylacetonate) in anhydrous isopropanol.

  ▲ **CRITICAL** Freshly prepare before use.

PROCEDURE

Glass-SU-8 fabrication (Optional) ● TIMING ~ 1 h per wafer

▲ **CRITICAL STEP** For users who elect to perform scWB using uniform microgels, proceed to the standard Si-SU-8 fabrication procedure at the MicroChem website (http://www.microchem.com/pdf/SU-82000DataSheet2025thru2075Ver4.pdf).
▲ **CRITICAL STEP** Here we detail the steps for fabricating ~30 µm height SU-8 micropillars on top of a glass wafer using SU-8 2025. We recommend using SU-8 2025 for fabricating a 30-60 µm height. Instructions are available from the MicroChem website (http://www.microchem.com/pdf/SU-82000DataSheet2025thru2075Ver4.pdf) and previous publications[106,284].
! **CAUTION** The SU-8 photoresist, SU-8 developer, acetone and isopropyl alcohol are all toxic and flammable. Perform all the steps inside the chemical fume hood with proper personal protection equipment, including lowered hood sash, fire-resistant lab coat and nitrile gloves. The fabrication is recommended to be performed in the cleanroom to prevent contamination from dust particles.

1 | Dehydrate a 3-inch glass wafer by placing it on a 110 °C hot plate for a minimum of 10 min.

Once dehydrated, transfer the 3-inch glass wafer to the chuck center of the spin coater. Apply a vacuum and verify the wafer is strongly adhered to the chuck.

▲ CRITICAL STEP A clean glass wafer is extremely important for the subsequent homogenous SU-8 coating. The wafer can be cleaned by rinsing with acetone, followed by isopropyl alcohol. The wafer should be fully dehydrated before coating.

2 | Use the dropper to homogenously distribute the adhesion primer on the wafer.

3 | After 30 s in contact with the glass wafer, remove the adhesion primer by spinning as tabulated below:

Recommended coating condition	Spinning Speed	Acceleration	Time
Distribute adhesion primer on the wafer	500 rpm	100 rpm s^{-1}	5 s
	3000 rpm	500 rpm s^{-1}	30 s

4 | Immediately after the spin is complete, pour ~5 ml of SU-8 2025 on to the wafer and spin as tabulated below to create a homogenous 30 µm base SU-8 layer on the wafer:

Recommended coating condition	Spinning Speed	Acceleration	Time
Distribute SU-8 evenly on the wafer	500 rpm	100 rpm s^{-1}	30 s
Achieve the desired SU-8 height	2500 rpm	500 rpm s^{-1}	30 s

5 | Soft-bake the wafer on a 110 °C hot plate for 3 min. Allow the wafer to cool to room temperature before proceeding to step 6.

6 | Place the wafer on the mask aligner and expose at 360 nm for 250 mJ cm^{-2}. No photolithography mask is applied in this step as the purpose is to create a uniform SU-8 base layer.

▲ CRITICAL STEP The exact UV exposure power and time is instrument-dependent. The UV exposure dose recommended here is according to the MicroChem guidelines.

7 | Bake the wafer on a 110 °C hot plate for 5 min. Allow the wafer to cool to room temperature before proceeding to step 8.

8 | Place the wafer on the chuck center of the spin coater and make sure the wafer adheres by applying vacuum.

9 | Pour ~5 ml of SU-8 2025 on to the wafer and spin as tabulated below to create the other homogenous 30 µm height SU-8 layer on the wafer:

Recommended coating condition	Spinning Speed	Acceleration	Time
Distribute SU-8 evenly on the wafer	500 rpm	100 rpm s^{-1}	30 s
Achieve the desired SU-8 height	2500 rpm	500 rpm s^{-1}	30 s

10 | Soft-bake the wafer on a 65 °C hot plate for 6 min. Allow the wafer to cool to room temperature before proceeding to step 11.

11 | Place the wafer on the mask aligner and expose at 365 nm for 250 mJ cm^{-2} through the desired mask.
▲ CRITICAL STEP For the U373 glioblastoma cell line used to generate the data in the **ANTICIPATED RESULTS**, we designed the photolithography mask to have microwells with a 30 µm diameter.

12 | Place the wafer on a 65 °C hot plate for 3 min. Ramp the hot plate up to 90 °C and hold the temperature for 7 min. Afterwards, allow the wafer to cool to room temperature before proceeding to step 13.

13 | Prepare a SU-8 developer bath for development, and place it on a rotator. Submerge the wafer with the SU-8 side facing up. Gently swirl the SU-8 developer bath for 2-2.5 min.
▲ CRITICAL STEP Over- and under-developing the SU-8 will lead to deformed micropillars. To check whether the development is complete, remove the wafer from the SU-8 developer bath and spray with isopropyl alcohol. If a white film appears during the isopropyl alcohol rinse additional development time is required. Perform development in 20 s increments. For fine SU-8 features, we recommend to use the spray bottle to spray the SU-8 developer on the wafer for an extra 30 s.

14 | After development, rinse the wafer with water and dry with a nitrogen gun.

15 | Place the wafer on a 110 °C hot plate to hard-bake for 10-15 min. Allow the wafer to cool slowly to room temperature.
▲ CRITICAL STEP Performing the hard bake step will increase wafer durability. Ensure the wafer is cooled down slowly otherwise the wafer may crack owing to the thermal stress.

Batch silanization of glass slides ● TIMING 40–50 min per batch

! CAUTION The 3-(Trimethoxysilyl)propyl methacrylate, methanol, and acetic acid are all flammable, and methanol is toxic. Perform Steps 19-24 inside a chemical fume hood with proper personal protection equipment, including lowered hood sash, fire-resistant lab coat and nitrile gloves.

16 | Score the corner of the glass microscope slides (75 mm x 25 mm) with a diamond-tipped pen. The mark will reference the methacrylate-functionalized glass side (silanized slide), which is facing down when the score is positioned in the upper right corner of the slide.

17 | Arrange the marked microscope slides in a removable slide rack (i.e., 30-slot rack) and place the slide rack in a glass slide staining dish. Two glass slides can be placed back to back in a single slot. In this configuration, ensure the eventual silanized side is in contact with the silane solution.

18 | Prepare the silane solution and degas for 30 min.

19 | Pour the degassed silane solution into the glass slide staining dish. Ensure the silane solution fully covers all the slides.

20 | Tap the glass slide staining dish to remove all the bubbles trapped in between the slides. Let the silanization reaction proceed for 30 min.

21 | Remove the slide rack and place it in a glass slide staining dish containing methanol. Hold the handle of the slide rack and gently shake (with the glass slide submerged in methanol) to remove any residual silane solution.

22 | Repeat the washing step in Step 21 with fresh methanol.

23 | Remove the slide rack from the methanol solution and place it in a container containing fresh deionized water. Hold the handle of the slide rack and gently shake (with the glass slide submerged in deionized water) to remove methanol.

24 | Repeat Step 22 and 23 two more times in the same methanol and deionized water containers.

25 | Place the slides in a container with fresh deionized water. Quickly dry the slides with a nitrogen gun.

26 | Store the silanized slides in a standard slide storage box. The silane solution can be reused to coat a total of three batches of glass slides.

■ **PAUSE POINT** The silanized slides can be stored at room temperature for up to 2 months.

scWB PAG slide fabrication ● TIMING 20-30 min per slide

27 | Based on the parameters for selecting suitable PAGE separation conditions, the user should prepare either uniform (option A) or pore-gradient (option B) PAG slides.

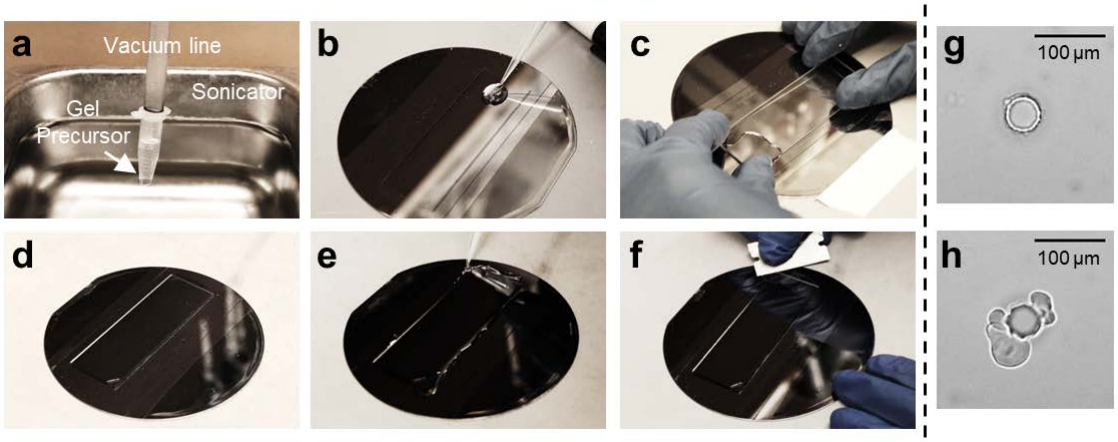

Figure A.1: scWB PAG slide fabrication. (a) Step 27A(ii): degas the gel precursor solution. (b) Step 27A(iii): pipette the gel precursor solution onto the SU-8 mold. (c) Step 27A(iv): place a silanized slide against the SU-8 mold. (d) Step 27A(v): gently press the silanized slide to remove excess solution. (e) Step 27A(vi): rehydrate the edge of the slide with PBS. (f) Step 27A(vii): detach the PAG slide from the SU-8 mold with a razor blade. Fabrication of the PAG slide is complete. Bright-field micrographs show a well-formed (g) and deformed (h) microwell. Scale bars, 100 µm. The PAG slide in the image is a standard microscope slide (25 × 75 mm).

Option A. uniform scWB PAG slide fabrication ● TIMING 20-30 min per slide

(i) Tape an SU-8 mold onto the lab bench to hold in place during processing.

(ii) Make the gel precursor solution and degas with a bath sonicator and vacuum line to eliminate bubbles (**Error! Reference source not found.**a).

(iii) Add detergents (SDS and Triton X-100) and initiators (APS and TEMED) to gel precursor solution, mix well without forming bubbles. Pipet a 250 µl droplet near one of the short edges of the SU-8 mold (**Error! Reference source not found.**b).

(iv) Hold a silanized slide with silanized side facing down. Lower one of the short edges until the silanized slide is in contact with the SU-8 mold and the precursor droplet. The slide should be at an approximately 30^{o} angle. Slowly lower the slide until the silanized slide is flat against the SU-8 mold (**Error! Reference source not found.**c).

(v) After loading, press gently on the slide to squeeze excess precursor from the gap and to ensure the micropillars on the SU-8 mold are in contact with the slide (**Error! Reference source not found.**d). Depending on the amount of the initiator added, the chemical polymerization process can complete in ~15 min.

? TROUBLESHOOTING

(vi) After chemical polymerization of the PAG, add 1-2 ml of PBS to rehydrate the edge of the slide and facilitate release of the slide from the SU-8 mold (Error! Reference source not found.e).

(vii) Gently slide a razor blade underneath the slide and lift straight up to detach the PAG slide from the SU-8 mold (Error! Reference source not found.f).

? TROUBLESHOOTING

! CAUTION The gel precursor solution, containing acrylamide, APS, and TEMED, has oral and inhalation acute toxicity and is a skin irritant. The acrylamide also has neurotoxicity. The SU-8 mold needs to be rinsed in running deionized water after each use to remove any residual precursor solution.

(viii) Check the PAG slide under a brightfield microscope to ensure the integrity of the microwells (**Error! Reference source not found.** g and h).

? TROUBLESHOOTING

(ix) Place the PAG slide in a 4-well rectangular slide plate filled with PBS before use. The side of the slide with the PAG layer faces up.

■ **PAUSE POINT** The PAG slides can be stored in PBS at 4 °C up to a week before use.

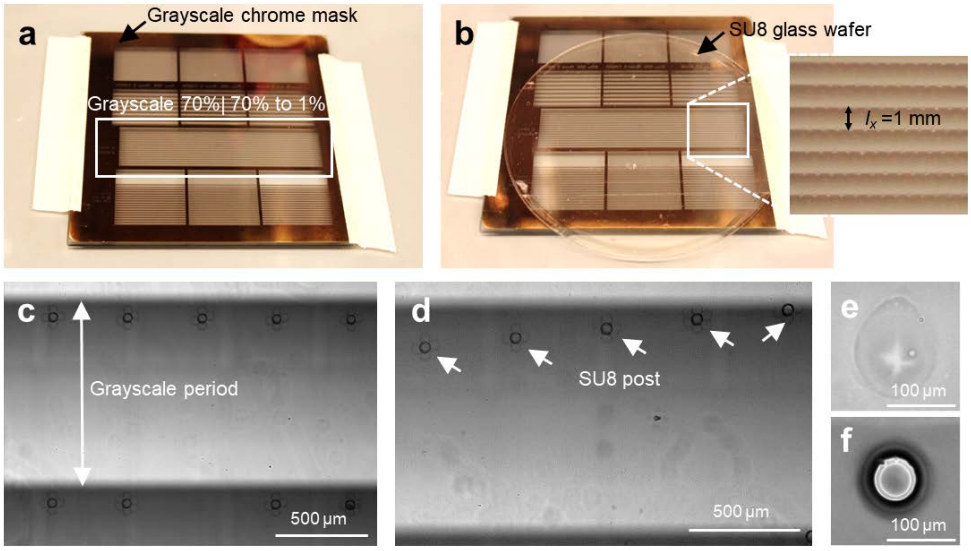

Figure A.2: Pore-gradient PAG slide fabrication. (a) Step 27B(i): tape the chrome mask in place. (b) Step 27B(vii): align the SU-8 glass mold to the chrome mask. Determine whether the SU-8 micropillars are aligned (c) or misaligned (d) to the grayscale gradient; scale bars, 500 µm. The arrows point to SU-8 micropillars under the microscope. After photopolymerization, a bright-field micrograph shows a shallow and deformed microwell (e) that suggests under-

photopolymerization of the PAG near the microwell; scale bar, 100 µm. (f) Bright-field micrograph shows a circular, well-formed microwell, indicating suitable photopolymerization conditions; scale bar, 100 µm.

Option B. Pore-gradient scWB PAG slide fabrication ● TIMING 15-20 min per slide

(i) Tape a chrome mask onto the borosilicate glass plate (chrome side facing up) to hold in place during alignment and exposure steps (Figure A.2a).

(ii) Place the hydrophobic SU-8 glass mold on top of the gradient chrome mask with the SU-8 micropillar facing up.

(iii) Pipet a droplet of the pore-gradient gel precursor solution or 99:1 de-crosslinking gel precursor solution atop the SU-8 glass mold near one of its short edges (similar placement as depicted Error! Reference source not found.b). The volume of the droplet should be sufficient to fill the mold when the glass slide is added with little to no excess. A 150 µl droplet volume is typical, but will vary with height of the micropillars on the SU-8 mold and the size of the silanized slide used.

(iv) Hold a silanized slide with silanized face down. Lower one of the short edges until the silanized slide is in contact with the SU-8 mold and the precursor droplet. The slide should be at an approximately 30^{o} angle. Slowly lower the slide until the silanized slide is flat against the SU-8 glass mold.

(v) After placing the silanized slide atop the mold, press gently on the slide to squeeze excess precursor from the gap and to ensure the micropillars on the SU-8 mold are in contact with the slide. Remove excess precursor solution with a task wipe.
▲ CRITICAL STEP Excess solution can lead to the silanized slide slipping on the mold when the setup is moved - resulting in a misaligned array.

(vi) Holding the base borosilicate glass plate, slowly transfer the plate to a brightfield microscope stage.

(vii) First by eye, align the micropillars on the SU-8 glass mold with the grayscale gradient on the chrome mask (Figure A.2b). Once the alignment is close, use the microscope to verify the alignment and adjust as necessary. Confirm on both the left and right sides of the array that the micropillars are similarly aligned to the grayscale mask (as demonstrated in Figure A.2c).
▲ CRITICAL STEP Misalignment of the SU-8 micropillars and the grayscale mask opacity gradient will result in fabrication of PAG separation lanes each with a different pore-gradient microgel relative to the microwell, thus resulting in unwanted protein mobility variation among the different PAGE separation lanes (Figure A.2d).

(viii) Carefully move the entire assembly on to the UV system. If the mold slips with respect to the mask, repeat the previous alignment step (Step vii).

(ix) Apply UV light to photopolymerize the pore-gradient microgel. From the UV light source, the components for fabrication are arranged in the following order: UV filter, glass plate, chrome mask, SU-8 glass mold, gel precursor solution, and a silanized slide.
▲ CRITICAL STEP Optimization of the UV exposure conditions will be required for every new condition. UV exposures that are of insufficient duration or intensity will result in under-photopolymerization of pore-gradient microgel. Under-polymerized gels will lead to deformation of the microwell and poor cell settling in the deformed

microwells (Figure A.2e). Over-photopolymerization of the pore-gradient microgel will create a small pore size at the head of the microgel, thus resulting in incomplete electrophoretic injection of protein into the PAG.

(x) Carefully move the whole assembly to the benchtop.

(xi) Gently slide a razor blade underneath the slide and lift straight up to detach the PAG slide from the SU-8 mold.

(xii) Check the pore-gradient PAG slide under a brightfield microscope to ensure the integrity of the microwells (Figure A.2 e and f).

? TROUBLESHOOTING

(xiii) Place the pore-gradient PAG slide in a 4-well rectangular slide plate with the gel side facing up. If the pore-gradient microgel contains diacrylamide ketal (DK) crosslinker (DK PAG slide), fill the plates with the 1X Tris-CAPS buffer solution. The Tris-CAPS buffer will be exchanged with PBS prior to proceeding to cell settling (Steps 28-33).

■ **PAUSE POINT** The gradient PAG slides can be stored in buffer at 4 ºC up to a week before use. The scWB of pore-gradient PAG slides are performed under the same procedures (Steps 28-50) of uniform PAG slides.

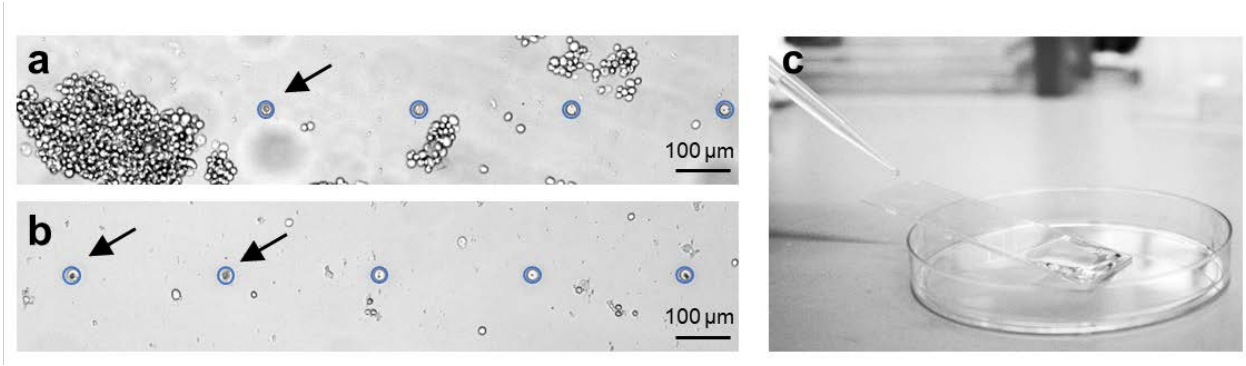

Figure A.3: Examples of poor and ideal single-cell settling into microwells. (a) Bright-field micrograph of microwell array and cells shows that U373 cells may aggregate during settling and lead to unfavorable cell settling into the microwells. (b) Bright-field micrograph of microwell array and cells shows good cell settling into microwells with limited cell clumping. Scale bars, 100 µm; blue circles indicate microwells, and arrows point to microwells with a single cell per microwell occupancy. (c) Step 37: PBS wash of excess cells from the PAG slide.

Settling of cells into microwells ● TIMING 30–60 min

▲ CRITICAL STEP When working with mammalian cells, Steps 28-33 should be performed in a biohazard cabinet in an enclosed laboratory facility. All work with cell lines should comply with institutional and governmental biosafety regulations.

28 | Use an ~80% confluent monolayer of cells in a T75 flask. With respect to U373 glioblastoma cells, an 80% confluent T75 flask corresponds to ~2 × 10^6 cells. As 2 x 10^5 cells gives adequate settling per PAG slide, one T75 flask is sufficient to perform 10 different scWB experiments. A full microscope slide (75 mm x 25 mm) is used as a standard here; however a half slide (37.5 mm x 25 mm) can also be used for rapid prototyping. A half slide can be made

by using a diamond scribe to score a silanized slide and then breaking at that score using a slide breaker either before or after PAG polymerization.

29 | Harvest the cells from the flask using a general tissue culture procedure. Pellet the cells by centrifugation and resuspend the cells in ice-cold PBS with a concentration of ~1 x 10^6 cells per ml.

30 | If applicable, employ cell imaging such as nucleus staining (Hoechst 33342) and apoptotic cell staining (Alexa Fluor 647 conjugated-Annexin V) using standard methods[66].

31 | Filter the cell suspension through a cell strainer with 35 μm PET filter cap to create a single cell suspension.

▲ CRITICAL STEP Obtaining a single cell suspension is important for settling cells at one cell per microwell occupancies, as aggregated cells are excluded from the microwells during settling (Figure A.3a). If cell clumping or aggregation is observed, filter the cell suspension through the cell strainer. The selection of the filter cap is cell-size dependent.

32 | Remove the PAG slides from PBS. With a task wipe, dry the glass side of the PAG slide. Place the slide in a Petri dish with the PAG side up.

33 | Pipette 200 μl of filtered cell suspension (containing ~2 × 10^5 cells) and gently disperse the cell suspension on top of a PAG slide. Periodically, check the cell settling efficiency using brightfield microscopy (Figure A.3b). The cell settling efficiency (microwell occupancy) is defined in **Box 2**. Gently tap the Petri dish to agitate the cell suspension. The 10 min of settling is sufficient for most cell lines tested. Place the Petri dish with cells on ice to maintain cell viability.

▲ CRITICAL STEP Continue directly to the "Single-cell PAGE and photoblotting" procedure (Steps 34-50). Some protein expression and/or post-translational modifications may be altered over time[285,286].

? TROUBLESHOOTING

Single-cell PAGE and photoblotting ● TIMING 5–10 min per slide

▲ CRITICAL STEP Appropriate precautions should be taken to protect users from UV exposure.

34 | Turn on the UV illumination system in advance to stabilize the UV light bulb. Set the power

to a UV dose sufficient for subsequent protein photocapture to the PAG.

35 | Aliquot 10-15 ml of lysis/electrophoresis buffer into a 15 ml conical tube and preheat in a 50-55 ^{o}C water bath.

36 | After confirming sufficient cell settling under a brightfield microscope, remove excess cell suspension by tilting the PAG slide at a 45° angle.

37 | Gently apply a steady stream of 1 ml PBS by pipetting to the higher edge of the tilted PAG slide to gently wash excess cells off the surface of the PAG slide (Figure A.3c).

38 | Verify that the majority of cells on the surface have been removed by visual inspection with a light microscope (Figure A.3b). Repeat the rinsing process (Step 37) if excess cells are observed on the gel surface.

▲ **CRITICAL STEP** Do not tilt the scWB slide over 90 degrees, flush PBS solution rigorously, or flush the PBS solution in the middle of the PAG slide as these handling processes may remove settled cells from the microwells.

? TROUBLESHOOTING

39 | Apply a 1 cm diameter spot of petroleum jelly to the bottom of the scWB electrophoresis chamber to temporarily adhere the PAG slide to the chamber.

40 | Place the PAG slide in the scWB electrophoresis chamber with the PAG layer facing up.

41 | If applicable, employ whole-cell imaging.

42 | Connect the electrophoresis chamber to the high voltage power supply.

43 | Set up the electrophoresis power supply to provide a constant voltage. The suggested *E* is 40 V cm^{-1}.

44 | Pour 50 ^{o}C preheated lysis/electrophoresis buffer rapidly over the PAG slide to fill the electrophoresis chamber. Immediately upon pouring, start timing the lysis duration.

▲ **CRITICAL STEP** Lysis/electrophoresis buffer should be applied quickly so that cells lyse simultaneously. Abrupt pouring of the lysis/electrophoresis buffer from >15 cm above the electrophoresis chamber in a fully vertical orientation may dislodge cells and wash out protein lysate. We suggest pouring the lysis/electrophoresis buffer from the short side of the electrophoresis chamber at a ~30 deg tilt to minimize the number of dislodged cells[66].

45 | At 25 s of lysis duration, apply the electric field to initiate PAGE. For separating GAPDH and βTub in a 10%T, 2.7%C PAG, a 30 s electrophoresis duration is a good starting point.

! **CAUTION** The high voltage power supply can source a lethal electrical current. Please consult the instruction manual before use and use proper safety precautions. Confirm that the power supply is properly and safely connected to the electrophoresis chamber.

46 | Immediately at PAGE completion apply UV light (350~360 nm, ~1.8 J cm^{-2})[65] to immobilize the separated proteins in the PAG.

▲ **CRITICAL STEP** Apply UV to activate protein immobilization immediately after PAGE, otherwise the proteins will rapidly diffuse out of the PAG and adversely impact LOD.

! **CAUTION** Use proper UV protection, such as UV-blocking goggles and UV-blocking face shield to protect user and surrounding personnel from UV illumination.

! **CAUTION** Confirm that the electric field is turned off immediately after electrophoresis and before handling the electrophoresis chamber.

47 | After protein immobilization, carefully remove the PAG slide from the electrophoresis chamber using tweezers.

48 | Using a task wipe, wipe off the petroleum jelly from the glass side of the PAG slide.

49 | Place the PAG slide into a 4-well rectangular slide plate filled with TBST buffer.

50 | Place the plate on the rotator for at least 30 min to remove residual lysis/electrophoresis buffer, as residual SDS will impact antibody and antigen binding during the subsequent in-gel immunoprobing process (Steps 56-69).

■ **PAUSE POINT** The PAG slide can be stored in 1X TBST at 4 ºC for short-term storage (~1 week). For long-term storage (> 1 week), rinse the PAG slide three times with deionized water to remove salts retained in the PAG slide, gently blow-dry by nitrogen gun, and store in a slide mailer at room temperature protected from light.

De-crosslinking of DK PAG slide ● TIMING 30 min

▲ **CRITICAL STEP** Perform this step only if you are using a DK PAG slide. For uniform or pore-gradient PAG slides fabricated using methylene bisacrylamide and no DK, proceed directly to in-gel immunoprobing (Steps 56-69).

! **CAUTION** 1% HCl, pH 1.1 solution is used here to de-crosslink the DK PAG slide. Always handle the solution in a secondary container inside the fume hood with personal protective equipment.

51 | Place the DK PAG slide into a glass container with 1% HCl.

52 | Incubate 30 min to complete de-crosslinking reaction[106].

▲ **CRITICAL STEP** Performing de-crosslinking reaction for less than 10 min may result in partially de-crosslinked DK gels, resulting in spatially non-uniform immunoprobing.

53 | Carefully remove and place the DK PAG slide into a Petri dish filled with deionized water. Gently rinse 3 to 4 times.

54 | Carefully remove and place the DK PAG slide into a 4-well rectangular slide plate filled with TBST buffer.

55 | Place the plate on the rotator for at least 30 min for buffer equilibration before performing in-gel immunoprobing process (Steps 56-69).

■ **PAUSE POINT** The DK PAG slide can be stored in 1X TBST at 4 ºC for short-term storage (~1 week). For long-term storage (> 1 week), rinse the DK PAG slide three times with deionized water to remove salts contained in the PAG slide, gently blow-dry by nitrogen gun, and store in a slide mailer at room temperature protected from light.

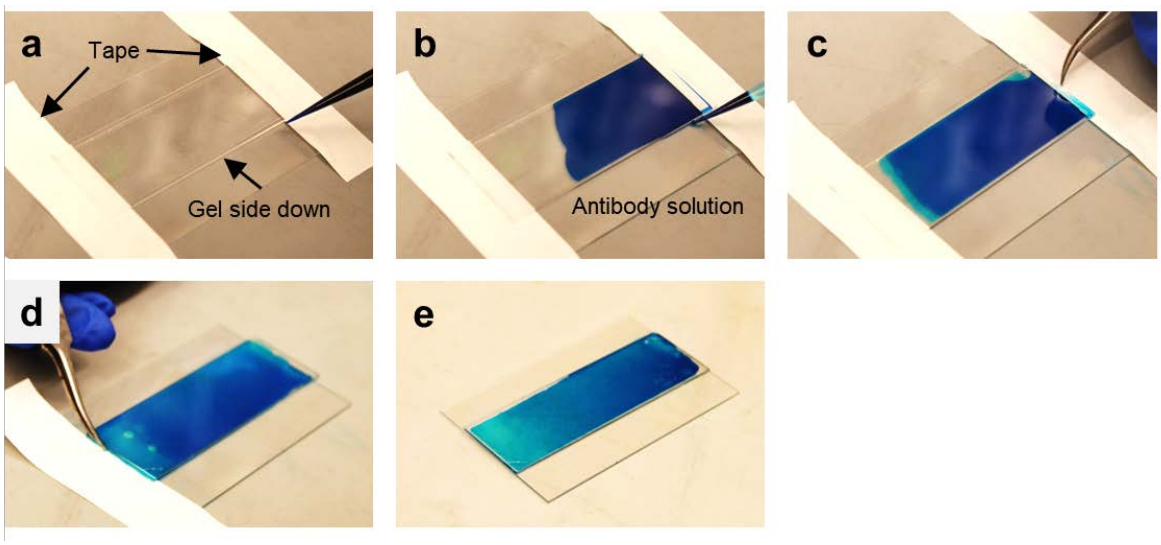

Figure A.4: Handling of the scWB device during immunoprobing. Bright-field images of blue dye visualize the scWB immunoprobing handling procedure. (a) Step 59: place lab tape on a clean glass surface and place the short sides of the slide on the tape to lift the PAG slide up with the gel side facing down. (b) Step 60: use capillary action to load the antibody solution between the two layers. (c–e) Step 61: remove tape strips to release the scWB device for the next assay steps. The PAG slide in the image is a standard microscope slide (25 x 75 mm).

In-gel immunoprobing ● TIMING 4–6 h

56 | Prepare 100 µl of primary antibody immunoprobing solution by diluting stock solution of primary antibodies in 2% BSA/TBST solution. 1-5 µg of primary antibody per slide is a recommended starting mass, although each assay must be optimized. Place the prepared primary antibody solution on ice before use.

57 | To perform immunoprobing on a single PAG slide, place two pieces of tape slightly shorter than the width of the PAG slide onto a clean surface, such as a plain 50 mm x 75 mm glass slide. The tape pieces will act as spacers to hold the scWB slide slightly off the glass surface creating a gap where Ab solution will wick in via capillary action. It is noted that two PAG slides can also be immunoprobed simultaneously with the gel sides facing each other.

58 | Remove PAG slide from TBST and remove excess TBST by tilting the slide and wipe the glass side of the PAG slide with a task wipe. Do not touch the gel side of the PAG slide as damage to the PAG may result.

59 | Place the PAG slide onto the tape with gel side facing down (Figure A.4a).

60 | Inject prepared primary antibody solution by pipetting into the air-filled gap between PAG slide and glass (Figure A.4b).

61 | Gently move both sides of the tape off the glass to deliver a uniform antibody solution (Figure A.4 c-e).

▲ CRITICAL STEP Do not create bubbles in the gap which will result in local antibody depletion and increased immunoprobing variance.

62 | Incubate primary antibody at room temperature for 1 to 2 h. This time interval is a general recommendation, with the exact duration not critical.

63 | Gently remove the PAG slides and place in a 4-well rectangular slide plate filled with TBST buffer.

64 | Place the 4-well rectangular slide plate on a rotator for a 10 to 30 min wash cycle. This time interval is a general recommendation, with the exact duration not critical.

65 | Repeat the washing steps (Steps 63-64) twice using fresh TBST.

66 | Prepare 100 µl secondary antibody immunoprobing solution per pair of slides by diluting stock solution of secondary antibody in 2% BSA/TBST solution. 1-5 µg of secondary antibody is the recommended starting mass, although each assay must be optimized. Place the prepared secondary antibody solution on ice before use.

67 | Repeat Steps 57-62 to prepare the slides for secondary antibody probing. Incubate at room temperature for 1 h.

▲ CRITICAL STEP Fluorophore conjugated secondary antibodies are used, so cover the slides with aluminum foil to shield from light exposure.

68 | Perform TBST washing as described in Steps 63-65.

69 | Remove TBST and rinse the PAG slide with deionized water three times to remove salts

contained in the PAG slide. Gently blow-dry with a nitrogen gun. The PAG slides are ready for imaging.

■ **PAUSE POINT** The PAG slides can be stored in a dehydrated condition in a slide mailer at room temperature, protected from light for over 4 months with negligible probing signal reduction[66].

? TROUBLESHOOTING

scWB PAG slide imaging ● TIMING varies with imaging apparatus

70 | After incubation of the scWB PAG slide with primary and fluorescently labeled secondary antibodies, proteins are quantified by fluorescence imaging. The scWB PAG slide can be imaged with a 2D fluorescence imaging system, such as a fluorescence microarray scanner or inverted epifluorescence microscope. The imaging system should have: (i) ~5 µm / pixel spatial resolution, (ii) compatibility with a standard microscope slide and an adjustable z-axis (depth) focus, (iii) a robust image stitching algorithm, as stitching artefacts will affect quantitation, and (iv) an LOD down to ~0.5 nM of Alexa Fluor-labeled secondary antibodies (27,000 molecules in a 50 µm diameter spot in a 40 µm thick gel), thus suitable for detection of ~50% of the mammalian proteome[65]. Representative imaging data is shown in the **ANTICIPATED RESULTS**.

scWB PAG slide stripping ● TIMING 30 min

71 | Place the PAG slide into the slide mailer.

72 | Fill the slide mailer with harsh stripping buffer. Close the cap of the slide mailer tightly.

! CAUTION β-mercaptoethanol has oral, inhalation, and dermal acute toxicity. Always handle the solution in a fume hood with personal protective equipment. Seal the slide mailer to prevent solution leakage during the stripping process.

73 | Place the slide mailer in a 55 ºC water bath for at least 30 min. Ensure the water level of the water bath is higher than the harsh stripping buffer level inside the slide mailer to achieve uniform stripping.

? TROUBLESHOOTING

74 | Remove the slide mailer from the water bath. Pour the harsh stripping buffer into a labeled waste container.

! CAUTION β-mercaptoethanol has both chronic and acute aquatic toxicity. Please consult your institutional safety guidelines for the appropriate disposal method.

75 | Rinse the PAG slides at least three times with deionized water.

▲ CRITICAL STEP Image the PAG slides after stripping to ensure thorough removal of the antibodies (i.e., undetectable protein signal or SNR < 3).

76 | If intending to perform another round of immunoprobing, place the PAG slides in a 4-well rectangular slide plate with TBST on the shaker for at least 30 min to reconstitute the proteins before repeating Steps 56-69. Otherwise, gently blow-dry with a nitrogen gun and store in a slide mailer at room temperature, with PAG slides shielded from light exposure.

■ PAUSE POINT The PAG slides can be stored dehydrated.

•TIMING

Step 1-15, Glass-SU-8 fabrication (Optional): ~ 1 h per wafer

Step 16-26, Batch silanization of glass slides: 40–50 min per batch

Step 27, scWB PAG slide fabrication: 20–30 min per slide

Step 28-33, Settling of cells into microwells: 30–60 min

Step 34-50, Single-cell PAGE and photoblotting: 5–10 min per slide

Step 51-55, De-crosslinking of DK PAG slide: 30 min

Step 56-69, In-gel immunoprobing: 4–6 h

Sep 70, scWB PAG slide imaging: time varies with imaging apparatus

Step 71-76, scWB PAG slide stripping: 30 min

Step 77-85, scWB image analysis (Optional): ~ 1 h per slide with multiple protein targets

? TROUBLESHOOTING

Troubleshooting advice can be found in **Table A1**.

Table A1 | Troubleshooting table.

Step	Problem	Possible reason	Solution
27A(v)	There are bubbles trapped in the PAG	The glass slide or the wafer is not clean	Confirm both the glass slide and the wafer are free of dust. The glass slide can be cleaned by methanol then rinsed by distilled water and blown dry
		The gel precursor solution is not fully degassed	Confirm there are no bubbles in the gel precursor solution before use
27A(vii)	The PAG peels off of the glass slide	Glass slide is not fully silanized	Confirm the glass slides are clean and methacrylate-functionalized before use
	The PAG adheres to the SU-8 mold	The SU-8 mold does not have a complete layer of dichlorodimethyl silane	Confirm the SU-8 mold is silanized before use
	The PAG does not polymerize	Wrong concentration or old APS or TEMED is used for polymerization	Prepare fresh APS or TEMED
		O_2 inhibits polymerization	Confirm the gel precursor solution is degassed. Use a cover to block O_2 flowing in during the polymerization process or perform polymerization under N_2 purge.
27A(viii)	Microwells are deformed (**Error! Reference source not found.**h)	The glass slide moved during polymerization	Confirm the polymerization is performed in a stationary environment

		The PAG slide moves during detachment from SU-8 mold	Hold the SU-8 mold in place while peeling up the gel
27B(xii)	Shallow microwells (Figure A.2e)	Low UV dose	Increase the UV exposure time, UV intensity, or the concentration of the gel precursor solution
	Deformed microwells	The SU-8 micropillar were misaligned to the grayscale gradient period (Figure A.2d)	Confirm the SU-8 micropillars are aligned to the grayscale gradient using brightfield microscopy
		The SU-8 micropillar are aligned to the edge of the grayscale gradient	Confirm the SU-8 micropillars are aligned 20 to 50 μm from the edge of the grayscale gradient (Figure A.2c).
33	Poor cell settling is observed	Not enough cells are used for settling on the PAG slide	Prepare cell suspension at a higher cell density
		Cell clumping	Filter the cells through a cell strainer multiple times and settle the cells immediately after filtering
		The microwell size and depth are not optimized	Fabricate a range of microwell diameters to select microwell size for the cell size under study
38	Poor cell settling is observed	Too many cells are rinsed off during washing	Gently rinse off excess cells during the washing step and check frequently under the microscope
69	No probing signal is observed	Poor cell settling	Optimize the cell density and microwell geometry

The lysis time is too long	Increased lysis time will increase protein diffusional loss during lysis; lysis time-dependent experiments may be needed to optimize this parameter
No UV photo-immobilization	Confirm the BPMAC is fresh and added into the gel precursor solution during polymerization
	Confirm the UV is on and the UV dose for protein immobilization is optimized. A housekeeping protein with high abundance can be used as a positive control
Primary antibodies are not target-specific	Verify the specificity and species reactivity of the primary antibody
Secondary antibodies do not recognize primary antibodies	Confirm species-specific secondary antibodies are used
Low-affinity protein	Increase the primary antibody concentration
Low abundance protein	Identify cell lines with higher expression levels of the target protein as positive controls
The PAG slides are over-stripped	Confirm the harsh stripping buffer composition and temperature. Reduce the stripping time if needed

	The detection system does not match with the fluorophore used	Verify the excitation wavelength and emission filter cube are suitable for the secondary antibodies used as well as verify the correct focal plane
Unexpected punctate signal	Aggregates from the secondary antibodies	Spin down the secondary antibodies (e.g., 10000g) before use
	Dust on the PAG slide	Confirm the PAG slides are probed and washed in a clean environment
High background	Primary or secondary antibody concentration is too high	Use a lower concentration of the primary or secondary antibodies
	Insufficient washing	Wash the PAG slides with fresh TBST 2-3 times after each incubation step
Poor protein injection	The PAG pore size is too small for large proteins with high molecular mass	Reduce and optimize the PAG pore size
Dispersed protein signal	Insufficient cell lysis or protein solubilization	Slightly increase the cell lysis time or increase the SDS concentration
Protein electro-migrates to an unexpected location	Insufficient solubilization or dissociation of protein complexes	Slightly increase the cell lysis time or increase the SDS concentration
Off-target probed signal	The primary or secondary antibodies are not target-specific	Verify the specificity and species reactivity of the antibodies

	Protein overrun to the next row of microwells	The electrophoresis time is too long	Slightly reduce the electrophoresis time
	Target protein bands are not resolved	Insufficient cell lysis or protein solubilization	Slightly increase the cell lysis time or increase the SDS concentration
		The PAG pore size or electrophoresis time is not optimized	Optimize the PAG pore size and electrophoresis time to fit the target proteins
73	Detectable protein signal after stripping	The antibodies are not fully removed during stripping process	Increase stripping time
			Prepare fresh harsh stripping buffer and reapply
			Confirm the water level of the water bath is higher than the harsh stripping buffer solution level in the slide mailer
			Confirm the temperature is 55 ^{o}C

Appendix B.

EP cytometry complex fractionation protocol

Goal: Separate and quantify protein complexes (e.g., F-actin) from monomeric protein species (e.g., G-actin) from single cells.

Prepare EP cytometry complex fractionation buffers

Materials:

- Tris HCl (1M, pH=7.5)
- Anhydrous $MgCl_2$
- Triton X-100
- Dithioerythritol (DTE)
- DI water
- 10X Tris glycine (pH=8.3)
- Sodium dodecyl sulfate (SDS)
- Sodium deoxycholate
- Urea

Prepare the stock buffer solutions listed in Tables 1-2. Store the buffers at 4 °C when not in use for up to 2 weeks. The F-actin stabilization buffer pH should be titrated to 7.4 by adding approximately 100 μL of 1.1% HCl.

Table B1: F-actin stabilization buffer based on formulation by Heacock[172].

Component	**MW (g/mol)**	**stock conc. (v/v%)**	**final conc. (M)**	**conc. v/v%**	**Amount, 500 mL buffer**	**unit**
Tris HCl (pH=7.5)	302.37	1 M	10 mM		5	mL
$MgCl_2$	95.211		0.002		0.0952	g
Triton X-100		100		1	5	mL
DTE	154.253		0.0005		Add fresh to aliquot prior to assay	g
Water					490	mL

Table B2: F-actin depolymerization buffer

Component	**stock conc. (v/v%)**	**final conc. (M)**	**conc. v/v%**	**Amount, 500 mL buffer**	**unit**
10x Tris Glycine (pH=8.3)	10x	0.5x		25	mL
SDS				2.5	g
Sodium deoxycholate				1.25	

Triton X-100	100		0.1	0.5	mL
Urea		8M		Add 12 g fresh to 25 mL buffer aliquot prior to assay	g
Water				318	mL

Prepare gel lids

Materials:

- 10x Tris glycine (pH=8.3)
- DI water
- 40%T 29:1 acrylamide/bisacrylamide
- 2% VA-086 (w/v) in DI water
- 500 μm thick spacers
- 2 glass plates
- GelSlick
- OAI UV source
- Triple-layer transparency mask taped to the bottom of one of the glass plates

1. Prepare gel precursor solution (10 mL) and degas for several minutes
    - 1 mL 10x Tris glycine
    - 5 mL 2% VA-086
    - 3.75 mL 40%T 29:1 acryalmide/bisacryalmide
    - 0.25 mL DI water
2. Treat glass plates with 1 mL of GelSlick solution and dry with KimWipe
3. Place spacers between the two glass plates
4. Pipette entire 10 mL gel precursor solution between the plates. Complete this step next to the UV source to prevent spilling PA gel precursor solution (Figure B.1)
5. Photopolymerize for 40s at 20 mW/cm^2 with no long-pass UV filter
6. Remove the top glass plate and use the spacer to pick up individual gel lids from the bottom glass plate. Put the gel lids directly into a 50 mL conical tube and fill with either the F-actin stabilization buffer or F-actin depolymerization buffer (25 mL). Store the gels at 4 °C and incubate in the buffer overnight before use. Gels may be put in fresh buffer after use, but should not be kept for more than 2 weeks.

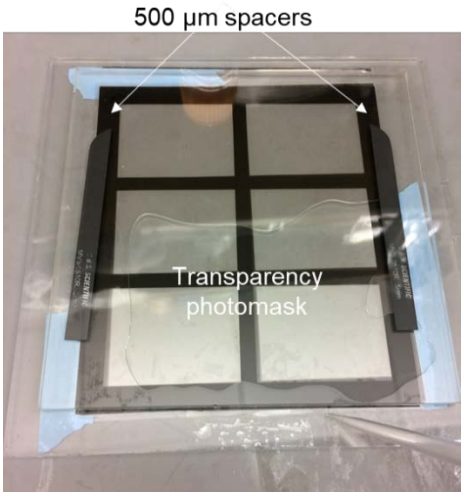

Figure B.1: Gel lid photopolymerization setup. The bottom glass plate is adhered to the transparency photomask which defines the length and width of the gel lid to be photopolymerized, while gel lid height is set by the spacers. Gel precursor solution is pipetted between the glass plates.

Prepare EP cytometry microwell array in PA gel

Materials

- Methacrylate silanized glass slides
- Polyacrylamide gel precursor solution (8%T, 29:1 acrylamide/bisacrylamide, 3 mM BPMAC)
- SU-8 micropost mold on silicon wafer

EP cytometry gel slides should be prepared as previously described and stored in 1X PBS at 4 °C until use[67].

Add fresh reagents to gel lid buffer solutions (at start of experiment)

F-actin depolymerization (1X RIPA+8M urea) gel lids:

1. Turn on water bath and set to 75 °C
2. Add 12 g of urea to separate 50 mL conical tubes for each separation assay to be performed.
3. Take out the gel lids in F-actin depolymerization buffer and remove 15.9 mL of buffer from the tube and add to the 12g urea conical tube to make 25 mL of 1X RIPA + 8M urea
4. Put the F-actin depolymerization buffer (1X RIPA + 8M urea) in the water bath to dissolve for ~10 min
5. Swirl the conical tubes to assist with dissolving the last of the urea
6. Remove excess buffer from the gel lid-containing tube and pour in the 1X RIPA + 8M urea solution in with the gel lid. Put the gel lid conical tube back in the 75 °C water bath

F-actin stabilization gel lids:

1. Add 25 mL of F-actin stabilization buffer (from the tubes containing the gel lids) multiplied by the number of separation assays to be performed in a glass bottle
2. Add 1.95 g of fresh DTE per 25 mL of buffer and swirl to dissolve
3. Remove excess buffer solution from the F-actin stabilization buffer gel lid conical tubes and replace with the buffer solution containing the DTE
4. Put the gel lid conical tubes in the water bath at 75 °C

Set up for separations

Materials:

- Custom 3D-printed electrophoresis chamber with graphite bar electrodes
- 1X PBS
- 10 mM Tris HCl pH=7.5
- 3 cm plastic dishes
- Loctite superglue
- 2 timers
- Microwell fractionation gels
- 4-well dish
- 25 mL of 1X TBST
- Tweezers
- Buffer waste bottles
- Biorad PowerPac basic power supply
- Banana plug electrical leads
- Hamamatsu LC-5 UV source

1. Attach leads to electrophoresis chamber and turn on power supply setting to constant voltage 90 V (30 V/cm)
2. Turn on Hamamatsu UV source lamp and allow to warm up for 10 minutes
3. Set up buffer waste bottles next to separation station
4. Fill a 3 cm dish with 10 mM Tris HCl (pH=7.5)

Prepare cell suspension and settle into microwell devices

1. Wash dish of cells with 1X PBS
2. Trypsinize cells for 3 min at 37 °C
3. Rinse dish with media and spin cells at 1000 rpm for 3 min
4. Resuspend cells in 1X PBS and immediately settle in microwell device as previously described[67]. Gently move the microwell gel back and forth every few minutes to disperse cells. Settle for a total of 10 minutes. Freshly trypsinized cells are required for each separation assay. Thus, experiments require as many dishes of cells as experiments. Confluent 1 cm dishes of BJ fibroblasts resuspended in 500 µL of PBS provide sufficient cell numbers. The cell suspension should be added at ~300 µL to the microwell gel.
5. Wash excess cells of the surface gently 3x with 1 mL 1X PBS

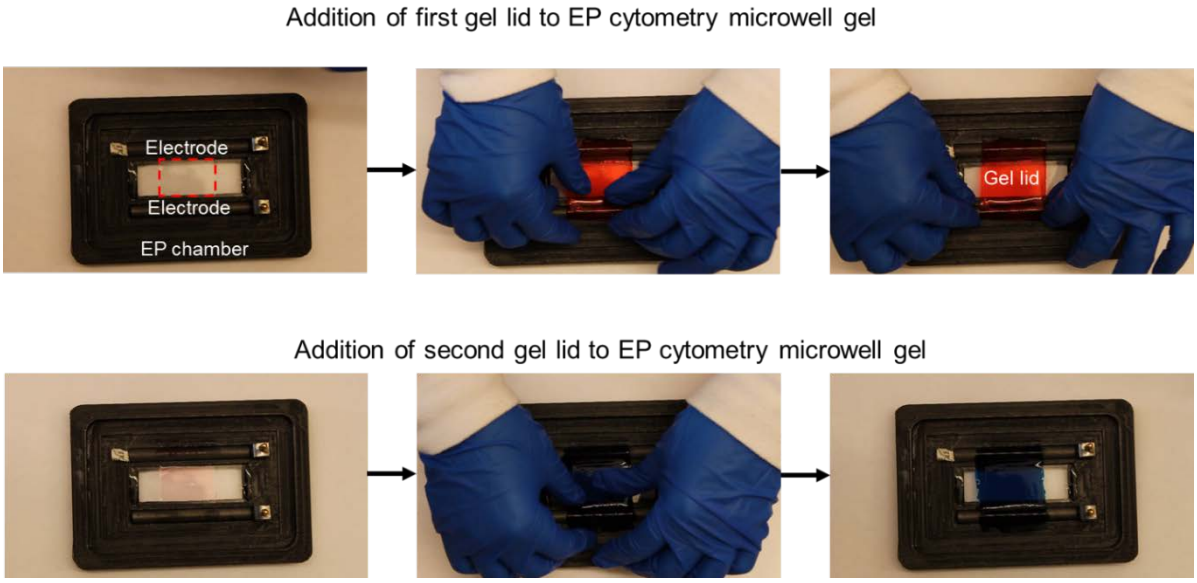

Figure B.2: Interfacing the gel lids with the EP cytometry microwell gel in the custom electrophoresis chamber. The microwell gel is outlined with a red dashed line in the upper left panel. A red and blue gel lid are added to the array in series.

Perform complex fractionation separations

1. Submerge EP cytometry microwell gel in the dish of Tris HCl buffer for ~10s
2. Add a ~1 mm diameter dab of superglue to the glass of the EP chamber where you will place the lower left corner of the EP cytometry gel
3. Remove the EP cytometry gel from the buffer and dry the back of the slide with a Kimwipe
4. Place the gel on the superglue (glass side down, gel side up) and press down lightly. Ensure the slide is straight (parallel to graphite electrodes).
5. Remove a tube of F-actin stabilization buffer containing the gel lid from the water bath. Lightly swirl the tube to remove the gel from the walls of the tube. Pour the buffer into buffer waste and let the gel lid slide to the opening of the tube.
6. Place the gel lid in contact with the two electrodes and over the surface of the microwell gel (Figure B.2)
7. Lyse cells for 45s
8. Turn on the E-field (30 V/cm) for 45-60s (45 for actin, 60 for GFP-actin in a 1-mm separation lane).
9. Turn off the E-field and turn on the UV source for 45s at 100% power. Be sure to wear UV goggles and face mask during UV exposure.
10. Reverse the lead connections to the EP chamber
11. Remove the gel lid from the microwell gel

12. Retrieve the F-actin depolymerization gel lid buffer tube and once again swirl the tube prior to pouring the contents into buffer waste, allowing the gel lid to slide to the opening of the tube.
13. Place the gel lid on the microwell gel and allow depolymerization to proceed for 45s.
14. Perform electrophoresis for 45-60s at 30 V/cm
15. Apply the UV for 45s at 100%
16. Remove the microwell gel from the EP chamber and put in a 4-well dish containing 1X TBST. Wash for at least 1 hour prior to immunoprobing

Immunoprobing, detection and quantitation

Immunoprobing, fluorescence imaging (on a Genepix Microarray scanner) and quantitation are all performed as previously described[110]. The EP cytometry image processing algorithm was slightly modified to accommodate the bi-directional separation format by shifting the ROIs to center the microwell in the ROI.

Appendix C.

On-chip chip culture of adherent fibroblasts

Prepared in collaboration with Dr. Yizhe Zhang and adapting aspects from a protocol prepared by Dr. Kevin Yamauchi

Goal: Fabricate and ECM-coated polyacrylamide gel on top of which a polyacrylamide gel microwell array can be fabricated. Cells can then be cultured within the microwell.

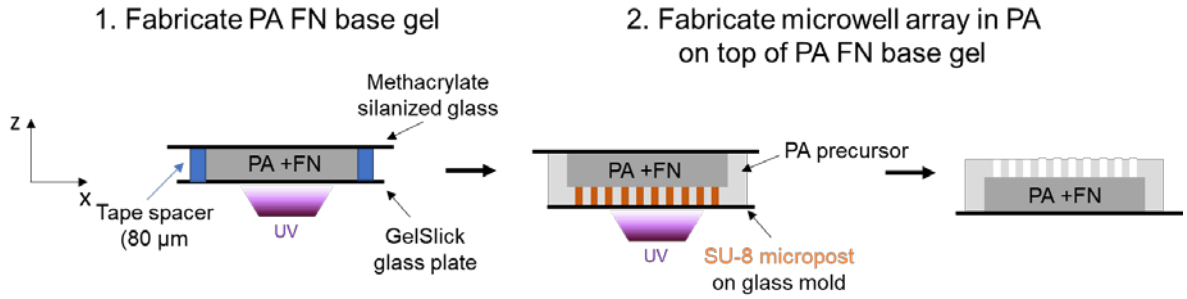

Figure C.1: Schematic workflow for fabrication of a polyacrylamide (PA) gel base layer containing fibronectin (FN) in a PA gel microwell device. First, the base layer is photopolymerized on methacrylated glass. Second, the polyacrylamide microwell gel is photopolymerized on top of the PA+FN base gel.

Preparing Glass SU8 mold

Materials:

- SU8 glass wafer,
- Adhesion primer solution (freshly prepared)
- Photomask
- SU8-2025

SU-8 microposts were patterned on glass wafers as previously described[67,106].

Prepare ECM-patterned EP cytometry device

Materials:

- ECM protein (e.g. Rhodamine Fibronectin, FN, or unlabeled FN prepared as a 20 μg/mL stock solution)
- Silanized glass slides
- GelSlick Solution (Lonza)
- Clean glass plate (or large glass slide)
- Scotch or Kapton tape (80 μm thick)
- Polyacrylamide gel precursor described below
- OAI UV source

I. Fabricate the substrate gel
    a. Prepare the polyacrylamide gel precursor containing FN (Table A1) and degas for several minutes
    b. GelSlick treat the glass plate by adding several hundred microliters of GelSlick to the glass and drying with a Kimwipe
    c. Add two strips of Kapton tape on the glass plate spaced apart by just under 1.5 cm
    d. Place the methacrylate silanized half glass slide on top of the Kapton tape spacers (silanized side down)
    e. Pipette the gel precursor between the glass plate and silanized glass (~100 μL per half slide; similar to the process for immunoprobing EP cytometry devices previously described[67])
    f. Wick excess precursor from the edges of the half slide with a Kimwipe
    g. Photopolymerize the polyacrylamide gel base layer and photocapture the FN with the OAI UV source (20 mW/cm^2 for 60s, no long-pass UV filter)
    h. Add 1 mL of water to the edges of the half slide and wait several minutes
    i. Remove the half slide from the bottom glass plate using a razor blade to carefully peel up the edge of the half slide

j. Rinse the half slide in DI water and dry in a nitrogen stream. The FN functionalized gel slide should be used immediately to fabricate the microwell array and seed cells (do not store prior to use because the FN is not stable).

Table C1: Polyacrylamide gel precursor solution composition including FN for an ECM-containing base layer

Component	Volume (μL)	Final Concentration
40%T 29:1 acrylamide/bisacrylamide	80	8%T
100 mM BPMAC	12	3 mM
10x Tris glycine	40	1x
LAP photoinitiator	20	0.2% v/v
FN (20 μg/mL)	200	10 μg/mL
DI water	48	-

II. Fabricate the microwell gel
   a. Prepare the microwell separation gel precursor solution (Table A2) and degas for several minutes
   b. (Optional) introduce 200 μL of GelSlick to the SU-8 on glass mold and spread across the surface with a full glass slide. Briefly rinse the mold with water and dry in a nitrogen stream.
   c. Pipette 200 μL of gel precursor solution on top of the mold
   d. Place the dried 8%T FN base layer gel down (gel side down) in the precursor solution. Move the gel slide around to remove air bubbles if necessary
   e. Allow the precursor components to diffuse into the PA FN gel base layer for 15 minutes
   f. Photopolymerize with OAI UV source (20 mW/cm^2 for 300s, with long-pass UV filter)
   g. Add 1 mL of water to the edge of the photopolymerized gel on the mold and wait for several minutes
   h. Use a razor blade to peel up the microwell gel from the mold surface
   i. Rinse the microwell gel device in DI water and dry in a nitrogen stream

Table C2: Polyacrylamide gel precursor solution composition including FN for an ECM-containing base layer

Component	Volume (μL)	Final Concentration

40%T 29:1 acrylamide/bisacrylamide	80	8%T
100 mM BPMAC	12	3 mM
10x Tris glycine	40	1x
VA-086 photoinitiator (2% w/v)	100	0.5% v/v
DI water	168	-

Cell Seeding

Materials:

- Ethanol
- sterile PBS
- BJ fibroblast cells
- DMEM media (DMEM (11965, Life Technologies) supplemented with 10% FBS, 1% penicillin/streptomycin, and 1% non-essential amino acids)
- 4-well plate or 3 cm petri dish for cell culture
- EP cytometry microwell device with 8%T FN base layer

III. Introduce cells to the ECM-patterned microwell device
   a. Sterilize the fabricated microwell gel in ethanol (100%) for ~30 minutes in the biosafety cabinet (cover with aluminum foil)
   b. Aspirate ethanol out of the container
   c. Immerse the gel in sterile PBS for 10 minutes (covered with aluminum foil)
   d. Aspirate PBS out of the container
   e. Trypsinize cells and re-suspend in media
   f. Pipette cell suspension onto the patterned gel (~150 µl for a half slide). Use the side of a pipette tip to spread the cell suspension across the slide if necessary. Suggested cell dilution for single-cell occupancy on the 100-µm well device (separation length: 1 mm; well-to-well spacing: 500 µm): ~90,000 cells/ml
   g. Let cells adhere to ECM pattern at 37 °C for 1 hour,
   h. Rinse the gel surface with media for cell culture and aspirate excess media before adding sufficient fresh media to submerge the gel slide. Check that excess cells are not still on the gel surface and repeat rinses until few remain on the gel surface
   i. Culture the cells overnight (at least 16 hours)

Appendix D.

EP cytometry algorithm complete code

```
function [struct] = roiGeneration(filename,horzspacing,vertspacing,struct)
% This function rotates and aligns a raw fluorescent image of a single-cell
% Western blot array and segments the image into regions-of-interest (ROIs)
% for downstream analysis. Each region of interest encompasses single-cell Western blot protein peak(s) in an area
% defined by the horizontal and vertical spacing between microwells in the
% array.

%   Outputs:
% Struct [structure]: A data structure containing objects:
%   struct.rois: 3D matrix with each ROI contained in a different z.
%   struct.angle: The angle of rotation to straighten the image (number, in degrees).
%   struct.rotate: The angle of rotation required to display the image with
%   separations running vertically instead of horizontally (number, in
%   degrees).
%   struct.array_bounds: User selected boundaries of the array as a 3x2
%   matrix (rows contain upper left, upper right, and lower left
%   coordinates respectively; first column contains x-coordinates; second column contains y-coordinates).
%   struct.name: The name of the protein target entered by the user
%   (string).
%   struct.wells_per_row: The number of wells per row based on the user
%   selected array bounds and horizontal well spacing.
%   struct.rows: Number of rows in the array

%   Inputs:
% filename [string]: A string containing the name of the fluorescence image
%                    to be processed.
% horzspacing [num]: Well-to-well spacing (horizontal, in pixels)
% vertspacing [num]: Well-to-well spacing (vertical, in pixels)
% struct [structure] (optional): A structure containing "angle" and
% "array_bounds" if the same image has already been analyzed by
% roiGeneration. The same ROIs will automatically be generated.
%% versions
% 0.1-Created April, 2016
% 0.2 (5.15.16): Updated to apply same transform for ROI generation if user
% inputs a struct with the fields "angle" and "rotate".
%0.3 (5.20.16): Added "rows" and "wells per row" fields to structure.

%% Check input arguments
switch nargin
   % If the user only provides the image, horizontal and vertical spacing
   case 3
      transform = 0;
   case 4
      transform = 1;

      tf = isstruct(struct);
         if tf == 0
             error('Input argument "struct" is not a structure.');

         return

         end
```

```
        % retrieve previously determined angle for transformation of image
        angle = struct.angle;

        % retrieve previously determined array boundaries
        array_bounds = struct.array_bounds;

        % extract the individual x an y coordinates of the array boundaries
        x_upperleftwell = array_bounds(1, 1);
        y_upperleftwell = array_bounds(1, 2);

        x_upperrightwell = array_bounds(2, 1);
        y_upperrightwell = array_bounds(2, 2);

        x_lowerrightwell = array_bounds(3, 1);
        y_lowerrightwell = array_bounds(3, 2);


    otherwise

        error('Invalid number of input arguments');

        return

end
%%
% ask the user the name of their protein target
prompt = 'What is the name of your protein target?';
str = input(prompt, 's');
struct.name = str;


% Load the image file in MATLAB
img = imread(filename);

    if transform == 0

        % Display more contrasted image in window
        contrasted_img = histeq(img);
        imshow(contrasted_img);

        % Display a message to the user asking them to look at the array
        title('Take a look at the array and determine if the wells are oriented left of the bands or right of the bands.
Then press any key');
        pause()

        % Construct a questdlg to ask the user how the image is currently oriented
        % for coarse rotation
        choice = questdlg('Are the wells currently left of the bands or right of the bands?', ...
        'Current array orientation', ...
        'Wells are left of bands','Wells are right of bands','Wells are right of bands');

        % Handle response
        switch choice

            case 'Wells are left of bands';
```

```
            disp([choice 'Okay, the image will be rotated to the right!'])
            rotate = -90;

        case 'Wells are right of bands';
            disp([choice 'Okay, the image will be rotated to the left!'])
            rotate = 90;
    end

    % Store the course rotation angle to orient the array vertically to
    % the struct

    struct.rotate = rotate;
  else

    rotate = struct.rotate;
  end

 % Display the course-rotated image
 imgrotated = imrotate(img, rotate);
 contrasted_img_r = histeq(imgrotated);
 imshow(contrasted_img_r);

 %If struct was not an input argument (and there is no previous
 %angle/array boundary values to draw from), the user will now manually
 %select the array boundaries.

while transform == 0
 test = 1;

 while test == 1
    % Prompt user to select the upper right well of the array.
    title('Please zoom in on the the middle of the upper left well and press any key.');

    % use mouse button to zoom in or out
    zoom on;
    pause()
    zoom off;

    % preallocate array bounds matrix
    array_bounds = zeros(3, 2);

    % prompt user to click on the middle of the upper left well
    title('Please click on the middle of the upper left well.');

    [x_click,y_click] = ginput(1);

    % store the coordinates the user selected for the upper left well
    x_upperleftwell = x_click;
    y_upperleftwell = y_click;
    zoom out;

    array_bounds(1,:) = [x_upperleftwell, y_upperleftwell];

    % Change message displayed in figure window to indicate the user should zoom in on the
    % upper right well
```

```
title('Please zoom in on the middle of the upper right well and press any key.')

% use mouse button to zoom in or out
zoom on;
pause()

zoom off;

% prompt user to click on the middle of the upper right well
title('Please click on the middle of the upper right well.');

[x_click,y_click] = ginput(1);

% store the coordinates of the user-selected upper right well
x_upperrightwell = x_click;
y_upperrightwell = y_click;
zoom out;

array_bounds(2,:) = [x_upperrightwell, y_upperrightwell];

% Change display in imaged window to indicate user should zoom in
% on the middle of the lower right well
title('Please zoom in on the middle of the lower right well and press any key.')

% use mouse button to zoom in or out
zoom on;
pause()
zoom off;

% prompt user to click on the middle of the lower right well
title('Please click on the middle of the lower right well.');

[x_click,y_click] = ginput(1);

% store the user-selected coordinates of the lower right well
x_lowerrightwell = x_click;
y_lowerrightwell = y_click;

array_bounds(3,:) = [x_lowerrightwell, y_lowerrightwell];

% store all of the coordinates of the array bounds to the struct
struct.array_bounds = array_bounds;

% Construct a questdlg to ask the user if they are happy with their
 % well selection
choice = questdlg('Are you happy with your well selections?', ...
'Well selections for array boundaries', ...
'Yes','No','Yes');

% Handle response
switch choice

   case 'Yes';
      disp([choice 'Great, let''s keep going then!'])
      test = 0;
```

```
            case 'No';
                disp([choice 'That''s okay, try again!'])
                test = 1;
        end

    % check whether the user selected array boundaries are correct
    if (x_upperrightwell<x_upperleftwell || y_upperrightwell>y_lowerrightwell)
        test = 1;

        title('Oh no! We detected you selected the wells in the wrong order. Please try again. Press any key to
continue')
        pause()
    else
        test = 0;
    end
  end

    % store the coordinates of the direction vector that extends from the upper left well to the right most point of the
array
    dir_vector1 = [x_upperrightwell,y_upperleftwell] - [x_upperleftwell,y_upperleftwell];

    % store the coordinates of the direction vector that extends from the upper left well to the upper right well
    dir_vector2 = [x_upperrightwell,y_upperrightwell] - [x_upperleftwell,y_upperleftwell];

    % Find angle between the two direction vectors [angle in degrees]
    cosangle = dot(dir_vector1, dir_vector2) / (norm(dir_vector1) * norm(dir_vector2));
    angle = acosd(cosangle);

        if (y_upperrightwell<y_upperleftwell)
            angle=-angle;
        end

    % store the angle used to straigten the image in the struct
    struct.angle=angle;
    transform=1;
end


% Display the rotated image so the array is aligned
b = imrotate(imgrotated, angle, 'nearest','crop');
b_contrasted = histeq(b);
imshow(b_contrasted);
hold on
sz = size(b) / 2;

% Generate a rotation matrix to multiply by the array boundary coordinates
% to attain the new array boundaries in the rotated image
rotation_matrix = [cosd(-angle), -sind(-angle);sind(-angle), cosd(-angle)];

% Multiply the rotation matrix by the upper left well coordinates
new_upper_left = rotation_matrix * [(x_upperleftwell - (sz(2)));(y_upperleftwell - sz(1))];

% Multiply the rotation matrix by the upper right well coordinates
new_upper_right = rotation_matrix * [(x_upperrightwell - sz(2));(y_upperrightwell - sz(1))];
```

```
%Multiply the rotation matrix by the lower right well coordinates
new_lower_right = rotation_matrix * [(x_lowerrightwell - sz(2));(y_lowerrightwell - sz(1))];

% store the new upper left x and y coordinates
x_new_upper_left = new_upper_left(1) + sz(2);
y_new_upper_left = new_upper_left(2) + sz(1);

% store the new upper right x and y coordinates
x_new_upper_right = new_upper_right(1) + sz(2);
y_new_upper_right = new_upper_right(2) + sz(1);

% store the new lower right x and y coordinates
x_new_lower_right = new_lower_right(1) + sz(2);
y_new_lower_right = new_lower_right(2) + sz(1);


% Determine number of wells per row
wells_per_row = round((x_new_upper_right - x_new_upper_left) / horzspacing);
struct.wells_per_row = wells_per_row;

% Determine number of rows
rows = round((y_new_lower_right - y_new_upper_right) / vertspacing);
struct.rows = rows;

% Determine total number of wells
total_wells = wells_per_row * rows;


% for loop to fill in the 3D matrix with ROIs from the image (proceeds row by row of the microwell array from left
to right)
% pre-allocate 3D matrix with zeros
mat = zeros(vertspacing, horzspacing, total_wells);

for i = 1:rows
   for j = 1:wells_per_row

      % determine z-coordinate for the current ROI
      z = (wells_per_row) * (i-1)+j;

      % set row start and end boundaries
      row_start = (round(x_new_upper_left) - horzspacing/2) + ((j-1)*horzspacing);
      row_end = row_start + horzspacing;

      % set column start and end boundaries
      col_start = (round(y_new_upper_left) + ((i-1)*vertspacing));
      col_end = col_start + vertspacing;

      %generate lines that span the x and y coordinates of all the ROIs
      %to overlay over image to show the ROIs
      x = row_start:1:(row_end - 1);
      y = repmat(col_start, 1, length(x));
      y2 = col_start:1:(col_end - 1);
      x2 = repmat((row_end-1), 1, length(y2));
```

```
        % fill the matrix with the image pixels within the current ROI
        % boundaries
        mat(: ,: ,z) = b(col_start:(col_end - 1), row_start:(row_end - 1));

        % plot the ROI grid overlay on the image
        plot(x', y', 'Color', 'w', 'LineStyle','-');
        plot(x', y', 'Color', 'k', 'LineStyle',':');
        plot(x2', y2', 'Color', 'w', 'LineStyle','-');
        plot(x2', y2', 'Color', 'k', 'LineStyle',':');
    end
end

% store the 3D matrix of ROIs to the struct
struct.rois = mat;
end


function [struct] = intProf(struct,backgroundwidth)
% Generate intensity profiles from the ROI stacks in the output of roiGeneration
% and perform background subtraction on the profiles
%
% Outputs
% Struct [structure]: A data structure containing objects (Intensity
%                   profiles for each ROI, 3D matrix with each ROI
%                   contained in a different z, and coordinates of
%                   the ROIs).
%   struct.rois: 3D matrix with each ROI contained in a different z.
%   struct.angle: The angle of rotation to straighten the image (number, in degrees).
%   struct.rotate: The angle of rotation required to display the image with
%   separations running vertically instead of horizontally (number, in
%   degrees).
%   struct.array_bounds: User selected boundaries of the array as a 3x2
%   matrix (rows contain upper left, upper right, and lower left
%   coordinates respectively; first column contains x-coordinates; second column contains y-coordinates).
%   struct.name: The name of the protein target entered by the user
%   (string).
%   struct.wells_per_row: The number of wells per row based on the user
%   selected array bounds and horizontal well spacing.
%   struct.rows: Number of rows in the array
%   struct.int_prof: a 3D matrix containing an array of the intensity
%                   profiles [x, intensity value] indexed by the
%                   third dimension
%
%
% Inputs
%   Struct [structure]: The data structure from roiGeneration containing the
%                     ROIs for each lane
%   backgroundWidth [int]: width of the background region for axial
%                       background subtraction (in pixels)
%

% Load the matrix of ROIs
mat=struct.rois;

% Determine the number and size of the intensity profiles
```

```
[x_dim,y_dim,z_dim]=size(mat);

% Preallocate the intensity profile matrix with zeros

int_profiles=zeros(x_dim,2,z_dim);

% pix_conversion is the number of microns per pixel
pix_conversion=5;

% for loop to generate the intensity profiles for each ROI in the z-stack
%of the matrix Mat. The intensity profile is an average of the pixel intensities
%across the short-axis of the ROI. The background regions are defined by the
%parameter backgroundWidth, and the average pixel intensity in the left and
%right background regions are calculated. The background subtracted intensity
%profile is generated by subtracting the mean background intensity at each
%point along the long-axis of the ROI from the average pixel intensity.
figure
 for i=1:z_dim

    % Get the image of the lane
    lane = mat(:,:,i);

    % Get a list of the x coordinates
    dist = (0:pix_conversion:pix_conversion*(x_dim-1));

    % Sum the image along the y-axis (transverse to separation axis) to
    % generate an intensity profile
    int = sum(lane,2);
    avg_int = int / (y_dim);

    % Get the background regions to the left and right of the lane
    left_backgroundregion = lane(:, (1:backgroundwidth));
    right_backgroundregion = lane(:, (((end + 1) - backgroundwidth):end));

    % Calculate average background intensity in the left and right regions
    left_background_int = (sum(left_backgroundregion, 2)) / backgroundwidth;
    right_background_int = sum(right_backgroundregion, 2)/ backgroundwidth;

    % Create a vector containing the background intensity for each
    % x-coordinate along the lane
    mean_background = (left_background_int + right_background_int) / 2;

    % Subtract the background vector from the intensity profile
    bsub_int = avg_int - mean_background;

    % Create a matrix with one column containing the x-coordinates and a
    % second column containing the background subtracted intensity profile
    lane_profile=[dist',bsub_int];

    % Add the intensity profile to the matrix of intensity profiles
    int_profiles(:,:,i) = lane_profile;

    % Add the intensity profile to the plot
    plot(dist',bsub_int);
```

```
    hold on
end

% Save the intensity profiles to the data structure
struct.int_prof = int_profiles;



end


%% Header
%
%   This function fits Gaussian functions to the intensity profiles
%   generated by fitPeaks for peak calling and quantification.
%
%   Inputs: data_struct: data structure containing the data set with the
%                   following fields:
%                       - int_prof: matrix containing the intensity
%                               profiles
%
%           num_peaks (optional): number of expected peaks
%                           can be 1, 2, or 3. Default is 1
%
%           snr_threshold(optional): Threshold value of signal-to-noise
%                           ratio (SNR).Lanes with at least 1 peak
%                           with an estimated SNR greater than the
%                           threshold value will be curve fit.
%                           Typical threshold value is 3.
%
%
%   Outputs:
% Struct [structure]: A data structure containing objects (Intensity
%                 profiles for each ROI, 3D matrix with each ROI
%                 contained in a different z, and coordinates of
%                 the ROIs).
%   struct.rois: 3D matrix with each ROI contained in a different z.
%   struct.angle: The angle of rotation to straighten the image (number, in degrees).
%   struct.rotate: The angle of rotation required to display the image with
%   separations running vertically instead of horizontally (number, in
%   degrees).
%   struct.array_bounds: User selected boundaries of the array as a 3x2
%   matrix (rows contain upper left, upper right, and lower left
%   coordinates respectively; first column contains x-coordinates; second column contains y-coordinates).
%   struct.name: The name of the protein target entered by the user
%   (string).
%   struct.wells_per_row: The number of wells per row based on the user
%   selected array bounds and horizontal well spacing.
%   struct.rows: Number of rows in the array
%   struct.int_prof: a 3D matrix containing an array of the intensity
%                 profiles [x, intensity value] indexed by the
%                 third dimension
%   struct.good_indices: vector of indices of the intensity profiles and
%                   ROIs that were fit with Gaussian peaks (i.e.
%                   passed the SNR threshold)
```

```
%   struct.good_devices: boolean vector indicating the good devices
%   struc.fit_coefficients: m x 3 x p matrix containing the gaussian fit
%                       coefficients. m is the number of peaks and p
%                       is the number of good devices (good_devices)
%   struct.R2: m x 1 matrix containing the R^2 valuesof the Gaussian fits.
%           m is the numberof good devices (good_devices)
%   struct.ci: 2m x 3 x p matrix containing the gaussian fit confidence
%           intervals for each parameter. m is the number of peaks and p
%           is the number of good devices
%
%   Versions: - 0.1 (4.7.16) Function created
%           - 0.2 Now should be called before goodProfiles()
%           - 0.3 (5.15.16) Data between the user selected  peak boundaries
%               is now used for the gaussian fit (instead of the entire
%               intensity profile).
%           - 0.4 (8.18.17) Function updated with iterative Gaussian fitting
%               for noisy data (first fit refines data to be fit within
%               the peak bounds of the first fit). Also added a field
%               to the struct that contains the confidence intervals
%               for the Gaussian fit parameters.
%
%
%
function data_struct = fitPeaks_beads(data_struct, num_peaks, snr_threshold)
%% Check input arguments
switch nargin

    % If only the data_structure is provided, set num_peaks = 1
    case 1

        num_peaks = 1;

    % If provided, ensure the number of peaks is valid
    case 2
        % Exit function if an invalid number of peaks is input
        if ((num_peaks > 3) || (num_peaks < 1))

            error('Invalid number of peaks');

            return

        end
        %If only 2 input arguments provided, user does not want to run the
        %SNR threshold
        apply_snr_threshold=0;
    case 3
        apply_snr_threshold=1;
        %
    otherwise

        error('Invalid number of input arguments');

        return
```

```
end


%% Get the peaks

% Get the intensity profiles
try
   intensity_profiles = data_struct.int_prof;

catch

   error('Error accessing data_struct.int_prof');

end

% Find all of the good wells
[x_dim,y_dim,z_dim]=size(intensity_profiles);

%store to the structure the starting number of wells analyzed
struct.total_wells=z_dim;


if apply_snr_threshold==1
   % for loop to filter out SNR<3 lanes with a conservative SNR estimate
   %calculated from the max intensity of a smooth data set and the standard
   %deviation of the last 5 pixels of the lane.
   snr3_devices=zeros(z_dim,1);
   snr_est=zeros(z_dim,1);

   %figure
      for i=1:z_dim
         device=intensity_profiles(:,:,i);
         xval=device(:,1);
         yval=device(:,2);
         yvalsmooth=smooth(yval);

         noise_est=std(yval(end-5:end));

         signal_est=max(yvalsmooth);

         snr_est(i)=signal_est/noise_est;

            if snr_est(i)<snr_threshold
               snr3_devices(i)=0;
            else
               snr3_devices(i)=1;
               %plot(xval,yval);
               %hold on
            end
      end
   struct.snr_est=snr_est;

   % Get the number of good wells
   num_good_devices = sum(snr3_devices);
   good_indices=find(snr3_devices==1);
```

```
    % Exit if there are no good wells
    if (num_good_devices == 0)

        error('No good wells in data_struct');

    end
else
    num_good_devices=ones(z_dim,1);
    good_indices=find(num_good_devices==1);
end

% Save the good indices
data_struct.good_indices = good_indices;

%% Get the seed parameters



% Let the user select the points for the parameter estimation

bounds_set = false;

while (~bounds_set)

    % Plot the good devices
    figure(1);
    hold on

    for i = 1:num_good_devices

        device_index = good_indices(i);

        plot(intensity_profiles(:,1, device_index),...
            intensity_profiles(:,2, device_index), '-k');

    end

    hold off

    uiwait(msgbox('Please select left and right boundaries of each peak'));

    % Get the limits of the plot
    y_lim = get(gca, 'YLim');

    % Preallocate the nx2 matrix to hold the peak bounds, where n is the
    % number of peaks. Col 1 is the left bound, col 2 is the right bound
    peak_bounds = zeros(num_peaks, 2);

    for peak = 1:num_peaks

        % Get the left peak boundary
        [x1, y1] = ginput(1);

        % Draw the selected peak boundary
        line([x1, x1], y_lim, 'Color', [0, 0, 1]);
```

```
        % Get the right peak boundary
        [x2, y2] = ginput(1);

        % Draw the selected peak boundary
        line([x2, x2], y_lim, 'Color', [0, 1, 0]);

        % Save the selected bounds

        peak_bounds(peak, :) = [x1, x2];


    end

    % Ask if the peaks are correct
    choice = questdlg('Are the peak bounds correct?', ...
    'Done with bound selection?', ...
    'Yes', 'No','No');

    close

    % If they are done, exit loop
    if (strcmp(choice, 'Yes'))

        bounds_set = true;

    end



end
close all;

% Save the bounds
data_struct.fit_bounds = peak_bounds;

%% Create the fit options

% Create the fit options object with the specified number of peaks

fit_type = 'gauss1';

fit_options = fitoptions(fit_type);

% Assign the locations to the fit options object
for peak = 1:num_peaks

    % Get the left and right bound for the peak
    left_bound = peak_bounds(peak, 1);
    right_bound = peak_bounds(peak, 2);

    % Set the sigma bounds
    sigma_min = 0;
    sigma_max = right_bound - left_bound;
```

```
    % Set the peak center bounds
    x_min = left_bound;
    x_max = right_bound;

    x_min_all(peak) = x_min;
    x_max_all(peak) = x_max;

    % Set the ampitude bounds
    a_min = 0;
    a_max = y_lim(2);

    % set the upper and lower bounds. correct for difference in c and
    % sigma terms
     lower_mat(((3*peak)-2):3*peak) = [a_min, x_min, (sigma_min * sqrt(2))];
     upper_mat(((3*peak)-2):3*peak) = [a_max, x_max, (sigma_max * sqrt(2))];

end


%% Fit each peak

% Preallocate the m x 3 x p matrix for the fit coefficients were m is the
% number of peaks per roi and p is the number of ROIs and col 1 is the
% amplitude, col 2 is the peak center, and col 3 is sigma
data_struct.fit_coefficients = zeros(num_peaks, 3, length(good_indices));
data_struct.ci = zeros(num_peaks*2, 3, length(good_indices));

% Preallocate the m x 1 matrix for the R^2 values for each fit where
% m is the number of good devices
data_struct.R2 = zeros(num_good_devices, 1);

for i = 1:num_good_devices

    device_index = good_indices(i);

    % Display the device number every 50 devices
    %if(mod(i, 50) == 0)

        %fprintf('Fitting lane %d/%d\n', i, num_good_devices);

    %end

    % Get the x and y values
    x = intensity_profiles(:,1, device_index);
    y = intensity_profiles(:,2, device_index);

    for peak = 1:num_peaks

      upper_lim = upper_mat(((3*peak)-2):3*peak);
      lower_lim = lower_mat(((3*peak)-2):3*peak);

      x_min = lower_lim(2);
      x_max = upper_lim(2);
```

```
   fit_options.Lower = lower_lim;
   fit_options.Upper = upper_lim;

   % Determine index of x_min and x_max for selection of x and y values in
   %the region of the peak
   left_diff=abs(x-x_min);
   left_data=find(left_diff==min(left_diff));

   right_diff=abs(x-x_max);
   right_data=find(right_diff==min(right_diff));

   % Get the x and y values in the peak region
   x_fit=x(left_data:right_data);
    y_fit=y(left_data:right_data);

   % Fit the peaks

[fit_object, gof2] = fit(x_fit, y_fit, fit_type, fit_options);

% Get the coefficients
fit_coeffs = coeffvalues(fit_object);
ci = confint(fit_object, 0.95);

% Get peak center and width for re-fitting of peak
    center=fit_coeffs(2);
    sigma=fit_coeffs(3);
    width=sigma/sqrt(2);

   % Determine index of x_min and x_max for selection of x and y values in
   %closer to the peak
   left_diff=abs(x_fit-(center-2*width));
   left_data=find(left_diff==min(left_diff));

   right_diff=abs(x_fit-(center+2*width));
   right_data=find(right_diff==min(right_diff));

   % Get the x and y values in the peak region
   x_fit2=x_fit(left_data:right_data);
    y_fit2=y_fit(left_data:right_data);

   if length(x_fit2) > 3
    % Fit the peaks again
     [fit_object2, gof2] = fit(x_fit2, y_fit2, fit_type, fit_options);

    % Get the coefficients
    fit_coeffs = coeffvalues(fit_object2);
    ci = confint(fit_object2, 0.95);
   end
   % Get peak center and width for AUC calculation
    center=fit_coeffs(2);
    sigma=fit_coeffs(3);
    width=sigma/sqrt(2);

    %determine location of +/- 2 peak widths from the peak center
    auc_left_bound=center-2*width;
```

```
        auc_right_bound=center+2*width;

        % Determine index of auc_left_bound and auc_right_bound for selection of x and y values in
        %the region of the peak
        left_diff_auc=abs(x-auc_left_bound);
        left_data_auc=find(left_diff_auc==min(left_diff_auc));

        right_diff_auc=abs(x-auc_right_bound);
        right_data_auc=find(right_diff_auc==min(right_diff_auc));

        % Make sure the left bound is within the array
        if (left_data_auc < 1)

          left_data_auc = 1;

        end


        % Check to make sure the AUC bounds are within the bounds of the
        % array
        if (right_data_auc > length(y))

           right_data_auc = length(y);


        end

        %Sum data within the peak bounds
        peak_region_intensities=y(left_data_auc:right_data_auc);
        AUC(peak,1,i)=sum(peak_region_intensities);

        data_struct.fit_coefficients(peak, :, i) =...
           fit_coeffs;
        data_struct.ci((peak*2-1):(peak*2), :, i) =...
           ci;
        data_struct.AUC(peak,1,i)=AUC(peak,1,i);

        %get the R^2 values
        all_r2(peak,1,i) = gof2.rsquare;
    end

    % Save the R^2 value to the struct
    data_struct.R2 = all_r2;

end

end

function [data_struct] = goodProfiles_beads(data_struct,r2_threshold,num_peaks)
% Perform quality control on intensity profiles, removing lanes with SNR<3
% and allowing the user to select lanes to remove upon visual inspection
% Generate intensity profiles from the ROI stacks in the output of roiGeneration
% and perform background subtraction on the profiles
%
% Outputs
```

```
% Struct [structure]: A data structure containing objects (Intensity
%                   profiles for each ROI, 3D matrix with each ROI
%                   contained in a different z, and coordinates of
%                   the ROIs).
%   struct.rois: 3D matrix with each ROI contained in a different z.
%   struct.angle: The angle of rotation to straighten the image (number, in degrees).
%   struct.rotate: The angle of rotation required to display the image with
%   separations running vertically instead of horizontally (number, in
%   degrees).
%   struct.array_bounds: User selected boundaries of the array as a 3x2
%   matrix (rows contain upper left, upper right, and lower left
%   coordinates respectively; first column contains x-coordinates; second column contains y-coordinates).
%   struct.name: The name of the protein target entered by the user
%   (string).
%   struct.wells_per_row: The number of wells per row based on the user
%   selected array bounds and horizontal well spacing.
%   struct.rows: Number of rows in the array
%   struct.int_prof: a 3D matrix containing an array of the intensity
%                 profiles [x, intensity value] indexed by the
%                 third dimension
%   struct.good_devices: boolean vector indicating the good devices
%   struct.good_indices: vector of indices of the intensity profiles and
%                    ROIs that were fit with Gaussian peaks
%                    (i.e. passed the SNR threshold)
%   struc.fit_coefficients: m x 3 x p matrix containing the gaussian fit
%                      coefficients. m is the number of peaks and p
%                      is the number of good devices (good_devices)
%   struct.R2: m x 1 matrix containing the R^2 valuesof the Gaussian fits.
%            m is the numberof good devices (good_devices)
%   struct.dev_to_analyze: a bitmask of the good devices The indices refer
%                       to the lanes that were fit (struct.good_indices)
%   struct.index_dev_to_analyze: a vector of the indices to the devices
%                           that passed QC. The indices refer to the
%                           lanes that were fit (struct.good_indices)
%
%
% Inputs
%   Struct [structure]: The data structure from fitPeaks containing the
%                    intensity profiles and fit parameters for each lane
%

% v05 (8.18.17) Gaussian fits are now displayed with the intensity profiles
%              during quality control. Also, a "zoom off" button was added
%              so the user may use zoom features in the GUI, and press the
%              "zoom off" button to re-activate the curve selection/next
%              button.

%% Check input arguments
switch nargin

    % If only the data_structure is provided, set r2_threshold = 0.7
    case 1

        r2_threshold = 0.7;
```

```
    % If provided, ensure the r2 value is valid
    case 2
        % Exit function if an invalid r2 value is input
        if ((r2_threshold<0) || (r2_threshold > 1))

            error('Invalid R^2 value');

            return

        end
end

% Get the intensity profiles
int_prof_all = data_struct.int_prof;

% Determine the number and size of the intensity profiles
[x_dim, y_dim, z_dim] = size(int_prof_all);

% Get the R^2 values from fitPeaks and find all of the lanes that exceed
% the minimum R^2 value
r2 = data_struct.R2;

fit_coeffs = data_struct.fit_coefficients;

if num_peaks == 1
    good_r2 = find(r2 >= r2_threshold);
else

    for i = 1:length(r2)
        r2_comparison(i) = min(r2(:,i));
    end
    good_r2 = find(r2_comparison >= r2_threshold);
end
% determine array position of high r2 value fit lanes
good_indices = data_struct.good_indices;
good_fits = good_indices(good_r2);

good_int_profiles = zeros(x_dim,y_dim,length(good_r2));

% Slice out the lanes that meet the R^2 value threshold
for i = 1:length(good_r2)
    good_int_profiles(:,:,i) = int_prof_all(:, :, good_fits(i));
    good_coeffs(:,:,i) = fit_coeffs(:,:,good_r2(i));
end

% set number of rows/columns of subplots to display in each figure window
n=5;
num_subplots = n * n;

% Calculate the number of plots that need to be displayed and the number of
% n x n panels that are required
plots_display=length(good_r2);
number_subplots = ceil(plots_display/(n*n));

% Preallocate a bitmask to indicate the lanes that pass QC
```

```
good_devices = ones(length(good_r2), 1);

% Preallocate a vector containing the indices of devices to analyze
dev_to_analyze=zeros(z_dim, 1);

% Preallocate a vector for the intensity profiles that pass QC
good_subplots = ones(plots_display,1);

disp(number_subplots);


% for loop to generate subplots for user inspection of the intensity profiles
for i=1:number_subplots

   disp(i);

   h = figure;
   if i==1
      devices_subplot = (1:(n*n));

   elseif i*n*n <= plots_display
      devices_subplot=((i*n*n)-(n*n)+1):((i*n*n));

   else

      devices_subplot=((i*n*n)-(n*n)):(plots_display);
   end

   % Plot all of the intensity profiles
   for j=1:length(devices_subplot)

         % Get the index for the intensity profile subplot
         dev_number = devices_subplot(j);

         % Get the intensity profiles
         device = good_int_profiles(:,:,dev_number);
         xval=device(:,1);
         yval=device(:,2);

         device_coeffs = good_coeffs(:,:,dev_number);
         % Make the subplot
         subplot(n, n, j);

         % Plot. The buttondownfucn Toggles the subplot selection.
         % Function at the bottom of the script
         plot(xval,yval,'LineWidth',2,'Tag', sprintf('%d', dev_number),...
            'buttondownfcn', @clickTest);


         hold on
         for k = 1:num_peaks
            coeff = device_coeffs(k,:);
            a = coeff(1);
            b = coeff(2);
            c = coeff(3);
```

```
            yGauss = a*exp(-((xval-b)/c).^2);
            plot(xval, yGauss,'r','LineWidth',2);
            hold on
        end



    end
    next=0;

    % Add a button to go to the next set of intensity profiles. Function
    % at the bottom of the script
    btn = uicontrol('Style', 'pushbutton', 'String', 'Next',...
        'Position', [500 15 50 30],...
        'Callback',@continueButton2);

    zoom_off = 0;
    btn = uicontrol('Style', 'pushbutton', 'String', 'Zoom Off',...
    'Position', [250 15 50 30],...
    'Callback',@zoomOff);

      hManager = uigetmodemanager(h);
        try
            set(hManager.WindowListenerHandles, 'Enable', 'off');  % HG1
        catch
            [hManager.WindowListenerHandles.Enabled] = deal(false);  % HG2
        end
        set(h, 'WindowKeyPressFcn', []);
        set(h, 'buttondownfcn', []);
        set(h, 'buttondownfcn', @clickTest);
        set(h, 'KeyPressFcn', @myKeyPressCallback);


     % Wait for the user to be done selecting lanes before moving to the
    % next panel
    while next == 0

       pause(0.01);
    end

    %good_devices(devices_subplot(1):devices_subplot(end))=good_subplots;

% Close the current window before creating the next one
close(gcf)
end

% Save the a bitmask of the good devices The indices refer to
% the lanes that were fit (struct.good_indices)
data_struct.dev_to_analyze = good_subplots;

% Save a vector of the indices to the good devices. The indices refer to
% the lanes that were fit (struct.good_indices)
good_subplot_ind = find(good_subplots == 1);
data_struct.index_dev_to_analyze = good_r2(good_subplot_ind);
end
```

```
function [exitZoom] = zoomOff(zoom_off,event)
zoom_off = 1;
if zoom_off ==1
   zoom off
end
end


function [next]=continueButton2(qstring,title,str1,str2,default)
% This function is called with the button the QC GUI is pressed. It
% determines if the is satisified with their selection and moves to the
% next set of intensity profiles if they are.

% Create a dialog to ask the user if they are done.
qstring = 'Are you done selecting devices to throw out?';
title = 'Device Quality Control';
str1 = 'Yes';
str2 = 'No';
default ='Yes';
choice = questdlg(qstring,title,str1,str2,default);

   % If the user is done, move to the next set of intensity profiles. If
   % they are not, allow them to continue selecting intensity profiles
      switch choice
         case 'Yes';
            disp([choice 'Great, let''s keep going then!'])
            next=1;
         case 'No';
            disp([choice 'Okay, please finish selecting devices to throw out'])
            next=0;
      end

% Set the "next" variable to true to allow the while loop to terminate and
% the next set of intensity profiles to be displayed
assignin('caller', 'next', next);

end


function clickTest(line_handle, event)
  % This function handles toggling the subplot state when it is clicked

  % Get the vector of subplot states from the calling workspace.
  good_subplots = evalin('caller', 'good_subplots');

  % Determine the subplot number of the selected plot.
  current_tag = get(line_handle, 'Tag');

  % Get the current state of the selected intensity profile
  subplot_num = str2num(current_tag);
  subplot_state = good_subplots(subplot_num);

  % Uncomment the line below to display which subplot is selected and its
  % current state (for debugging)
```

```
 %disp(sprintf('%d, %d', subplot_num, subplot_state));

 % Toggle the selection based on the last character in the tag
 % (0 = off, 1 = on)

 if (subplot_state)

   set(line_handle, 'Color', [1, 0, 0]);

   good_subplots(subplot_num) = 0;

 else

   set(line_handle, 'Color', [0, 0, 1]);


   good_subplots(subplot_num) = 1;


 end

%  disp(good_subplots);
 assignin('caller', 'good_subplots', good_subplots);


end



function [separation_resolution,wells_to_analyze] = separationPlot(data_structs)
%This function calculates separation resolutions across a microwell array
%for two protein targets. A representative intensity profile for each
%protein is displayed in a figure window with a merged false color image of
%the separation.

% inputs:
% - data_structs: a cell array containing each data structure to
%   analyze% (note: the cell array should contain data structs for proteins separated
%on the SAME gel slide, and the same ROIs should be used in the
%roiGeneration function.

%data_struct2 (struct): Structure containing fit coefficients for gaussian
%fits of a protein peak and indices of lanes to analyze

%outputs:
%separation_resolution (matrix): A matrix containing the separation
%resolutions for each of the separations (from protein peak data in
%data_struct1 and data_struct2).

%wells_to_analyze (cell array): A cell array containing indices of good wells for both targets (referenced
%back to the fit coefficient matrix).

%Versions: - 0.1 (6.1.16) Function created
%         - 0.2 (8.17.16) Fixed indexing bug in selection of good fit
%         coefficients
```

```
%         - 0.3 (5.11.17) Fixed indexing bug in mapping good lanes back to
%         original lane index
%         - 0.4 (6.30.17) Added output variable wells_to_analyze, which is
%         a cell array containing indices for wells for which both proteins passed the QC
%          (note: these indices will not necessarily match because each
%          protein does not necessarily have the same number of lanes for
%          which fitting was performed). Also, updated plotting of the
%          representative separation so that the plot displays two y-axes
%          and each peak is scaled so that y=0 is alligned for both axes.
%          Finally, changed input variable to a cell array data_structs,
%          containing the data structs for the two proteins.

%%
data_struct1 = data_structs{1};
data_struct2 = data_structs{2};

%get good indices of data_struct1 and data_struct2
ind1=data_struct1.index_dev_to_analyze;
ind2=data_struct2.index_dev_to_analyze;

 % Get the indices of the lanes used in the QC step (NOTE: this is
 % different than the indices of the good fits)

   r2_indices1 = data_struct1.good_indices;
   r2_indices2 = data_struct2.good_indices;

   % Map the QC'd lane indices back to the intensity profile indices
   int_prof_ind1 = r2_indices1(data_struct1.index_dev_to_analyze);
   int_prof_ind2 = r2_indices2(data_struct2.index_dev_to_analyze);


    %determine indices of lanes that contained peaks for both proteins
    inds_both = intersect(int_prof_ind1,int_prof_ind2);

    rois = data_struct1.rois;
    zdim = size(rois,3);
    bit_mask_all = zeros(zdim,1);
    bit_mask_all(inds_both) = 1;

    bit_mask_fits1=bit_mask_all(r2_indices1);
    bit_mask_fits2=bit_mask_all(r2_indices2);

    %bit_mask_coeffs1=bit_mask_fits1(ind1);
    %bit_mask_coeffs2=bit_mask_fits2(ind2);

    sep_ind1 = find(bit_mask_fits1==1);
    sep_ind2 = find(bit_mask_fits2==1);

%get all fit coefficients for protein 1 and 2
coeffs1 = data_struct1.fit_coefficients;
coeffs2 = data_struct2.fit_coefficients;

%preallocate matrix of fit coefficients for protein 1 and 2
good_fits1 = zeros(1,3,length(inds_both));
good_fits2 = zeros(1,3,length(inds_both));
```

```
%get fit coefficients for good wells for each protein target
for i=1:length(inds_both)
   index1(i)=sep_ind1(i);
   index2(i) = sep_ind2(i);
   good_fits1(:,:,i)=coeffs1(:,:,index1(i));
   good_fits2(:,:,i)=coeffs2(:,:,index2(i));
end
wells_to_analyze = {index1,index2};
%get peak center locations for protein 1 and 2
peak_loc1=good_fits1(:,2,:);
peak_loc1_all=peak_loc1(:);
peak_loc2=good_fits2(:,2,:);
peak_loc2_all=peak_loc2(:);

%get peak widths for protein 1 and 2
peak_sigma1=good_fits1(:,3,:);
peak_sigma1_all=peak_sigma1(:);

peak_sigma2=good_fits2(:,3,:);
peak_sigma2_all=peak_sigma2(:);

peak_width1=peak_sigma1_all/(sqrt(2));
peak_width2=peak_sigma2_all/(sqrt(2));

%determine separation resolution
delta_x=abs(peak_loc2_all-peak_loc1_all);
separation_resolution=delta_x./(0.5*((4*peak_width1)+(4*peak_width2)));

%% Next we find representative intensity profiles to plot!

%determine mean separation resolution
mean_separation_res=mean(separation_resolution);

%find the difference between the separation resolution of each lane and
%the mean separation resolution for all lanes
separation_res_diff=abs(mean_separation_res-separation_resolution);

%find lane indices that have a separation resolution closest to the mean
representative_lane=find(separation_res_diff==min(separation_res_diff));

%get representative lane index in terms of inds_both
rep_lane=inds_both(representative_lane);

%get good_indices from either data_struct
%good_indices=data_struct1.good_indices;

%get representative lane index in terms of good_indices;
%lane_to_plot=good_indices(rep_lane);


%get intensity profiles
int_prof1=data_struct1.int_prof;
int_prof2=data_struct2.int_prof;
```

```
%plot intensity profiles for protein 1 and 2
int_prof1_plot=int_prof1(:,:,rep_lane);
int_prof2_plot=int_prof2(:,:,rep_lane);

figure
yyaxis left
plot(int_prof1_plot(:,1),int_prof1_plot(:,2),'LineWidth',2);
ylabel('Fluorescence Intensity (AFU)','FontSize',14)
ylim([(0-0.2*max(int_prof1_plot(:,2))) (1.2*max(int_prof1_plot(:,2)))]);
hold on

yyaxis right
plot(int_prof2_plot(:,1),int_prof2_plot(:,2),'LineWidth',2);
ylim([(0-0.2*max(int_prof2_plot(:,2))) (1.2*max(int_prof2_plot(:,2)))]);
title('Representative Separation','FontSize',14)
xlabel('Distance (microns)','FontSize',14)
set(gca,'fontsize',14);
end


% Header
%   Inputs: - data_structs: a cell array containing each data structure to
%                           analyze
%           - wells_to_analyze: a vector containing a bitmask of wells to
%                               analyze (true = analyze,
%                               false = don't analyze)
%           v01: Function created (June 2016)
%           v02: Indexing bug fixed; function now takes wells_to_analyze
%           (an output of separationPlot) as an input argument to correctly
%           select indices to analyze. (07.01.17)



function [rho, p_val, S, AX] = corrPlot(data_structs, wells_to_analyze)

%% Get the variables from the data structures
% Get the number of targets
num_targets = length(data_structs);

% Get the number of wells to correlate
num_wells = length(wells_to_analyze{1});

% Preallocate the AUC matrix
all_auc = zeros(num_wells, num_targets);

% Preallocate the target names cell array
target_names = cell(num_targets, 1);

% Get the AUC and target names for each dataset
% AUC should be a vertical vector. Slicing with only the wells_to_analyze
for struct_index = 1:num_targets

  % Get the AUC vector from the data structure
```

```
    all_auc(:, struct_index) =...
        data_structs{struct_index}.AUC(:,wells_to_analyze{struct_index})';

    % Get the target name from the data structure
    target_names{struct_index, 1} = data_structs{struct_index}.name;


end

%% Take the correlation

% Take the correlation between each target
[rho, p_val] = corr(all_auc);


%% Create the plots

% Create the plot of AUC combinations
 [S, AX] = plotmatrix(all_auc);


% Add the x labels
for x = 1:num_targets

    xlabel(AX(num_targets, x), target_names{x})

end

% Add the y labels
for y = 1:num_targets


    ylabel(AX(y, 1), target_names{y})

end


end % function (corrPlot)
```

Appendix E.

Description of the data structure

The data from the scWB analysis script are stored in a structure array with the following fields:

- **rois**: 3D matrix with each ROI contained in a different z.
- **angle**: The angle of rotation to straighten the image (number, in degrees).
- **rotate**: The angle of rotation required to display the image with separations running vertically instead of horizontally (number, in degrees).

- **array_bounds**: User selected boundaries of the array as a 3x2 matrix (rows contain upper left, upper right, and lower left coordinates respectively; first column contains x-coordinates; second column contains y-coordinates).
- **name**: The name of the protein target entered by the user (string).
- **wells_per_row**: The number of wells per row based on the user selected array bounds and horizontal well spacing.
- **rows**: Number of rows in the array
- **int_prof**: a 3D matrix containing an array of the intensity profiles [x, intensity value] indexed by the third dimension
- **good_indices**: vector of indices of the intensity profiles and ROIs that were fit with Gaussian peaks (i.e. passed the SNR threshold)
- **good_devices**: boolean vector indicating the good devices
- **fit_coefficients**: m x 3 x p matrix containing the gaussian fit coefficients. m is the number of peaks and p is the number of good devices (good_devices)
- **R2**: m x 1 matrix containing the R^2 values of the Gaussian fits. m is the number of good devices (good_devices)
- **dev_to_analyze**: a bitmask of the good devices The indices refer to the lanes that were fit (struct.good_indices)
- **index_dev_to_analyze**: a vector of the indices to the devices that passed QC. The indices refer to the lanes that were fit (struct.good_indices)
- **ci**: a matrix of the upper and lower bound confidence intervals for the fit parameters

To access a field in the data structure, use the following syntax: <structure name>.<field name>. For example, to access the "name" field in a structure named example_struct, use: example_struct.name.

Appendix F.

Allyl Agarose Functionalization of Glass

Goal: Covalently attach agarose to a glass slide to use as a base layer for agarose molding

Reagents:

1. Allyl agarose (Lucidant Polymers)
2. VA-086 Photoinitiator (Wako Chemicals)
3. 1X TAE Buffer
4. Methacrylate silanized glass slides
5. GelSlick solution (Lonza)

Equipment and materials:

1. OAI Collimated UV light source

2. Heat block for Eppendorf tubes (that can go up to 95 C)
3. Hotplate
4. Glass plate that can fit several microscope slides
5. Microwave
6. Glass slide container

Protocol:

Allyl agarose mixture preparation

1. Prepare 2% (w/v) VA-086 in 1X TAE
2. Mix allyl agarose in a 1.7 mL Eppendorf tube with VA-086 in TAE to prepare 2% (w/v) allyl agarose and 0.5% (w/v) VA-086 (total volume should not exceed 1.5 mL)
3. Vortex and use a needle to pierce the cap of the eppendorf tube with the allyl agarose mixture
4. Place the allyl agarose tube on a heat block set to 95 C until the agarose melts
5. Pipette the allyl agarose solution up and down several times to mix

Allyl agarose attachment to glass

6. Place two pieces of tape (80 um thick) on a glass plate just under 3" apart (length of microscope slide).
7. Pipette several hundred microliters of GelSlick solution on the glass plate and use a kimwipe to distribute
8. Place the glass plate on a hotplate with a surface temperature of at least 70 C
9. Pipette 250-300 ul of the allyl agarose solution on the glass plate (keeping the tube in the heat block) and immediately add a methacrylated glass slide functionalized side down.
10. Apply pressure to the glass slide to remove bubbles
11. Repeat until all allyl agarose solution is used (typically 3-4 slides per tube of allyl agarose solution)
12. Remove the glass plate from the hotplate (careful, it's hot!) and place the plate in the OAI UV source, exposing UV for 40s at ~20 mW/cm^2 (make sure the plastic filter is not in the OAI)

Agarose coated glass melting and storage

13. Put the glass plate on a hotplate with a surface temperature over 100 C so that the agarose layer melts (leaving a thin monolayer of agarose bound to the glass surface)
14. Heat a glass slide holder with DI water to a boil in the microwave (use temperature resistant gloves to bring the heated water to the hotplate)
15. Carefully use a razor blade to peel up the agarose coated glass from the glass plate and place in the hot water
16. Use tweezers to remove the agarose glass from the slide container and place on a hotplate to dry. Slides can be stored in a container and used for at least 2 weeks.

Appendix G.

Lab-on-a-chip device

Figure G.1: Lab-on-a chip device fabricated in a Mexican restaurant using hot sauce and a white corn tortilla substrate. Minimum feature sizes are ~7-10 mm, but increase after consumption of sangria or margaritas.

Appendix H.

Fabrication of PDMS Micropost Arrays

Adapted from Sniadecki et al and Yang et al.[287,288]

Goal: Fabricate a PDMS negative mold for repeated casting of a PDMS micropost array.

Materials

- SU-8 micropost master mold (e.g. 30 micron diameter posts, ~40 um height)
- Fluorosilane (tridecafluoro-1,1,2,2-tetrahydrooctyl)-1-trichlorosilane)
- Plastic weigh boat or cup
- Plastic stirrer (e.g. P1000 pipette tip or 5 mL pipette)
- Sylgard 184 (PDMS) base and curing agent (Dow Midland)
- Aluminum foil
- Razor blade
- Pipette for adding PDMS to wafer

Equipment

- Vacuum Dessicator
- Analytical balance

- Hotplate
- Nitrogen stream

Procedure:

SU-8 Mold Pre-treatment

1. Plasma oxidize the SU-8 wafer for ~60s at 100W
2. Use a transfer pipette to add a few drops of fluorosilane to a small petri dish and place with wafer inside a vacuum dessicator
3. Apply vacuum to the dessicator and incubate for at least 1 hour

PDMS Preparation

4. Mix the PDMS elastomer base and curing agent at a 10:1 ratio, stirring vigorously for 3-5 min with a P1000 pipette (the uncured PDMS should be slightly opaque with many small bubbles throughout)
5. Degas the PDMS for at least 1 hour to remove bubbles from the PDMS

PDMS Negative Casting

6. Place the silanized SU-8 wafer in an a small dish fashioned from aluminum foil (with high enough sidewalls to prevent poured PDMS from leaking out of the dish)
7. Pour the PDMS on the silanized SU-8 wafer and use a low pressure N2 stream to blow any bubbles off of the wafer surface
8. Degas the PDMS for at least 30 min (or until bubbles have been removed)
9. Cure the PDMS for 9-11 min at 110C (preferably in an oven, but on a hotplate is also acceptable)
10. Allow the PDMS to cool and use a razor blade to cut out the PDMS from the SU-8 mold

PDMS Negative Mold Pre-treatment

11. Plasma oxidized the PDMS negative mold for 90s at 100W
12. Use a transfer pipette to add a few drops of fluorosilane to a small petri dish and place with the negative PDMS mold inside a vacuum dessicator
13. Apply vacuum to the dessicator and incubate for at least 1 hour

PDMS Preparation

14. Mix the PDMS elastomer base and curing agent at a 10:1 ratio, stirring vigorously for 3-5 min with a P1000 pipette (the uncured PDMS should be slightly opaque with many small bubbles throughout)
15. Degas the PDMS for at least 1 hour to remove bubbles from the PDMS

PDMS Replica Casting

16. Place the silanized PDMS negative mold in an a small dish fashioned from aluminum foil
17. Plasma oxidize a 3x5” glass slide for 90s at 100W
18. Pour the PDMS on the silanized PDMS negative mold and use a low pressure N2 stream to blow any bubbles off of the mold surface

19. Place the plasma cleaned glass slide on top of the uncured PDMS, minimizing bubble introduction by slowly lowering the glass on to the PDMS
20. Cure the PDMS for at least 6 hours (or overnight) at 110C
21. Allow the PDMS to cool to room temperature
22. Apply pressure on the glass to peel away the PDMS replica from the PDMS negative mold

Note: the PDMS negative mold should be re-silanized after every two castings of the PDMS replica.

Appendix I.

Safety addendum

"Where is the glove?"

To the tune of "Where is the Love" by the Black-Eyed Peas

Written by Julea Vlassakis and Britta Berg-Johanssen

Performed by Julea Vlassakis and Amy E. Herr, Ph.D.

Lyrics:

What's wrong with the lab, Amy?

People living like they ain't got no safety.

I think the whole lab to busy being brainy,

Not worrying about toxins that they can't see.

In the hood, yeah, we try to stop the germs spreadin'

But we still got pathogens hear livin'.

In the BUA* the big PSA**,

The blood and the CRISPR and the DNA.

But if you only have gloves in your own size

And your labmates ain't protecting their nice eyes

We got the finest safety shades that money buys
You say you don’t need ‘em but you’re full of lies, yeah

People spillin', hotplates fryin'
Labmates don’t want to hear cryin'
Can you practice good safety
And would you wear your PPE?

Safety officer help us
Send some guidance from above
'Cause people got me, got me questionin'
Where is the glove (glove)?

Where is the glove? (The glove)
Where is the glove? (The glove)
Where is the glove, the glove, the glove.

*BUA: Biological Use Authorization
**PSA: Prostate Specific Antigen

Figure I1: Julea and Amy performing the above safety public service announcement.

Appendix J.

Protocol for Latrunculin Treatment and Phalloidin Staining of Actin in Cells

Goal: To determine the concentration of latrunculin necessary to block actin filament formation of MDA-MB-231 GFP-actin expressing cells by phalloidin staining of F-actin in drug-treated cells.

Latruculin drug treatment

Treatment of MDA-MB-231 cells with as little as 0.5 uM latrunculin A (latA) for 60 minutes has been shown to disrupt the actin cytoskeleton[289]. Other cell types treated with 2 uM latA for at least 10 min display loss of F-actin[290].

Proposed initial conditions: 0, 0.5, 2 uM latrunculin

Stock is 100 ug in ethanol. Gently dry in a nitrogen stream and replace with 23.7 ul of DMSO to make a 10 mM stock (4.2 mg/mL, compared with ~25 mg/mL solubility limit). Stock can be frozen at -20C.

1. Prepared DMEM with 0.1% DMSO (10 mL media, 1 uL of DMSO)
2. Prepare 1000 ul of 2 uM latA: 0.2 ul in 999.8 ul of DMEM+0.1% DMSO
3. Prepared 700 ul of 0.5 uM latA: 175 ul of 2 uM latA in 525 ul of DMEM+0.1% DMSO
4. Aspirate wells of culture slide and add 200 ul of latA solution, or DMEM+0.1% DMSO vehicle control solution. Incubate for 30 min
5. Aspirate wells and replace with 1X PBS

Cell fixation and Phalloidin staining

Prepare 3.7% paraformaldehyde (methanol-free) in PBS solution: 370 ul of formaldehyde in 9.63 mL of PBS

Prepare 0.1% Triton X-100: 10 ul in 10 mL of 1X PBS

Prepare methanolic stock of phalloidin: add 1.5 mL to vial of AF647-phalloidin

Prepare staining solution of phalloidin: Dilute 80 ul of methanolic phalloidin stock in 1.6 mL of solution containing 1600 ul total (with 160 ul 100x Hoechst, and 320 ul BSA+1120 ul of PBS

1. Wash cells twice w/ pre-warmed PBS
2. Fix cells in 3.7% paraformaldehyde solution for 10 min at room temperature
3. Wash cells twice in PBS
4. Add 0.1% Triton X-100 for 3-5 min
5. Wash cells twice in PBS
6. Add 50-100 ul of staining solution to each well of the culture slide and incubate at room temperature for 20 min
7. Wash cells twice in PBS
8. Image on epifluorescent microscope with the 40x objective

Appendix K.

Protocol for fluorescent labeling of total protein in fixed cells

Goal: Covalently attach fluorescent dye to all proteins of fixed cells

Cell Labelling

- Use AlexaFluor 647 Antibody Labeling kit (including sodium bicarbonate buffer and lyophilized Alexa-Fluor dye vial)

1. Centrifuge 5 min @ 3000 RPM to pellet the fixed cells.
2. Resuspend in 1-2 mL PBS.
3. Spin down cell suspension in eppendorf tube to pellet the fixed cells (3000 RPM for 3 min)
4. Remove the buffer supernatant leaving the cell pellet, and add 90 ul of 1X PBS
5. Add 10 ul of 1 M sodium bicarbonate buffer to the cell suspension and pipette up and down to mix well
6. Add the 100 ul solution of fixed cells to the lyophilized dye vial and pipette up and down to mix well (for AF555, dissolve dye in DMSO first)
7. Cover the vial in aluminum foil and place in the eppendorf tube rotator for 1 hour at room temperature
8. Remove the 100 ul cell suspension in the dye vial and pipette into a fresh eppendorf tube
9. Spin down the dyed cell suspension for 5 min at 3000 RPM, remove the supernatant and replace with 100 ul of 1x PBS, mixing well by pipetting up and down (repeat this step 2x)
10. Count labelled cells with hemacytometer
11. Confirm successful fluorescent labeling of the cells by preparing a 1:10 dilution of the re-suspended cells in 1X PBS and imaging on an epifluorescent microscope (10x objective, 100 ms exposure)

Appendix L.

Towards on-chip extraction of protein from fixed cells

This work was performed in collaboration with Dr. Chi-Chih Kang and Dr. Samantha Grist

Archiving clinical samples is commonly performed with formalin-fixed paraffin embedded (FFPE) tissue. However, methylene bridge crosslinks between proteins in the fixed cells hinders downstream protein separation-based analyses. Antigen retrieval buffers have been demonstrated for Western blotting of FFPE samples, however the harsh chemical treatment conditions (~80 °C incubation in high-salt buffers) are incompatible with the recently developed single-cell Western blot. We seek to design a system that enables separation of Her2 isoforms in FFPE breast cancer tissue in the single-cell Western blot to assess isoform heterogeneity at the single-cell level.

One concept considered would allow use of a high density lid gel to minimize losses during fixed lysis, but which could be removed for probing (Figure L.1). Since the fixed cell can be exposed to unpolymerized polyacrylamide without any acute toxicity, high density DK gel precursor containing the antigen retrieval lysis buffer can be introduced to the microwell array with settled fixed cells. Upon heating, the cells will lyse in the gel, and following a buffer exchange to a lower conductivity (and cold) buffer, the protein can be electrophoresed into the separation gel and photocaptured. Upon complete decrosslinking of the DK gel (which contains no bisacrylamide), the separation gel may be probed with antibodies.

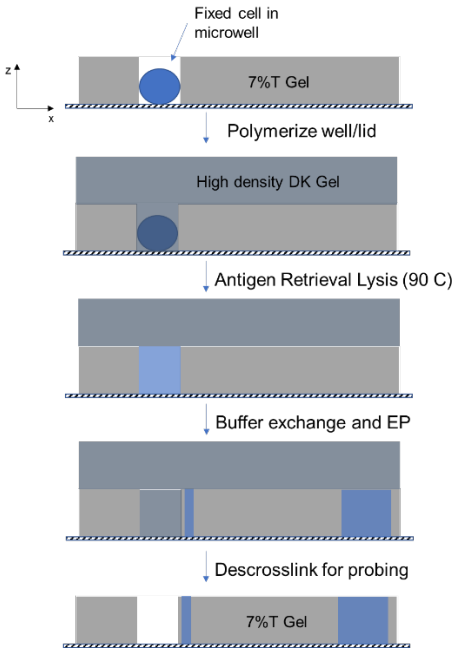

Figure L.1: Concept schematic for well/gel lid to retain protein from fixed cells during harsh antigen retrieval lysis.

In order to evaluate this concept, estimates of diffusive timescales for proteins of interest to leave the well region (assuming a 40 μm tall gel), are provided in Figure L.2, below. The diffusive tau of the smallest Her2 isoform of interest was approximately 4 min in an 18%T gel, which would allow us to perform lysis for 5-10 min, while still retaining an appreciable quantity of protein). However, electrophoresis of the uncleaved Her2 protein would be too slow (requiring over 1000s just for the protein to migrate 76 um). In contrast, the protein would migrate into the separation gel in ~100s if the electric field were increased from ~40 V/cm to ~160 V/cm.

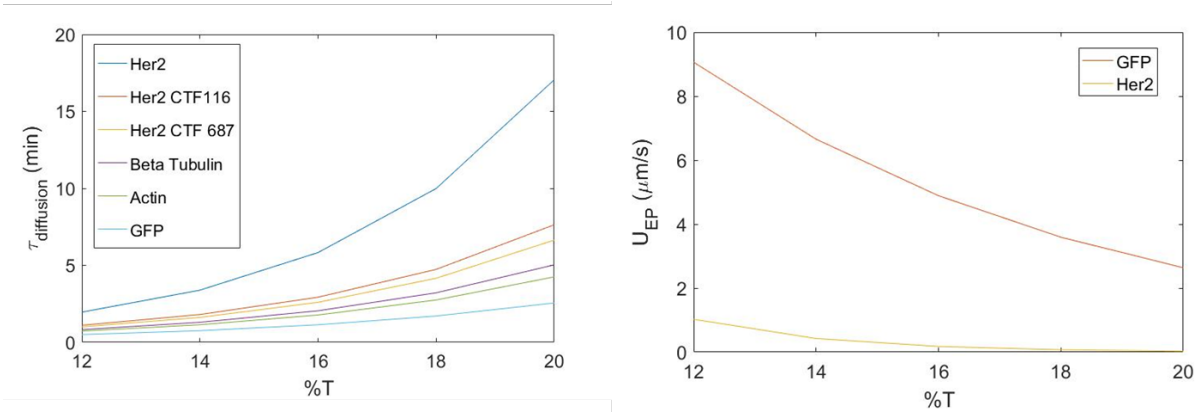

Figure L.2: Analytical estimates of diffusive timescale (left) and electrophoretic velocity (right) for proteins in high percent T gels. The diffusive time scale was estimated assuming a diffusive length scale of 40 microns, and an in-gel diffusion coefficient at 90 degrees C (where the in-gel diffusion factor was determined from Park et al (1990)[87], and the hydrodynamic radius of the protein was found using the expression given in Wilkins et al. (1999)[291]). The electrophoretic velocities were determined from electrophoresis data presented in Duncombe and Kang (2015)[106], assuming an electric field of 40 V/cm.

The scaling estimates provided above were supported by experimental data collected evaluating protein extraction from fixed BT474 cells. As shown in Figure L.3, below, the dense top gel maintains ~50% of the starting protein content (as assessed by measuring fluorescence signal of the fixed cell after direct labeling with AF647 dye, described in the protocol in the previous Appendix) over 20 minutes of antigen retrieval (AR) versus 10% maintained in an open device. However, protein was poorly solubilized and electrophoretically injected into the separation gel.

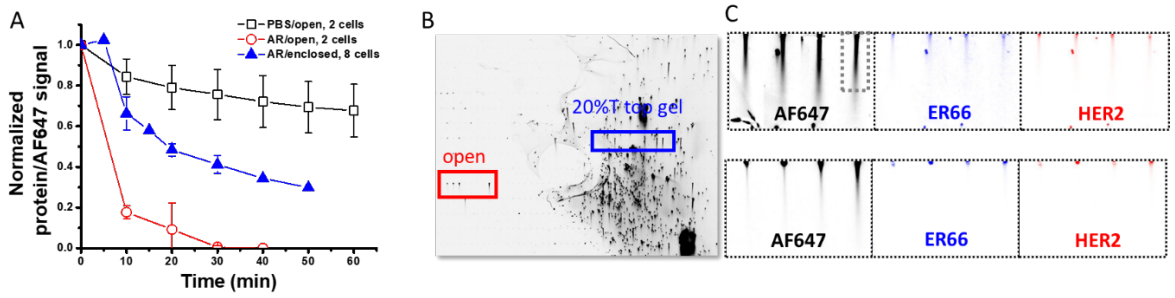

Figure L.3: Quantitation of BT474 fixed cell protein extraction in EP cytometry. (A) Quantification of the normalized AlexaFluor 647 (AF647) signal of proteins in BT474 fixed cells (fixed for 30 min in formalin) directly labeled with AF647 dye, and incubated with the specified buffer at 80°C in a microwell with no gel (open) or 20%T gel (closed). The PBS buffer is a photobleaching control. The antigen retrieval (AR) lysis buffer was 500 mM Tris + 2% SDS. Microwell fluorescence was imaged in a temperature-controlled chamber. (B) Fluorescence micrograph of an EP cytometry device after antigen retrieval lysis and electrophoresis with two regions: open (no gel over the top of the microwell device) and 20%T top gel. (C) Corresponding representative micrographs of the AF647 signal, and ER66 and HER2 immunoprobing signal.

Future efforts to extract protein directly from fixed cells may leverage alternative assay formats such as the SlipChip[292]. Ideally the antigen retrieval would be performed in a fluidically isolated microwell prior to introduction to a separation gel.

Appendix M.

Protocol for DNA functionalization on glass towards barcoding EP cytometry microwells

<u>Silanization of Glass Slides with glycidoxypropyltrimethoxysilane and DNA Functionalization</u>

The following protocol outlines a procedure for functionalizing glass microscope slides with an epoxy silane. This allows for a coupling reaction between amino-modified DNA oligonucleotides and the glass surface, as described.

Part 1: Cleaning of glass slides[293,294]

Reagents:

- Hydrochloric acid (HCl)
- Methanol (MeOH)
- Sulfuric Acid (H_2SO_4)

1. Prepare 1:1 v/v HCl:MeOH solution, add it to a glass container and submerse glass slides in the container for 30 min.
2. Rinse the glass slides 3x in ddH_2O.
3. Add the glass slides to a container of concentrated H_2SO_4 for 30 min.
4. Rinse the glass slides 3x in ddH_2O.
5. Submerse the glass slides in a container of boiling ddH_2O for 30 min.
6. Remove the glass slides from the boiling water and allow to air dry.

Part 2: Epoxy silane functionalization of glass slides[295]

Reagents:

- Glycidoxypropyltrimethoxysilane (GPS)
- Anhydrous toluene

1. Prepare desired v/v % GPS in anhydrous toluene (at least 0.1% for DNA functionalization and 5% to polymerize PA gel on glass), add the solution to a glass container and submerse cleaned glass slides in the container for 30 min at 40° C.
2. Rinse the glass slides 3x in anhydrous toluene
3. Place glass slides in a dish and cure in a convection oven or on a hotplate in a fume hood for 20 min at 110° C.

Part 3: DNA functionalization on glass slides[295]

Reagents:

- DNA oligonucleotides (0.002-2 ug/ul in ddH_2O)
- Betaine
- Saline sodium citrate buffer
- GPS functionalized glass slides

1. Prepare 2x arraying buffer (3M betaine and 6x SSC) and mix 1:1 with the DNA oligonucleotide in the specified concentration range.
2. Spot the DNA solution on the glass surface (needs to be kept humidified to prevent evaporation).
3. Incubate for 8 hr at 42° C in ~50% humidity chamber on a hotplate.
4. Rinse for 2 min in 0.2% SDS solution on a shaker.
5. Wash 3x in DI H_2O and then incubate in DI H_2O for 20 min at 50° C
6. Dry with a nitrogen line, and store slide covered in a dessicator until used.

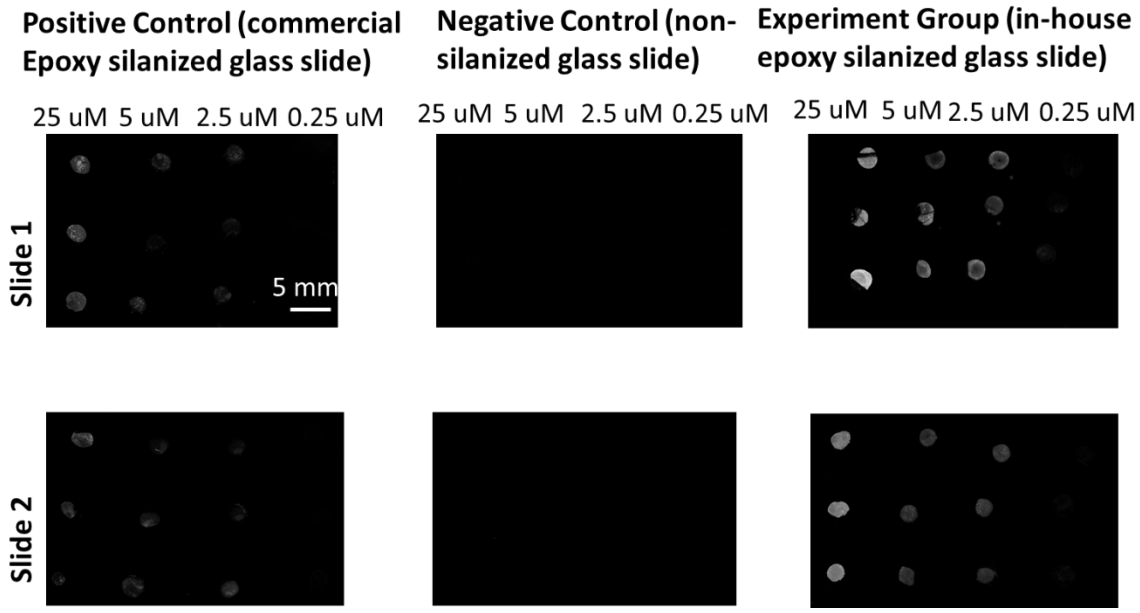

Figure M.1: Initial attempt at fluorescent DNA functionalization of epoxy-silanized glass slides. Above protocol was carried out on three types of glass slides (1 µl of solution at specified concentration in each spot): commercially epoxy silanized (positive control, left), un-silanized

(negative control, center) and in-house cleaned and epoxy silanized slides (experimental group, right).

Appendix N.

Preliminary efforts towards dual RNA and protein measurements in EP cytometry

Measuring multiple types of biomolecule per single cell may shed critical insight on regulation of signaling events at the single cell level. In the case of processes that result in proteoforms that regulate cancer progression, mapping the proteoform expression to the corresponding RNA could elucidate the regulatory events that yield the proteoform.

A method for collecting the transcriptome from a single cell and performing EP cytometry protein detection was proposed. The method would utilize TIVA tagged cells for single-cell RNA-sequencing[296]. Cells uptake the TIVA tags and upon UV photo-lysis of the tag, and exposed poly-u tail can bind to the poly-a tail of cytoplasmic mRNA in the cell. The tag also includes a biotin group, and thus the transcriptome may be collected on a streptavidin coated bead. Thus, by including a streptavidin-coated bead in the microwell (Figure N.1), the transcriptome may be collected on the EP cytometry device. Transfer of the bead off of the device would allow for off-chip RNA-sequencing (Figure N.2).

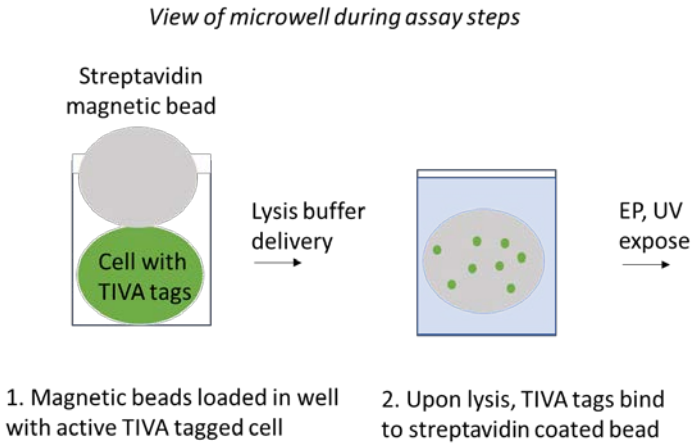

Figure N.1: Proposed schematic workflow for collection of the transcriptome of a single cell with a magnetic bead in the EP cytometry microwell. TIVA-tagged cells are lysed and the TIVA tags are collected on the streptavidin coated bead (via the biotinylated tag). The EP cytometry assay is performed and beads are collected from the device.

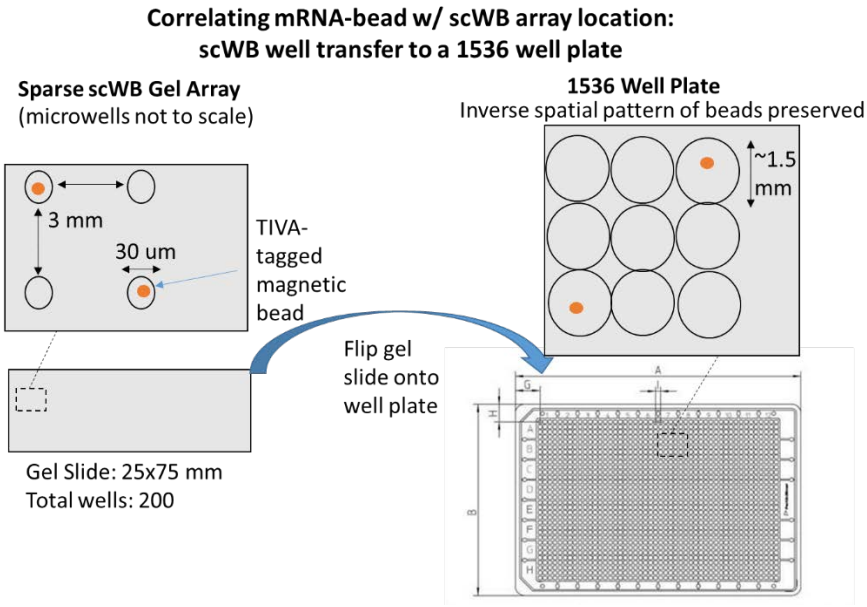

Figure N.2: Approach for preserving spatial pattern of beads in EP cytometry array taken off-chip for cDNA synthesis, library prep and RNA-sequencing. A sparse EP cytometry array with ~3 mm well-to-well spacing (total of 200 microwells) will be flipped upside down over a 1536 well plate (well diameters ~ 1.5 mm) on which downstream cDNA synthesis and library prep may be performed prior to sequencing. Fluorescence measurements of Cy3 on the TIVA-tagged magnetic beads in the 1536 well plate will be used to correlate position of bead in plate back to the scWB array (the inverse spatial pattern). Image of well plate from Perkin Elmer (http://www.perkinelmer.com/catalog/family/id/viewplates).

We assessed the role of BSA blocking and UV exposure of the EP cytometry gel and magnetic microparticles in evaluating the transfer efficiency of beads out of the the EP cytometry wells. Blocking was performed by incubating the beads and EP cytometry gel overnight in 1X TBST with the specified BSA percentage. Transfer was performed by applying a magnetic field below the EP cytometry device, inverting the device over a 1536 well plate and then removing the magnet and placing it under the well plate. A high-grade N52 magnet with a ~3600 gauss B-field through the well-plate (based on finite element analysis simulations) was used. Interestingly, the impact of the UV exposure on bead retention in the wells was dependent on the blocking strategy employed. As shown in Figure N.3, below, in a blocking condition with 4% BSA on both the beads and gel surface, complete transfer occurred in 75% of UV exposed wells, and 80% of non-exposed wells (on a different gel slide). In contrast, as shown in Figure N.4 when no blocking was performed, complete transfer occurred in only 37% of UV exposed wells vs. 76% in non-UV exposed wells. Notably, BSA blocking also impacted biotin loading on the streptavidin bead (Figure N.5), so further investigation is warranted to determine if the blocking, biotin bead binding and bead transfer scheme described here could be usable for transfer of biomolecules off chip.

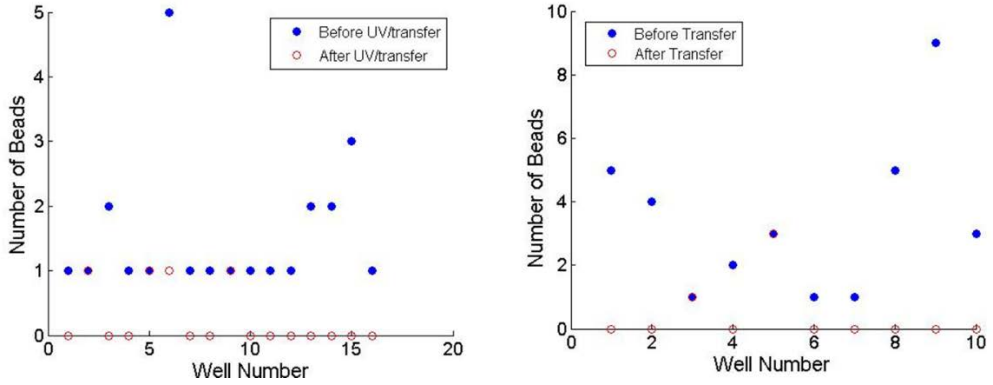

Figure N.3: Evaluation of UV exposure on magnetic bead transfer (with gel/beads blocked in 4% BSA 1X TBST). Left: UV exposed gel (75% complete transfer). Right: No UV negative control (80% complete transfer).

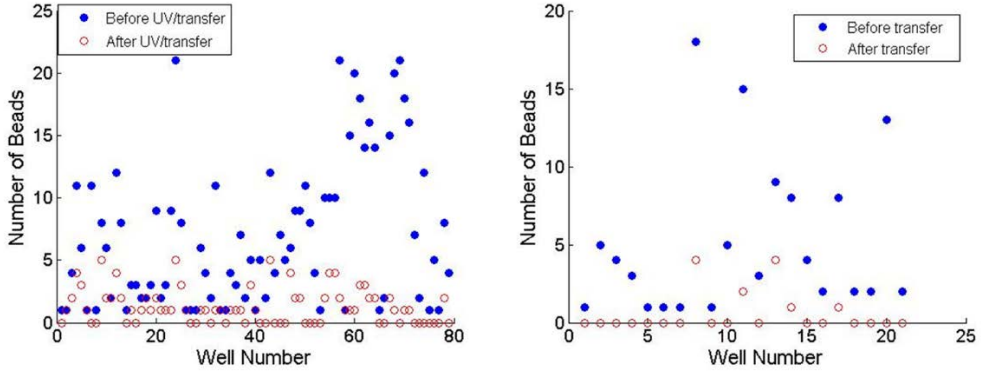

Figure N.4: Evaluation of UV exposure on magnetic bead transfer (without blocking). Left: UV exposed gel (37% complete transfer). Right: No UV negative control (76% complete transfer).

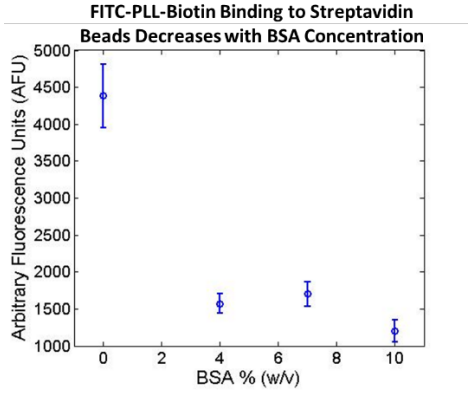

Figure N.5: Streptavidin bead binding of FITC-PLL-Biotin falls by ~34% when BSA blocking utilized. Beads previously blocked in BSA at the specified w/v% were incubated in stock FITC-PLL-Biotin (80 μM for 1 hr) were washed 3x in 1X PBS and imaged.

TIVA tags were generously provided by the Eberwine Lab at the University of Pennsylvania. The UV-activation of the tags was tested in a glass microchannel by fluorescence imaging of the

FRET probes on the TIVA tag (Figure N.6). Recovery of the Cy3 fluorescence signal upon UV photolysis of the probe yielded a 2 to 2.5-fold fluorescence increase (Figure N.7), suggesting successful photolysis and probe activation.

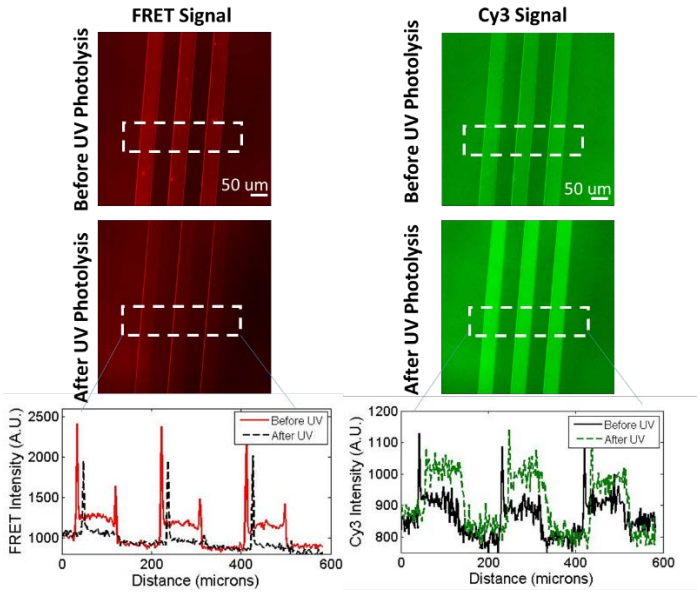

Figure N.6: Visualizing FRET reduction (left) and Cy3 recovery (right) upon UV photolysis of 1 μM TIVA solution in microchannels (20 mW/cm^2 at 365 nm on the OAI collimated UV source for 5 min).

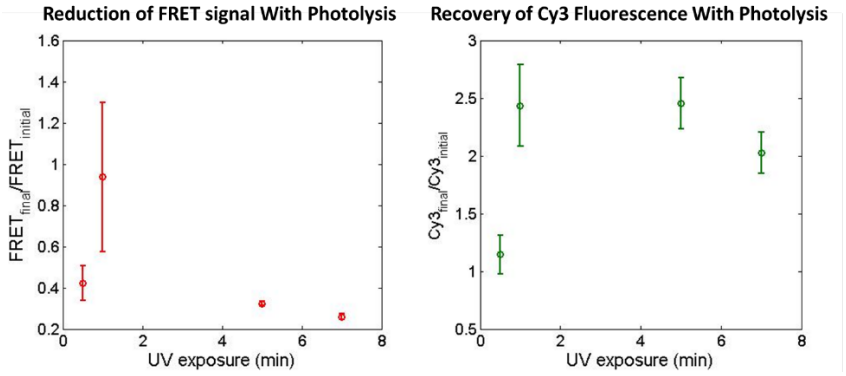

Figure N.7: Quantitation of the mean reduction of FRET signal (left) and recovery of Cy3 fluorescence (right) from microchannels in Figure N.3 upon UV photolysis (20 mW/cm^2 at 365 nm on the OAI collimated UV source for the specified time). FRET signal was recorded with Cy3 excitation and Cy5 emission filters, and final signal refers to after-UV, while initial is before the UV exposure. Fluorescent signal at various channel locations was background subtracted and averaged. Error bars are standard deviations from n=3 channels.

Appendix O.

Cell line authentication certificates

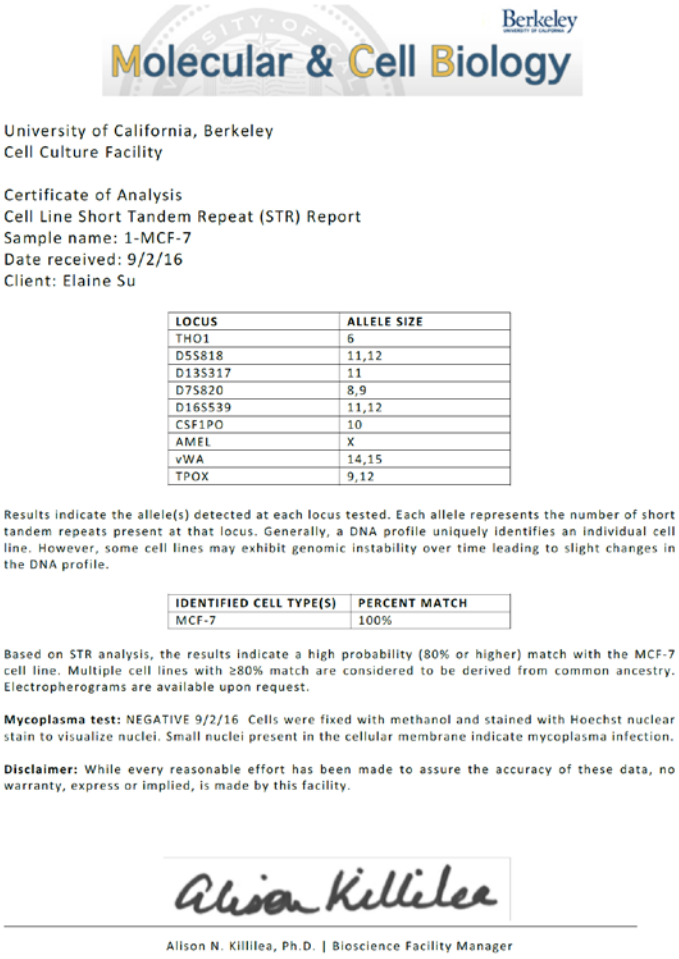

Berkeley
Molecular & Cell Biology

University of California, Berkeley
Cell Culture Facility

Certificate of Analysis
Cell Line Short Tandem Repeat (STR) Report
Sample name: 1-MCF-7
Date received: 9/2/16
Client: Elaine Su

LOCUS	ALLELE SIZE
THO1	6
D5S818	11,12
D13S317	11
D7S820	8,9
D16S539	11,12
CSF1PO	10
AMEL	X
vWA	14,15
TPOX	9,12

Results indicate the allele(s) detected at each locus tested. Each allele represents the number of short tandem repeats present at that locus. Generally, a DNA profile uniquely identifies an individual cell line. However, some cell lines may exhibit genomic instability over time leading to slight changes in the DNA profile.

IDENTIFIED CELL TYPE(S)	PERCENT MATCH
MCF-7	100%

Based on STR analysis, the results indicate a high probability (80% or higher) match with the MCF-7 cell line. Multiple cell lines with ≥80% match are considered to be derived from common ancestry. Electropherograms are available upon request.

Mycoplasma test: NEGATIVE 9/2/16 Cells were fixed with methanol and stained with Hoechst nuclear stain to visualize nuclei. Small nuclei present in the cellular membrane indicate mycoplasma infection.

Disclaimer: While every reasonable effort has been made to assure the accuracy of these data, no warranty, express or implied, is made by this facility.

Alison Killilea

Alison N. Killilea, Ph.D. | Bioscience Facility Manager

Figure O.1: Cell line authentication certificate for MCF-7 cells.

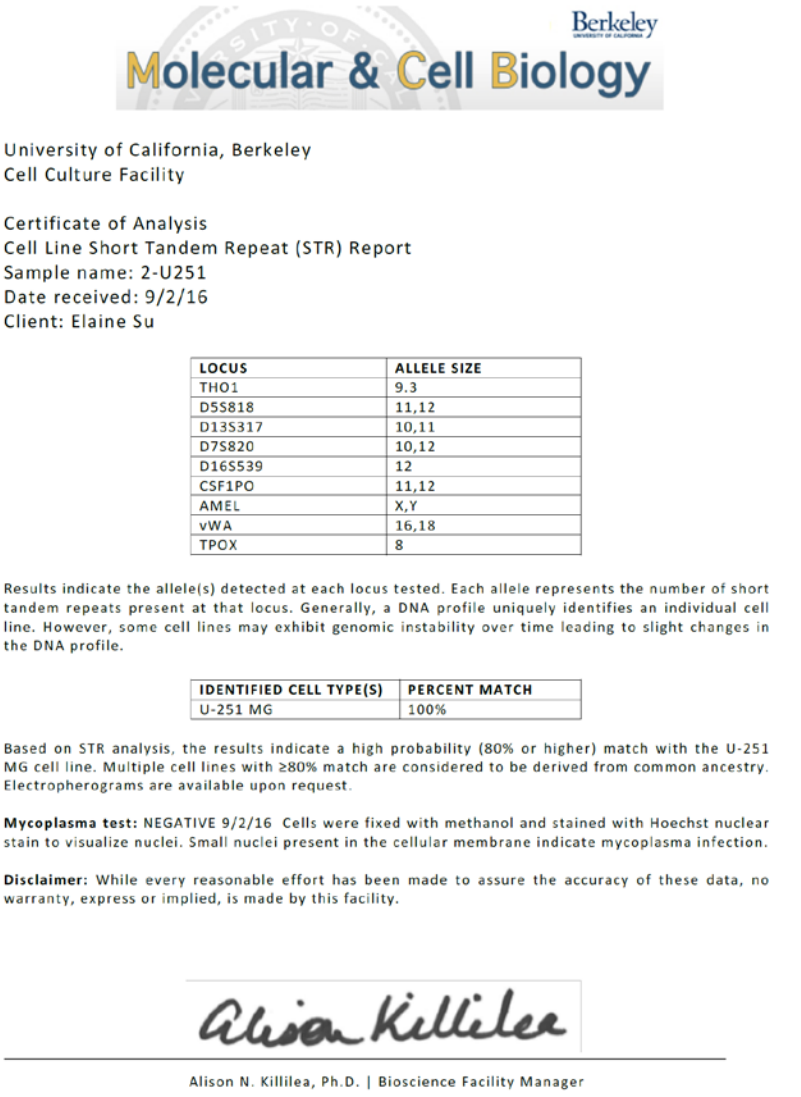

Berkeley
Molecular & Cell Biology

University of California, Berkeley
Cell Culture Facility

Certificate of Analysis
Cell Line Short Tandem Repeat (STR) Report
Sample name: 2-U251
Date received: 9/2/16
Client: Elaine Su

LOCUS	ALLELE SIZE
THO1	9.3
D5S818	11,12
D13S317	10,11
D7S820	10,12
D16S539	12
CSF1PO	11,12
AMEL	X,Y
vWA	16,18
TPOX	8

Results indicate the allele(s) detected at each locus tested. Each allele represents the number of short tandem repeats present at that locus. Generally, a DNA profile uniquely identifies an individual cell line. However, some cell lines may exhibit genomic instability over time leading to slight changes in the DNA profile.

IDENTIFIED CELL TYPE(S)	PERCENT MATCH
U-251 MG	100%

Based on STR analysis, the results indicate a high probability (80% or higher) match with the U-251 MG cell line. Multiple cell lines with ≥80% match are considered to be derived from common ancestry. Electropherograms are available upon request.

Mycoplasma test: NEGATIVE 9/2/16 Cells were fixed with methanol and stained with Hoechst nuclear stain to visualize nuclei. Small nuclei present in the cellular membrane indicate mycoplasma infection.

Disclaimer: While every reasonable effort has been made to assure the accuracy of these data, no warranty, express or implied, is made by this facility.

Alison Killilea

Alison N. Killilea, Ph.D. | Bioscience Facility Manager

Figure O.2: Cell line authentication certificate for U251 (U373) GFP-cells.

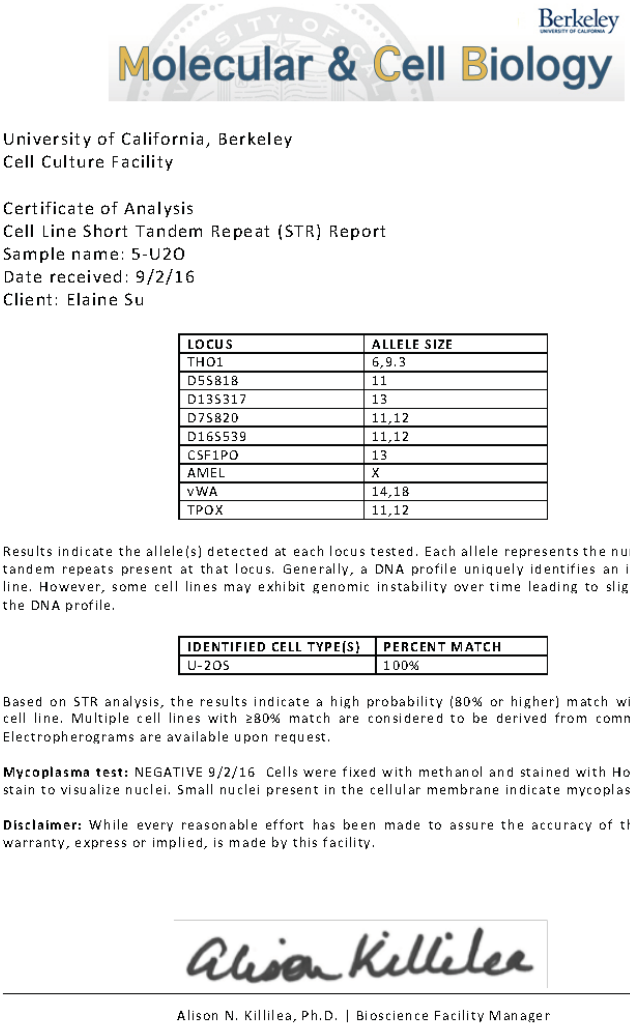

Berkeley
Molecular & Cell Biology

University of California, Berkeley
Cell Culture Facility

Certificate of Analysis
Cell Line Short Tandem Repeat (STR) Report
Sample name: 5-U2O
Date received: 9/2/16
Client: Elaine Su

LOCUS	ALLELE SIZE
THO1	6,9.3
D5S818	11
D13S317	13
D7S820	11,12
D16S539	11,12
CSF1PO	13
AMEL	X
vWA	14,18
TPOX	11,12

Results indicate the allele(s) detected at each locus tested. Each allele represents the number of short tandem repeats present at that locus. Generally, a DNA profile uniquely identifies an individual cell line. However, some cell lines may exhibit genomic instability over time leading to slight changes in the DNA profile.

IDENTIFIED CELL TYPE(S)	PERCENT MATCH
U-2OS	100%

Based on STR analysis, the results indicate a high probability (80% or higher) match with the U-2OS cell line. Multiple cell lines with ≥80% match are considered to be derived from common ancestry. Electropherograms are available upon request.

Mycoplasma test: NEGATIVE 9/2/16 Cells were fixed with methanol and stained with Hoechst nuclear stain to visualize nuclei. Small nuclei present in the cellular membrane indicate mycoplasma infection.

Disclaimer: While every reasonable effort has been made to assure the accuracy of these data, no warranty, express or implied, is made by this facility.

Alison N. Killilea, Ph.D. | Bioscience Facility Manager

Figure O.3: Cell line authentication certificate for U20S-RFP-LifeAct cells.

University of California, Berkeley
Cell Culture Facility

Certificate of Analysis
Cell Line Short Tandem Repeat (STR) Report
Sample name: 6-MDA-D
Date received: 9/2/16
Client: Elaine Su

LOCUS	ALLELE SIZE
THO1	7,9.3
D5S818	12
D13S317	12,13
D7S820	8,9
D16S539	12
CSF1PO	12,13,14
AMEL	X
vWA	15,19
TPOX	8,9

Results indicate the allele(s) detected at each locus tested. Each allele represents the number of short tandem repeats present at that locus. Generally, a DNA profile uniquely identifies an individual cell line. However, some cell lines may exhibit genomic instability over time leading to slight changes in the DNA profile.

IDENTIFIED CELL TYPE(S)	PERCENT MATCH
MDA-MB-231	89%

Based on STR analysis, the results indicate a high probability (80% or higher) match with the MDA-MB-231 cell line. Multiple cell lines with ≥80% match are considered to be derived from common ancestry. Electropherograms are available upon request.

Mycoplasma test: NEGATIVE 9/2/16 Cells were fixed with methanol and stained with Hoechst nuclear stain to visualize nuclei. Small nuclei present in the cellular membrane indicate mycoplasma infection.

Disclaimer: While every reasonable effort has been made to assure the accuracy of these data, no warranty, express or implied, is made by this facility.

Alison Killilea

Alison N. Killilea, Ph.D. | Bioscience Facility Manager

Figure O.4: Cell line authentication certificate for MDA-MB-231 GFP-actin cells.

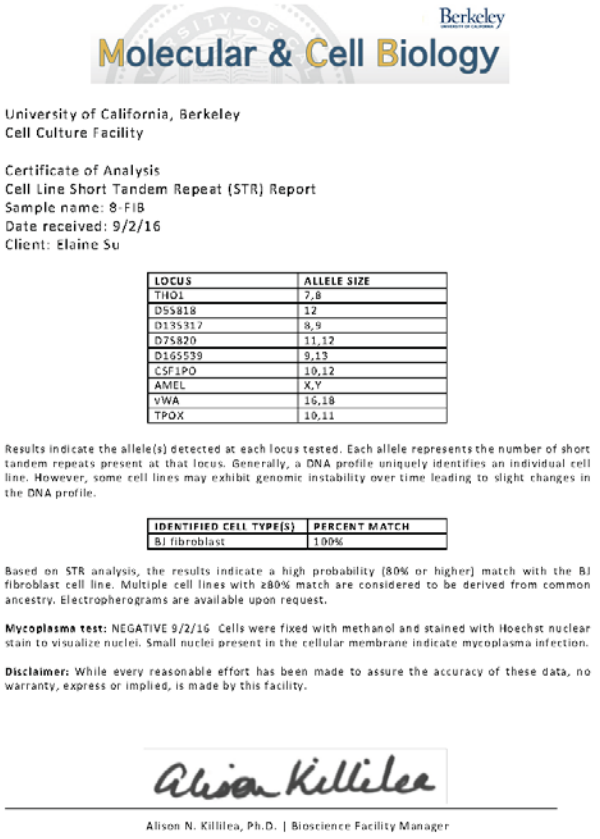

Berkeley
Molecular & Cell Biology

University of California, Berkeley
Cell Culture Facility

Certificate of Analysis
Cell Line Short Tandem Repeat (STR) Report
Sample name: 8-FIB
Date received: 9/2/16
Client: Elaine Su

LOCUS	ALLELE SIZE
THO1	7,8
D5S818	12
D13S317	8,9
D7S820	11,12
D16S539	9,13
CSF1PO	10,12
AMEL	X,Y
vWA	16,18
TPOX	10,11

Results indicate the allele(s) detected at each locus tested. Each allele represents the number of short tandem repeats present at that locus. Generally, a DNA profile uniquely identifies an individual cell line. However, some cell lines may exhibit genomic instability over time leading to slight changes in the DNA profile.

IDENTIFIED CELL TYPE(S)	PERCENT MATCH
BJ fibroblast	100%

Based on STR analysis, the results indicate a high probability (80% or higher) match with the BJ fibroblast cell line. Multiple cell lines with ≥80% match are considered to be derived from common ancestry. Electropherograms are available upon request.

Mycoplasma test: NEGATIVE 9/2/16 Cells were fixed with methanol and stained with Hoechst nuclear stain to visualize nuclei. Small nuclei present in the cellular membrane indicate mycoplasma infection.

Disclaimer: While every reasonable effort has been made to assure the accuracy of these data, no warranty, express or implied, is made by this facility.

Alison N. Killilea, Ph.D. | Bioscience Facility Manager

Figure O.5: Cell line authentication certificate for BJ fibroblast cells.

Appendix P.

Autofluorescence in EP cytometry

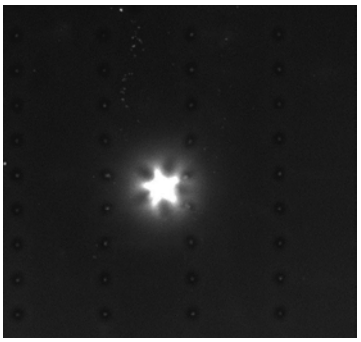

Figure P.1: Encouragement comes from unexpected sources. Fluorescence micrograph of an adorable star-shaped auto-fluorescent object on an EP cytometry device. Remember, you're a star!